Dissertation
submitted to the
Combined Faculties of the Natural Sciences and Mathematics
of the Ruperto-Carola University of Heidelberg, Germany
for the degree of
Doctor of Natural Sciences

Put forward by

Dipl. Phys. Raphael Scelle
Born in: Bad Mergentheim, Germany

Oral examination: 19. June, 2013

Dynamics and Motional Coherence of Fermions Immersed in a Bose Gas

Referees: Prof. Dr. Markus K. Oberthaler
Prof. Dr. Selim Jochim

Zusammenfassung

Die vorliegende Arbeit untersucht den Einfluss eines Bosegases aus Natriumatomen auf die Kohärenz fermionischer Lithiumatome, die sich in einer Superposition zweier Bewegungszustände befinden. Zu diesem Zweck implementieren und charakterisieren wir ein Lithium-selektives Gitterpotential. Das Verschieben der Gitterposition koppelt Zustände aus Blochbändern unterschiedlicher Parität und führt bei periodischer Modulation zu Rabi-Oszillationen zwischen dem ersten und zweiten Blochband. Mit Hilfe dieses Kopplungsmechanismus untersuchen wir die zeitliche Entwicklung der Lithiumatome in Ramsey- und Spin-Echo-Experimenten. Die Wechselwirkung mit den Natriumatomen verursacht einen Kohärenzzerfall der Lithiumatome, dessen Zerfallszeit wir durch den Vergleich der Spin-Echo-Signale mit und ohne bosonischem Hintergrund bestimmen. Wir beobachten, dass der Verlust der Kohärenz auf einer etwas längeren Zeitskala als die Relaxation zwischen den Blochbändern erfolgt und schließen daraus, dass der Kohärenzzerfall durch Relaxationsprozesse getrieben ist. Zudem überprüfen wir diese Schlussfolgerung anhand einer Mastergleichung, die die zeitliche Entwicklung einzelner Teilchen in einem Bosegas beschreibt. Unsere Berechnungen stimmen qualitativ mit unseren Beobachtungen überein und bestätigen, dass die Dynamik der Lithiumatome durch Relaxationsprozesse dominiert ist.

Abstract

This thesis investigates the motional coherence of fermionic lithium atoms immersed in a Bose gas of sodium atoms. For this purpose, we implement and characterize a species-selective lattice potential for lithium. Shifting the lattice position couples Bloch bands of opposite parity and we observe Rabi oscillations between the first and second band for periodic modulation. We employ the coherent coupling between the bands to study the evolution of the lithium atoms in Ramsey and spin echo-type experiments. The interaction between the bosonic bath and the lithium atoms causes the loss of motional coherence, and we determine the decoherence time by analyzing the corresponding spin echo signal relative to the signal without Bose gas. We observe that the coherence decay occurs on a slightly longer time scale than the relaxation dynamics of motionally excited lithium atoms, and conclude that the loss of motional coherence is primarily induced by relaxation processes. Moreover, we test this interpretation by means of a master equation which governs the evolution of a single particle immersed in a Bose gas. Our calculations agree qualitatively with our experimental observations and confirm that the dynamics of the lithium atoms are dominated by relaxation processes.

Contents

1. Introduction

Since the development of quantum mechanics in the early 20^{th} century, physicists have debated about its interpretation and the transition from the quantum to the classical world [1, 2, 3]. The most common approach dates back to 1928 when Niels Bohr and Werner Heisenberg formulated the Copenhagen interpretation which states that a quantum mechanical measurement corresponds to an instantaneous collapse of the system's wavefunction to an eigenstate of the measured observable. In general, this collapse is non-deterministic and the probability to measure a certain eigenvalue is determined by the projection of the wavefunction onto the corresponding eigenstate. The Copenhagen interpretation proved to be a powerful tool in order to describe the observations of many quantum mechanical experiments, but its probabilistic character runs contrary to our classical intuition. The most prominent example for this objection originates from Erwin Schrödinger who indicated that according to quantum mechanics a cat could be simultaneously dead and alive [4].

However, this paradox can be resolved phenomenologically as superpositions of quantum states are only preserved in closed systems, whereas the superpositions decay in open systems due to coupling to the environment and the corresponding density matrix evolves towards its classical counterpart. This process is commonly referred to as decoherence [5] and prevents the observation of quantum superpositions in everyday life. Because of its fundamental importance for the transition between the classical and quantum mechanical regime, decoherence has been studied in a variety of experiments which analyzed the decay of superpositions by controlling the interaction with the classical environment [6, 7]. More recent measurements aim to understand the decoherence mechanisms from first principles [8, 9] and are based on the ideas of Richard Feynman, who proposed to use a so-called quantum simulator in order to emulate quantum systems with large Hilbert spaces [10]. These experiments prepare a single well-controlled particle in a superposition and investigate its subsequent evolution in a quantum mechanical bath. As these model systems evolve overall unitary, the initial wavefunction does not instantaneously collapse and the information about the coherence is preserved. Though, due to the coupling between both components, the information is transferred to the bath's degrees of freedom. Because of their large number, the particle does never recover the initial superposition and its coherence is effectively lost.

These experiments directly relate the decoherence of the particle to the bath's large Hilbert space and present a remarkable demonstration of Feynman's quantum simulator. Indeed, his concept is not restricted to bridging the gap between the classical and quantum world, but also helped to address other long standing questions of quantum mechanics. A further famous example for its realization is the investigation of the Bardeen-Cooper-Schriefer (BCS) pairing mechanism in ultracold Fermi gases [11, 12, 13]. The high degree of control over this quantum system enabled to set a two-component Fermi gas into rotation and to tune the interaction between its species by

means of a Feshbach resonance [14, 15]. The direct observation of a vortex lattice in the strongly attractive regime revealed the superfluid character of the Fermi gas and proofed the existence of a BCS-like pairing mechanism.

Whereas these experiments studied the mechanisms for BCS-type superconductivity in an ultracold quantum gas, similar experiments could also contribute to the comprehension of high-temperature superconductors. A debated but so far unconfirmed mechanism for their superconductivity is the formation of bound polaron pairs [16]. In the context of condensed matter, a polaron consists of an electron, which polarizes an ion crystal lattice due to its Coulomb potential, and its self-induced polarization field i. e. the lattice phonons. It has been shown theoretically that an equivalent quasi-particle exists in the framework of ultracold quantum gases [17, 18]. In this case, the polaron is composed of an impurity atom immersed in a Bose-Einstein condensate [19, 20] and the self-induced elementary excitations of the Bose gas, which form the counterpart to the lattice phonons. This polaron manifestation is of special interest as Feshbach resonances provide the opportunity to tune the coupling between its constituents into the strongly interacting regime, which could not be accessed yet by solid state experiments. Though, polaron formation has so far not been clearly verified in ultracold quantum gases. First investigations revealed the mediation of the boson-boson interaction due to Bose-Fermi interaction [21] and showed evidence for polaronic behavior in a one-dimensional Bose-Fermi mixture [22].

Our experiment aims to test the analogy between the two polaron versions. For this purpose, we immerse fermionic lithium atoms into a sodium Bose-Einstein condensate and intend to map out their trapping frequency in a species-selective lattice potential. The formation of quasi-particles manifests in a lower frequency compared to freely evolving atoms as the polaron's dynamics are governed by an effective mass which exceeds the pure mass of the lithium atoms.

In order to detect also small frequency shifts, we need to develop appropriate experimental techniques. Moreover, the precision of the frequency measurements is fundamentally limited by the probe time and by mechanisms which cause the collapse of the impurity's wavefunction during the probe time. Hence, the interaction between the lithium atoms and the sodium Bose-Einstein condensate does not only give rise to the formation of quasi-particles, but also restricts their investigation due to decoherence processes.

However, these processes do not only limit our measurements, but provide beyond that the opportunity to investigate decoherence mechanisms in a closed quantum system which is not governed by spin-spin interactions as previous experiments [8, 9]. Instead, the dynamics of the lithium atoms in the sodium background are controlled by a density-density-type interaction, and the coherence of the lithium atoms decays due to coupling to the elementary excitations of the degenerate Bose gas. Thus, the coherence loss depends on the interaction between the background atoms, and the characteristics of the loss mechanisms differ from those in spin systems due to the continuity of the excitation spectrum.

Contents of this Thesis

This thesis is organized as follows. Chapter 2 presents briefly the basic concepts of ultracold quantum gases and introduces our experimental setup producing a mixture of fermionic lithium

and bosonic sodium. The following chapters 3, 4 and 5 discuss the species-selective lattice potential which is our main tool to address the lithium atoms and probe their evolution in the sodium cloud. Chapter 3 starts with a general discussion of basic lattice theory and is directed to design the lattice according to our needs. Subsequently, we characterize the lattice potential in chapter 4, and investigate the coherent control over the lithium atoms with the help of the optical lattice in chapter 5. In this context, a spin echo technique is developed in order to explore the motional coherence of the lithium atoms during the immersion in the sodium bath.

The following chapters focus on the dynamics of the lithium atoms in the Bose gas. First, chapter 6 introduces the corresponding theoretical framework and deduces the master equation for an impurity immersed in a bosonic bath. Subsequently, the relaxation dynamics of motionally excited lithium atoms due to interaction with the sodium background are studied in chapter 7, and we compare the experimental findings to our previous, theoretical considerations. Finally, we investigate the interaction induced loss of motional coherence in chapter 8 and analyze the loss mechanisms by means of the relaxation dynamics.

2. Bose-Fermi Mixture of Sodium and Lithium

This chapter presents a brief theoretical overview of ultracold Bose and Fermi gases. It is not meant to provide a complete theoretical description, but rather introduces the basic concepts which are necessary for the analysis of the experimental data and measurements presented in the following chapters. Hereby, the chapter focuses mainly on the density distribution of the two gases as we finally intend to investigate the dynamics of immersed (fermionic) atoms in a bosonic bath which depend on the density of both components.

The first section starts with a discussion of the Gross-Pitaevskii equation for weakly interacting bosons in order to obtain their density distribution in a trapping potential. Furthermore, we introduce the Bogoliubov excitations which approximate the quantum mechanical fluctuations of the Bose gas to first order and are connected to density fluctuations. These fluctuations become important in the context of the interaction between the bosonic bath and immersed atoms in chapter 6. The second section investigates the basic properties of a non-interacting Fermi gas with an emphasis on the density distribution in an external trapping potential. The final part of this chapter applies the considerations of the previous sections to the Bose-Fermi mixture of fermionic lithium (^{6}Li) and bosonic sodium (^{23}Na) realized in our experiment. In this context, we provide a short overview of the experimental setup and extract the quantities which are relevant for the following chapters, as e. g. the gas temperature and the density profiles, from the experimental data.

2.1. Weakly Interacting Bosons

2.1.1. The Gross-Pitaevskii Equation

Bose gases realized in ultracold atom gas experiments are prepared and cooled in an external trapping potential V_{ext} which isolates the atoms from the environment to prevent their heating [23]. Besides the external trapping potential the atoms usually interact weakly with each other via a Van der Waals potential. Because of the low temperatures in our experiments, the de Broglie wavelength of the atoms is typically much larger than the effective range of the Van der Waals potential. Therefore, the details of the potential are not resolved by the interacting atoms and the interaction can be described by a contact potential [24]

$$V(\vec{r}-\vec{r}') = g\delta(\vec{r}-\vec{r}') \tag{2.1}$$

with $g = 4\pi\hbar^2 a/m$ being the coupling constant, a the scattering length and m the mass of the atoms. $\vec{r}$ and $\vec{r}'$ denote the positions of the interacting atoms.

As ultracold Bose gases are typically dilute, which means that the inter-particle spacing is much larger than the range of the interaction potential, two body interactions play the dominant role and interactions involving higher particle numbers can be neglected. In this case, the Heisenberg equation of motion for the bosonic field operator $\hat{\Psi}(\vec{r},t)$ is given by [24]

$$i\hbar\frac{\partial}{\partial t}\hat{\Psi}(\vec{r},t)=\left[-\frac{\hbar^2}{2m}\nabla^2+V_{\text{ext}}(\vec{r})+\int\hat{\Psi}^\dagger(\vec{r}\,',t)V(\vec{r}-\vec{r}\,')\hat{\Psi}(\vec{r}\,',t)\,\mathrm{d}\vec{r}\,'\right]\hat{\Psi}(\vec{r},t). \tag{2.2}$$

In order to find the approximate ground state of the Bose gas, the bosonic field operator can be rewritten and split into the condensate wavefunction $\langle\hat{\Psi}(\vec{r},t)\rangle=\Psi_0(\vec{r},t)$ which describes the Bose-Einstein condensate and a term $\delta\hat{\Psi}(\vec{r},t)$ which accounts for thermal and quantum mechanical fluctuations

$$\hat{\Psi}(\vec{r},t)=\Psi_0(\vec{r},t)+\delta\hat{\Psi}(\vec{r},t). \tag{2.3}$$

This approach is particularly useful if the temperature of the Bose gas is well below the critical temperature which means that thermal fluctuations are suppressed and if the number of particles in the condensate is large such that quantum mechanical fluctuations can be neglected. In this case, the field operator can be replaced by the condensate wavefunction which leads to the time-dependent Gross-Pitaevskii equation (GPE) [25, 26]

$$i\hbar\frac{\partial}{\partial t}\Psi_0(\vec{r},t)=\left[-\frac{\hbar^2}{2m}\nabla^2+V_{\text{ext}}(\vec{r})+g\left|\Psi_0(\vec{r},t)\right|^2\right]\Psi_0(\vec{r},t). \tag{2.4}$$

The time-independent GPE can be obtained by factorizing the condensate wavefunction into a position- and a time-dependent part $\Psi_0(\vec{r},t)=\Psi_0(\vec{r})e^{-i\mu t/\hbar}$

$$\mu\Psi_0(\vec{r})=\left[-\frac{\hbar^2}{2m}\nabla^2+V_{\text{ext}}(\vec{r})+g\left|\Psi_0(\vec{r})\right|^2\right]\Psi_0(\vec{r}), \tag{2.5}$$

where $\mu=\partial E/\partial N$ is the chemical potential.

In general, the exact solution of the stationary GPE has to be calculated numerically. But in many experimentally relevant cases the interaction energy is much larger than the kinetic energy and thus the kinetic term in the GPE can be neglected. According to this so-called Thomas-Fermi approximation, the density distribution of the Bose-Einstein condensate $n(\vec{r})$ reads as

$$n(\vec{r})=|\Psi_0(\vec{r})|^2=\begin{cases}\frac{\mu-V_{\text{ext}}(\vec{r})}{g} & \text{if } \mu-V_{\text{ext}}(\vec{r})\geq 0\\ 0 & \text{otherwise.}\end{cases} \tag{2.6}$$

Hence, a Bose-Einstein condensate confined in a harmonic potential characterized by the trapping frequencies $\omega_{\text{x,y,z}}$

$$V_{\text{ext}}(\vec{r})=\frac{1}{2}m\left(\omega_{\text{x}}^2x^2+\omega_{\text{y}}^2y^2+\omega_{\text{z}}^2z^2\right) \tag{2.7}$$

has a parabolically shaped density distribution whose peak density is given by the ratio of the chemical potential μ and the coupling constant g. As the chemical potential is restricted by the

normalization condition $N = \int n(\vec{r})\,\mathrm{d}\vec{r}$, it can be expressed in terms of experimentally accessible parameters [27]

$$\mu = \frac{\hbar\bar{\omega}}{2}\left(\frac{15Na}{\bar{a}_{\mathrm{ho}}}\right)^{2/5}. \tag{2.8}$$

Here $\bar{\omega}$ denotes the mean trapping frequency $\bar{\omega} = \sqrt[3]{\omega_{\mathrm{x}}\omega_{\mathrm{y}}\omega_{\mathrm{z}}}$ and $\bar{a}_{\mathrm{ho}}$ the corresponding harmonic oscillator length $\bar{a}_{\mathrm{ho}} = \sqrt{\hbar/(m\bar{\omega})}$.

The Thomas-Fermi approximation requires that the kinetic energy of the bosons is small compared to the interaction energy, but it also assumes that the Bose gas is at zero temperature as the Gross-Pitaevskii equation does not account for temperature effects.

Despite the fact that the temperature in our experiment is finite, the Thomas-Fermi approximation provides a helpful tool to describe the observed density profiles. The reason is that the bosonic gas shows at ultracold temperatures a bimodal density distribution. As the temperature decreases the bosons start occupying the ground state of the system macroscopically and the density distribution of this Bose-Einstein condensate is well reflected by the Thomas-Fermi approximation. In contrast, the density distribution of the atoms which do not occupy the ground state can be described by the Maxwell-Boltzmann distribution [23]

$$n_{\mathrm{th}}(\vec{r}) = \frac{N_{\mathrm{th}}}{\pi\sigma_{\mathrm{x}}\sigma_{\mathrm{y}}\sigma_{\mathrm{z}}} e^{-x^2/\sigma_x^2} e^{-y^2/\sigma_{\mathrm{y}}^2} e^{-z^2/\sigma_{\mathrm{z}}^2} \quad \text{with} \quad \sigma_{\mathrm{x,y,z}} = \sqrt{\frac{2k_{\mathrm{B}}T}{m\omega_{\mathrm{x,y,z}}^2}} \tag{2.9}$$

with N_{th} denoting the number of thermal atoms and k_{B} the Boltzmann constant . The ratio of the atoms in the Bose-Einstein condensate and the total number of atoms is referred to as condensate fraction $\eta = N_{\mathrm{BEC}}/N_{\mathrm{total}}$, and is for a harmonic trapping potential given by [28]

$$\eta = 1 - \left(\frac{T}{T_{\mathrm{C}}}\right)^3, \tag{2.10}$$

where the critical temperature $k_{\mathrm{B}}T_{\mathrm{C}} \approx 0.94\hbar\bar{\omega}N^{1/3}$ has been introduced.

The observation of the density profile therefore allows two complementary routes to measure the temperature of the Bose gas. On the one hand, the wings of the thermal cloud reflect the temperature of the gas and on the other hand the condensate fraction can also be used for a temperature determination if the trapping potential and therefore the trapping frequencies are well known.

2.1.2. Elementary Excitations

So far, we treated the Bose gas as a classical field and neglected all fluctuations. We will see in the last section of this chapter that this approach already yields a good description of our experimentally observed density profiles.

Nevertheless we will investigate the elementary excitations and fluctuations of the Bose gas in the following as they give rise to density fluctuations which become important for the interaction between the bosonic bath and atoms immersed in this bath discussed in chapter 6. The interaction between the two components is a density-density-type interaction. In absence of density

fluctuations, the immersed atoms experience a constant bath density if the extent of their wave-function is small compared to the size of the Bose-Einstein condensate, and the interaction causes therefore only a constant correction to the energy of the immersed atoms. However, the density fluctuations of the Bose gas modulate the bath density on smaller length scales and induce the dynamics of the immersed atoms which we investigate later on.

In order to derive the density fluctuations of the Bose gas, we consider the correction of first order in $\delta\hat{\Psi}(\vec{r},t)$ by plugging $\hat{\Psi}(\vec{r},t) = \Psi_0(\vec{r},t) + \delta\hat{\Psi}(\vec{r},t)$ into equation (2.2) and dropping all terms of higher than linear order in $\delta\hat{\Psi}(\vec{r},t)$. This approach is justified as long as the number of excitations is much lower than the particle number in the condensate. As $\Psi_0(\vec{r},t)$ is a solution to the Gross-Pitaevskii equation, this leads to

$$i\hbar\frac{\partial}{\partial t}\delta\hat{\Psi}(\vec{r},t) = \left[-\frac{\hbar^2}{2m}\nabla^2 + V_{\text{ext}}(\vec{r}) + 2g|\Psi_0(\vec{r},t)|^2\right]\delta\hat{\Psi}(\vec{r},t) + g\Psi_0(\vec{r},t)^2\delta\hat{\Psi}^\dagger(\vec{r},t) \tag{2.11}$$

and for the Hermitian adjoint

$$-i\hbar\frac{\partial}{\partial t}\delta\hat{\Psi}^\dagger(\vec{r},t) = \left[-\frac{\hbar^2}{2m}\nabla^2 + V_{\text{ext}}(\vec{r}) + 2g|\Psi_0(\vec{r},t)|^2\right]\delta\hat{\Psi}^\dagger(\vec{r},t) + g\Psi_0^*(\vec{r},t)^2\delta\hat{\Psi}(\vec{r},t). \tag{2.12}$$

Usually, this set of equations is solved by using the ansatz [24]

$$\delta\hat{\Psi}(\vec{r},t) = \sum_{\vec{q}}\left[u_{\vec{q}}(\vec{r})\hat{b}_{\vec{q}}e^{-i\omega_{\vec{q}}t} + v^*_{\vec{q}}(\vec{r})\hat{b}^\dagger_{\vec{q}}e^{i\omega_{\vec{q}}t}\right]e^{-i\mu t/\hbar}. \tag{2.13}$$

Here, $u_{\vec{q}}(\vec{r})$ and $v_{\vec{q}}(\vec{r})$ are functions which have to be determined such that the equations for $\delta\hat{\Psi}(\vec{r},t)$ and $\delta\hat{\Psi}^\dagger(\vec{r},t)$ are fulfilled. $\hat{b}^\dagger_{\vec{q}}$ and $\hat{b}_{\vec{q}}$ denote the creation and annihilation operator for the elementary excitation with momentum $\vec{q}$ and energy $\epsilon_{\vec{q}} = \omega_{\vec{q}}\hbar$. Inserting this ansatz and selecting the terms oscillating with the same frequency $\omega_{\vec{q}}$ yields the so-called Bogoliubov equations [29]

$$\left[-\frac{\hbar^2}{2m}\nabla^2 + V_{\text{ext}}(\vec{r}) + 2gn(\vec{r}) - \mu - \epsilon_{\vec{q}}\right]u_{\vec{q}}(\vec{r}) + gn(\vec{r})v_{\vec{q}}(\vec{r}) = 0 \tag{2.14}$$

$$\left[-\frac{\hbar^2}{2m}\nabla^2 + V_{\text{ext}}(\vec{r}) + 2gn(\vec{r}) - \mu + \epsilon_{\vec{q}}\right]v_{\vec{q}}(\vec{r}) + gn(\vec{r})u_{\vec{q}}(\vec{r}) = 0. \tag{2.15}$$

In general, the solution to the Bogoliubov equations is non-analytical and has to be calculated numerically. But in the most trivial case of a uniform repulsive Bose gas ($n(\vec{r}) = n_0$, $V_{\text{ext}}(\vec{r}) = 0$, $g > 0$, $\mu = gn_0$), the solution has to be translationally invariant and can be found by considering the functions $u_{\vec{q}}(\vec{r})$ and $v_{\vec{q}}(\vec{r})$ as plane waves

$$u_{\vec{q}}(\vec{r}) = \frac{u_{\vec{q}}}{\sqrt{V}}e^{i\vec{q}\vec{r}} \quad \text{and} \quad v_{\vec{q}}(\vec{r}) = \frac{v_{\vec{q}}}{\sqrt{V}}e^{i\vec{q}\vec{r}} \tag{2.16}$$

with V being the normalization volume. This approach leads to a set of coupled equations for $u_{\vec{q}}$ and $v_{\vec{q}}$ which can be fulfilled if

$$\epsilon_{\vec{q}} = \sqrt{\frac{gn_0}{m}(\hbar\vec{q})^2 + \frac{(\hbar\vec{q})^4}{(2m)^2}}. \tag{2.17}$$

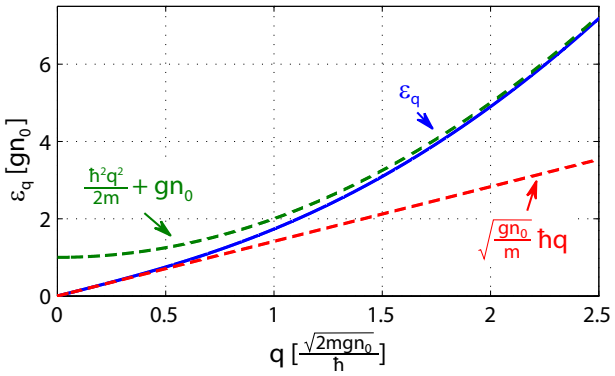

Figure 2.1.: Dispersion relation of the Bogoliubov excitations $\epsilon_{\vec{q}}$ (blue solid line) with its linear, phonon-like behavior for low momenta (red dashed line) and the free-particle-like behavior for high momenta (green dashed line).

Figure 2.1 depicts the dispersion relation of the elementary excitations $\epsilon_{\vec{q}}$ and reveals a linear behavior for low momenta $\omega_{\vec{q}} \approx c|\vec{q}|$ with $c = \sqrt{gn_0/m}$ being the so-called speed of sound. This phonon-like energy spectrum turns for higher momenta gradually into a free-particle-like spectrum as the dispersion relation becomes quadratic in $|\vec{q}|$.

The two coupled equations for $u_{\vec{q}}$ and $v_{\vec{q}}$ become linearly dependent if $\epsilon_{\vec{q}}$ is given by equation (2.17) and therefore there is no unique solution. But both coefficients are restricted up to a phase factor as the bosonic field operator, the creation and the annihilation operator for the elementary excitations have to satisfy the bosonic commutator relations. Taking $u_{\vec{q}}$ and $v_{\vec{q}}$ as real yields

$$u_{\vec{q}} = \sqrt{\frac{\frac{(\hbar\vec{q})^2}{2m} + gn_0}{2\epsilon_{\vec{q}}} + \frac{1}{2}} \tag{2.18}$$

$$v_{\vec{q}} = -\sqrt{\frac{\frac{(\hbar\vec{q})^2}{2m} + gn_0}{2\epsilon_{\vec{q}}} - \frac{1}{2}}. \tag{2.19}$$

As mentioned in the beginning of this section, we are particularly interested in the elementary excitations of the Bose gas because they are used to describe the interaction process between an impurity and the bosonic bath. We will see that this process does not only depend on the characteristics of the energy spectrum $\epsilon_{\vec{q}}$ which determines the possibly involved excitation modes, but also on the coefficients $u_{\vec{q}}$ and $v_{\vec{q}}$ which carry information about the bath structure and therefore determine the likeliness of the interaction process.

2.2. Fermions

After recapturing the basic concepts of weakly interacting bosons, the following section concentrates on the characteristics of identical fermions and their density distribution in an external

trapping potential. During our discussion, we consider the fermions as an ideal, non-interacting Fermi gas. This is justified by the fact that our experiments are performed with samples of spin-polarized and thus identical fermions for which the Pauli exclusion principle forbids s-wave scattering. Moreover, the temperature of our Fermi gases ($T \sim 1\,\mu\mathrm{K}$) is typically much lower than height of the centrifugal barrier ($\sim 1\,\mathrm{mK}$ for p-wave scattering) and hence the interaction between the spin-polarized fermions can be neglected.

For an ideal Fermi gas, the occupation number $f(\vec{r},\vec{p})$ per phase space cell $\mathrm{d}\vec{r}\mathrm{d}\vec{p}/(2\pi\hbar)^3$ at temperature T is given by the Fermi-Dirac distribution

$$f(\vec{r},\vec{p}) = \frac{1}{\exp\left(\left(\frac{\vec{p}^2}{2m} + V_{\mathrm{ext}}(\vec{r}) - \mu\right)/\left(k_{\mathrm{B}}T\right)\right) + 1}. \tag{2.20}$$

As for the bosons, the chemical potential μ of the fermions is fixed by the normalization condition for the particle number $N = \int f(\vec{r},\vec{p})\,\mathrm{d}\vec{r}\mathrm{d}\vec{p}/(2\pi\hbar)^3$, and depends on the temperature.

In the special case of a Fermi gas at zero temperature, the chemical potential is also referred to as the Fermi energy $E_{\mathrm{F}} = \mu(T=0)$. According to equation (2.20) all states which fulfill $\frac{\vec{p}^2}{2m} + V_{\mathrm{ext}}(\vec{r}) < \mu$, i. e. have an energy lower than the chemical potential, are in this limit occupied by exactly one fermion and all others are empty. Applying the normalization condition to a Fermi gas at zero temperature confined in a three-dimensional harmonic trapping potential yields for the Fermi energy

$$E_{\mathrm{F}} = (6N)^{1/3}\hbar\bar{\omega}. \tag{2.21}$$

As the temperature of Fermi gases realized in experiments is finite, the Fermi energy can only serve as an estimate for the chemical potential. The validity of this estimation can be checked by comparing the actual temperature with the temperature connected to the Fermi energy, i. e. the Fermi temperature $T_{\mathrm{F}} = E_{\mathrm{F}}/k_{\mathrm{B}}$. For $T \ll T_{\mathrm{F}}$, the chemical potential can be expanded in terms of T/T_{F}

$$\mu(T) = E_{\mathrm{F}}\left[1 - \frac{\pi^2}{3}\left(\frac{T}{T_{\mathrm{F}}}\right)^2\right] \tag{2.22}$$

which is known as the Sommerfeld expansion [30].

For the evaluation of our experimental data, particularly the density distribution of the Fermi gas is of interest. This distribution can be obtained by integrating equation (2.20) over the momentum space

$$n(\vec{r}) = \int f(\vec{r},\vec{p})\,\frac{\mathrm{d}\vec{p}}{(2\pi\hbar)^3} \tag{2.23}$$

This integration is non-trivial for finite temperature, but can be related to the polylogarithmic function[1] $Li_{3/2}(x)$ and yields [31]

$$n(\vec{r}) = -\left(\frac{mk_{\mathrm{B}}T}{2\pi\hbar^2}\right)^{3/2} Li_{3/2}\left(-e^{(\mu - V_{\mathrm{ext}}(\vec{r}))/(k_{\mathrm{B}}T)}\right). \tag{2.24}$$

In contrast to the Bose gas, where for a decreasing temperature the appearance of a bimodal density distribution reveals the onset of degeneracy, the change of the fermionic density distribution

[1] $Li_n(x) = \frac{1}{\Gamma(n)}\int_0^\infty \frac{t^{n-1}}{e^t/x - 1}\mathrm{d}t$, where $\Gamma(n)$ is the gamma function.

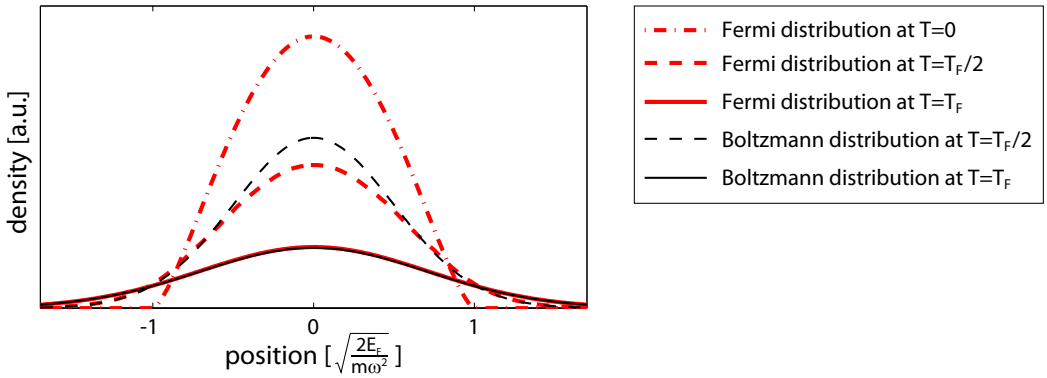

Figure 2.2.: Density distribution of a Fermi gas in a three-dimensional harmonic potential with trapping frequency ω for different temperatures. At $T = T_\mathrm{F}$ the density profile of a Fermi is hardly distinguishable from the Maxwell-Boltzmann distribution of an ideal gas.

is more subtle. It smoothly changes from a thermal distribution (eq. (2.9)) to a distribution of the form

$$n(\vec{r}) = \frac{1}{6\pi^2}\left(\frac{2m}{\hbar^2}\right)^{3/2}\left(E_\mathrm{F} - V_\mathrm{ext}(\vec{r})\right)^{3/2} \tag{2.25}$$

in the limit of zero temperature, which is illustrated in figure 2.2. Due to this fact, thermometry using fermions is much more difficult than with bosons. Therefore, our temperature determination for Bose-Fermi mixtures usually relies on the analysis of the Bose gas and assumes that both gases have the same temperature. This approach is well justified as long as both gases are in thermal contact and are at least close to thermal equilibrium.

2.3. Sodium-Lithium Mixture in an Optical Dipole Trap

Whereas the previous sections concentrated on the theory of bosons and fermions at ultracold temperatures, this section deals with the experimental realization of a Bose-Fermi mixture of sodium and lithium and our data analysis.

We start each experiment with a double-species magneto-optical trap [32] for bosonic sodium (^{23}Na) and fermionic lithium (^{6}Li). Both species are simultaneously transferred to a cloverleaf magnetic trap [33]. In order to increase the transfer efficiency, we apply an optical pumping scheme [34] and purify the sodium cloud by a subsequent microwave sweep. This leads to a stable, spin-polarized cloud of sodium atoms in the $|F = 2, m_f = 2\rangle$ hyperfine state and of lithium atoms in the $|F = 3/2, m_f = 3/2\rangle$ state.[2] Subsequently, the sodium atoms are cooled by forced evaporation using a microwave transition, while the lithium atoms are cooled sympathetically by the sodium atoms [35]. Both species are finally transferred from the magnetic trap to an optical

[2]Here, F denotes the atom's total angular momentum and m_F its projection onto the magnetic field.

dipole trap in which we perform our experiments and which is discussed in the following. A more precise description of the experimental setup, sample preparation and the cooling stages can be found in [36, 37, 38, 39, 40, 41].

2.3.1. Optical Dipole Trap

In each experimental cycle we prepare a mixture of bosonic sodium and fermionic lithium in the optical dipole trap. We are particularly interested in the impact of the sodium bath on the dynamics of the lithium atoms immersed in the bath. Hence, we usually prepare an imbalanced Bose-Fermi mixture with lithium being the minority species. Depending on the type of measurement, the lithium atom number typically ranges from $0.3 \cdot 10^5$ to $2 \cdot 10^5$ and the sodium atom number from $3 \cdot 10^5$ to $10 \cdot 10^5$.

Figure 2.3 a) shows a schematic of the optical dipole trap setup consisting of two intersecting laser beams at a wavelength of 1064 nm. The axes of the displayed coordinate system are chosen such that they coincide with the axes of the magnetic trap and the axes of the optical lattice discussed in the next chapters. Furthermore, the z-axis points in vertical direction. The horizontal beam lying in the x-y-plane is elliptically shaped with a minimal waist of 100 µm in vertical and 230 µm in horizontal direction. Its axis encloses a small angle of 8° with the y-axis. The second beam propagating in the x-z-plane has a symmetric shape with a minimal waist of 80 µm and is tilted by angle of about 40° with respect to the x-axis.

Atoms exposed to the inhomogeneous light field of a laser beam experience a force as the light field induces a dipole moment due to the opposite charge of the atom's electrons and protons.

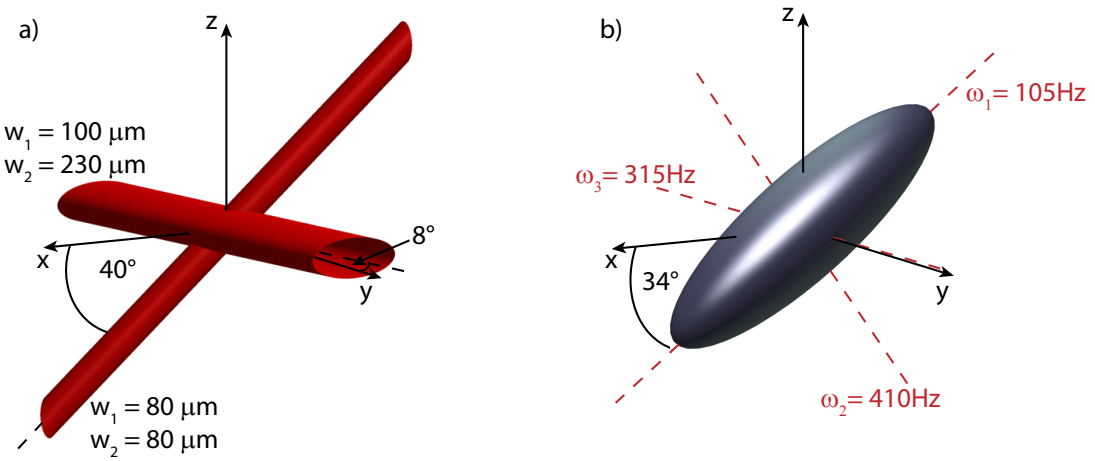

Figure 2.3.: a) Two intersecting laser beams are used to generate an optical dipole trap potential for sodium and lithium. b) Isosurface of the trapping potential and trapping frequencies for sodium. The trapping frequencies for lithium are about a factor of 2.10 higher, but the potential shape and orientation are identical.

This dipole moment is, depending on its orientation, either attracted or repulsed from the light field which leads to the optical dipole potential. In case of the optical dipole trap, the sodium and lithium atoms are both attracted by the laser beams, but experience a different trapping potential $V_{\text{dipole}}(\vec{r})$ due to their different optical properties [42]

$$V_{\text{dipole}}(\vec{r}) = \frac{3\pi c^2}{2\omega_0^3}\left(\frac{\Gamma}{\omega-\omega_0}+\frac{\Gamma}{\omega+\omega_0}\right) I(\vec{r}). \tag{2.26}$$

Here, ω is the laser frequency and $I(\vec{r})$ the light field intensity. Γ and ω_0 denote the decay rate and frequency of the involved optical transition. Additionally, the mass of both elements differs which leads to a factor of 2.10 higher trapping frequencies for lithium. This causes a different shift of the trap minimum for both species as the optical dipole trap potential competes with the gravitational potential. For a harmonic trapping potential, this differential gravitational sag is given by

$$\Delta x = \frac{g_{\text{grav}}}{\omega_{\text{Na}}^2} - \frac{g_{\text{grav}}}{\omega_{\text{Li}}^2}, \tag{2.27}$$

where g_{grav} denotes the standard acceleration of gravity and ω_{Na}, ω_{Li} the angular trapping frequencies for sodium and lithium.

In order to increase the effect of the bath on the impurities, it is beneficial to minimize the differential gravitational sag and therefore maximize the trapping frequencies. Hence, we usually perform our experiments with the maximal intensity in both dipole trap beams. This leads to trapping frequencies of $61\,\text{Hz}$ and $160\,\text{Hz}$ for sodium trapped in the horizontal beam alone, where the stronger confinement acts against gravity, and $315\,\text{Hz}$ and $374\,\text{Hz}$ for sodium in the second beam. Here, the slightly weaker axis is parallel to the y-axis. Due to the asymmetry of the laser beams, the overall trapping potential is elliptically shaped and the weakest semiaxis of the ellipsoid is tilted by angle of about $34°$ with respect to the x-axis (see figure 2.3 b). The trapping frequencies for sodium along the semiaxes are $(\omega_{1,\text{Na}}, \omega_{2,\text{Na}}, \omega_{3,\text{Na}}) = 2\pi\,(105, 315, 410)\,\text{Hz}$ and for lithium $(\omega_{1,\text{Li}}, \omega_{2,\text{Li}}, \omega_{3,\text{Li}}) = 2\pi\,(221, 662, 860)\,\text{Hz}$ which corresponds to a shift between the sodium and lithium cloud of $7.4\,\mu\text{m}$ along the x- and $-6.2\,\mu\text{m}$ along the z-axis.

2.3.2. Analysis of Atom Density Distributions

The analysis of the bath's impact on immersed atoms requires the knowledge of the involved density distributions in order to quantify the interaction between the two components. However, as we image the atom clouds along the z-axis by absorption imaging [23], the imaging process automatically integrates the density distributions along the imaging direction and we do not detect the density profiles of the sodium and lithium clouds. Nevertheless, the atom numbers and the temperature can be extracted from these pictures which allows for the calculation of the density distributions if the trapping frequencies are well known.

Usually, we do not analyze the atom distributions on the basis of in-situ images, but release the atoms from the trapping potential before the imaging process. The subsequent expansion of the atom clouds during the time-of-flight t_{TOF} reduces their optical density, and the larger cloud size makes the data analysis less sensitive to the resolution of the imaging system. In order to determine the temperature of our Bose-Fermi mixture, we analyze the time-of-flight images of

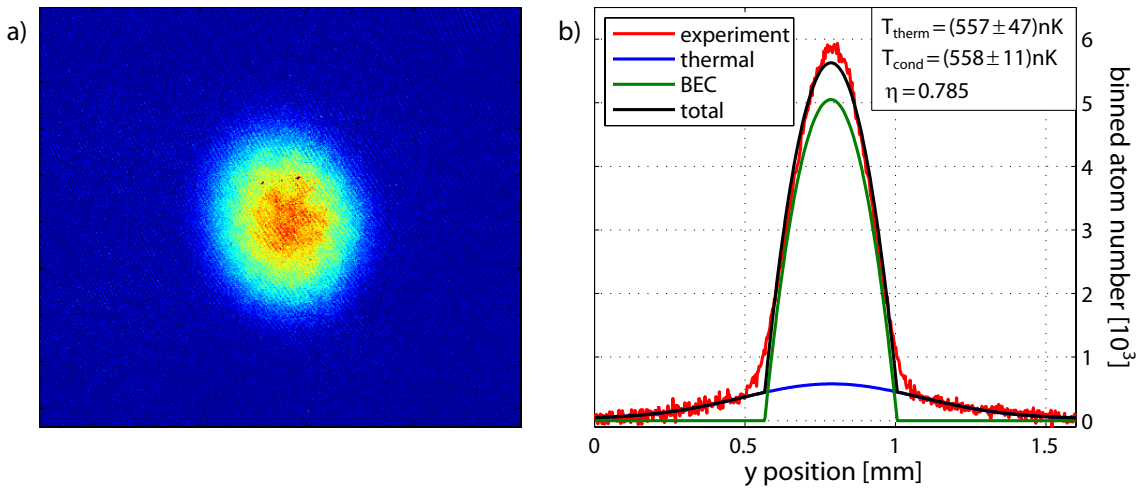

Figure 2.4.: a) Absorption image of the sodium cloud after 21 ms time-of-flight. b) The atom distribution binned per camera pixel is obtained from the absorption picture via integration along the horizontal direction which is shown in red. The curve in black depicts the fit of a bimodal distribution to the data, which can be split into a Gaussian for the thermal fraction (blue) and a parabola for the Bose-Einstein condensate (green). The temperature can either be determined from the condensate fraction or the thermal wings.

sodium as the bimodal density distribution of the bosonic cloud allows a robust temperature determination.

In case of a harmonic potential, the density distribution after time-of-flight $n_{\mathrm{TOF}}(\vec{r})$ is for bosons as well as fermions directly connected to the in-situ density distribution $n(\vec{r})$ [43]

$$n_{\mathrm{TOF}}(\vec{r}) = \frac{n(\vec{r}\,')}{\gamma_{\mathrm{x}}\gamma_{\mathrm{y}}\gamma_{\mathrm{z}}} \quad \text{with} \quad \gamma_{\mathrm{x,y,z}} = \sqrt{1 + t_{\mathrm{TOF}}^2\omega_{\mathrm{x,y,z}}^2} \quad \text{and} \quad \vec{r}\,' = \begin{pmatrix} x/\gamma_{\mathrm{x}} \\ y/\gamma_{\mathrm{y}} \\ z/\gamma_{\mathrm{z}} \end{pmatrix}. \tag{2.28}$$

This means that the characteristic shape of the density distribution does not change during the expansion, but the characteristic length scales do. Figure 2.4 displays a typical sodium absorption picture after 21 ms time-of-flight and the distribution of the integrated atom number along the y-axis. The profile shows a clear bimodal distribution which can be fitted by a combination of a Thomas-Fermi profile (eq. (2.6)) and a thermal distribution (eq. (2.9)). The obtained condensate fraction of 79 % translates to a temperature $T = (558 \pm 11)$ nK (eq. (2.10)),[3] where the error is due to the uncertainty in the trapping frequencies and to a smaller degree to the fit accuracy.

[3] Throughout this document, errors are denoted in two standard deviations, whereas the error bars displayed in the figures correspond to one standard deviation.

Alternatively, the temperature can be determined from the extent of the thermal cloud whose width is after rescaling of the in-situ width (eq. (2.9)) given by

$$\sigma_{\mathrm{x,y,z}} = \sqrt{\frac{2k_{\mathrm{B}}T}{m\omega_{\mathrm{x,y,z}}^2}}\gamma_{\mathrm{x,y,z}} = \sqrt{\frac{2k_{\mathrm{B}}T}{m}\left(\frac{1}{\omega_{\mathrm{x,y,z}}^2} + t^2\right)} \overset{t \gg 1/\omega_{\mathrm{x,y,z}}}{\rightarrow} \sqrt{\frac{2k_{\mathrm{B}}T}{m}}t. \tag{2.29}$$

This approach yields a temperature of $T = (557 \pm 47)$ nK which agrees within the mutual error bars with the result obtained from the condensate fraction. Here, the error is mainly given by the fit uncertainty as the thermal wings become dilute for large condensate fractions making the fitting process less reliable. The uncertainty due the magnification of our imaging system is a factor of three smaller.

Although, the temperature determination via the thermal wings has a larger error and seems less reliable than the analysis using the condensate fraction, it still serves as a valuable cross check of the latter as it does not rely on the trapping geometry.

The temperature, the sodium and lithium atom number obtained from the absorption images allow calculating the in-situ density distributions. Exemplarily, figure 2.5 shows the sodium density distribution (eq. (2.6) and (2.9)) as well as the lithium density distribution (eq. (2.24)) for parameters typical for our experiment. The density profiles are depicted along along the x-, y- and z-direction introduced in figure 2.3.

So far, we only considered the trapping potential and the mutual interaction of the bosons in order to determine the density distributions, but neglected the interaction between the two components of the Bose-Fermi mixture. However, we will see in the following that especially the lithium atoms experience a significant additional potential due to the large density of the Bose

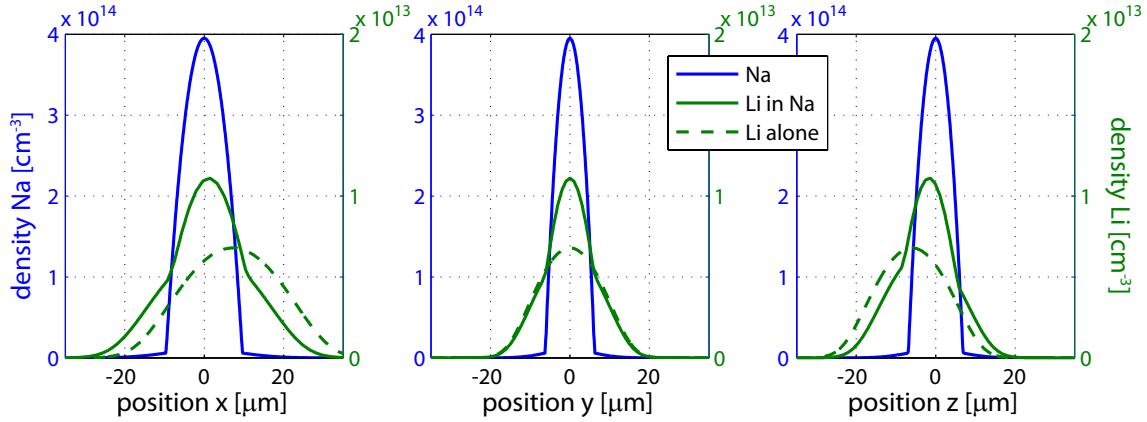

Figure 2.5.: Sodium and lithium density distribution in the optical dipole trap along the x-, y- and z-axis including the differential gravitational sag ($T = 550$ nK, $6 \cdot 10^5$ sodium and $1.5 \cdot 10^5$ lithium atoms). The attractive interaction between sodium and lithium drags the lithium atoms into the Bose-Einstein condensate and reduces the differential sag between the two components.

gas. The interspecies interaction potential can be derived in analogy to the mean-field interaction term of the Gross-Pitaevskii equation (2.5). Accordingly, the sodium atoms experience due to the interaction with the lithium atoms an additional potential which reads as

$$V_{\mathrm{Li}\rightarrow\mathrm{Na}}(\vec{r}) = g_{\mathrm{NaLi}} n_{\mathrm{Li}}(\vec{r}) \tag{2.30}$$

and the interspecies interaction potential for the lithium atoms is given by

$$V_{\mathrm{Na}\rightarrow\mathrm{Li}}(\vec{r}) = g_{\mathrm{NaLi}} n_{\mathrm{Na}}(\vec{r}). \tag{2.31}$$

Here, $n_{\mathrm{Li,Na}}(\vec{r})$ denotes the density of the lithium and sodium atoms, respectively. The coupling constant [27]

$$g_{\mathrm{NaLi}} = \frac{2\pi\hbar^2 a_{\mathrm{NaLi}}}{m_{\mathrm{red}}} \tag{2.32}$$

is factor of 2 lower than for identical bosons as the particles are distinguishable. The coupling constant g_{NaLi} depends on the scattering length between sodium and lithium a_{NaLi} as well as their reduced mass $m_{\mathrm{red}} = m_{\mathrm{Li}} m_{\mathrm{Na}}/(m_{\mathrm{Li}} + m_{\mathrm{Na}})$. The exact approach for including the interaction between the two species demands the calculation of the density distributions in a self-consistent way which leads to a set of coupled equations for the sodium and lithium density. However, the lithium density is more than one order of magnitude lower than the density of the sodium atoms, and the interaction potential is only for the lithium atoms on the order of the external trapping potential. Thus, the impact of the interaction on the sodium density distribution can be neglected in first order. Therefore, only the lithium density changes and reads as

$$n(\vec{r}) = -\left(\frac{m k_{\mathrm{B}} T}{2\pi\hbar^2}\right)^{3/2} Li_{3/2}\left(-e^{(\mu - V_{\mathrm{ext}}(\vec{r}) - g_{\mathrm{NaLi}} n_{\mathrm{Na}}(\vec{r}))/(k_{\mathrm{B}}T)}\right). \tag{2.33}$$

Because of the attractive interaction between the two species, the lithium atoms are dragged into the sodium Bose-Einstein condensate as depicted in figure 2.5. The interspecies interaction increases the central lithium density and reduces the distance between the maxima of the two density distributions due to gravitation from $7.4\,\mu\mathrm{m}$ to $1.5\,\mu\mathrm{m}$ in x- and $-6.2\,\mu\mathrm{m}$ to $-1.4\,\mu\mathrm{m}$ z-direction.[4] This interaction induced enhancement of the lithium density has already been studied in the context of sodium-lithium Feshbach resonances [41, 44] and helped to pin the sign of the scattering length a_{NaLi}.

Concluding Remarks

This chapter introduced the experimental setup used to prepare our Bose-Fermi mixture of sodium and lithium, and presented the basic theory of ultracold Bose and Fermi gases in order to analyze the atom distributions after release from the trapping potential. By determining the temperature of the Bose-Fermi mixture as well as the number of the sodium and lithium atoms, we reconstructed the density distributions of both components in the trapping potential. In this context, we found that the extent of the lithium cloud exceeds the size of the Bose-Einstein condensate

[4] The density profiles are calculated for both species in the lowest hyperfine state which corresponds to $a_{\mathrm{NaNa}} = 55\,\mathrm{a_0}$ and $a_{\mathrm{NaLi}} = -75\,\mathrm{a_0}$.

for our typical experimental parameters. Moreover, we also noticed that the interaction between the sodium and lithium atoms reduces the differential gravitational sag significantly meaning it becomes negligible compared to the size of the atom clouds. With regard to our investigations of the dynamics of the lithium atoms immersed in the sodium background, we keep both effects in mind as the impact of the sodium bath depends on the density experienced by the lithium atoms.

3. Species-Selective Lattice for Lithium

In order to study the impact of the bosonic bath on the dynamics of the immersed lithium atoms, we need to prepare the lithium atoms in an out-of-equilibrium state. For this purpose, the preparation scheme has to address the external degrees of the lithium atoms without any direct impact on the bath. Thus, we implement a species-selective optical lattice [45, 46] created by interfering laser beams whose frequency is close to the lithium transition frequency. Because of the small detuning, already limited beam intensities result in a sufficiently deep potential for lithium, whereas the impact on sodium stays negligible. A single optical dipole potential fulfills the same requirements, but a lattice potential offers a larger versatility. For instance, a lattice enables a confinement on a smaller scale and thus the impurity atoms act as a local bath probe. In addition, the bath physics can be investigated in different lattice dimensions which e. g. changes the possible decay channels of motionally excited impurities.

In the following, we investigate the species-selective lattice with which we address and manipulate the lithium atoms. At first, we concentrate on the basic theory of lattice potentials and discuss the dispersion relation of single atoms in one- and three-dimensional lattices. We use these considerations to derive the design criteria for our species-selective lattice at the end of this chapter. Moreover, we will need this knowledge in the subsequent chapters in order to characterize and analyze the dynamics of the lithium atoms.

3.1. Optical Lattice Potentials

The optical lattice potential employs the same physical principles as the dipole potential realizing the trapping potential for the Bose-Fermi mixture (eq. (2.26))

$$V_{\text{dipole}}(\vec{r}) = \frac{3\pi c^2}{2\omega_0^3}\left(\frac{\Gamma}{\omega-\omega_0}+\frac{\Gamma}{\omega+\omega_0}\right) I(\vec{r}) \approx \frac{3\pi c^2}{2\omega_0^3}\frac{\Gamma}{\Delta} I(\vec{r}). \tag{3.1}$$

On the right hand side we made use of the rotating wave approximation which is valid as long as the detuning $\Delta = \omega - \omega_0$ between the laser and the transition frequency fulfills $|\Delta| \ll \omega_0$. According to this formula, a species-selective potential can be achieved by a low intensity light field combined with a small detuning as long as the detuning for the other species is much larger. However, the laser frequency cannot be tuned arbitrarily close to the transition frequency as the photon scattering rate [42]

$$\Gamma_{\text{scatter}}(\vec{r}) = \frac{3\pi c^2}{2\hbar\omega_0^3}\left(\frac{\omega}{\omega_0}\right)^3\left(\frac{\Gamma}{\omega-\omega_0}+\frac{\Gamma}{\omega+\omega_0}\right)^2 I(\vec{r}) \approx \frac{3\pi c^2}{2\hbar\omega_0^3}\left(\frac{\Gamma}{\Delta}\right)^2 I(\vec{r}) \tag{3.2}$$

increases faster with decreasing detuning than the potential depth. These spontaneous emission processes restrict the possible laser frequencies as they lead to heating and atom loss. In order to

avoid complications due to scattering processes, the time scale imposed by light scattering should be much smaller than the exposure time to the lattice potential.

Commonly, lattice potentials are created by the interference pattern of two or more laser beams intersecting at the position of the atoms. If the intensity of the laser beams remains constant over the extent of the atom cloud, the optical potential produced by two laser beams takes the form of a standing wave

$$V_{\text{lat}}(x) = \frac{V_0}{2}\Big(1 + \cos\left(2k_{\text{lat}}x\right)\Big). \tag{3.3}$$

The lattice wavevector $k_{\text{lat}} = \frac{2\pi}{\lambda}\sin\left(\alpha/2\right)$ is determined by the angle α between the two beams as well as their wavelength λ. Furthermore, the lattice vector is connected to the spacing d_{lat} between two adjacent lattice sites

$$d_{\text{lat}} = \frac{\lambda}{2\sin\left(\alpha/2\right)} = \frac{\pi}{k_{\text{lat}}}. \tag{3.4}$$

The lattice depth V_0 determined by equation (3.1) is commonly expressed in terms of the recoil energy $E_{\text{rec}} = \hbar^2 k_{\text{lat}}^2/(2m)$.

3.2. Lattice Theory

In this section we investigate the dispersion relation of a single atom in a lattice potential. Because of its periodicity, a band structure emerges in the energy spectrum which is similar to the one of electrons in crystals. We begin our considerations with a one-dimensional and homogeneous lattice potential. Subsequently, we discuss the limitations of this approach due to the inhomogeneity of our lattice potential which is caused by the envelope of the lattice beams as well as the dipole trap confinement. Finally, we extend our discussion to higher dimensional lattice potentials and illustrate the results on the basis of a two-dimensional lattice with non-perpendicular lattice axes.

3.2.1. Band Structure of the One-Dimensional Homogeneous Lattice

In order to determine the energy spectrum in a one-dimensional and homogeneous lattice potential, we are searching the eigenfunctions $\psi_{n,q}(x)$ and eigenenergies $E_{n,q}$ of the lattice Hamiltonian

$$\left[\frac{-\hbar^2}{2m}\frac{\partial^2}{\partial x^2} + \frac{V_0}{2}\Big(1 + \cos\left(2k_{\text{lat}}x\right)\Big)\right]\psi_{n,q}(x) = E_{n,q}\psi_{n,q}(x). \tag{3.5}$$

Here, n denotes the band index and q the quasimomentum whose origin will become clear in the following. According to the Bloch theorem, the eigenfunctions of the lattice Hamiltonian can be written as a product of plane waves and the Bloch functions $u_{n,q}(x)$ [30]

$$\psi_{n,q}(x) = e^{iqx/\hbar}u_{n,q}(x). \tag{3.6}$$

The Bloch functions share the same periodicity as the lattice $u_{n,q}(x + d_{\text{lat}}) = u_{n,q}(x)$ and can thus be expanded into a Fourier series

$$u_{n,q}(x) = \sum_{\nu \in \mathbb{Z}} c_\nu^{n,q} e^{i2\nu k_{\text{lat}} x}. \tag{3.7}$$

Furthermore, the lattice potential can be expanded in the same set of plane waves as the Bloch functions

$$\frac{V_0}{2}\Big(1 + \cos\left(2k_{\text{lat}}x\right)\Big) = \frac{V_0}{2} + \frac{V_0}{4}\Big(e^{-i2k_{\text{lat}}x} + e^{i2k_{\text{lat}}x}\Big) \tag{3.8}$$

Plugging these two expansions into the Schrödinger equation (3.5) yields

$$\begin{aligned} &\sum_{\nu \in \mathbb{Z}} e^{i2\nu k_{\text{lat}} x} \left[\left(\frac{\left(q + 2\hbar\nu k_{\text{lat}}\right)^2}{2m} + \frac{V_0}{2}\right) c_\nu^{n,q} + \frac{V_0}{4}\left(c_{\nu-1}^{n,q} + c_{\nu+1}^{n,q}\right)\right] \\ &= \sum_{\nu \in \mathbb{Z}} E_{n,q} c_\nu^{n,q} e^{i2\nu k_{\text{lat}} x} \end{aligned} \tag{3.9}$$

As the plane waves $e^{i2\nu k_{\text{lat}} x}$ are orthogonal, the set of Fourier coefficients $c_\nu^{n,q}$ fulfills the equation above if and only if

$$\begin{pmatrix} T + \frac{V_0}{2} & \frac{V_0}{4} & 0 & \cdots & 0 \\ \frac{V_0}{4} & T + \frac{V_0}{2} & \frac{V_0}{4} & & \\ 0 & \frac{V_0}{4} & T + \frac{V_0}{2} & & \vdots \\ \vdots & & & \ddots & \\ 0 & & \cdots & & T + \frac{V_0}{2} \end{pmatrix} \cdot \begin{pmatrix} c_1^{n,q} \\ c_2^{n,q} \\ c_3^{n,q} \\ \vdots \\ c_{\text{m}}^{n,q} \end{pmatrix} = E_{n,q} \begin{pmatrix} c_1^{n,q} \\ c_2^{n,q} \\ c_3^{n,q} \\ \vdots \\ c_{\text{m}}^{n,q} \end{pmatrix}. \tag{3.10}$$

with $T = \left(q + 2\hbar\nu k_{\text{lat}}\right)^2 / (2m)$. Thus, we get the eigenenergies $E_{n,q}$ and the corresponding set of Fourier coefficients determining the eigenfunction $\psi_{n,q}(x)$ by solving the eigenvalue problem given in equation (3.10).

Figure 3.1 exemplarily depicts the eigenenergy spectrum obtained for a $V_0 = 4\, E_{\text{rec}}$ deep lattice with $d_{\text{lat}} = 1.1$ µm lattice spacing. For energies much larger than the lattice depth, the dispersion relation is only slightly affected by the lattice potential and resembles the dispersion relation of a free particle. However, for smaller energies a band structure emerges whose energy bands are referred to as Bloch bands and are labeled by the band index n. In the deep lattice regime, the lowest energy bands become almost flat, the energy gaps get broader and the energy spectrum resembles the spectrum of a harmonic oscillator.

A further characteristic feature of the band structure is its periodicity in the quasimomentum of $2\hbar k_{\text{lat}}$. Thus, the full spectrum can be obtained by restricting the quasimomentum to an interval of the same size. Conventionally, the quasimomentum is limited to the interval $[-\hbar k_{\text{lat}}; \hbar k_{\text{lat}}]$ which is referred to as first Brillouin zone. Accordingly, the n^{th} Brillouin zone ranges from $[-n\hbar k_{\text{lat}}; -(n-1)\hbar k_{\text{lat}}]$ and $[(n-1)\hbar k_{\text{lat}}; n\hbar k_{\text{lat}}]$.

With respect to the design of the optical lattice in the last part of this chapter, we investigate the band structure more thoroughly. Figure 3.2 depicts the widths of the two lowest Bloch bands and the band gaps between the first and second band

$$\Delta E_{1\text{-}2} = \min(E_{2,q}) - \max(E_{1,q}) \tag{3.11}$$

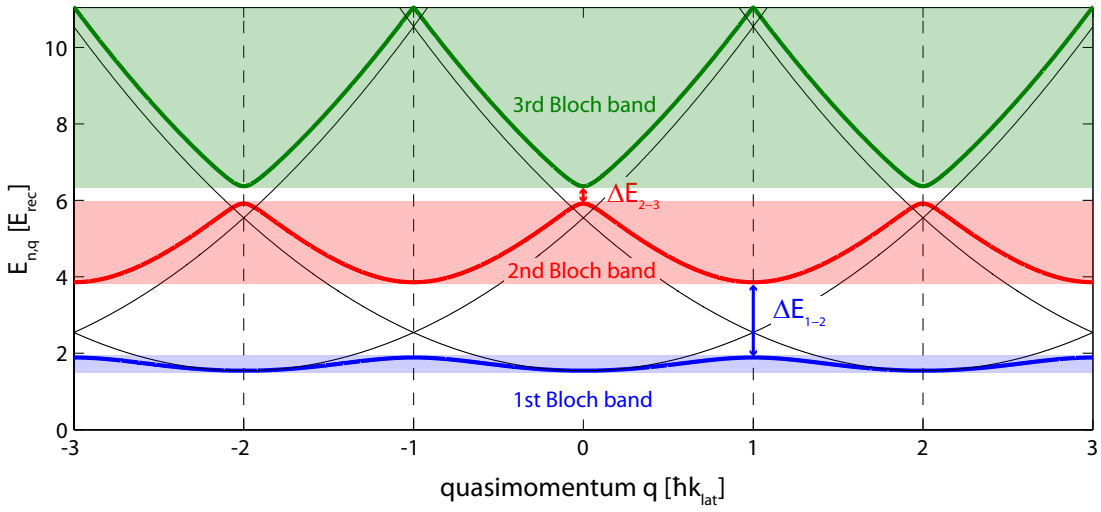

Figure 3.1.: Band structure for a $V_0 = 4\,E_{\mathrm{rec}}$ deep lattice. The first, second and third Bloch band are depicted as blue, red and green line and the color shading indicates the band widths. The (shifted) dispersion relation of a free particle is displayed as thin black line, and the vertical dashed lines denote the borders of the different Brillouin zones. The energy gap $\Delta E_{1\text{-}2}$ between the 1st and 2nd as well as the gap $\Delta E_{2\text{-}3}$ between the 2nd and 3rd band are represented by the blue and red arrow.

as well as between second and third band

$$\Delta E_{2\text{-}3} = \min(E_{3,q}) - \max(E_{2,q}) \tag{3.12}$$

for various lattice configurations. As expected, the band gaps get larger and the band widths thinner for deeper lattices. In the deep lattice regime ($V_0 \gg E_{\mathrm{rec}}$) the lattice potential is more and more resembled by a set of independent harmonic oscillator potentials and the energy bands can be approximated by the energy levels of the harmonic oscillator. The Taylor expansion of the lattice potential (eq. (3.3)) at the potential minima yields for the angular frequency of each harmonic oscillator

$$\omega_{\mathrm{ho}} = \frac{\Delta E_{1\text{-}2}}{\hbar} = \sqrt{\frac{2V_0 k_{\mathrm{lat}}^2}{m}} = \frac{2E_{\mathrm{rec}}}{\hbar}\sqrt{s} \propto \frac{\sqrt{s}}{d_{\mathrm{lat}}^2} \quad \text{with} \quad V_0 = sE_{\mathrm{rec}}. \tag{3.13}$$

Thus, we expect a square root like relation between the band gap and the lattice depth in the deep lattice regime.

To interpret the dependency of the band structure on the lattice spacing by means of figure 3.2, we need to take into account that the lattice depth is depicted in terms of the recoil energy, which depends itself on the lattice spacing ($E_{\mathrm{rec}} \propto 1/d_{\mathrm{lat}}^2$). According to equation (3.13), we anticipate that the band gap scales in the deep lattice regime as $\omega_{\mathrm{ho}} \propto 1/d_{\mathrm{lat}}$ for a fixed potential depth and as $\omega_{\mathrm{ho}} \propto 1/d_{\mathrm{lat}}^2$ for $V_0 = sE_{\mathrm{rec}}$. The band gaps increase with smaller lattice spacing gaps as the

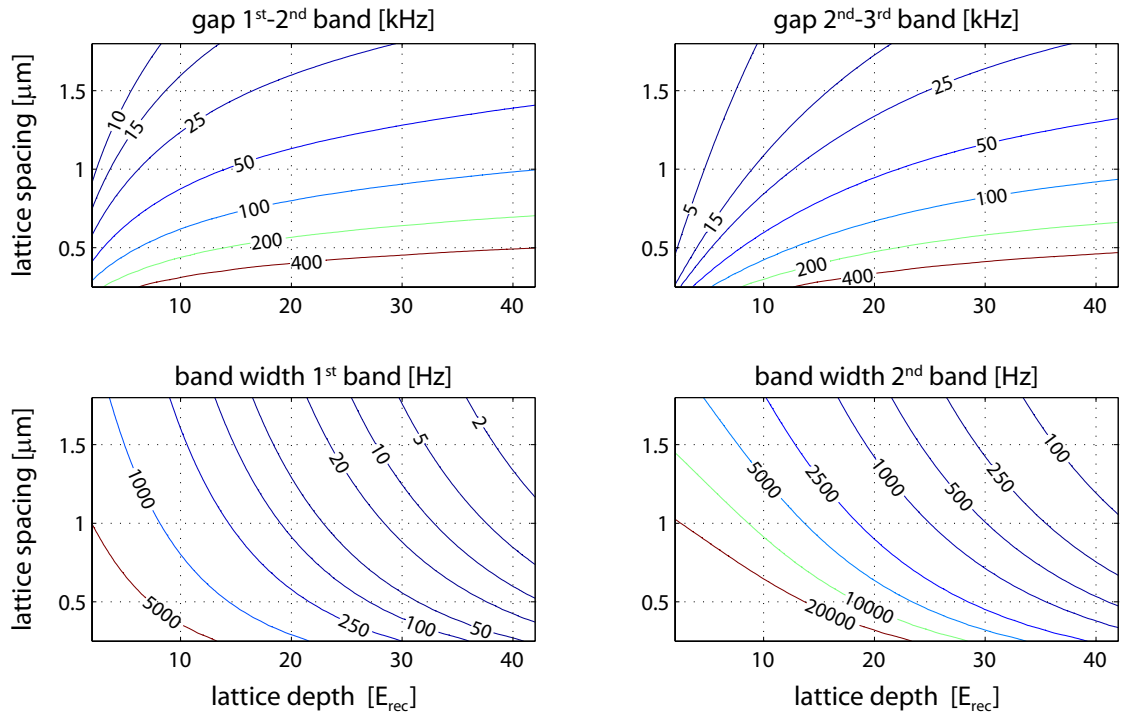

Figure 3.2.: Band gap from the 1st to 2nd $\Delta E_{1\text{-}2}$ and 2nd to 3rd $\Delta E_{2\text{-}3}$ band as well as band width of the 1st and 2nd Bloch band for various lattice depths and lattice spacings.

atoms gain kinetic energy due to the stronger confinement, and this effect is more pronounced for higher energy bands.

The effect of the lattice spacing on the band width is more obvious and can be understood in terms of tunneling between different lattice sites. In the deep lattice regime the atoms become more and more localized, but can still tunnel between neighboring sites. In this regime the wavefunctions are often approximated by the Wannier functions $w_n(x)$ [30] [1] which are localized to a few lattice sites and allow a more intuitive description than the Bloch functions which spread over the whole lattice. The tunneling rate between two neighboring lattice sites i and j is determined by the kinetic energy gain due to the tunneling process. This energy gain is referred to as the tunneling matrix element [47]

$$J_n = \int w_n(x - x_i) \left[\frac{-\hbar^2}{2m} \frac{\partial^2}{\partial x^2} + \frac{V_0}{2} \left(1 + \cos\left(2k_{\text{lat}} x\right)\right) \right] w_n(x - x_j)\, \mathrm{d}x \tag{3.14}$$

which is for deep lattices directly related to the band width, and is e. g. for the first Bloch band given by [48]

$$J_1 \approx \frac{E_{1,\pm k_{\text{lat}}} - E_{1,0}}{4}. \tag{3.15}$$

[1] $w_n(x - x_j) = \frac{1}{\sqrt{\mathcal{N}}} \sum_q e^{-iqx_j} \psi_{n,q}(x)$, where $\mathcal{N}$ is a normalization factor.

The correlation between the band width and the tunneling rate illustrates the impact of lattice spacing on the band width. In quantum mechanics the tunneling rate through a potential barrier drops exponentially with the barrier height as well as the barrier width. Thus, the band width decreases with increasing lattice spacing and the dependency is in the deep lattice regime almost exponential.

3.2.2. One-Dimensional Inhomogeneous Lattice Potential

So far, we considered the energy spectrum and scales of a homogeneous lattice potential in one dimension and neglected all inhomogeneities. In the following, we will investigate the limitations of this approach and discuss the impact of the inhomogeneity onto the energy spectrum and the eigenstates. In our case, there are two major contributions to the inhomogeneity. The first one stems from the non-uniform intensity distribution of the laser beams which create the lattice potential. The second contribution originates from the optical dipole trap potential which is superimposed with the lattice potential.

Inhomogeneity due to the Lattice Beams

In order to quantify the effect of the inhomogeneous lattice beams, we need to consider the resulting variation of the lattice potential with respect to the extent of the atom cloud. If two counterpropagating laser beams are used to create the lattice potential, the depth of the different lattice wells varies according to the beams' Rayleigh length. As the latter is typically in the centimeter range, which is large compared to the size of the atom cloud of several micrometers, it is well justified to neglect the inhomogeneity and consider the lattice potential as homogeneous. However, if the lattice potential is created by two beams intersecting at a small angle, their waists and the intersection angle determine the lattice potential along the lattice axis and the lattice potential reads as

$$V_{\mathrm{lat}}(x) = \frac{V_0}{2} e^{-2x^2/w_{\mathrm{beam}}^2} \Big(1 + \cos\left(2k_{\mathrm{lat}}x\right)\Big). \tag{3.16}$$

Here, w_{beam} denotes the effective waist of the Gaussian beams along the lattice axis which differs from their actual waist due to the intersection angle. Hence, the relative potential variation between the central and an outer populated lattice site scales as $1 - 2x^2/w_{\mathrm{beam}}^2$ if the waists of the lattice beams are much larger than the atom cloud. We can consider the effect of this potential inhomogeneity on the band structure by means of the deep lattice regime for which $\omega_{\mathrm{ho}} \propto \sqrt{V_0}$. Thus, we expect that the band gaps behave as $1 - x^2/w_{\mathrm{beam}}^2$ which means that the variation along the lattice axis is only about $0.25\,\%$ if the atom cloud is a factor of 20 smaller than the effective beam waist w_{beam}.

Inhomogeneity due to the Optical Dipole Trap

The second contribution to the inhomogeneity of lattice potential stems from the superposition of the optical dipole trap and the lattice potential. The trapping potential does not influence the depth of the different lattice wells, but leads to an offset potential between the lattice sites. This offset causes a localization of the wavefunction similar to the one observed for the Wannier-Stark

effect [49] and therefore reduces the tunneling between neighboring lattice sites. In contrast to the Wannier-Stark effect, for which the potential superimposed to the lattice potential is linear and all wavefunctions are affected in the same way, the offset caused by the harmonically shaped trapping potential increases with the distance from the minimum, and atoms further away from the trap center become more and more localized.[2]

To investigate the impact of the dipole trap potential, we consider the eigenfunctions and -energies in the inhomogeneous lattice potential. In case of the homogeneous lattice, the plane waves offer a convenient basis for the solution of the Schrödinger equation due to the periodicity of the lattice. In this way, the Schrödinger equation can be reduced to an eigenvalue problem (eq. (3.10)). However, for the inhomogeneous lattice potential, this basis provides no additional advantage and in the following we will work with the delta distributions $\delta(x-x_j)$ as real space basis set. Rewriting the Schrödinger equation of the inhomogeneous lattice potential

$$\left[\frac{-\hbar^2}{2m}\frac{\partial^2}{\partial x^2} + \frac{V_0}{2}\underbrace{e^{-2x^2/w_{\text{beam}}^2}}_{\text{beam profile}}\Big(1+\cos\left(2k_{\text{lat}}x\right)\Big) + \underbrace{\frac{1}{2}m\omega_{\text{dipole}}^2 x^2}_{\text{dipole trap}}\right]\psi_n(x) = E_n\psi_n(x) \quad (3.17)$$

with the delta distributions as basis corresponds to a discretization onto a spatial grid, and transforms the Schrödinger equation into a matrix equation

$$\begin{pmatrix} -2T+V(x_1) & T & & 0 \\ T & -2T+V(x_2) & \ddots & \\ 0 & T & \ddots & \vdots \\ \vdots & & \ddots & \\ 0 & \cdots & & -2T+V(x_{\text{m}}) \end{pmatrix} \cdot \begin{pmatrix} \psi_n(x_1) \\ \psi_n(x_2) \\ \psi_n(x_3) \\ \vdots \\ \psi_n(x_{\text{m}}) \end{pmatrix} = E_n \begin{pmatrix} \psi_n(x_1) \\ \psi_n(x_2) \\ \psi_n(x_3) \\ \vdots \\ \psi_n(x_{\text{m}}) \end{pmatrix}. \quad (3.18)$$

Here, $T = -\frac{\hbar^2}{2m\Delta x^2}$ and $\Delta x = x_j - x_{j-1}$ is the grid spacing. $V(x_j)$ denotes the total potential and $\psi_n(x_j)$ the wavefunction at position x_j. The second derivative in the Schrödinger equation accounting for the kinetic energy leads to a coupling between the $\psi_n(x_j)$ at different positions as the second derivative can be approximated by

$$-\frac{\hbar^2}{2m}\frac{\mathrm{d}^2}{\mathrm{d}x^2}\psi_n(x_j) \approx T\big(\psi_n(x_{j+1}) + \psi_n(x_{j-1}) - 2\psi_n(x_j)\big)\,. \quad (3.19)$$

The eigenenergies and the corresponding wavefunctions can be obtained numerically by solving the eigenvalue problem given in equation (3.18).

In order to quantify the localization of the energy eigenfunctions due to the trapping potential, we characterize their extent by the root-mean-square size

$$\sigma = \sqrt{\langle x^2\rangle - \langle x\rangle^2}. \quad (3.20)$$

[2] The inhomogeneity of the lattice potential has a similar effect as the different lattice well depths cause a shift of the ground state energy for each harmonic oscillator. However, this shift is for our experimental parameters much smaller than the one due to the optical dipole trap potential.

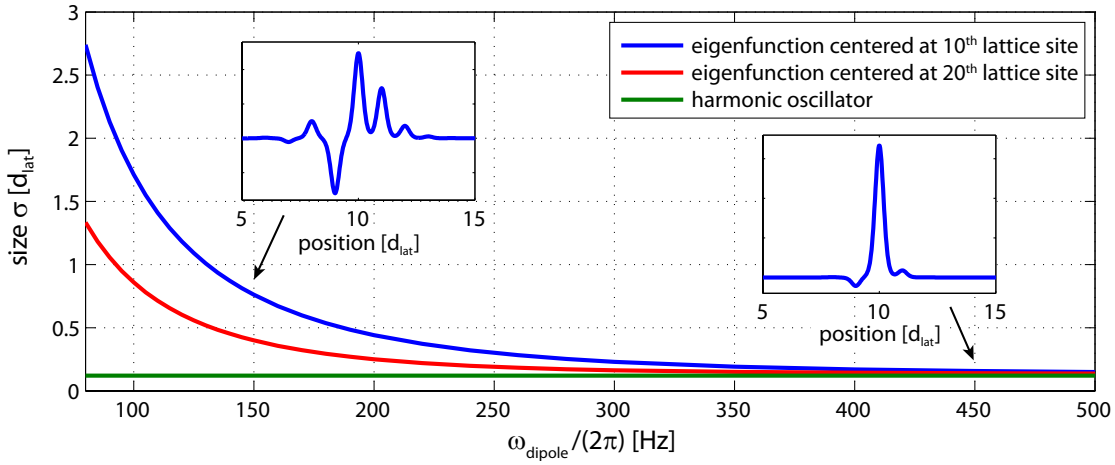

Figure 3.3.: The root-mean-square size σ of the inhomogeneous lattice eigenfunctions in the first Bloch band localized at the 10^{th} (blue) and 20^{th} (red) lattice site for various trapping frequencies ($V_0 = 12\,E_{\text{rec}}$, $d_{\text{lat}} = 1.1\,\mu\text{m}$). The eigenfunctions become for a stronger confinement more and more localized and their extent approaches the one of the corresponding harmonic oscillator ground state ($\omega_{\text{ho}} = \Delta E_{1\text{-}2}/\hbar$). The two insets exemplarily depict the eigenfunction localized at the 10^{th} lattice site for a trapping frequency of $\omega_{\text{dipole}} = 2\pi\,150$ and $450\,\text{Hz}$.

Figure 3.3 depicts the dependency between the root-mean-square size and the external confinement for the eigenfunctions in the first band centered at the 10^{th} and 20^{th} lattice site. Clearly, the eigenfunctions become more and more localized for increasing confinement which is consistent with our earlier analogy to the Wannier-Stark effect. The size of the eigenfunctions reaches quickly the size of the harmonic oscillator ground state for the considered lattice depth (eq. (3.13)) which demonstrates that the dipole trap confinement decreases the tunneling rates between neighboring sites significantly. We also observe that the eigenstates further away from the trap center become localized earlier due to the non-linear trapping potential.

3.2.3. Band Structure of the Three-Dimensional Homogeneous Lattice

So far, we considered the energy spectrum of a periodic potential in one dimension. In the following, we will extend our considerations to three-dimensional homogeneous lattice potentials[3] in order to characterize the interplay between our different lattice directions.

Most frequently, a three dimensional lattice potential is created by superimposing three standing wave potentials whose axes point along different directions. To obtain the energy spectrum of such a lattice configuration, we have to solve a Schrödinger equation of the form

$$\left[\frac{-\hbar^2}{2m}\nabla^2 + V_{\text{lat},1}(\vec{r}) + V_{\text{lat},2}(\vec{r}) + V_{\text{lat},3}(\vec{r})\right]\psi_{n,\vec{q}}(\vec{r}) = E_{n,\vec{q}}\psi_{n,\vec{q}}(\vec{r}), \tag{3.21}$$

[3]We skip the inhomogeneous case as it requires a lot more computational power due to the large number of grid points necessary for a three-dimensional grid.

where $V_{\text{lat},i}(\vec{r})$ denotes the potential of a standing wave in three dimensions

$$V_{\text{lat},i}(\vec{r}) = \frac{V_0}{2}\left(1 + \cos\left(2\vec{k}_{\text{lat},i}\vec{r}\right)\right). \tag{3.22}$$

In the case of three perpendicular standing wave potentials, we can split the Hamiltonian governing the equation (3.21) into three separate parts

$$\left[\sum_{i=\text{x,y,z}}\left(\frac{-\hbar^2}{2m}\frac{\partial^2}{\partial x_i^2} + \frac{V_{0,i}}{2}\left(1 + \cos\left(2k_{\text{lat},i}x_i\right)\right)\right)\right]\psi_{n,\vec{q}}(\vec{r}) = E_{n,\vec{q}}\psi_{n,\vec{q}}(\vec{r}), \tag{3.23}$$

where each part corresponds to the Hamiltonian of the one-dimensional lattice potential. Thus, the solution of the Schrödinger equation is given by $\psi_{n,\vec{q}}(\vec{r}) = \psi_{n_\text{x},q_\text{x}}(x)\psi_{n_\text{y},q_\text{y}}(y)\psi_{n_\text{z},q_\text{z}}(z)$ and $E_{n,\vec{q}} = E_{n_\text{x},q_\text{x}} + E_{n_\text{y},q_\text{y}} + E_{n_\text{z},q_\text{z}}$ where the E_{n_i,q_i} and ψ_{n_i,q_i} are the solutions to the one-dimensional standing wave potentials in x-, y- and z-direction (section 3.2.1).

Though, the situation is different if the lattice axes are not perpendicular to each other. Still, we do not have to perform a completely new calculation, but can generalize the scheme applied in the one-dimensional case. The Bloch theorem holds in three dimensions as well as in one dimension and states that the wavefunctions solving a Hamiltonian with a periodic potential

$$V_{\text{lat}}(\vec{r} + \vec{R}) = V_{\text{lat}}(\vec{r}) \tag{3.24}$$

can be written as

$$\psi_{n,\vec{q}}(\vec{r}) = e^{i\vec{q}\vec{r}/\hbar}u_{n,\vec{q}}(\vec{r}) \text{ with } u_{n,\vec{q}}(\vec{r} + \vec{R}) = u_{n,\vec{q}}(\vec{r}). \tag{3.25}$$

Here, $\vec{R} = n_1\vec{d}_{\text{lat},1} + n_2\vec{d}_{\text{lat},2} + n_3\vec{d}_{\text{lat},3}$, $n_\text{i} \in \mathbb{Z}$ is a possible lattice vector composed of the primitive vectors $\vec{d}_{\text{lat},i}$ which are connected to the wavevectors $\vec{k}_{\text{lat},i}$ of the three single standing wave potentials

$$\vec{d}_{\text{lat},i}\vec{k}_{\text{lat},j} = \pi\delta_{i,j}. \tag{3.26}$$

As for the one-dimensional case, the Bloch functions

$$u_{n,\vec{q}}(\vec{r}) = \sum_{\vec{k}} c_{\vec{k}}^{n,\vec{q}} e^{i2\vec{k}\vec{r}} \text{ with } \vec{k} = \sum_{i=1}^{3} m_i\vec{k}_{\text{lat},i}\ ,\ m_i \in \mathbb{Z} \tag{3.27}$$

and the lattice potential

$$V_{\text{lat}}(\vec{r}) = \sum_{\vec{k}} V_{\vec{k}} e^{i2\vec{k}\vec{r}} = \sum_{j=1}^{3}\left(\frac{V_{0,j}}{2} + \frac{V_{0,j}}{4}\left(e^{-i2\vec{k}_{\text{lat},j}\vec{r}} + e^{i2\vec{k}_{\text{lat},j}\vec{r}}\right)\right) \tag{3.28}$$

can be expanded in plane waves where the sum covers the reciprocal or Bravais lattice. Plugging the wavefunction (eq. (3.25)) with the expansion of the Bloch function (eq. (3.27)) as well as the lattice potential (eq. (3.28)) into the Schrödinger equation (3.21) yields

$$\sum_{\vec{k}} e^{i2\vec{k}\vec{r}}\left(c_{\vec{k}}^{n,\vec{q}}\frac{\left(\vec{q} + 2\vec{k}\hbar\right)^2}{2m} + \sum_{\vec{k}'} c_{\vec{k}-\vec{k}'}^{n,\vec{q}} V_{\vec{k}'}\right) = \sum_{\vec{k}} e^{i2\vec{k}\vec{r}} E_{n,\vec{q}} c_{\vec{k}}^{n,\vec{q}}. \tag{3.29}$$

Because the plane waves are orthogonal, we get again a set of coupled equations for the Fourier coefficients $c_{\vec{k}}^{n,\vec{q}}$ which corresponds to an eigenvalue problem. As in the one-dimensional case, n denotes the band index and $\vec{q}$ the quasimomentum which can be restricted to the first Brillouin zone due to the periodicity of the solutions of the Schrödinger equation. The energy bands are sorted in increasing order and labeled by the band index n.

Figure 3.4 exemplarily depicts the lattice structure of a two-dimensional lattice with perpendicular and slightly tilted lattice axes as well as the corresponding band structure. The displayed energy spectrum originates from two lattice potentials with different lattice spacing and depth, but almost identical gaps from the first to the second band.

First, we discuss the lattice configuration with perpendicular lattice axes. In this case, the shape of the energy bands can be understood in terms of two one-dimensional band structures as the potential and thus the wavefunctions can be factorized. Along the axis of the first lattice (figure 3.4 b)), the first and second Bloch band show the characteristic bending known from the one-dimensional lattice potential. However, the third band has a different bending than in the one-dimensional case and is flatter than the second band. This is due to the fact that it corresponds to an excitation along the second lattice direction. The harmonic oscillator potentials between

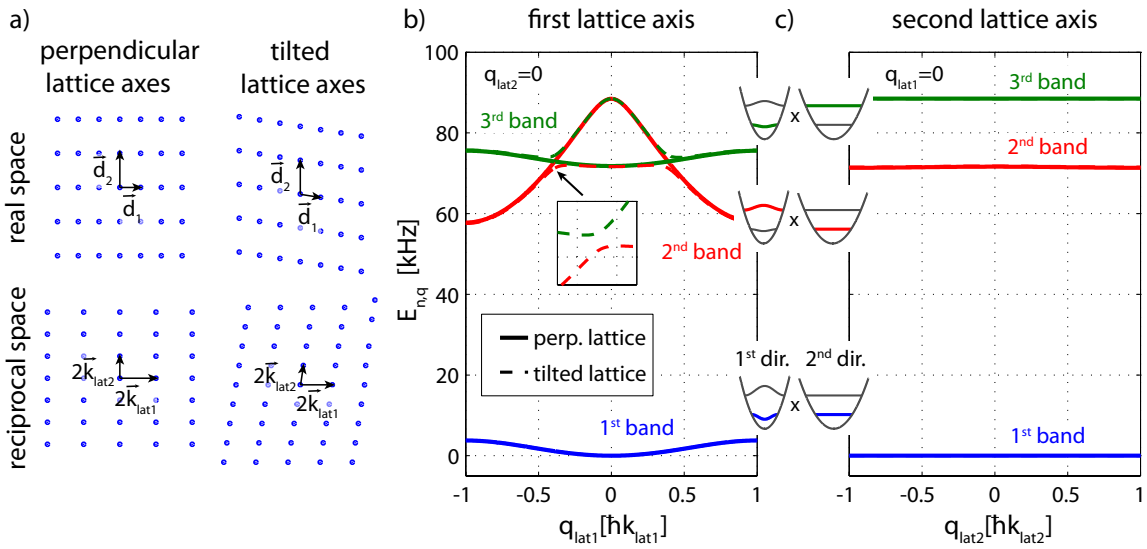

Figure 3.4.: a) 2d lattice structures in real and reciprocal space for a lattice with perpendicular and slightly titled lattice axes. b) and c) Band structure along the first and second lattice axis, respectively ($V_0 = 6$ and $33\,E_{\mathrm{rec}}$, $d_{\mathrm{lat}} = 0.67$ and $1.1\,\mu\mathrm{m}$). For the titled lattice configuration, the lattice axes deviate 3° from the perpendicular configuration causing an avoided crossing between the 2nd and 3rd band along the first lattice axis. The other energy bands coincide due to the small tilting angle almost perfectly for the two lattice configurations and can be hardly distinguished. The inset in b) displays the avoided crossing in case of tilted lattice axes more clearly. The harmonic potentials between b) and c) indicate the origin of the energy bands.

figure 3.4 b) and c) illustrate this explanation by assigning the analog two-dimensional harmonic oscillator modes to each energy band.

Next, we consider the band structure of a lattice with tilted lattice directions which is in general more challenging to understand. But in the depicted case, the lattice axes intersect almost perpendicular and thus the band structure can be understood by means of the band structure of the perpendicular lattice configuration. However, the two lattice directions are not independent and hence the dynamics along the different lattice directions are coupled. This coupling is manifested in the avoided crossing between the second and third Bloch band as depicted in figure 3.4 b).

For the subsequent lattice design and our later experiments, we have to keep this coupling in mind as different lattice directions are due to experimental imperfections never perpendicular to each other. Hence, if we need to exclude dynamics along certain lattice directions, it is not sufficient if the gap between the first and second for the corresponding lattice direction is larger than for the other lattice directions. But we also need to take the widths of the energy bands and their bending into account in order to eliminate dynamics between different Bloch bands.

3.3. Lattice Design and Implementation

In the following, we turn our attention to the experimental implementation of our lattice setup. For this purpose, we discuss the design criteria of our lattice and derive the lattice parameters according to the preceding theoretical considerations. The final part of this section presents the lattice setup and its implementation into the experiment.

3.3.1. Lattice Design Criteria

Longitudinal Lattice

Our lattice consists of different lattice axes which have different purposes and thus partly different requirements. The main lattice (in the following also referred to as longitudinal lattice) is used to prepare the lithium atoms in an out-of-equilibrium situation which is achieved by shaking the lattice along its lattice axis. As we want to address as many lithium atoms as possible but no sodium atoms, the longitudinal lattice potential has to be

- homogeneous over the extent of the lithium cloud such that all lithium atoms experience the same lattice potential and are affected by the shaking in the same way.
- species-selective for lithium which means that the chemical potential of the sodium cloud is much larger than the lattice potential for sodium.
  $\rightarrow \mu_{\mathrm{Na}} \gg V_{\mathrm{lat,Na}}$

Both these requirements can be met by large lattice beams whose frequencies are only slightly detuned from the lithium resonance frequency (eq. (3.1)). However, the maximal beam size is limited by the available laser power P as the lattice potential depth V_0 is proportional to the beam intensity I and scales as $V_0 \propto I \propto P/w_{\mathrm{beam}}^2$. The laser power restricts the waist of our lattice beams w_{beam} to $550\,\mu\mathrm{m}$ which yields a variation of the lattice potential of about $0.3\,\%$ over the $40\,\mu\mathrm{m}$ wide lithium cloud. Additionally, we require that

- the life time of the lithium atoms due to spontaneous emission, characterized by the photon scattering Γ_{scatter}, is much longer than the exposure time to the lattice potential t_{lat}.
  $\rightarrow 1/\Gamma_{\text{scatter}} \gg t_{\text{lat}}$

The latter condition puts a lower bound on the detuning (eq. (3.2)) and restricts the possible lattice depth for a certain lattice intensity.

As we will see in chapter 5, we prepare and probe the lithium atoms by pulsed lattice shaking and e. g. perform Ramsey type experiments. For these kind of experiments, we rely on the fact that all lithium atoms evolve in the same way because all atoms are detected simultaneously and different evolutions diminish the signal. Thus, beside the homogeneity of the lattice potential

- the width of the involved energy bands (for us the 1^{st} and 2^{nd} band) has to be small such that the lattice is in the harmonic oscillator regime and tunneling between neighboring sites occurs on a time scale shorter than the duration of the measurement t_{meas}.
  $\rightarrow h/J_1^{\text{long}} > t_{\text{meas}}$ and $h/J_2^{\text{long}} > t_{\text{meas}}$ [4]

- all atoms initially need to occupy the same and thus lowest band which means that the gap between the first and second band $\Delta E_{1\text{-}2}^{\text{long}}$ has to be larger than the corresponding energy scales of the lithium atoms. Depending on the experimental conditions, these energy scales are the temperature T and/or the chemical potential of the lithium atoms μ_{Li}.
  $\rightarrow \Delta E_{1\text{-}2}^{\text{long}} > \mu_{\text{Li}}, k_{\text{B}}T$

These last two conditions imply an optimal lattice spacing under the constraint that the lattice depth and thus the impact on the sodium atoms is minimized as both the band gap and width decrease with increasing lattice spacing (fig. 3.2). In order to determine the lattice parameters, we need a lower bound for the band gap from the chemical potential of the lithium atoms. In each experimental cycle we typically prepare about $1.5 \cdot 10^5$ lithium atoms in the optical dipole trap whose mean trapping frequency for lithium is about $\bar{\omega}_{\text{Li}} = 2\pi\, 500\,\text{Hz}$ (section 2.3). From these numbers, we approximate the chemical potential by the Fermi energy (eq. (2.21)) and get $\mu_{\text{Li}}/h \approx E_{\text{Fermi}}/h = 48\,\text{kHz}$. On the contrary, the temperature of the lithium atoms is typically about $T = 550\,\text{nK}$ which corresponds to $11\,\text{kHz}$. Furthermore, we estimate the duration of each measurement from damped oscillations of the lithium atoms in the dipole trap. These oscillations damp due to the interaction between the sodium and lithium atoms [41], and we expect that the time scale for interaction in the lattice experiments is on the same order of magnitude. Then, the damping time of 3 ms yields an upper bound of $300\,\text{Hz}$ for the width of the first and second band.

For these parameters, a rather large lattice spacing is advantageous due to the small lithium mass causing high tunneling rates. Thus, our longitudinal lattice potential is created by two laser beams intersecting at an angle of 35° instead of 180° as for two counterpropagating beams (fig. 3.6), and we get a lattice spacing of $d_{\text{lat}}^{\text{long}} = 1.1\,\mu\text{m}$. Typically our lattice is about $33\, E_{\text{rec}}^{\text{long}}$ deep which leads to a band gap of $\Delta E_{1\text{-}2}^{\text{long}}/h = 71.5\,\text{kHz}$, a band width of $8\,\text{Hz}$ and $280\,\text{Hz}$ for the first and second Bloch band, respectively.

Now, as we fixed the lattice spacing and depth, we return to the previous criteria and investigate the photon scattering rates for the lithium atoms and the impact on sodium. For the latter purpose,

[4] To distinguish between the different lattice directions, we label the corresponding quantities according to the lattice direction. But we omit the labeling in the following if we consider one-dimensional lattice potentials.

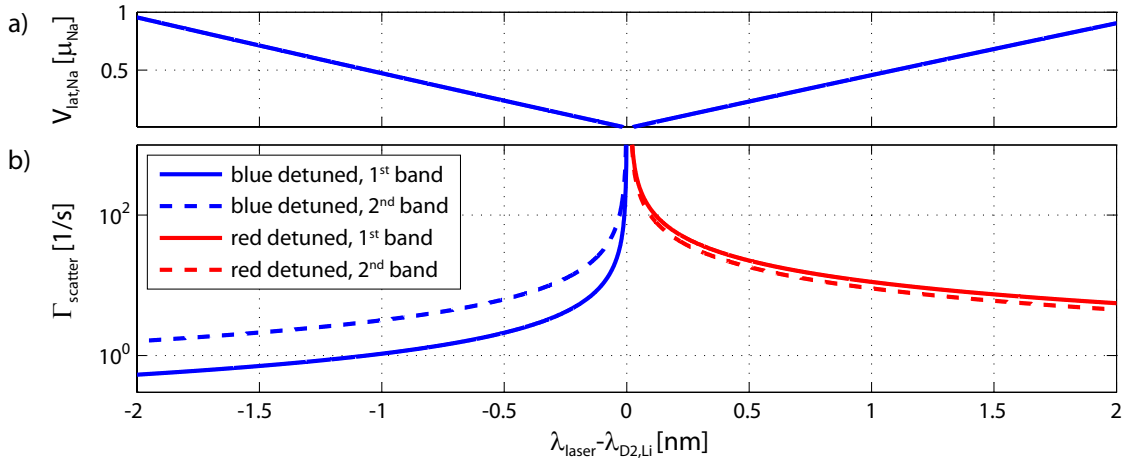

Figure 3.5.: Impact of the longitudinal lattice potential for different wavelengths of the lattice laser. The lattice depth is fixed to $V_0 = 33\, E_{\mathrm{rec}}^{\mathrm{long}}$ for the lithium atoms by compensating the detuning with the lattice intensity. a) Lattice depth for sodium in terms of the chemical potential ($\mu_{\mathrm{Na}}/h = 6.2\,\mathrm{kHz}$). b) The lithium photon scattering rates deviate for the first and second Bloch band and different detunings due to the different overlap with the high intensity regions of the lattice (logarithmic plot).

we have to compare the lattice height for sodium with its typical chemical potential of about $\mu_{\mathrm{Na}}/h = 6.2\,\mathrm{kHz}$ ($6 \cdot 10^5$ sodium atoms, $\bar{\omega}_{\mathrm{Na}} = 2\pi\, 238\,\mathrm{Hz}$). Figure 3.5 a) depicts the lattice depth for sodium in terms of its chemical potential for various wavelengths of the lattice laser and the corresponding lattice intensities which are determined by the fixed potential depth for lithium ($V_0 = 33\, E_{\mathrm{rec}}^{\mathrm{long}}$). In contrast to the optical dipole trap, the lattice potential for lithium can either be repulsive or attractive as long as the anti-confinement due to the curvature of the lattice beams is smaller than the confinement of the optical dipole trap. Thus, we consider lattice potentials which are blue and red detuned with respect to the lithium D2-line. The sign of the detuning barely affects the sodium atoms as the detuning of the lattice laser to the sodium D2-line differs only slightly for the investigated wavelength range. But close to the lithium D2-line the impact of the lattice on the sodium atoms vanishes as the intensity in the lattice beams shrinks for decreasing detuning and fixed lattice height for lithium (eq. (3.1)) which suggests using a rather small detuning.

However, the photon scattering rate for the lithium atoms diverges in vicinity of the lithium D2-line and thus their life time vanishes. Figure 3.5 b) depicts the scattering rate for lithium atoms in the first as well as the second Bloch band and shows a distinct asymmetry between the red and blue detuned lattice potential. This is due to the different overlap of the wavefunctions $\psi(x)$ with the lattice light $\Gamma_{\mathrm{scatter}} \propto \int \psi^*(x) I(x) \psi(x)\, \mathrm{d}x$ as atoms are for a blue detuned lattice repulsed from and for a red detuned lattice attracted to the high intensity regions.[5] The different overlap with the laser light also accounts for the difference between the scattering rates for the first and

[5] A further asymmetry arises from the influence of the lithium D1-line at $\lambda_{\mathrm{D1,Li}} = \lambda_{\mathrm{D2,Li}} + 0.002\,\mathrm{nm}$.

second Bloch band.

In summary, a blue detuned lattice is more suitable than a red detuned lattice but nevertheless we have to trade off between the impact on the sodium atoms and the photon scattering rates for the lithium atoms. Most of our experiments are performed with $-0.5\,\mathrm{nm}$ detuned lattice light as the lattice potential is due to the loading procedure applied for about $150\,\mathrm{ms}$ and smaller detunings already reduce the lithium atom number significantly. This results in a lattice potential for sodium of about $24\,\%$ of its chemical potential.

Transversal Lattices

As mentioned in the beginning of this section, our lattice setup consists of different lattice axes with different purposes. So far, we discussed the design of the main lattice axis which is used to manipulate the lithium atoms via a lattice shaking procedure. The other lattice directions (or transversal lattices) have to fulfill less strict criteria as we use them to tune the dimensionality for the lithium atoms in order to manipulate their dynamics in the sodium bath. Hence, we do not require that their first and second Bloch band are essentially flat. The lithium atoms are kinematically reduced in a lattice dimension if the following criteria are fulfilled [50, 51]

- their chemical potential μ_{Li} is below the energy gap to the next excited state.
  $\rightarrow \Delta E_{1\text{-}2}^{\mathrm{trans}} > \mu_{\mathrm{Li}}$
- the atoms cannot be thermally excited from the ground state to the next excited state.
  $\rightarrow \Delta E_{1\text{-}2}^{\mathrm{trans}} > k_{\mathrm{B}} T$

Additionally, we want to suppress excitations in the transversal directions if we shake the lattice along the longitudinal direction, and thus we require that

- the energy gap along the transversal lattice directions is larger than along the longitudinal direction.
  $\rightarrow \Delta E_{1\text{-}2}^{\mathrm{trans}} > \Delta E_{1\text{-}2}^{\mathrm{long}}$

However, we know from the previous discussion of the two-dimensional lattice potential that fulfilling the last condition is not completely sufficient in order to suppress excitations along the transversal lattice directions. For this purpose, we also have to account for the band widths of the longitudinal and transversal lattices. Though, in our case the restriction for the band gap of the transversal lattice is not much stronger because the widths of the first and second Bloch band of the longitudinal lattice direction are small compared to the corresponding band gap.

In order to fulfill the conditions above while keeping the required laser intensity small, the lattice spacing of the transversal lattice directions is chosen smaller than for the longitudinal direction (eq. (3.13)). Smaller intensities provide longer lithium life times due to less photon scattering processes and reduce the impact of the transversal lattice directions on the sodium atoms. Additionally, a tighter lattice spacing allows more lithium atoms in a three-dimensional lattice without occupying lattices sites multiply.

The transversal lattice directions are derived from the same laser source as the longitudinal lattice that means the wavelength of the lattice light is fixed to $\lambda_{\mathrm{laser}} \approx 670.5\,\mathrm{nm}$. The horizontally oriented transversal lattice (fig. 3.6) is created by a retro-reflected laser beam and has

therefore a lattice spacing of $d_{\text{lat}}^{\text{hor}} = 0.335\,\mu\text{m}$. The vertically oriented transversal lattice results from two lattice beams intersecting at an angle of 60° which yields a spacing of $d_{\text{lat}}^{\text{ver}} = 0.67\,\mu\text{m}$. The asymmetry between the two transversal lattice directions is not intended and arises from the restricted optical access in our experiment, but does not constrain their purpose.

Furthermore, the homogeneity of the transversal lattice potentials is not as crucial as for the longitudinal potential as long as the potential height at each lattice sites is large enough to freeze the dynamics along the transversal directions.

3.3.2. Lattice Setup

In the following, we briefly introduce the setup of the optical lattice (fig. 3.6 a)). For each lattice direction, we monitor the beam intensity on a photodiode and regulate the beam power via a feedback loop driving an acousto-optic modulator (not depicted). As all lattice axes are derived from the same laser, the acousto-optic modulators run on different frequencies in order to avoid lattice potentials due to the interference between lattice beams from different lattice axes.[6] To provide a well defined polarization, each lattice beam passes a polarizing beam splitter cube before entering the glass cell.

Longitudinal Lattice

The longitudinal lattice direction is our main tool to manipulate the lithium atoms and requires most care. For this reason, we derive the two lattice beams from a polarization cleaned beam with a non-polarizing beam splitter cube. This beam splitter delivers two beams with almost the same power and is less sensitive to temperature drifts than the combination of a polarizing beam splitter and a wave plate. Nevertheless, we monitor both lattice beams on photo diodes in order to detect any power drifts. An electro-optical modulator (EOM) placed in one of the two beam lines allows shifting the relative phase between the two lattice beams which leads to a spatial shift of the lattice potential.

Both lattice beams pass the atoms' position with a waist of $550\,\mu\text{m}$ and intersect at an angle of 35° which yields a lattice spacing of of $d_{\text{lat}}^{\text{long}} = 1.1\,\mu\text{m}$. Because of the intersection angle, the beam polarization needs to be linear along the y-axis to allow for maximal interference between the two lattice beams. A more detailed description of the longitudinal lattice and particularly the electro-optical modulator can be found in [52].

Transversal Vertical Lattice

For the same reason as for the longitudinal lattice direction, the polarization of the transversal vertical lattice beams points linearly along the y-axis. The initial lattice beam is recycled and interferes with itself to spare laser power. However, due to its polarization only about $50\,\%$ of the initial light passes the glass cell. Thus, the intensity of the back reflected beam is enhanced by a

[6] Despite their different frequencies, beams from different lattice direction still interfere and the interference pattern oscillates with their frequency difference (which is in our case larger than 20 MHz). However, the atoms do not follow the oscillating lattice potential as long as their trapping frequencies are well below the oscillation frequency. Thus, the atoms experience only a constant offset potential.

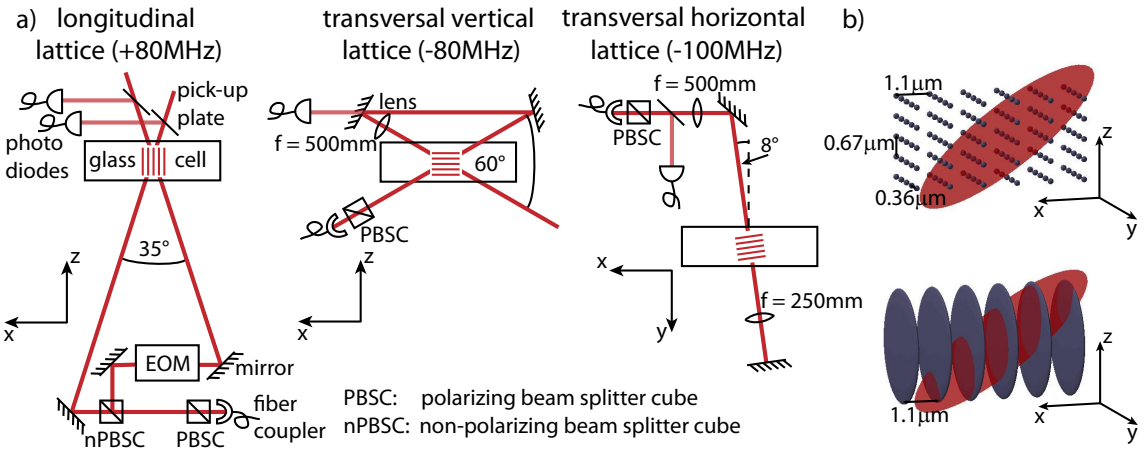

Figure 3.6.: a) Lattice setup for the different lattice directions. The frequencies in the captions denote the relative shift of the lattice beams to the laser frequency. A coordinate system displays the orientation of each lattice axis. b) Sketch of the three-dimensional (top) and longitudinal lattice potential (bottom) together with an isosurface of the optical dipole trap potential. The lattice spacings are depicted to scale, and the size of the lithium cloud in the dipole trap is about a factor of 10 larger than the displayed isosurface.

lens with a focal length of 500 mm. In order to compensate the power loss, the 500 µm waist of the initial beam has to be decreased to about 350 µm which is achieved by positioning the lens 35 cm from the atom cloud. The resulting difference between the intensity distributions of both beams is only about 1 % over the extent of the atom cloud and thus negligible.

The lattice beams intersect at an angle of about 60° which yields a lattice spacing of $d_{\mathrm{lat}}^{\mathrm{ver}} = 0.67\,\mu\mathrm{m}$.

Transversal Horizontal Lattice

The third lattice direction consists of a retro-reflected laser beam and thus has a lattice spacing of $d_{\mathrm{lat}}^{\mathrm{hor}} = 0.335\,\mu\mathrm{m}$. To avoid interference patterns between the lattice beams and their reflections from the glass cell, the lattice beams are tilted 8° with respect to the perpendicular of the glass cell and focused to 200 µm at the position of the atoms.[7] The latter is achieved by a telescope consisting of two lenses with a focal length of 500 mm and 250 mm. The polarization of the lattice beams points linearly along the x-axis.

Figure 3.6 b) illustrates the lattice structure arising from the three lattice directions and their different spacings as well as an isosurface of the optical dipole trap potential. The latter is espe-

[7] The atoms are located 2 cm from the wall of the glass cell which yields a 5.6 mm spacing between a 8° tilted lattice beam and its reflection.

cially relevant if we perform experiments with the longitudinal lattice only as the optical dipole trap provides in this case the confinement along the transversal directions.

After the discussion of the lattice theory and our lattice design criteria, we turn our focus in the following chapter onto its practical implementation and characterize the lattice setup experimentally.

4. Lattice Characterization

Before we investigate the dynamics of the lithium atoms in the Bose-Einstein condensate, we need to understand the evolution of the lithium atoms in the lattice potential in absence of the bosonic background. In order to provide a well-defined starting point for our investigations, this chapter characterizes the corresponding lattice potentials. As the lattice spacing is sufficiently well determined from the intersection angle and the wavelength of the lattice light, we can infer the band structure from the lattice depth alone. Hence, we focus in the following on the determination of the lattice depth and start with the discussion of our lattice loading procedure.

4.1. Lattice Loading and Brillouin Zone Mapping

Lattice Loading

After the last evaporative cooling step in the dipole trap, we apply the species-selective lattice for the lithium atoms. In order to avoid heating of the lithium atoms, we try to keep the loading procedure as adiabatic as possible and increase the intensity in the lattice beams exponentially $e^{t/\tau}$ with the time constant $\tau = 25\,\mathrm{ms}$ to its final value.

However, even if the lattice potential is increased adiabatically, some lithium atoms occupy states in excited Bloch bands after the loading procedure, whereas the first Bloch band is not completely filled. The underlying mechanism for this behavior is illustrated in figure 4.1 which depicts the eigenenergies for different lattice depths and a fixed dipole trap potential in one dimension. Without the lattice potential the energy spectrum resembles the equally spaced energy states of a harmonic oscillator, whereas we observe a band structure for deep lattice potentials. The exact transition between the harmonic oscillator spectrum and the lattice spectrum is rather complicated, but the important point is that only harmonic oscillator states with an energy lower than the recoil energy E_{rec} evolve definitively into states of the first Bloch band if the lattice depth is increased [53]. The final state for lithium atoms which initially occupy an energy above the recoil energy depends on the exact initial state and can either be located in the first or in higher Bloch bands.

Because of the fermionic nature of the lithium atoms, we can load only a limited amount of atoms into the lattice if we want to ensure that only the lowest Bloch band is occupied. We get an upper bound for the maximal number of atoms by considering the lattice loading in the limit of zero temperature. In this case, the lowest energy levels are occupied by exactly one fermion. In order to occupy only the first Bloch band, the chemical potential of the lithium atoms, or equivalently the Fermi energy, has to be lower than the recoil energy of the corresponding lattice direction. If we consider the longitudinal lattice with its rather large lattice spacing and thus low recoil energy ($E_{\mathrm{rec}}/h = 6.9\,\mathrm{kHz}$), we get a maximal number of $5 \cdot 10^2$ atoms (eq. (2.21)). To circumvent this limitation in the lithium atom number, we load the lattice with a background

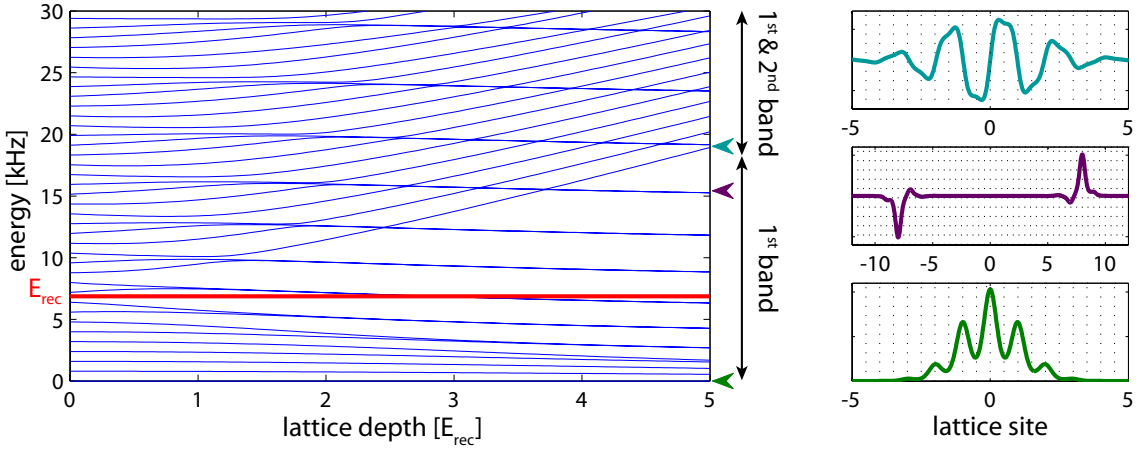

Figure 4.1.: Evolution of the energy spectrum in a harmonic trapping potential ($\omega = 2\pi\,800\,\mathrm{Hz}$) for increasing lattice depth ($d_{\mathrm{lat}} = 1.1\,\mu\mathrm{m}$, calculated according to section 3.2.2). The initially equally spaced energy spectrum of the harmonic oscillator develops for increasing lattice depth into a band structure. The vertical arrows at the right of the main graph indicate in which energy bands the energy levels evolve. The graphs on the right hand side display three characteristic eigenfunctions at a lattice depth of $5\,E_{\mathrm{rec}}$ whose corresponding energy levels are indicated by the color-coded arrows.

of sodium atoms. Because of the interaction between the sodium and the lithium atoms, the latter relax during the lattice loading from excited states, e. g. in the second Bloch band, to lower states in the first Bloch band. If the gap between the first and second Bloch band is larger than the temperature of the sodium atoms, all lithium atoms will finally occupy the first Bloch band as long as the number of background atoms is sufficiently large and the first Bloch band is not completely occupied.

As a consequence of this loading procedure, we prepare for a $V_0 = 33\,E_{\mathrm{rec}}$ deep longitudinal lattice about $85\,\%$ of $1 \cdot 10^5$ lithium atoms ($E_{\mathrm{F}} \approx 6\,E_{\mathrm{rec}}$) in the first Bloch band if we add a sodium background at $T = 550\,\mathrm{nK}$ ($\hat{=}\ 1.6\,E_{\mathrm{rec}}$). We are always left with a finite number of lithium atoms in higher Bloch bands as the extent of the lithium cloud is, for our trapping geometry, larger than the sodium cloud (see section 2.3.2) which prevents the relaxation of lithium atoms located outside of the sodium cloud. If the sodium background is removed before the lattice loading procedure, the relative occupation of the first Bloch band reduces to about $60\,\%$.

So far, our considerations did not include the location of the lithium atoms transferred to higher Bloch bands during the lattice loading. As indicated on the right hand side of figure 4.1, these states are prominently located in the central trapping region, whereas the unoccupied states in the first Bloch band are located in the outer regions. Thus, the relaxation process should be slow in a one-dimensional trapping geometry as the lithium atoms have to be redistributed between different lattice wells. We observe that the relaxation during the lattice loading is on the same time scale as the relaxation from the second to an empty first band (see chapter 7). We attribute this discrepancy to the dimensions transversal to the lattice potential. For a deep one-

dimensional lattice, thousands of empty transversal mode exist whose energy is lower than the band gap. Hence, the lithium atoms can decay from higher Bloch bands to the first Bloch band if they simultaneously change their transversal mode.

In a three-dimensional lattice geometry, the situation is more complicated as the lattice loading can lead to occupation of exited Bloch bands in all lattice directions, and the atoms cannot as easily be redistributed in the transversal directions as for a one-dimensional lattice potential. Thus, we find for a three-dimensional lattice potential a slightly lower occupation of the first Bloch band ($\approx 75\,\%$) in the longitudinal lattice than for a one-dimensional lattice potential.

If we intend to perform experiments with lithium only, we remove the sodium atoms by a resonant light pulse after the lattice loading procedure. We do not observe heating of the lithium atoms or a population change in the different Bloch bands due to the sodium removal. In order to ensure a clean preparation of the lithium atoms in the first Bloch band, we extract the sodium atom number from the shadow on the resonant light pulse as for common absorption imaging, and discard the data for which low sodium atom numbers did potentially not provide a clean preparation of the lithium atoms in the first Bloch band.

Brillouin Zone Mapping

For the detection of the band population, we apply a band mapping technique [54, 55] whose working principle is illustrated in the main graph of figure 4.2. The detection scheme relies on the fact that the quasimomenta of particles exposed to a lattice potential and the band population do not change if the lattice potential is decreased as long as the change is slow with respect to the time scale imposed by the band gaps. Additionally, the reduction of the lattice potential has to be fast compared to collision and redistribution processes.[1] If these requirements are fulfilled while the lattice potential is turned off, the quasimomentum $q \in [-\hbar k_{\mathrm{lat}}; \hbar k_{\mathrm{lat}}]$ of a particle which occupies the n^{th} Bloch band is adiabatically transferred to the real space momentum

$$p = q - \mathrm{sgn}\,(q)\,(-1)^n 2\hbar k_{\mathrm{lat}}(n-1). \tag{4.1}$$

Because the momentum distribution can be detected via a time-of-flight measurement, this procedure allows determining the band population as well as the quasimomentum distribution.

The graphs on the right hand side of figure 4.2 exemplarily depict two spatial distributions of the lithium atoms after $4\,\mathrm{ms}$ time-of-flight and a typical exponential lattice decrease $e^{-t/\tau}$ with $\tau = 125\,\mu\mathrm{s}$. The distributions show the integrated atom numbers for a sample mainly occupying the first and a sample mainly occupying the second band. We infer the population in the Bloch bands from counting the atom numbers in the different Brillouin zones (color-coded areas).

In case of filled Brillouin zones, we can alternatively fit the atom distribution by a function which resembles their almost rectangular shape. This fitting approach is appropriate for deep one-dimensional lattice potentials with sufficiently high atom numbers. In this case, the chemical potential of the lithium atoms is much larger than the dipole trap frequencies. Thus, the lattice loading procedure populates each quasimomentum with multiple lithium atoms as the atoms occupy the same quasimomentum but different modes of the dipole trap potential. Moreover, each

[1] These requirements can be fulfilled if the particles are not strongly interacting and if the trapping frequencies of the dipole trap are smaller than the band gaps.

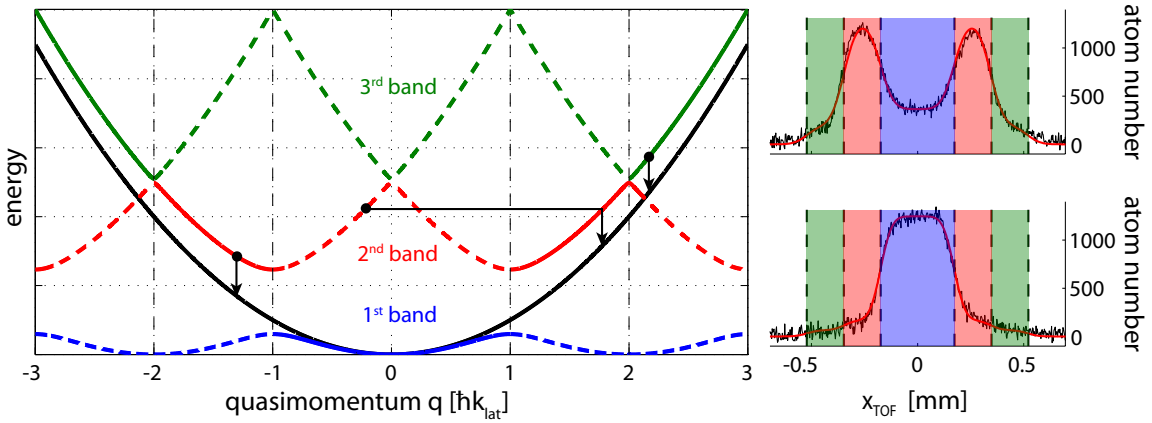

Figure 4.2.: The main graph illustrates the Brillouin zone or band mapping technique. For each Bloch band, the quasimomenta are uniquely mapped onto real momenta if the lattice potential is turned off with the appropriate timing. The smaller graphs depict band mapped atom distributions after time-of-flight with color-coded Brillouin zones.

quasimomentum is in average populated by the same amount of lithium atoms because the width of the first band is for a deep lattice potential small compared to the chemical potential. Thus, the atom distributions integrated along the transversal directions show the characteristic shape of a filled Brillouin zone as all quasimomenta with $q \in [-\hbar k_{\mathrm{lat}}; \hbar k_{\mathrm{lat}}]$ are equally occupied (see figure 4.2). We will see later on that we populate higher Bloch bands with an excitation scheme which is in the deep lattice regime not quasimomentum-selective and hence the population in the higher Bloch bands also reveals a sharp momentum distribution.

We empirically found that a sum of error functions matches the shape of the observed Brillouin zones, and we fit the distributions by

$$\sum_i f_i(x) + c_{\mathrm{offset}}, \tag{4.2}$$

where f_i is the fit to the i^{th} Brillouin zone and c_{offset} the overall offset. Each f_i is composed of error functions

$$\begin{aligned} f_i(x) = a_i \left(\mathrm{erf}\left(\frac{x - x_0 + i w_{\mathrm{BZ}}}{b_i} \right) - \mathrm{erf}\left(\frac{x - x_0 + (i-1) w_{\mathrm{BZ}}}{b_i} \right) \right) & \quad \Big\} \; q < 0 \\ + a_i \left(\mathrm{erf}\left(\frac{x - x_0 - (i-1) w_{\mathrm{BZ}}}{b_i} \right) - \mathrm{erf}\left(\frac{x - x_0 - i w_{\mathrm{BZ}}}{b_i} \right) \right) & \quad \Big\} \; q > 0. \end{aligned} \tag{4.3}$$

Here, the parameter b_i determines the steepness of the i^{th} Brillouin zone edge, x_0 denotes the central position of the atom cloud, a_i the amplitude for the i^{th} Brillouin zone and w_{BZ} the half width of the Brillouin zones. If we leave the a_i's, b_i's, c_{offset} and x_0 as free parameters but fix $w_{\mathrm{BZ}} = \hbar k_{\mathrm{lat}} t_{\mathrm{TOF}}$, the data is well fitted and we find good agreement between the population determination by the fitting and by the counting algorithm. Whereas the latter one is the more

robust approach, the fitting procedure offers the opportunity to determine the band populations for smaller expansion times for which the Brillouin zones have not split up yet.

4.2. Lattice Oscillations

4.2.1. Calibration of the Lattice Displacement

As mentioned in the previous chapter, the electro-optical modulator (EOM) placed in one of the longitudinal lattice beams allows controlling the relative phase between the two beams. An abrupt change of the voltage applied to the EOM results in a sudden phase shift and displacement of the longitudinal lattice potential. This displacement induces dynamics of the lithium atoms as long as the change in the lattice position is fast compared to the trapping frequencies of the lattice. However, if the lattice is instantaneously shifted by multiples of the lattice spacing, the lithium atoms stay at rest.

Figure 4.3 a) depicts the impact of sudden lattice displacements on the lithium atoms.[2] Before each displacement, about $85\,\%$ of all atoms occupy the first Bloch band. The atoms are excited to higher energy bands if the lattice is displaced via a phase jump resulting from the changed EOM voltage. We observe a decreasing amount of atoms in the first band and an increasing number of excited atoms for increasing phase jumps. However, at some point the atom number in the lowest band rises again an reaches a first maximum, which is shown in figure 4.3 a). We interpret the location of the first maximum as a lattice displacement by one lattice site ($d_{\mathrm{lat}} = 1.1\,\mu\mathrm{m}$) or a relative phase shift of 2π between the lattice beams, respectively. Because of the finite speed of the EOM and the supplying amplifier, the lattice position does not change instantaneously which causes excitations to higher Bloch bands even if the lattice is displaced by multiples of the lattice spacing. Thus, the occupation of the first Bloch band is at the first maximum lower than the initial occupation of $85\,\%$. By fitting a cosine to the fraction in the first band, we get the EOM voltage jump corresponding to a displacement by one lattice site and thus the lattice displacement per voltage

$$\frac{\Delta x_{\mathrm{dis}}}{\Delta U} = (95.5 \pm 0.3)\frac{\mathrm{nm}}{\mathrm{V}}. \tag{4.4}$$

4.2.2. Oscillations in the Lattice Potential

The lattice displacement can also be employed for a determination of the lattice depth. The lattice kick leads for each atom to a coherent occupation of different Bloch bands and induces an oscillation in position and momentum space whose frequency is given by the energy difference of the involved Bloch bands [56]. We usually investigate the oscillations in momentum space by time-of-flight measurements which yields larger oscillation amplitudes than in position space and is thus experimentally easier to detect. We extract the central position of the lithium atoms by a Gaussian fit to their density distribution. Figure 4.3 b) depicts a characteristic oscillation in the deep lattice regime with a frequency of $\omega = 2\pi\,(68.95 \pm 0.34)\,\mathrm{kHz}$ corresponding to a lattice depth of $V_0 = (30.8 \pm 0.3)\,E_{\mathrm{rec}}$.

[2] The measurements presented in this section are performed with only the longitudinal lattice and our previous dipole trap setup corresponding to trapping frequencies of $(\omega_{1,\mathrm{Li}}, \omega_{2,\mathrm{Li}}, \omega_{3,\mathrm{Li}}) = 2\pi\,(155, 158, 323)\,\mathrm{Hz}$.

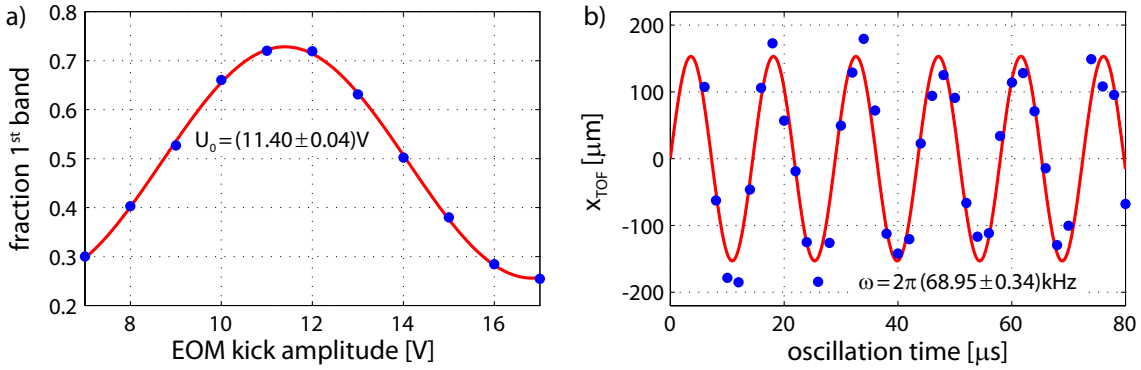

Figure 4.3.: a) An abrupt change of the EOM voltage causes a sudden lattice displacement and excitations from the first to higher Bloch bands. The number of unexcited atoms (blue dots) reaches a first maximum for a displacement by one lattice site and is fitted by a cosine (red line). b) Oscillations of lithium atoms in the species-selective lattice induced by a lattice displacement. The position of the atoms (blue dots) is detected for different oscillation times after 4 ms time-of-flight. Thus, the observed oscillation corresponds to an oscillation in momentum space which is fitted by a sine (red line).

We can use the oscillation amplitude to check if our understanding of the lattice kicks is correct. For this purpose, we extract the maximal velocity during an oscillation from the oscillation amplitude and the time-of-flight $v_{\mathrm{max}} = x_{\mathrm{max}}/t_{\mathrm{TOF}} = (153 \pm 15)\,\mu\mathrm{m}/4\,\mathrm{ms}$. Assuming a harmonic potential relates the initial lattice displacement to the maximal velocity $x_{\mathrm{ini}} = v_{\mathrm{max}}/\omega$ and yields $x_{\mathrm{ini}} = (88.3 \pm 8.6)\,\mathrm{nm}$. Because of the EOM kick amplitude of 1 V which induced the oscillation, we naively expect a value of $x_{\mathrm{ini}} = (95.5 \pm 0.3)\,\mathrm{nm}$ which is slightly higher than the measured one but agrees within the error bars. Moreover, we also anticipate to some extent a higher theoretical value as we observed that a displacement by one lattice site induces some excitations. Hence, the lattice displacement is only approximately instantaneous which effectively leads to smaller lattice displacements.

So far, we discussed the oscillations of the lithium atoms in the longitudinal lattice and the deep lattice regime. In this regime, each lattice site can be considered as an independent harmonic oscillator, and one observes distinct oscillations as long as the different harmonic oscillator frequencies do not deviate. As the inhomogeneity of our lattice is on the order of 1 % (see section 3.3.1), we expect for a 70 kHz lattice a dephasing of the different oscillations on the scale of some milliseconds which is much longer than the period depicted in figure 4.3 b).

However, for lower lattice potentials, we observe a damping of the lattice oscillations as displayed in figure 4.4 a) which cannot be attributed to the lattice inhomogeneity as the dephasing mechanism for lower lattice depths is even slower. But due to the lower lattice depth, the lattice oscillations cannot be interpreted in the frame of independent harmonic oscillators as the atoms start tunneling between neighboring lattice sites on time scales on the order of the observed period. Additionally, the energy gaps between the Bloch bands populated by the lattice displace-

ment vary as the lattice potential at each lattice site cannot be approximated by a parabola, and the deviation due to the sine shaped potential has to be taken into account. To test our interpretation of the damping mechanisms, we perform in the following numerical simulations of the lattice oscillations.

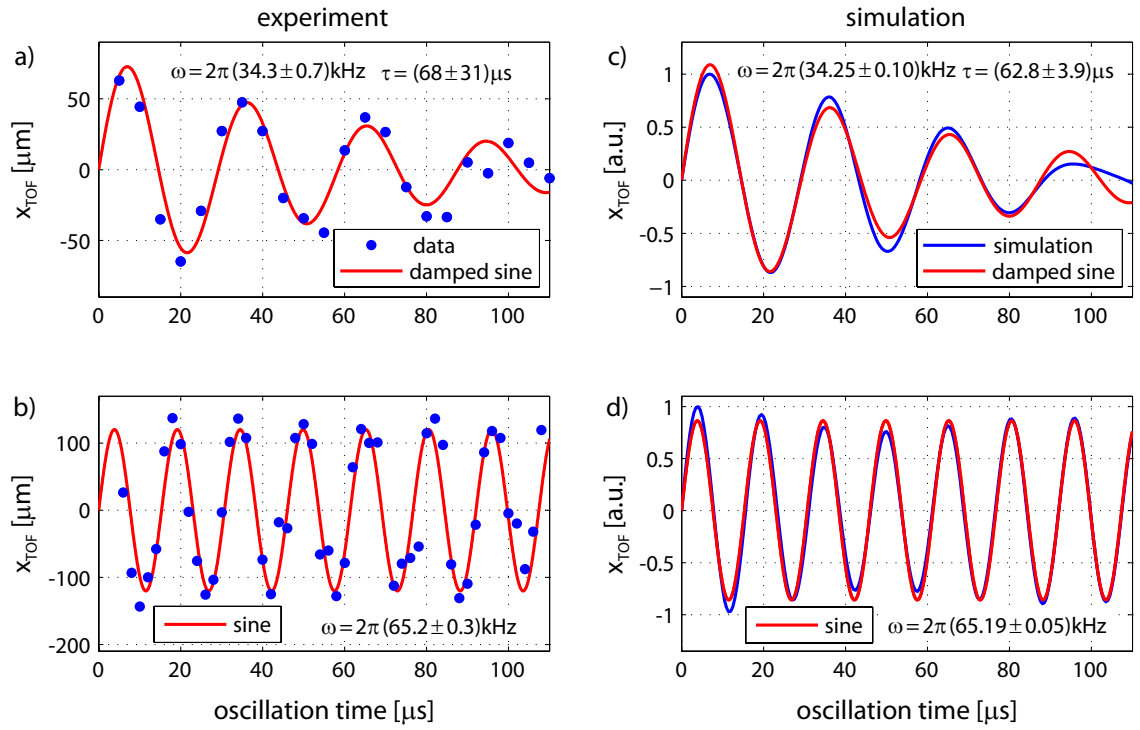

Figure 4.4.: a) Lattice oscillations (blue dots) after 2 ms time-of-flight in a $V_0 = (9.7 \pm 0.3)\, E_{\mathrm{rec}}$ deep lattice. The oscillations are fitted by a damped sine (red line) and compared to a one-dimensional simulation of the lattice oscillations (blue line) shown in c). The simulated data depicts the oscillation of the averaged momentum of the lithium cloud, which corresponds to the position after time-of-flight, and is also fitted by a damped sine (red line). Both data sets show the same damping behavior and their damping constants τ agree within the error bars. b) and d) show the data sets corresponding to a) and c) but in a deeper lattice potential ($V_0 = (27.9 \pm 0.2)\, E_{\mathrm{rec}}$). Here, no damping is observed. The oscillations in the deeper lattice show a larger amplitude for the same lattice displacement due to the stronger confinement.

4.3. Simulating the Dynamics in the One-Dimensional Inhomogeneous Lattice Potential

To calculate the oscillations of the lithium atoms in the lattice potential, we start our considerations for feasibility with the time evolution of a single lithium atom. However, experimentally we do not observe the dynamics of single lithium atoms, but detect all atoms at once. We account for this fact by averaging over multiple single atom dynamics with different initial conditions. For this purpose, we select the energy eigenstates of the lattice potential as initial states and weight the corresponding time evolutions according to the occupation probability for a Fermi gas.

In the following, we do not restrict the calculations to the lattice oscillations, but consider the time evolution more generally in a time-dependent potential as we intend to return to the numerical simulations in the context of Rabi- and Ramsey-type experiments in the subsequent chapter.

The time evolution of a state $|\psi, t\rangle$ is governed by the time-dependent Schrödinger equation

$$i\hbar\frac{\partial}{\partial t}|\psi, t\rangle = \hat{H}|\psi, t\rangle = \left(\frac{\hat{p}^2}{2m} + \hat{V}(x, t)\right)|\psi, t\rangle . \tag{4.5}$$

Here, $V(x, t)$ is an arbitrary potential which depends on time and position. This equation is fulfilled by [57]

$$|\psi, t\rangle = e^{-i\hat{H}(t-t_0)/\hbar}|\psi, t_0\rangle , \tag{4.6}$$

where $|\psi, t_0\rangle$ is the state at an earlier time t_0. In order to calculate the time evolution of $|\psi, t_0\rangle$, we apply the split-step Fourier method [58] and split the time evolution operator $e^{-i\hat{H}(t-t_0)/\hbar}$ into a part diagonal in the momentum basis $|p\rangle$ and a part diagonal in the position basis $|x\rangle$. This can be achieved using the Baker-Campbell-Hausdorff identity [57]

$$e^{\hat{A}}e^{\hat{B}} = e^{\hat{C}} \text{ with } \hat{C} = \hat{A} + \hat{B} + \frac{1}{2}[\hat{A}, \hat{B}] + \frac{1}{12}[\hat{A}, [\hat{A}, \hat{B}]] - \frac{1}{12}[\hat{B}, [\hat{A}, \hat{B}]] + \dots . \tag{4.7}$$

Thus, the time evolution operator can be approximately replaced by

$$e^{-i\frac{\hat{V}(x,t)}{2}\frac{\tau}{\hbar}}e^{-i\frac{\hat{p}^2}{2m}\frac{\tau}{\hbar}}e^{-i\frac{\hat{V}(x,t)}{2}\frac{\tau}{\hbar}} = e^{-i(\frac{\hat{p}^2}{2m}+\hat{V}(x,t))\frac{\tau}{\hbar}+\mathcal{O}(\tau^3)} \approx e^{-i\hat{H}\frac{\tau}{\hbar}} \tag{4.8}$$

as long as the time evolution interval $\tau = t - t_0$ is small compared to the eigenfrequencies of $\hat{H}$.[3] To compute the evolution for long time scales, the evolution can be split into small steps and for each step the evolution is performed with the operator given in equation (4.8). Due to the splitting of the time evolution operator into a momentum and a position dependent part, it is convenient to apply these operators in the corresponding basis. For this purpose, we use the identity $\mathbb{1} = \int \mathrm{d}x\,|x\rangle\langle x|$ and $\mathbb{1} = \int \mathrm{d}p\,|p\rangle\langle p|$ to compute the wavefunction $\psi(x, t) = \langle x|\psi, t\rangle$

$$\psi(x, t) = \langle x|\, e^{-i\hat{H}\frac{\tau}{\hbar}}|\psi, t_0\rangle = \int \mathrm{d}x'\,\langle x|\, e^{-i\hat{H}\frac{\tau}{\hbar}}|x'\rangle\langle x'|\psi, t_0\rangle$$

[3] The operator on the left hand side of equation (4.8) is symmetrized to reduce the error from $\mathcal{O}(\tau^2)$ to $\mathcal{O}(\tau^3)$.

$$\approx \int \mathrm{d}x' \int \mathrm{d}p' \underbrace{\langle x|\, e^{-i\frac{\hat{V}(x,t)}{2}\frac{\tau}{\hbar}}\, |p'\rangle}_{=e^{-i\frac{V(x,t)}{2}\frac{\tau}{\hbar}}\langle x|p'\rangle} \underbrace{\langle p'|\, e^{-i\frac{\hat{p}^2}{2m}\frac{\tau}{\hbar}} e^{-i\frac{\hat{V}(x,t)}{2}\frac{\tau}{\hbar}}\, |x'\rangle}_{e^{-i\frac{p'^2}{2m}\frac{\tau}{\hbar}} e^{-i\frac{V(x',t)}{2}\frac{\tau}{\hbar}}\langle p'|x'\rangle} \langle x'|\psi, t_0\rangle$$

$$= e^{-i\frac{V(x,t)}{2}\frac{\tau}{\hbar}} \int \mathrm{d}p' e^{-i\frac{p'^2}{2m}\frac{\tau}{\hbar}} \langle x|p'\rangle \int \mathrm{d}x' e^{-i\frac{V(x',t)}{2}\frac{\tau}{\hbar}} \langle p'|x'\rangle\, \psi(x', t_0). \tag{4.9}$$

Thus, the time evolution of the wavefunction can be calculated by two basis transformations, from the position to the momentum $\langle p'|x'\rangle$ and back to the position basis $\langle x|p'\rangle$. These transformations are numerically easy to handle as the wavefunctions of the momentum eigenstates $|p'\rangle$ are the plane waves $\langle x|p\rangle = \frac{1}{\sqrt{2\pi\hbar}} e^{ipx/\hbar}$ and hence the integrals correspond to a Fourier and an inverse Fourier transformation.

The presented split-step Fourier method calculates the time evolution of a single wavefunction. However, we usually prepare several thousands of lithium atoms in each experiment which occupy due to their fermionic nature different states and detect all atoms at once. In order to compare the experimentally observed dynamics to the one-dimensional time-dependent calculations, we assume that the lithium atoms evolve independently and neglect many-body effects. Furthermore, we ignore dynamics in directions transversal to the time-dependent lattice potential as the dynamics separate in case of perpendicular potential axes. In this case, we can calculate the outcome of the measurement in one dimension for each atom separately and average over all results.

In the experiment, the lithium atoms are initially prepared in the first Bloch band and thus we can restrict the calculation to the time evolution of the energy eigenfunctions $\psi_{1,j}(x)$ of the first Bloch band as initial wavefunctions.[4] To include the occupation probability of the initial wavefunctions, we compute a weighting factor w_j for each $\psi_{1,j}(x)$ with energy E^1_j. For this purpose, we take the Fermi-Dirac statistics into account and sum over all excitation modes perpendicular to the lattice axis

$$w_j = \sum_k \frac{1}{e^{(E^1_j + E^{\mathrm{exc}}_k - \mu)/(k_\mathrm{B}T)} + 1}. \tag{4.10}$$

Here, E^{exc}_k is the energy corresponding to the k^{th} excitation mode transversal to the lattice axis. E. g. in case of a one-dimensional lattice potential, E^{exc}_k is a sum of optical dipole trap modes in y- and z-direction $E^{\mathrm{exc}}_k = (m+1/2)\hbar\omega_\mathrm{y} + (n+1/2)\hbar\omega_\mathrm{z}$. Furthermore, the chemical potential is fixed by the normalization condition for the particle number of the lithium atoms $\sum_j w_j = N_{\mathrm{Li}}$.

According to these considerations, we obtain the expectation value $o(t)$ for an observable $O(x)$ (denoted in the position basis) after a perturbation of the lattice potential by calculation of

$$o(t) = \frac{\sum_j w_j \int \psi^*_{1,j}(x,t) O(x) \psi_{1,j}(x,t) \mathrm{d}x}{\sum_j w_j}. \tag{4.11}$$

[4] Instead of $\psi_{1,q}(x)$, the energy eigenfunctions are denoted by $\psi_{1,j}(x)$ as there is no clear attribution of the quasi-momentum due to potential inhomogeneity. The initial energy eigenfunctions evolve in time as they are no eigenfunctions of the time-dependent Hamiltonian of the perturbed lattice potential.

At this point, we return to lattice oscillations discussed earlier and test our interpretation of the damping mechanism with the help of the split-step Fourier method. For this purpose, we calculate the time evolution of the position and momentum expectation values according to equation (4.11) for the atom number and temperature determined from the experiment. The simulations are performed for the inhomogeneous lattice potential which includes the underlying optical dipole trap potential as well as inhomogeneity of the lattice beams.

The results are presented next to the experimental data in figure 4.4 c). The lattice depth used for the simulations is adjusted to $V_0 = 10\,E_{\mathrm{rec}}$ such that the frequency of the calculated lattice oscillations matches the frequency of the experimental data. The simulated data shows the same damping behavior as the observed oscillations. For a more quantitative comparison, the experimental and simulated data are fitted by a damped sine. The damping times obtained from these fits agree within their error bars and support the interpretation of the lattice oscillations on the basis of the one-dimensional simulations. This observation is consistent with the fact that the experimental conditions for the lattice oscillation measurements are close to the assumption made for the simulations. Particularly, the short time scales of the lattice oscillations allow neglecting the dynamics in directions transverse to the lattice axis as those evolve due to the lower transversal confinement on time scales two orders of magnitude slower than the lattice oscillations. Hence, the dynamics can be well described by a one-dimensional approach.

Additionally, figure 4.4 b) and d) depict a lattice oscillation and the corresponding simulations in a deeper lattice potential where no damping is detected during the observation time. Also in this regime, the simulation and the experimental data are consistent and support the interpreta-

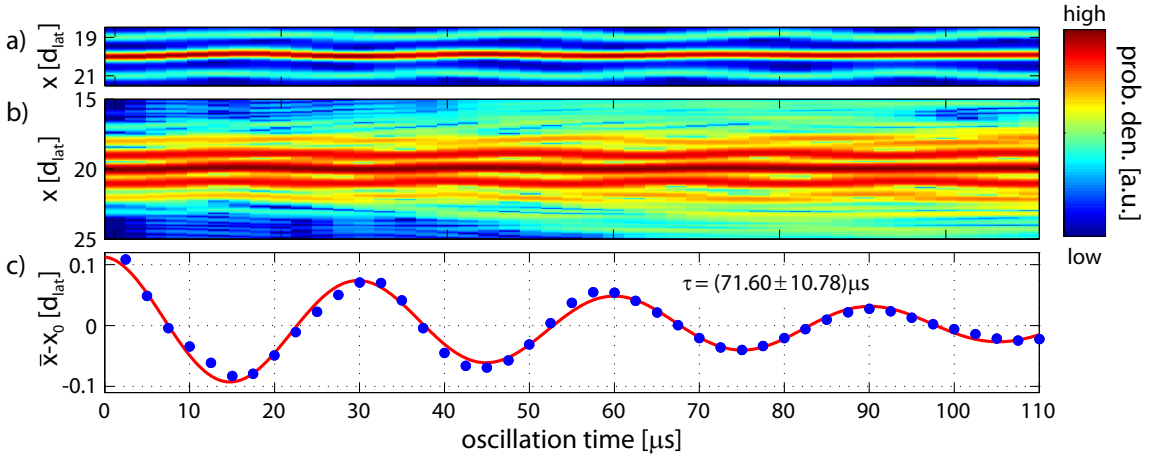

Figure 4.5.: Simulated time evolution of a single energy eigenfunction of the unperturbed lattice potential which is centered at the 20$^{\mathrm{th}}$ lattice site. a) After the lattice displacement, the probability density shows oscillations around the 20$^{\mathrm{th}}$ lattice site. These are accompanied by a spreading of the wavefunction which is shown in b) by a logarithmic plot of the probability density and which causes the damping of the oscillations. c) depicts the corresponding time evolution of the position expectation value $\bar{x}$ with respect to the initial position x_0. The red line displays the fit of a damped sine.

tion of the experimental data by means of the simulations.

To illustrate that the damping of the oscillations in the weak lattice potential $V_0 = 10\,E_{\text{rec}}$ is caused by single particle properties as the tunneling between different lattice sites and not by the averaging over the different evolutions of the lithium atoms, figure 4.5 depicts the time evolution of the initial energy eigenfunction centered at the 20^{th} lattice site after a sudden lattice displacement. The graphs depict the damped oscillation of the position expectation value for a single wavefunction. The damping of the oscillation is accompanied by a simultaneous spreading of the wavefunction. This fact demonstrates that the damping is associated with tunneling processes and appears on a single particle level, i. e. it does not originate from averaging over atoms oscillating at different frequencies. At this point, we skip a more rigorous investigation of the underlying mechanisms causing the damping of the oscillations due to tunneling as we will discuss these processes later in the context of Ramsey-type experiments (section 5.3), and we turn to an alternative calibration of the lattice depth.

4.4. Lattice Spectroscopy

Longitudinal Lattice

In the previous section, we used the EOM to induce oscillations of the lithium atoms by a sudden displacement of the lattice potential in order to calibrate its depth. Complementary, the EOM can also be utilized for spectroscopy measurements by periodically modulating the relative phase between the two lattice beams [59]. Thereby, the position of the lattice potential minima changes and atoms are transferred to higher Bloch bands if the shaking frequency ω_{exc} matches the band gap.

The Hamiltonian governing the evolution in the sinusoidally shaken lattice potential reads as

$$H_{\text{lat}}(t) = \frac{p^2}{2m} + V_{\text{lat}}(x,t) \;\text{ with }\; V_{\text{lat}}(x,t) = \frac{V_0}{2} + \frac{V_0}{2}\cos\left(2k_{\text{lat}}\left(x + x_0\sin\left(\omega_{\text{exc}}t\right)\right)\right). \tag{4.12}$$

As long as the shaking amplitude x_0 is small compared to the lattice spacing, the time-dependent lattice potential $V_{\text{lat}}(x,t)$ can be expanded to first order in $x_0 k_{\text{lat}}$ which splits the Hamiltonian into the original lattice Hamiltonian and a time-dependent perturbation $V_{\text{exc}}(x,t)$

$$H_{\text{lat}}(t) = H_{\text{lat}}(t=0) + V_{\text{exc}}(x,t) \;\text{ with }\; V_{\text{exc}}(x,t) = -V_0 x_0 k_{\text{lat}}\sin\left(2k_{\text{lat}}x\right)\sin\left(\omega_{\text{exc}}t\right). \tag{4.13}$$

As $V_{\text{exc}}(-x,t) = -V_{\text{exc}}(x,t)$, the lattice shaking couples states of opposite parity and transfers atoms from the first to the second Bloch band, whereas the transfer from the first to third Bloch band is suppressed.

In order to determine the lattice depth, we shake the lattice with different frequencies and detect the resulting excitation to the second Bloch band. Especially, for low lattice potentials, the observed resonance peak can be very broad due to the bending of the Bloch bands, and a precise determination of the lattice depth requires an analysis of the quasimomentum of the excited atoms [60]. However, for the longitudinal lattice, the gap between the first and the second Bloch band is usually much larger than their width and hence already a non-quasimomentum-selective

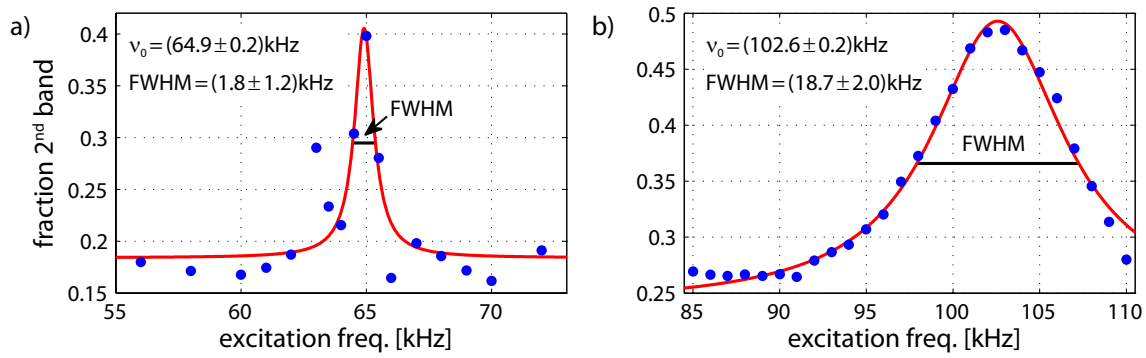

Figure 4.6.: Spectroscopy of the lattice potential by periodic modulation of the phase between the two lattice beams. a) Longitudinal lattice b) Transversal vertical lattice. Both data sets are fitted by a Lorentz distribution. The larger width of the resonance peak for the transversal direction compared to the longitudinal direction originates from the smaller lattice spacing causing a larger width of the second Bloch band.

detection of the resonance frequency suffices to infer the lattice depth. Figure 4.6 a) depicts such a spectroscopy measurement which is performed for the same lattice parameters as the oscillations in figure 4.4 b) and a shaking amplitude of about $x_0 = 10^{-3} d_{\mathrm{lat}}$. The resonance frequency determined by a fitted Lorentz distribution yields, within the uncertainties, the same value as the oscillation frequency. Thus, we can determine the depth of the longitudinal lattice potential to $V_0 = (27.7 \pm 0.2)\, E_{\mathrm{rec}}$. The corresponding width of the first and second Bloch band is 17 Hz and 525 Hz which is on the order of the full width half maximum of the observed resonance peak.

Transversal Lattice

So far, we discussed only the characterization of the longitudinal lattice. Now, we turn our view to the transversal vertical lattice for which we can also infer the lattice depth by modulation of the lattice potential. Due to the lack of an EOM, we induce a motion of the lattice potential by a periodic alternation of the radio frequency driving the acousto-optic modulator which regulates the power in the lattice beams. Because of the longer traveling range $L = 90$ cm of the back reflected lattice beam, the two lattice beams have a phase difference of $k_{\mathrm{lat}} L$ at the position of the atoms. If the frequency of the lattice beams is altered by $\delta\nu$, the phase between the lattice beams changes by $2\pi L \delta\nu / c$, where c is the speed of light. For instance, a radio frequency change of 10 MHz leads to a phase shift of $2\pi \cdot 0.06$ ($\delta\nu = 20$ MHz) and shifts the lattice position almost instantaneously ($\delta t = L/c = 3$ ns) by $0.06\, d_{\mathrm{lat}}$.

However, the modulation of the radio frequency causes also an alternating diffraction angle of the lattice beam from the modulator. Hence, we place the acousto-optical modulator before an optical fiber in order to avoid drifts of the lattice position. Moreover, the modulator is implemented in a double pass configuration which circumvents large variations of the fiber coupling efficiency and hence the lattice beam intensity. Nevertheless, the beam intensity changes during the spectroscopy measurement by about 3 % as the double pass configuration does not fully

compensate the drifts of the beam position and as the diffraction efficiency of the acousto-optic modulator depends on the applied radio frequency. We cannot compensate for this effect because these modulations occur on the time scale of the excitation frequency ($\approx 100\,\mathrm{kHz}$) which is beyond the speed of our regulation circuit for the lattice beam intensity. Though, as the band gap scales approximately with the square root of the lattice depth and hence the lattice beam intensity, we do not expect that the small variation of the beam intensity prevents the determination of the lattice depth by the modulation of the radio frequency.

Figure 4.6 b) shows a spectroscopy measurement for which we modulated the radio frequency between 95 and $105\,\mathrm{MHz}$ with various frequencies. We observe a clear resonance feature at $\nu_0 = (102.6 \pm 0.2)\,\mathrm{kHz}$ which corresponds to a lattice depth of $V_0 = (11.5 \pm 0.1)\,E_{\mathrm{rec}}$ and is consistent with a complementary oscillation measurement.[5] The spectroscopy peak for the transversal vertical lattice looks much broader than for the longitudinal lattice and shows deviations from a Lorentz distribution. The larger extent and probably also the different resonance shape is caused by the larger width of the second Bloch band due to the smaller lattice spacing which is for the displayed measurement $14\,\mathrm{kHz}$ wide.

4.5. Life Time of Lithium in the Optical Lattice

Besides the lattice depth, the life time of the atoms in the lattice potential is of interest as it impacts the maximal measurement duration and the data analysis. Because of the much smaller detuning for the lithium atoms, the lattice light mostly limits the life time of the lithium atoms, whereas the corresponding sodium atom loss is for our experiments negligible.

Figure 4.7 a) displays the number of lithium atoms in the first Bloch band and without sodium atoms versus the time for which the atoms are confined in a blue detuned one-dimensional longitudinal lattice potential ($\lambda_{\mathrm{laser}} = 670.5\,\mathrm{nm}$). We observe a clear decay of the atom number which we attribute to the scattering of lattice light, and an exponential fit to the data yields a life time of $\tau = (511 \pm 61)\,\mathrm{ms}$.

To verify our interpretation, we calculate the photon scattering rate from the intensity in the lattice beams which we infer from the lattice depth ($V_0 = 33\,E_{\mathrm{rec}}^{\mathrm{long}}$). Moreover, we account for the overlap with the lattice light by approximating the lattice potential as a set of harmonic oscillator potentials (see section 3.3.1). From the calculated scattering rate, we get an estimate for the life time of the lithium atoms of $465\,\mathrm{ms}$ under the assumption that each photon absorbed by a lithium atom leads to its loss. This assumption seems reasonable as the atoms gain about $4\,\mu\mathrm{K}$ in kinetic energy due to the photon kick which is on the order of the optical dipole trap height confining the atoms in the transversal directions. Furthermore, the redistribution of the kinetic energy to other lithium atoms can be neglected as the kinetic energy is still far below the height of the centrifugal barrier ($\sim 1\,\mathrm{mK}$ for p-wave collisions). Thus, the observed life time agrees remarkably well with the theoretical estimate.

Figure 4.7 c) depicts the same measurement performed in a three-dimensional lattice potential.

[5] The oscillation is induced by a sudden jump of the radio frequency.

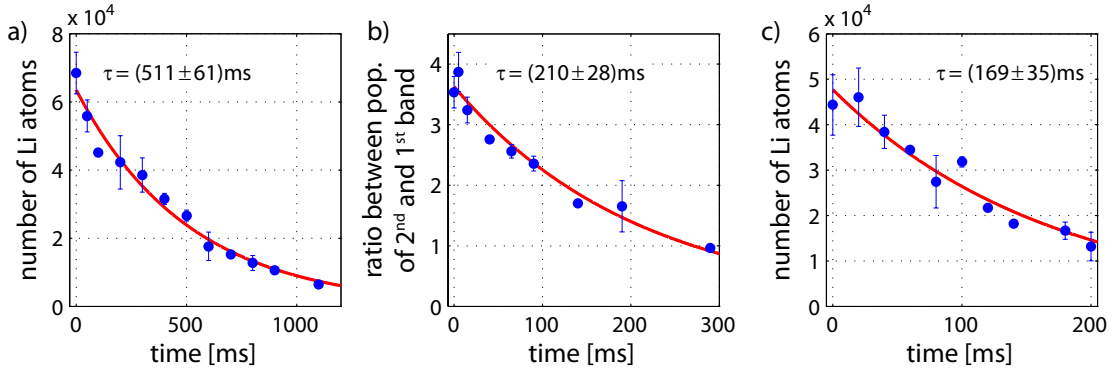

Figure 4.7.: a) Lithium life time in the first Bloch band of the longitudinal lattice ($V_0 = 33\, E_{\mathrm{rec}}^{\mathrm{long}}$). b) Evolution of the ratio between the lithium population in the second and first Bloch band for the same lattice as in a). c) Lithium life time in the first Bloch band of a three-dimensional lattice formed by a $33\, E_{\mathrm{rec}}^{\mathrm{long}}$ longitudinal, a $13\, E_{\mathrm{rec}}^{\mathrm{ver}}$ transversal vertical and a $8\, E_{\mathrm{rec}}^{\mathrm{hor}}$ transversal horizontal lattice. The red lines depict exponential fits to the data.

The shown data is gathered for lattice depths of $33\, E_{\mathrm{rec}}^{\mathrm{long}}$, $13\, E_{\mathrm{rec}}^{\mathrm{ver}}$ and $8\, E_{\mathrm{rec}}^{\mathrm{hor}}$ for the longitudinal, transversal vertical and transversal horizontal lattice potential. The intensity in the lattice beams leads to a theoretical life time of $\tau = 225\,\mathrm{ms}$ due to photon scattering. This value is fairly consistent with the observed life time of $\tau = (169 \pm 35)\,\mathrm{ms}$.

However, the situation is more complicated as before. First of all, the lattice potential is in each direction deeper than the different recoil energies. Hence, the photon absorption should not directly lead to atom loss but to heating of the lithium atoms which we do not observe. A possible explanation for the lack of hot lithium atoms are the enhanced scattering rates in higher Bloch bands. Thus, an atom which already absorbed a photon and occupies a higher Bloch band has a higher probability to scatter a second photon and finally gains enough energy to leave the trapping potential. Secondly, the overlap of the wavefunction with the high intensity regions is more complex for the three-dimensional lattice. Especially, the wavefunctions of the transversal horizontal lattice extend over several lattice sites due to the smaller lattice spacing. Hence, their overlap with the lattice light is larger than the one obtained by the harmonic oscillator approximation, and we expect a life time being shorter than the calculated one.

Finally, we discuss the life time in the second Bloch band of the one-dimensional longitudinal lattice. We will see later on that the different life times in the Bloch bands affect our data analysis, whereas the total life time limits the maximal duration of our experiments. Figure 4.7 b) depicts the evolution of the ratio between the atom numbers in the second and the first Bloch band while the atoms are trapped in the same lattice potential as for figure 4.7 a). We investigate the ratio instead of the atom number as it is a more robust observable and less sensitive to fluctuations of the atom number. Due to the fermionic nature of the lithium atoms and the absence of sodium atoms, the lithium atoms cannot redistribute their energy and hence we do

not observe transitions between different Bloch bands. Thus, we can infer the life time in the second Bloch band $\tau_{2^{\text{nd}}}$ from the life time in the first Bloch band $\tau_{1^{\text{st}}}$ if we investigate their relative evolution. We obtain $\tau_{\text{rel}} = (210 \pm 28)\,\text{ms}$ from the exponential fit to the data which yields $\tau_{2^{\text{nd}}} = \tau_{1^{\text{st}}}\tau_{\text{rel}}/(\tau_{1^{\text{st}}} + \tau_{\text{rel}}) = (149 \pm 15)\,\text{ms}$ [6] agreeing perfectly with our theoretical expectations of $155\,\text{ms}$.

[6] Because the atom number in the first and second Bloch band evolve as e^{-t/τ_1} and e^{-t/τ_2}, the ratio between the two decays as $e^{-t/\tau_2}/e^{-t/\tau_1} = e^{-t(\tau_1-\tau_2)/\tau_1\tau_2} = e^{-t/\tau_{\text{rel}}}$.

5. Coherent Control of Motional Degrees of Freedom

After the characterization of the species-selective lattice, we study the dynamics of the lithium atoms in the optical lattice. In order to isolate the impact of the Bose-Einstein condensate on the dynamics of the lithium atoms, we investigate in this chapter solely the evolution of the lithium atoms and remove the sodium atoms after the lattice loading.

At first, we inspect Rabi oscillations between the first and the second Bloch band induced by periodic shaking of the longitudinal lattice. The coherent coupling between different energy bands allows the controlled preparation and manipulation of superposition of states from the first and second Bloch band. We utilize this feature for Ramsey-type experiments which can be used to study the impact of a bath on motional coherences. Subsequently, we extend this technique by a spin echo pulse which compensates the dephasing between the evolutions of different lithium atoms due to the inhomogeneity of the lattice potential. This type of experiment allows us to probe the motional coherence of the lithium atoms for time scales one order of magnitude longer than for pure Ramsey experiments, and will enable us to investigate the impact of the bath on coherences in chapter 8.

5.1. Rabi Oscillations

In the previous chapter, we presented spectroscopy measurements of the longitudinal lattice by periodic lattice shaking. If we modify these experiments by extending the shaking duration and/or enhancing the shaking amplitude, we observe Rabi oscillations [32] between the first and the second Bloch band which have the maximal amplitude for resonant shaking (fig. 5.1). The Rabi oscillations can be intuitively understood in the deep lattice regime where the different lattice wells can be considered as independent harmonic oscillators and the lattice shaking couples the energy states of each harmonic oscillator. However, the lattice potential is at each site not perfectly harmonic which leads to different splittings between the energy levels. This difference becomes more pronounced for higher states and allows tuning the lattice potential in a regime in which the lattice shaking couples only the two lowest energy levels of each harmonic oscillator, whereas the coupling to higher levels is suppressed as they are off-resonant. In this simplified picture, the dynamics of the lithium atoms in a periodically shaken lattice are described by multiple driven two-level systems.

The Rabi oscillation depicted in figure 5.1 are performed in a one-dimensional longitudinal lattice with a depth of $V_0 = 20\,E_{\text{rec}}$ shaken at $\omega_{\text{exc}}/2\pi = 53\,\text{kHz}$. This frequency corresponds to the gap between the first and second band $\Delta E_{1\text{-}2}/h$, whereas the frequency of the gap between the second and third band is given by $\Delta E_{2\text{-}3}/h = 37\,\text{kHz}$. As the resulting detuning $\delta/2\pi = 16\,\text{kHz}$

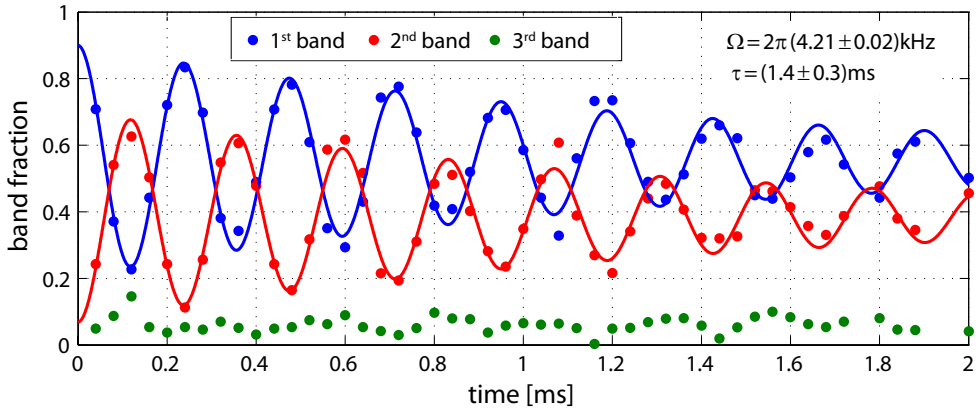

Figure 5.1.: Rabi oscillations between the first and second Bloch band in a $V_0 = 20\, E_{\mathrm{rec}}$ deep lattice potential. The Rabi frequency Ω and the decay time τ are obtained by fitting a damped sine (solid lines) to the experimental data (dots).

is large compared to the observed Rabi frequency $\Omega/2\pi = 4.2\,\mathrm{kHz}$, we do not transfer lithium atoms to the third band. Hence, we only observe oscillations between the first and second Bloch band, and our observations are well described by Rabi oscillations of multiple two-level systems.

Damping of the Rabi Oscillations

However, we also notice that the Rabi oscillations damp out on a time scale of milliseconds. The damping can either be caused by the loss of coherence or by dephasing of the different lithium atoms. The latter leads to vanishing Rabi oscillations as we detect the averaged evolution of all atoms. The loss of coherence could e. g. arise from light scattering (dominantly lattice light) or from p-wave interactions between the lithium atoms.[1] Though, we expect both time scales to be two orders of magnitude slower than the decay observed in the experiment (section 4.5). Dephasing on the other hand can occur on a faster time scale. We mentioned earlier that the inhomogeneity of the lattice potential over the lithium cloud is on the percent level which results in a detuning of about $\delta/2\pi = 0.5\,\mathrm{kHz}$ between the different lattice wells. Because of this detuning, the shaking frequency does not match the resonance frequency for each two-level system which leads to Rabi oscillations at different effective Rabi frequencies $\Omega_{\mathrm{eff}} = \sqrt{\Omega^2 + \delta^2}$. As our detection scheme integrates over all Rabi oscillations, we expect a damping of the Rabi oscillations on the time scale t_{damp}

$$t_{\mathrm{damp}} = \frac{\pi}{\sqrt{\Omega^2 + \delta^2} - \Omega} \approx 2\pi \frac{\Omega}{\delta^2}, \tag{5.1}$$

for $\Omega > \delta$. From this equation, we get for our parameters a damping time of $t_{\mathrm{damp}} \approx 17\,\mathrm{ms}$ which is already close to the observed decay time but cannot solely account for the damping.

[1] s-wave interactions are suppressed by the fermionic nature of the lithium atoms.

It turns out that we have to reverse the simple picture of independent two-level systems. The decay of the presented Rabi oscillations is also caused by a different mechanism, more specifically tunneling between neighboring lattice sites. Whereas the first Bloch band is for a $V_0 = 20\,E_{\text{rec}}$ deep lattice essentially flat ($J_1/h = 18\,\text{Hz}$) and tunneling processes occur slowly, tunneling in the second Bloch band is more likely as the potential barrier is smaller. The corresponding tunneling rates are on the order of milliseconds ($J_2/h = 420\,\text{Hz}$) and suggest that the decay of the Rabi oscillations is mostly due to tunneling processes.

We checked this interpretation by one-dimensional simulations of the Rabi oscillations (section 4.3).[2] The simulations show a damping on the same time scale as the experiment and reveal that both tunneling and detuning are responsible for the damping. The reason for our overestimation of the tunneling effects is that we considered the tunneling processes in a homogeneous lattice potential without external confinement. However, the lithium atoms also experience the potential of the optical dipole trap leading to an energy offset between neighboring lattice wells. This energy offset leads to the localization of the atoms' wavefunctions and thus to slower tunneling (fig. 3.3).

For conclusion, figure 5.2 a) summarizes the discussion of the Rabi oscillations graphically. Because of the different energy splittings between the Bloch bands, resonant lattice shaking couples only the two lowest bands. This approximation is valid as long as the shaking amplitude and the resulting Rabi frequency is smaller than the detuning to the third band which implies a lower and upper bound to the lattice depth. For very deep lattices (for which tunneling is completely suppressed), each lattice site can be considered as independent two-level system whose evolution can be visualized on a Bloch sphere as to be seen in figure 5.2 b). Because of the inhomogeneity of the lattice potential, each two-level system has a different resonance frequency (not shown in figure 5.2 a)). Thus, the states represented on the same Bloch sphere do not only rotate around the y- but also the z-axis which leads to vanishing Rabi oscillations as each state rotates around the z-axis at a different frequency. For lower lattice potentials, the detuning effect becomes less important, but the atoms start tunneling between neighboring lattice sites. The tunneling processes also cause a decay of the Rabi oscillations and dominantly occur in the second Bloch band.

Rabi Frequency

After discussing the damping mechanism, we turn now to the Rabi frequency. In order to check if our experimental observations match the theoretical expectations, we study the Rabi frequency for different shaking amplitudes. According to equation (4.13), we expect a linear dependence of the Rabi frequency on the shaking amplitude x_0

$$\hbar\Omega = V_0 x_0 k_{\text{lat}} \int \psi_2^*(x) \sin(2k_{\text{lat}}x)\, \psi_1(x)\, \mathrm{d}x, \tag{5.2}$$

[2] For this purpose, we compute the evolution of the energy eigenfunctions of the first band $\psi_{1,j}(x,t)$ and the corresponding probability $p^{2\text{nd}}_{k,j}(t) = |\int \psi^*_{2,k}(x)\psi_{1,j}(x,t)\mathrm{d}x|^2$ for occupying the energy eigenfunction $\psi_{2,k}(x)$ of the second band. The total probability for the occupation of the second Bloch band $p^{2\text{nd}}(t)$ is then given by summation over the single probabilities $p^{2\text{nd}}_{k,j}(t)$ with respect to their weighting factor w_j (eq. (4.10)) $p^{2\text{nd}}(t) = \sum_{j,k} w_j p^{2\text{nd}}_{k,j}(t) / \sum_j w_j$.

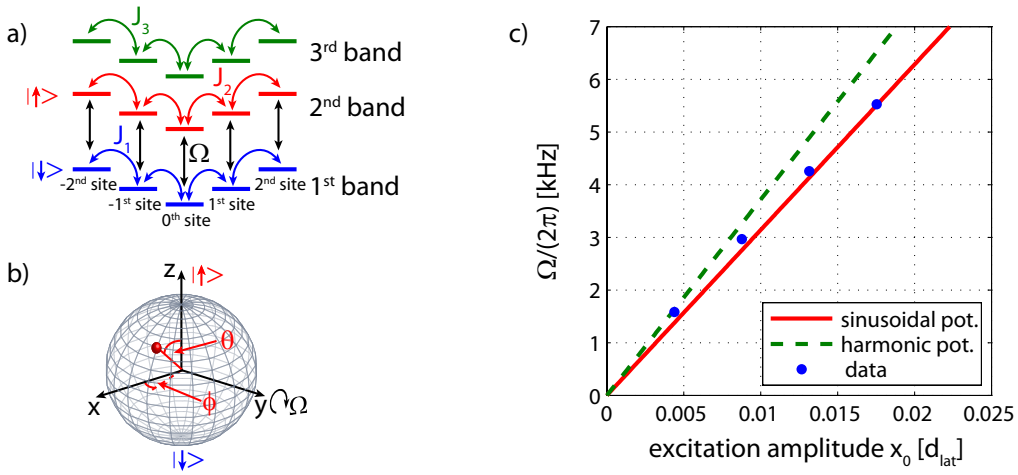

Figure 5.2.: a) Illustration of the Rabi oscillations in the deep lattice regime. The ground state (1st band or spin down) of each lattice site couples due to the lattice shaking to the first excited state (2nd band or spin up). b) The evolution of the corresponding two-level system can be represented on a Bloch sphere. This simple picture is modified due to tunneling between neighboring lattice sites (indicated by the tunneling matrix elements J_i in a)) and the energy offset due to the dipole trap potential. c) Comparison of the theoretical (lines) and experimental (dots) Rabi frequencies in a $V_0 = 28\,E_{\mathrm{rec}}$ deep lattice for varying excitation amplitudes. The error bars of the experimental data are smaller than the depicted point size.

where the $\psi_i(x)$'s are the wavefunctions of the coupled states. Figure 5.2 c) displays the Rabi frequencies obtained by fitting a damped sine to the Rabi oscillations in a $V_0 = 28\,E_{\mathrm{rec}}$ deep lattice for different amplitudes. We observe, as expected, a linear dependency between the shaking amplitude and the Rabi frequency.

Furthermore, the experimental data agrees well with the theoretical frequencies calculated for the energy eigenstates of a sinusoidal potential with a single well (eq. (5.2)). The calculations differ only for small shaking amplitudes for which they yield smaller Rabi frequencies. This discrepancy is probably due to off-resonant shaking for detuned lattice sites which thereby oscillate at higher effective Rabi frequencies. This effect becomes less pronounced for larger shaking amplitudes and Rabi frequencies as the detuning becomes comparatively smaller. Interestingly, the agreement between theory and experiment is worse if the Rabi frequencies are computed for a harmonic potential. In this case, the discrepancy grows for larger shaking amplitudes as the atoms probe more and more the anharmonicity of the lattice potential which leads to larger deviations.

In total, our theoretical considerations reproduce the shape of the Rabi oscillations. The agreement between the calculated and measured Rabi frequencies is almost perfect, and the damping occurs on the expected time scale. However, with the above considerations, we cannot make precise predictions about the decay time of the Rabi oscillations and also the simulations do not

agree as good as the for the lattice oscillations (see fig. 4.4). The simulated Rabi oscillations decay about 50 % slower than the observed oscillations. This is probably due to two reasons which will reappear in the context of the spin echo spectroscopy (section 5.3).

First of all, the simulations only include the inhomogeneity along the lattice direction, but the experimental setup is also inhomogeneous in the transversal directions. This effect could be compensated by averaging over many simulations with slightly different parameters which account for these inhomogeneities. Though, the more important issue cannot be tackled by the one-dimensional simulations. As the lattice axes are not perfectly perpendicular to each other and also not to the semiaxes of the optical dipole trap, the lattice shaking also induces dynamics along the transversal directions which affect our measurements. This issue has not been a problem for the simulations of the lattice oscillations as these occur on a time scale much shorter than the one given by the trapping frequencies of the optical dipole trap. But the Rabi oscillations last longer and thus this coupling mechanism becomes more important.

5.2. Ramsey Spectroscopy

In this section, we utilize the coherent coupling between the Bloch bands to perform Ramsey interferometry [61, 62]. Common applications of Ramsey interferometry are atomic interferometers based upon the atoms' internal states. The probably most prominent examples are atomic clocks [63] which provide the definition of the time standard. In our case, however, the motional states along the lattice direction, namely the states of the first and second Bloch band, take the role of the internal states.

We mentioned earlier that the atoms' evolutions in a deep lattice potential can be approximated by the dynamics of multiple two-level systems. Following this interpretation, figure 5.3 a) illustrates the evolution steps of a single lithium atom on a Bloch sphere during a Ramsey sequence.

- Initially, the atom populates the first Bloch band and we can e. g. consider it to be in a spin down state which is represented on the south pole of the sphere.

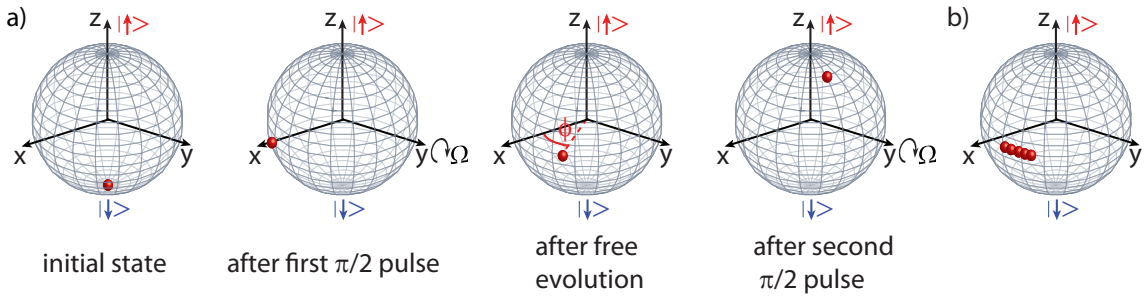

Figure 5.3.: a) Illustration of a Ramsey sequence on the Bloch sphere. A description of the sequence is given in the main text. b) Representation of multiple two-level systems on the same Bloch sphere after the free evolution time. Different energy splittings lead to the dephasing around the equator and cause a reduced Ramsey signal.

- The application of a $\pi/2$-pulse by shaking the lattice for $t = \pi/(2\Omega)$ ($\approx 70\,\mu s$) prepares the atom in an equal superposition of a state in the first and the corresponding state in the second Bloch band or equivalently into an equal superposition of spin down and spin up.
- After this pulse, the superposition evolves freely and the fraction in the spin up state accumulates a phase relative to the fraction in the spin down state due to the energy difference between the first and the second Bloch band. The free evolution corresponds therefore to a rotation around the equator of the Bloch sphere whose frequency is given by the energy difference.
- Finally, a second $\pi/2$-pulse translates the accumulated phase into a detection probability for spin up and down.

As we perform the Ramsey sequence with multiple lithium atoms at once, the detection probability is intrinsically converted into a population difference between the first and the second Bloch band. The rotation frequency and the corresponding energy difference can be measured by variation of the evolution time t_{ev} which leads to band populations oscillating with the rotation frequency. Figure 5.4 a) displays two so-called Ramsey fringes in a $V_0 = 32.9\,E_{rec}$ deep longitudinal lattice. By fitting a damped sine to the data, we obtain the rotation frequency and thereby the lattice depth. The uncertainty in the frequency of 101 Hz is about half the width of the second Bloch band and corresponds to a relative uncertainty of only $0.14\,\%$.

Damping of the Ramsey Signal

So far, the Ramsey spectroscopy is our most precise method to determine the depth of the longitudinal lattice. However, we are not interested in more precise lattice depth measurements, but intend to study the impact of a bath on the dynamics of the lithium atoms. Ramsey spectroscopy offers the opportunity to investigate the loss of motional coherence due to interaction with the background.

The first $\pi/2$-pulse prepares the lithium atoms in coherent superpositions which can decay due to interaction with the sodium bath. After the free evolution time, the second $\pi/2$-pulse determines how much of the initial coherences is left. As the experiment can be carried out with and without background, the impact of the interaction on the motional coherences can be isolated from other sources causing a decay of the Ramsey signal. Though, we notice from figure 5.4 a) and b) that the Ramsey signal vanishes even without background in less than 1 ms which is faster than the time scale for the loss of coherence on the order of 5 ms (see chapter 8).

The reasons are the same as for the Rabi oscillations, namely the finite width of the Bloch bands and the inhomogeneity of the lattice potential. The lattice inhomogeneity leads to different rotation frequencies around the z-axis of the Bloch sphere which causes dephasing rotations of the lithium atoms and hence a vanishing Ramsey signal (fig. 5.3 b)). In comparison to the Rabi oscillations (eq. (5.1)), the decay occurs faster as the system evolves freely, and the effect of the detuning is more pronounced

$$t_{damp} = \frac{\pi}{\delta} < \frac{\pi}{\sqrt{\Omega^2 + \delta^2} - \Omega} \approx 2\pi \frac{\Omega}{\delta^2} \tag{5.3}$$

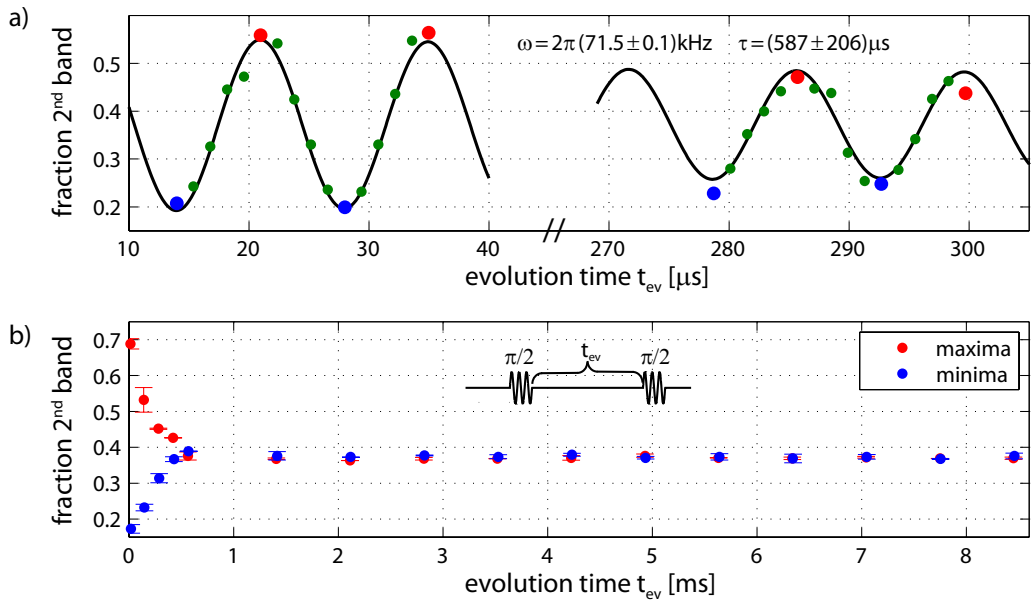

Figure 5.4.: a) Ramsey signal for a $V_0 = (32.9 \pm 0.1)\, E_{\mathrm{rec}}$ deep longitudinal lattice. The dots represent the experimental data and the solid line a fit of a damped sine. The red and blue dots mark the position of the fringe maxima and minima which are displayed in b) for longer evolution times. The envelope of the Ramsey signal decays in less than 1 ms, and we do not observe a revival of the signal due to rephasing of the lithium atoms' evolutions. The inset illustrates the Ramsey sequence.

as $\Omega > \delta$. Thus, for the presented Ramsey measurement, a lattice inhomogeneity of one percent already sets an upper bound of 1.4 ms for the decay time of the Ramsey signal and limits the suitability of the Ramsey interferometry for loss of coherence measurements.

Though, the investigation of the coherence loss on the basis of the Rabi oscillations is more involved as the system does not evolve freely, but is constantly driven. For this reason, we introduce and study an improved Ramsey sequence, a so-called spin echo sequence, in order to compensate the effect of the detuning which will enable the investigation of the coherence loss in a freely evolving system in chapter 8.

5.3. Spin Echo Spectroscopy

The previous discussion showed that the damping of the Rabi oscillations and of the Ramsey signal is mainly governed by tunneling processes between different lattice sites as well as detuning effects. Depending on the lattice depth, one of the two effects plays the major role. Our strategy to overcome this limitation and observe motional coherences for longer evolution times bases on a modification of the Ramsey sequence, namely the spin echo technique [64, 65]. This technique is insensitive to the dephasing between different lithium atoms and consists of three instead of

two pulses.

The initial procedure is identical to the Ramsey technique meaning that a coherent superposition of spin up and down is prepared by a $\pi/2$-pulse followed by a first free evolution of the atoms for a time $t_{\mathrm{ev}}^{1\mathrm{st}}$. Because of the energy difference between spin up and spin down, the spin up component accumulates during this evolution a phase ϕ with respect to the spin down component. Instead of probing the atoms by a second $\pi/2$-pulse, the spin echo technique utilizes a π-pulse to invert the population of spin up and down. Thereby, the relative phase between the components swaps and the spin down component carries a phase ϕ with respect to the spin up component. A second free evolution time $t_{\mathrm{ev}}^{2\mathrm{nd}}$ reduces the differential phase between the spin down and up component as the latter evolves faster. The phase difference finally becomes zero when the two evolution times are equal, and the detuning effect is fully canceled.

In case of dephasing being the only source for the decay of the Ramsey signal, we ideally expect all atoms in the first Bloch band after a spin echo sequence with symmetric evolution times as the sum of all pulses equals 2π. Oscillations between the first and second Bloch band can be achieved by asymmetric evolution times or by imposing a phase shift between the π- and the second $\pi/2$-pulse. Figure 5.5 a) shows the atom fraction in the second Bloch band obtained for the first procedure meaning a fixed first and a variable second evolution time. The displayed fringe

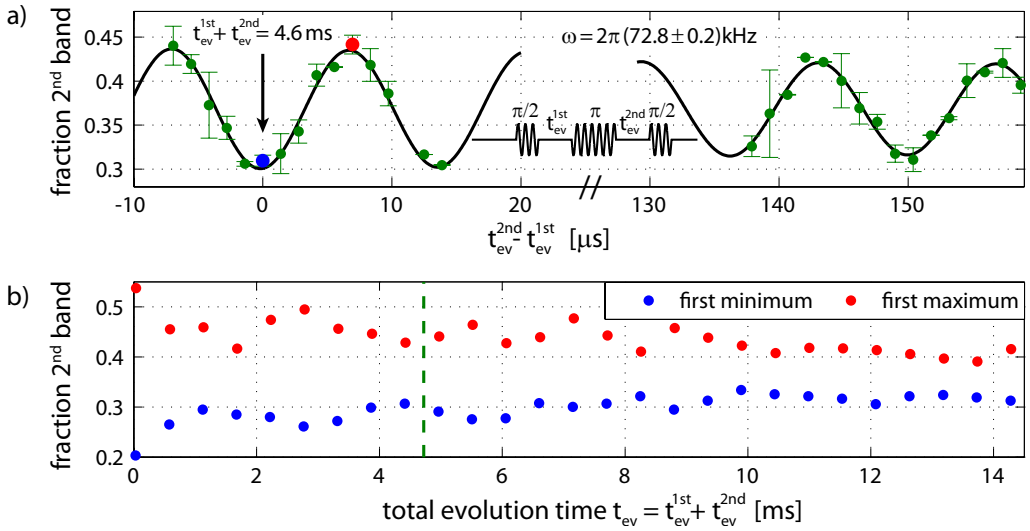

Figure 5.5.: a) Fraction of lithium atoms in the second Bloch band (green dots) for a spin echo sequence with fixed first evolution time ($t_{\mathrm{ev}}^{1\mathrm{st}} = 2.3\,\mathrm{ms}$) and variable second evolution time $t_{\mathrm{ev}}^{2\mathrm{nd}}$. The black solid line depicts a fitted damped sine whose frequency corresponds to a longitudinal lattice depth of $V_0 = (34.0 \pm 0.1)\, E_{\mathrm{rec}}$. The inset illustrates the spin echo sequence and the definition of the evolution times. The red and blue dot mark the first maximum and minimum which reflect the envelope of the spin echo signal and are displayed in b) for several total evolution times. The green dotted line labels the position of the measurement shown in a).

amplitude is smaller than for the Ramsey measurement depicted in figure 5.4 a). Though, the data is gathered for a total free evolution time of $t_{\mathrm{ev}} = t_{\mathrm{ev}}^{\mathrm{1st}} + t_{\mathrm{ev}}^{\mathrm{2nd}} = 4.6\,\mathrm{ms}$ and hence a duration for which the fringes for a pure Ramsey sequence have completely vanished. As before, the oscillation frequency corresponds to the energy difference between the first and the second Bloch band, and determines the depth of the longitudinal lattice to $V_0 = (34.0 \pm 0.1)\, E_{\mathrm{rec}}$.

The lower part of figure 5.5 displays the envelope of the spin echo signal. The graph depicts the fraction in the second Bloch band obtained for symmetric evolution ($t_{\mathrm{ev}}^{\mathrm{1st}} = t_{\mathrm{ev}}^{\mathrm{2nd}}$) which yields a minimal fraction in the second band. Additionally, it shows the fraction in the second Bloch band obtained for a second evolution time which is half an oscillation period longer than the first one resulting in a maximal number of the atoms in the second band. Altogether, we observe a decay of the spin echo signal on the order of 15-20 ms which is non-monotonic and whose envelope shows characteristic maxima and minima.

5.3.1. Envelope of the Spin Echo Signal

In the following, we study the spin echo signal more closely as it provides our main tool for the investigation of the loss of motional coherence in the sodium bath in chapter 8.

Spin Echo Sequence for a Single Lithium Atom

In order to understand the origin of the signal decay and the modulation of the envelope, we consider, at first, the evolution of a single lithium atom during the spin echo sequence. Figure 5.6 illustrates the dynamics of an atom which is initially located at the central lattice site:

- The first $\pi/2$-pulse ideally creates a 50:50 superposition of states in the first and second Bloch band.
- Because of the different tunneling rates, the fraction in the second band spreads much faster than the one in the first band, and we neglect for simplicity the tunneling processes in the first band. During the free evolution, the fractions at the different lattice sites of the second band accumulate a phase due to the energy offset (we consider the phases with respect to an atom resting at the central site of the first Bloch band).
- The subsequent π-pulse inverts the band populations and the fraction in the second band starts spreading, whereas the fractions in the first band do not.
- After the second free evolution, the fractions at the central site rephase, but the fractions at the outer lattice sites do not as their counterpart in the lower band accumulated an additional phase during the second free evolution.

Hence, one can think of the second $\pi/2$-pulse as a probe for several two-level systems with different relative phases as well as different spin lengths (determined by the expectation value for the corresponding lattice site). The fractions of these two-level systems do in general not rephase at once but for different durations of the second evolution as their energy offset differs. Though, if the tunneling rates in the first and second band were identical (in sign and magnitude), all lattice sites would rephase at once as the two evolution phases were symmetric. As this condition is not

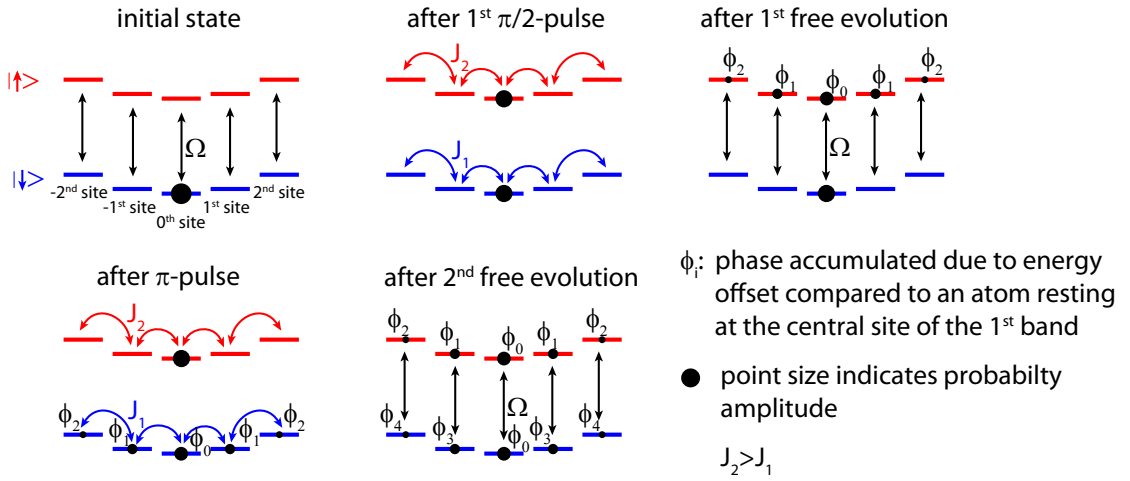

Figure 5.6.: Illustration of the decay mechanism of the spin echo signal in a one-dimensional lattice potential and for a single atom. The different tunneling matrix elements of the first and second Bloch band cause, for all but the initial lattice site, different phases ϕ_i between the amplitudes in the first and second Bloch band which leads to a diminished spin echo signal.

fulfilled in the experiment, we already expect a non-trivial behavior of the spin echo signal for a single atom. Moreover, we experimentally probe multiple atoms simultaneously and each atom evolves differently as the atoms are initially located at different lattice sites. As a result, we get a complex spin echo signal as shown in figure 5.5 b) which decays due to tunneling processes and whose structure originates from the phase accumulation due to the optical dipole trap potential.

Spin Echo Signal for Different Dipole Trap Confinements

In the following, we test the above interpretation of the decay mechanism by investigating the spin echo signal and its dependence on the optical dipole trap potential systematically. The impact of the dipole trap confinement on the evolution of the lithium atoms is ambiguous.

- On the one hand, a weaker confinement causes a slower phase accumulation between neighboring lattice sites due to the lower offset potential which scales quadratically with the trapping frequency.
- On the other hand, the tunneling rates increase for a weaker dipole trap potential as the lithium atoms become less localized. This effect is more pronounced than the slower phase accumulation because the localization of the atoms and hence the tunneling processes depend almost exponentially on the trapping frequency (see figure 3.3).

In order to isolate the effect of the dipole trap potential on the atoms' evolutions during the spin echo sequence, we need to eliminate its impact on the lattice loading procedure. As the extent of the lithium cloud depends on the trapping geometry, the dipole trap depth determines

the number of occupied lattice sites and their occupation number. Thus, we load the lattice for each measurement with the same parameter set. Afterwards, we decrease the intensity in one dipole trap beam and within 10 ms to its final value before starting the spin echo sequence. To avoid excitations of the lithium atoms due to this ramp down, the experiment is performed in a two-dimensional lattice potential (longitudinal and transversal vertical lattice) which freezes the atoms' motions along the lattice directions.[3] We set the depth of the longitudinal lattice to $V_0 = 34\, E_{\text{rec}}^{\text{long}}$ ($\Delta E_{1\text{-}2}/h = 73\,\text{kHz}$, $J_1/h = 1.8\,\text{Hz}$, $J_2/h = 63\,\text{Hz}$) and of the transversal vertical lattice to $V_0 = 11\, E_{\text{rec}}^{\text{ver}}$ ($\Delta E_{1\text{-}2}/h = 92\,\text{kHz}$, $J_1/h = 285\,\text{Hz}$) such that the lattice shaking is off-resonant for the transversal direction.

The data obtained for the spin echo experiments is shown on the left hand side of figure 5.7. The frequencies next to the graphs denote the overall trapping frequency along the longitudinal lattice direction including the relative alignment of the dipole trap and the lattice as well as the anti-confinement due to the blue detuned lattice potential. First of all, we clearly observe a faster decay of the spin echo signal for lower trapping potentials. This behavior is consistent with our earlier developed picture as a stronger confinement predominately leads to a higher localization of the atoms and to a smaller extent to a faster phase accumulation. Because of the higher localization, a larger fraction of the atoms' wavefunctions remains at their initial lattice sites for which the spin echo sequence cancels the dephasing effect, and the spin echo signal increases. We would have expected a similar effect if we changed the tunneling rate instead of the trapping potential.

Secondly, we observe a change in the structure of the spin echo signal. This effect is more subtle, but we notice a faster modulation of the signal for higher trapping frequencies. Though, it is hard to assign a precise frequency to the structure. Only the second measurement (351 Hz) shows a clear peak at about 240 Hz in its Fourier spectrum, whereas the other measurements do not. However, from our previous discussion, we would also not expect a clear relation between the structure and the offset potential as the energy offsets between the lattice sites differ. In the following, we compare our measurements with simulations in order to test if our observations are consistent with theory.

5.3.2. Comparison between Experiment and Simulations

To interpret the spin echo signal, we compare the experimental data with the one-dimensional simulations which were introduced in section 4.3. Additionally, we perform simulations of a simpler discrete model Hamiltonian which recovers the explanation for the decay of the spin echo signal displayed in figure 5.6. This approach offers a more intuitive interpretation of the computed dynamics than the complex simulations on the basis of the split-step Fourier method.

Simulations of the Discretized Lattice Hamiltonian

The Hamiltonian for the system depicted in figure 5.6 consists of several coupled two-level Hamiltonians. In the rotating frame and for resonant coupling, each of these Hamiltonians can be written as

[3] A three-dimensional lattice potential would have been superior, but we did not have one at that time.

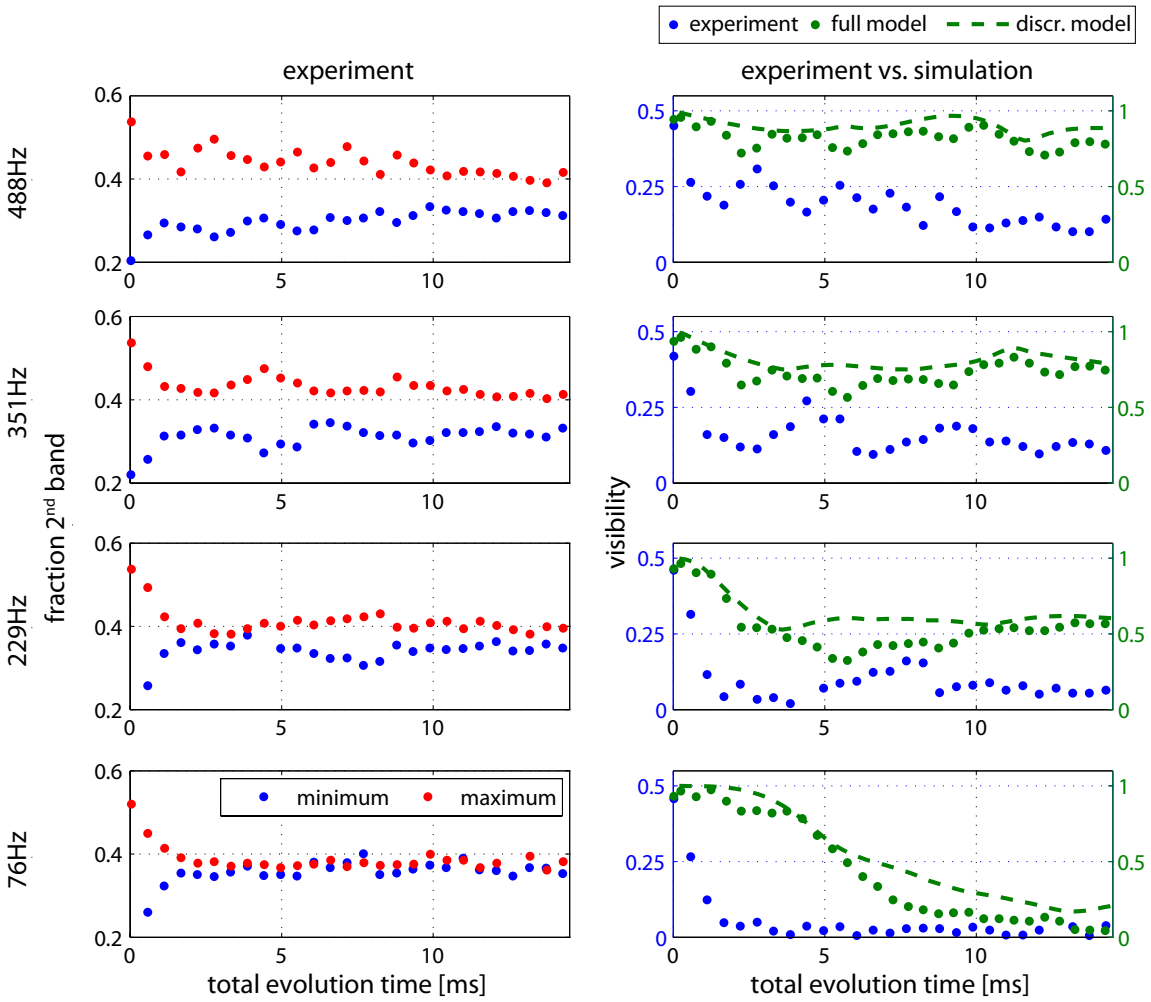

Figure 5.7.: Left side: Spin echo measurements in a two-dimensional lattice potential for various optical dipole potential depths and evolution times. The frequencies at the left hand side denote the overall trapping frequencies along the longitudinal lattice direction. Right side: Comparison between the experimentally observed visibility (left scale) and visibility obtained from the one-dimensional simulations involving the full lattice and dipole trap potential as well as the discrete model (both on the right scale).

$$\hat{H}_{\text{2-level}}(t) = \frac{\hbar\Omega(t)}{2} |\uparrow\rangle \langle\downarrow| + \frac{\hbar\Omega^*(t)}{2} |\downarrow\rangle \langle\uparrow| . \tag{5.4}$$

The coupling between the ground state ($\downarrow$) and excited state ($\uparrow$) is characterized by the Rabi frequency $\Omega(t)$. The time dependency of $\Omega(t)$ indicates that the ground and excited state are only coupled during the π- and $\pi/2$-pulses of the spin echo sequence and evolve freely during the mean time. In case of identical two-level systems whose neighboring ground and excited states

are coupled by J_1 and J_2, the total Hamiltonian reads as

$$\hat{H}_{\text{dis}}(t) = \sum_i \left(\frac{\hbar\Omega(t)}{2} \left|\uparrow\right\rangle_i \left\langle\downarrow\right|_i + \frac{\hbar\Omega^*(t)}{2} \left|\downarrow\right\rangle_i \left\langle\uparrow\right|_i + E_{\text{off},i} \left(\left|\downarrow\right\rangle_i \left\langle\downarrow\right|_i + \left|\uparrow\right\rangle_i \left\langle\uparrow\right|_i \right) \right)$$
$$+ \sum_{<i,j>} \left(J_1 \left|\downarrow\right\rangle_i \left\langle\downarrow\right|_j + J_2 \left|\uparrow\right\rangle_i \left\langle\uparrow\right|_j \right). \tag{5.5}$$

Here, the indices denote the lattice sites and $E_{\text{off},i}$ the offset potential at site i . The first sum runs over all lattice sites, whereas the second one includes all neighboring sites (indicated by $< i, j >$). In order to obtain the evolution of a single atom which initially occupies the ground state of site i, we need to calculate the effect of the time evolution operator $e^{-i\hat{H}_{\text{dis}}(t)t/\hbar}$ on the initial state

$$e^{-i\hat{H}_{\text{dis}}(t)t/\hbar} \left|\downarrow\right\rangle_i . \tag{5.6}$$

This calculation can be performed by splitting the time evolution into parts of free evolution ($\Omega = 0$) and in parts during which the π and $\pi/2$-pulses are applied (Ω =constant). The Hamiltonian for each step is then time-independent and we can transform equation (5.6) into successive matrix multiplications by selecting the $\left|\downarrow\right\rangle_i$'s and $\left|\uparrow\right\rangle_i$'s as basis [57]. Moreover, we need to choose an appropriate lattice size such that the finite system size does not affect our results. To compare the simulation with the experiment, we compute the time evolution for the ground state of each lattice site, and average all results multiplied by a weighting factor accounting for the occupation of the lattice sites (eq. (4.10)).

Experiment vs. Simulation

The right hand side of figure 5.7 compares the two simulation methods and the experimental data on the basis of the visibility $\mathcal{V}$

$$\mathcal{V} = \frac{\text{fringe amplitude}}{\text{fringe offset}} \tag{5.7}$$

which offers a better comparability of the different data sets.[4] Overall, the agreement between the simulations and the experiment is rather poor. However, the simulations and the experiment agree at the most important point qualitatively. All curves show a reduction of the spin echo signal for weaker dipole trap confinements and support therefore our previous interpretation of the decay mechanism. But the simulated curves show a slower decay as well as twice the visibility and do not reflect the structure of the experimental data.

Though, the simulation by means of the discretized Hamiltonian (eq. (5.5)) and the split-step Fourier algorithm (section 4.3) show a similar spin echo signal. Considering the fact that the discretized model assumes perfectly coupled two-level systems and does not include any inhomogeneity or detuning effects, the two models agree well. This observation indicates that the

[4] The parameters for simulating the single particle evolutions correspond to the experimental parameters (ω_{ODT} = variable, lattice: $V_0 = 34\,E_{\text{rec}}$ or $J_1/h = 1.8\,\text{Hz}$, $J_2/h = 63\,\text{Hz}$, $\Omega/2\pi = 3.6\,\text{kHz}$) . The parameters for averaging the different evolutions are obtained from the density profiles ($T \approx 550\,\text{nK}$, $\text{N}_{\text{Li}} \approx 1 \cdot 10^5$) and the trap geometry during the lattice loading (see section 2.3.1) .

tunneling processes and the optical dipole potential are the most relevant parameters for describing the evolution of a single atom in one dimension.

As both simulations show a similar behavior, we suppose that the difference between the experiment and the simulations arises from effects which are not captured by the simulations and are discussed below.

- Most of the initial difference between the experimental and simulated visibility can be explained by the non-perfect sample preparation, i. e. the finite occupation of the second band after the lattice loading. E. g. an initial fraction of $15\,\%$ in the second Bloch band reduces the achievable visibility to $70\,\%$. This is due to the fact that atoms starting in the second Bloch band perform the opposite evolution than atoms starting in the first Bloch band. Hence, our sample preparation accounts for the different initial visibilities. But this effect does not depend on the duration of the free evolution and is thus not responsible for the different decay times.

- The simulations account for the different lattice site occupations by averaging over the weighted evolutions of the single atoms. However, this approach is limited by e. g. the knowledge of the density distributions after the lattice loading as well as the relative alignment of the optical dipole trap and the lattice potential. We can calculate the lithium density distribution in the optical dipole potential, but we know that the lattice loading procedure alters the density distribution as we rely on the sodium background to transfer the lithium atoms to the first band. In order to determine the sensitivity of the simulations on the lithium density distribution and the lattice alignment, we performed the simulations with modified density distributions but did not observe a high sensitivity of the result. Thus, we expect that the mentioned issues modify the structure of the spin echo signal, but do not explain the difference in the decay times.

- It turns out that the deviation between the simulations and the experiment is mostly due to the fact that the simulations only cover one dimension. At first sight, we expect that the dynamics during the spin echo sequence can be described in one dimension as the lattice shaking couples only motional states of the corresponding lattice direction due to the perpendicularity of the different potential axes.
  However, we do observe different spin echo signals if we perform identical measurements (without any dipole potential ramps) in one- and two-dimensional lattice potentials (see figure 5.8 a)). In the case of the one-dimensional lattice, the initial visibility of the spin echo signal is higher which is due to a better preparation in the first Bloch band. But the spin echo signal is also stronger modulated in one dimension for which we lack a good explanation. We expect, even for non-perpendicular potential axes, only a small coupling to the transversal directions as the lattice shaking amplitude ($\approx 0.01\,\mu\text{m}$) is small compared to the lengths scales of the optical dipole potential (on the order of some micrometer). In spite of a conclusive explanation for the observed effect, we can still attribute the difference between the two spin echo signals to dynamics along the transversal directions as the two measurements are otherwise identical. Hence, the impact of the transversal directions on the dynamics during the spin echo sequence accounts at least partly for the discrepancy between the simulations and the experiment.

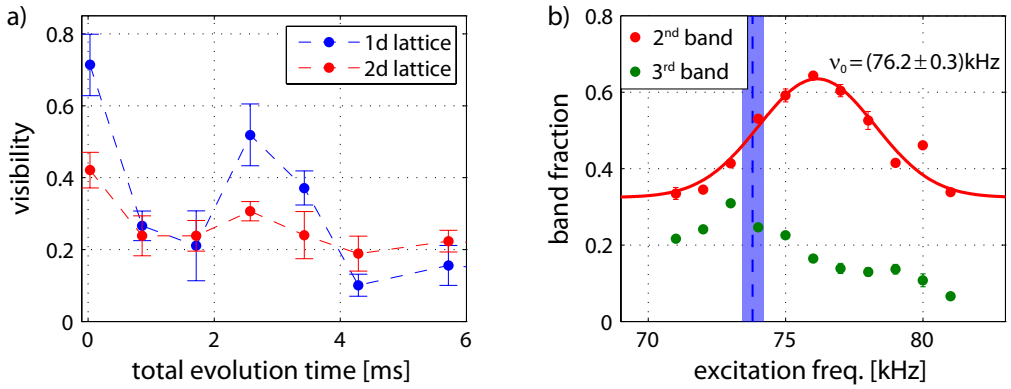

Figure 5.8.: a) Visibility of the spin echo signals in a one- and two-dimensional lattice potential with otherwise identical settings. b) Band fractions after a spin echo sequence at the fringe maximum and for a fixed evolution time. A Gaussian fit (solid red line) to the fraction in the second band shows that the fringe height is maximal for a lattice shaking frequency of (76.2 ± 0.3) kHz, whereas the independently determined resonance frequency is at (73.8 ± 0.4) kHz (blue shaded area). This discrepancy is due to the suppressed coupling to the third band for detuned lattice shaking. This interpretation is supported by the lower atom fraction in the third band at the position of the maximum.

In summary, we have seen that the spin echo signal vanishes faster for weaker dipole trap potentials. We attribute this behavior to the weaker localization of the atoms due to the smaller energy offset between neighboring lattice sites. The one-dimensional simulations support this interpretation but their decay is slower than the experimentally observed one. A possible explanation for this discrepancy are the transversal directions which are hard to simulate because of the large computational effort.

5.3.3. Optimal Lattice Parameters for Long Lasting Spin Echo Signals

The previous discussion revealed that the decay of the presented spin echo signals is strongly affected by tunneling between neighboring lattice sites. As our experiment offers various possibilities to tune the tunneling rates, the question arises if it is possible to slow down the decay even further or if the presented measurements are already taken for the optimal parameter set. In principle, we have two knobs to turn in order to reduce the tunneling rates, namely the optical dipole trap potential and the lattice potential.

In our case, however, it is unfavorable to further decrease the tunneling rates by increasing the trap frequencies of the optical dipole trap. This follows from the fact that we are interested in the evolution of the lithium atoms in a sodium bath, and we have observed that a further reinforcement of the optical dipole trap confinement significantly reduces the number of sodium atoms due to three-body losses [66].

Alternatively, we can change the parameters of the lattice potential. Lower tunneling rates

can either be achieved by a larger lattice spacing or by deeper lattice potentials. Increasing the lattice spacing requires for our experiment a major modification of the lattice setup due to the restricted optical access. Additionally, a larger lattice spacing has the drawback of increasing the atom number per lattice site and decreasing the gap from the first to the second band. Both effects cause a higher initial occupation of the second Bloch band and lead to a lower visibility of the spin echo signal.

The final possibility is to perform our experiments in deeper lattice potentials. Though, it turns out that the depth of the longitudinal lattice used for the presented measurements is already close to the optimal lattice depth. This fact is illustrated in figure 5.8 b) which displays a spin echo measurement in a $V_0 = 35\,E_{\mathrm{rec}}$ deep lattice for a fixed total evolution time ($t_{\mathrm{ev}} = 300\,\mu\mathrm{s}$). The graph shows the lattice shaking frequencies versus the fraction of atoms in the second band at the fringe maximum as a measure for the fringe height. We observe that the fringe height is maximal for an excitation frequency which is about 2 kHz higher than the resonance frequency (indicated by the dashed blue line and determined from lattice oscillations). This discrepancy is caused by the finite coupling between states in the second and third Bloch band as the gaps between the three lowest Bloch bands become equally spaced for deep lattice potentials. Hence, the spin echo sequence has to be interpreted in a three- instead of a two-level system and does not compensate the dephasing as well as in a two-level system. The measurement depicted in figure 5.8 b) is taken in a regime in which the coupling between the second and third band becomes important, but the energy gaps are still different ($\Delta E_{1\text{-}2}/h = 74\,\mathrm{kHz}$, $\Delta E_{2\text{-}3}/h = 63\,\mathrm{kHz}$). In this regime, a positive detuning to the resonance frequency enhances the spin echo signal as the reduced efficiency of the lattice pulses is overcompensated by the weaker coupling to the third band. This is due to the fact that the impact of the detuning on the coupling efficiency scales quadratically.[5] This interpretation is supported by our measurement which reveals that the increase in the fringe height is accompanied by a smaller atom fraction in the third Bloch band.

However, this also means that a further increase in the lattice height will suppress the tunneling processes, but also diminishes the efficiency of the spin echo sequence. This effect cannot be compensated by detuning the shaking frequency as the energy gaps between the Bloch bands approach each other for deeper lattice potentials. Overall, we observe the slowest decaying spin echo signals for lattice depths between 30-40 E_{rec} combined with slightly detuned lattice pulses.

Concluding Remarks

In the beginning of this chapter, we presented the coherent coupling between states in the first and second Bloch band. We used this ability to perform Ramsey spectroscopy, but noticed that the Ramsey signal vanishes faster than the time scale on which the sodium background influences the evolution of the lithium atoms. For this reason, we developed a spin echo technique which increases the observation time for motional coherences by more than a factor of 20. In this context, we exploited the fact that the spin echo technique is not restricted by dephasing mechanisms. Therefore, we could suppress the decay of the spin echo signal due to tunneling processes by deep lattice potentials which are for the Ramsey spectroscopy accompanied by a fast signal

[5] E. g. in a two level system, the occupation of the excited state does not exceed $\Omega^2/(\Omega^2+\delta^2)$ if the system is initially in the ground state.

decay due to dephasing effects.

We will apply the spin echo technique in chapter 8 in order to investigate the impact of the bath on the lithium atoms. But beforehand, we introduce the bath theory which will allow us to interpret the influence of the sodium atoms on the dynamics of the lithium atoms.

6. Independent Impurities Immersed in a Bosonic Bath

In this chapter, we theoretically investigate the impact of the sodium bath on the dynamics of the lithium atoms confined in a harmonic potential. For this purpose, we derive a master equation in Lindblad form [67, 68] in analogy to the derivation given in [69, 70], but we extend their calculations from one to three dimensions. Furthermore, we do not restrict our considerations to the population decay of motional states, but study also the loss of motional coherence of the lithium atoms due to interaction with the sodium atoms. Related calculations, which examine the evolution of motional coherences in a Bose-Einstein condensate, can be found in [71, 72, 73]. Though, these publications concentrate on the coherence of a two-level system, whereas our computations involve more than two states.

With the master equation at hand, we study the dynamics of the lithium atoms in the sodium bath by approximating each lattice site as harmonic oscillator potential. In this context, we consider the population decay or equivalently the relaxation of motionally excited lithium atoms in the one-dimensional lattice potential, and we investigate the impact of the transversal directions. Subsequently, we turn our focus to the evolution of lithium atoms prepared in a superposition of states belonging to the first and second Bloch band. We analyze the decay of the coherence due to the interaction with the sodium atoms by means of relaxation and heating processes.

6.1. Derivation of the Master Equation

6.1.1. The Hamiltonian

To theoretically investigate the dynamics of the lithium atoms in the bosonic bath, we start our considerations for simplicity with the evolution of a single atom and adapt our considerations in the subsequent chapters to larger atom numbers. First, we split the Hamilton operator of the total system $\hat{H}_{\text{tot}}$ into three operators

$$\hat{H}_{\text{tot}} = \hat{H}_{\text{bath}} + \hat{H}_{\text{atom}} + \hat{H}_{\text{int}}. \tag{6.1}$$

Here, $\hat{H}_{\text{bath}}$ is the Hamiltonian for the bath or reservoir, $\hat{H}_{\text{atom}}$ the Hamiltonian for a single lithium atom and $\hat{H}_{\text{int}}$ the Hamiltonian which accounts for the interactions between the two. As we consider a bath of weakly interacting bosons, the corresponding Hamiltonian is given by [24]

$$\hat{H}_{\text{bath}} = E_0 + \sum_{\vec{q}\neq 0} \epsilon_{\vec{q}} \hat{b}^\dagger_{\vec{q}} \hat{b}_{\vec{q}}. \tag{6.2}$$

Where, $\hat{b}^\dagger_{\vec{q}}$ and $\hat{b}_{\vec{q}}$ are the creation and annihilation operator for the elementary excitations (Bogoliubov excitations) with momentum $\hbar\vec{q}$ and energy $\epsilon_{\vec{q}}$, which were introduced in section 2.1.2,

and E_0 is the ground state energy of the Bose gas in absence of fluctuations.
As we investigate the impact of the bath on external (or motional) dynamics of the lithium atom, the Hamilton operator $\hat{H}_{\text{atom}}$ accounts only for the motional part of the atom's Hamiltonian and not for the internal one. In the following, we approximate the lattice potential as independent set of harmonic oscillator potentials as it is computational much less demanding. Hence, the lithium atom's Hamilton operator is given by [57]

$$\hat{H}_{\text{atom}} = \sum_{i=\text{x,y,z}} \left(\hat{n}_i + \frac{1}{2}\right) \hbar\omega_i, \tag{6.3}$$

where the ω_i's are the harmonic oscillator frequencies and the $\hat{n}_i$'s denote the number operators for the x-, y- and z-direction. The energy eigenstates of the harmonic oscillator Hamiltonian are the Fock states

$$|n\rangle := \left|n_{\text{x}}, n_{\text{y}}, n_{\text{z}}\right\rangle \tag{6.4}$$

with the eigenenergies

$$E_{\text{n}} := E_{\text{n}_\text{x},\text{n}_\text{y},\text{n}_\text{z}} = \left(n_{\text{x}} + \frac{1}{2}\right) \hbar\omega_x + \left(n_{\text{y}} + \frac{1}{2}\right) \hbar\omega_y + \left(n_{\text{z}} + \frac{1}{2}\right) \hbar\omega_z. \tag{6.5}$$

The interaction Hamiltonian $\hat{H}_{\text{int}}$ accounts for the density-density interaction between the lithium atom and the Bose gas. For s-wave interactions characterized by the coupling constant g_{NaLi} (eq. (2.32)), the interaction Hamiltonian reads as [69]

$$\hat{H}_{\text{int}} = g_{\text{NaLi}} \int \hat{\rho}_{\text{Bose}}(\vec{r}) \hat{\rho}_{\text{Li}}(\vec{r}) \, \mathrm{d}\vec{r}. \tag{6.6}$$

In order to simplify our calculations, we consider the density of the single lithium atom $\hat{\rho}_{\text{Li}}(\vec{r})$ as point-like ($\hat{\rho}_{\text{Li}}(\vec{r}) = \delta(\vec{r} - \hat{\vec{r}})$) which is well justified for a homogeneous Bose gas or a Bose gas whose density $\hat{\rho}_{\text{Bose}}(\vec{r})$ is constant over the extent of the lithium atom's wavefunction. Hence, this assumption is in case of a three-dimensional species-selective lattice potential well fulfilled but can only serve as approximation for lower dimensional lattice potentials. For a point-like lithium density, the interaction Hamiltonian becomes

$$\hat{H}_{\text{int}} = g_{\text{NaLi}} \, \hat{\rho}_{\text{Bose}}(\hat{\vec{r}}). \tag{6.7}$$

And the density of the Bose gas is according to equation (2.3) given by

$$\begin{aligned} \hat{\rho}_{\text{Bose}}(\vec{r}) = \hat{\Psi}^\dagger(\vec{r})\hat{\Psi}(\vec{r}) &= \left(\Psi_0^*(\vec{r}) + \delta\hat{\Psi}^\dagger(\vec{r})\right)\left(\Psi_0(\vec{r}) + \delta\hat{\Psi}(\vec{r})\right) \\ &\approx \rho_0 + \sqrt{\rho_0}\left(\delta\hat{\Psi}(\vec{r}) + \delta\hat{\Psi}^\dagger(\vec{r})\right). \end{aligned} \tag{6.8}$$

In the last step, we neglected density fluctuations in second order as they are small for large condensate fractions, and we introduced the mean condensate density $\rho_0 = |\Psi_0|^2 = |\Psi_0(\vec{r})|^2$ assuming a homogeneous condensate and Ψ_0 as real. This yields for the interaction Hamiltonian

$$\hat{H}_{\text{int}} = g_{\text{NaLi}}\left(\rho_0 + \sqrt{\rho_0}\left(\delta\hat{\Psi}(\hat{\vec{r}}) + \delta\hat{\Psi}^\dagger(\hat{\vec{r}})\right)\right). \tag{6.9}$$

In the following, we omit the first term of the interaction Hamiltonian as it is constant and leads only to an energy shift for the lithium atom, and we write the fluctuation terms in form of the creation and annihilation operators for Bogoliubov excitations (see section 2.1.2). As $u_{\vec{q}}$ and $v_{\vec{q}}$ are real, we get

$$\hat{H}_{\text{int}} = g_{\text{NaLi}}\sqrt{\frac{\rho_0}{V}}\sum_{\vec{q}}\left(u_{\vec{q}}+v_{\vec{q}}\right)\left(e^{i\vec{q}\hat{\vec{r}}}\hat{b}_{\vec{q}}+e^{-i\vec{q}\hat{\vec{r}}}\hat{b}^{\dagger}_{\vec{q}}\right). \tag{6.10}$$

As we will see later on, it is convenient to rewrite the interaction Hamiltonian as

$$\hat{H}_{\text{int}} = g_{\text{NaLi}}\sqrt{\frac{\rho_0}{V}}\sum_{\vec{q}}\left(u_{\vec{q}}+v_{\vec{q}}\right)\sum_{i=1}^{2}\hat{s}_{i,\vec{q}}\hat{\Gamma}_{i,\vec{q}} \tag{6.11}$$

with

$$\hat{s}_{1,\vec{q}} = e^{i\vec{q}\hat{\vec{r}}},\ \hat{s}_{2,\vec{q}} = e^{-i\vec{q}\hat{\vec{r}}},\ \hat{\Gamma}_{1,\vec{q}} = \hat{b}_{\vec{q}}\ \text{ and }\ \hat{\Gamma}_{2,\vec{q}} = \hat{b}^{\dagger}_{\vec{q}}.$$

6.1.2. General Master Equation

To compute the dynamics of the lithium atom within the sodium bath, we start our calculations with the time evolution of the complete density operator accounting for the bath and the lithium atom. Subsequently, we trace over the bath modes and end up with the time evolution of the reduced density matrix covering the evolution of the lithium atom only.

At first, we split the Hamiltonian into two parts $\hat{H}_{\text{tot}} = \hat{H}_0 + \hat{H}_{\text{int}}$ where $\hat{H}_0 = \hat{H}_{\text{bath}} + \hat{H}_{\text{atom}}$ governs the evolution of the bath and the lithium atom without interaction and $\hat{H}_{\text{int}}$ covers the interaction between the two. We calculate the evolution of the total density operator $\hat{w}(t)$ in the interaction or Dirac picture [57]

$$\frac{d}{dt}\hat{w}^{\text{I}}(t) = -\frac{i}{\hbar}\left[\hat{H}^{\text{I}}_{\text{int}}(t),\hat{w}^{\text{I}}(t)\right] \tag{6.12}$$

with $\hat{w}^{\text{I}}(t) = e^{i\hat{H}_0 t/\hbar}\hat{w}e^{-i\hat{H}_0 t/\hbar}$ and $\hat{H}^{\text{I}}_{\text{int}}(t)$ similarly. We formally integrate this equation

$$\hat{w}^{\text{I}}(t) = \hat{w}^{\text{I}}(0) - \frac{i}{\hbar}\int_0^t\left[\hat{H}^{\text{I}}_{\text{int}}(\xi),\hat{w}^{\text{I}}(\xi)\right]\,\mathrm{d}\xi, \tag{6.13}$$

and by inserting the solution into equation (6.12), we get

$$\frac{d}{dt}\hat{w}^{\text{I}}(t) = -\frac{i}{\hbar}\left[\hat{H}^{\text{I}}_{\text{int}}(t),\hat{w}^{\text{I}}(0)\right] - \frac{1}{\hbar^2}\int_0^t\left[\hat{H}^{\text{I}}_{\text{int}}(t),\left[\hat{H}^{\text{I}}_{\text{int}}(\xi),\hat{w}^{\text{I}}(\xi)\right]\right]\,\mathrm{d}\xi. \tag{6.14}$$

We could iteratively repeat this procedure for $\hat{w}^{\text{I}}(\xi)$, but we compute the time evolution only up to second order in $\hat{H}^{\text{I}}_{\text{int}}$ as the lithium atom and the sodium atoms interact weakly (Born approximation). So far, we considered the time evolution of the bath as well as the lithium atom. To reduce our considerations to the evolution of the lithium atom only, we take the trace over the bath's degrees of freedom Tr_{bath}. Additionally, we assume that the bath and the atom are initially

uncorrelated $\hat{w}^{\mathrm{I}}(0) = \hat{w}^{\mathrm{I}}_{\mathrm{atom}}(0) \otimes \hat{w}^{\mathrm{I}}_{\mathrm{bath}}(0)$ and that the impact of the interaction on the bath can be neglected.[1] In this case, the density operator for the bath becomes time-independent

$$\hat{w}^{\mathrm{I}}(t) \approx \hat{w}^{\mathrm{I}}_{\mathrm{atom}}(t) \otimes \hat{w}_{\mathrm{bath}}. \tag{6.15}$$

With these assumptions, we get for the reduced density operator $\hat{w}^{\mathrm{I}}_{\mathrm{atom}}(t)$

$$\frac{d}{dt}\hat{w}^{\mathrm{I}}_{\mathrm{atom}}(t) = -\frac{1}{\hbar^2}\int_0^t \mathrm{Tr}_{\mathrm{bath}}\left\{\left[\hat{H}^{\mathrm{I}}_{\mathrm{int}}(t), \left[\hat{H}^{\mathrm{I}}_{\mathrm{int}}(\xi), \hat{w}^{\mathrm{I}}_{\mathrm{atom}}(\xi)\otimes\hat{w}_{\mathrm{bath}}\right]\right]\right\}\mathrm{d}\xi \tag{6.16}$$

as $\mathrm{Tr}_{\mathrm{bath}}\{[\hat{H}^{\mathrm{I}}_{\mathrm{int}}(t), \hat{w}^{\mathrm{I}}_{\mathrm{atom}}(0)\otimes\hat{w}_{\mathrm{bath}}]\} = 0$ (for details see appendix A.1).

Finally, we assume that the correlation time of the bath τ_{C} is short compared to the evolution time scale of $\hat{w}^{\mathrm{I}}_{\mathrm{atom}}(t)$ and apply the Markov approximation.[2] As $\mathrm{Tr}_{\mathrm{bath}}\{\hat{H}^{\mathrm{I}}_{\mathrm{int}}(t)\hat{H}^{\mathrm{I}}_{\mathrm{int}}(\xi)\ \hat{w}_{\mathrm{bath}}\}$ vanishes for $t-\xi > \tau_{\mathrm{C}}$ and $\hat{w}^{\mathrm{I}}_{\mathrm{atom}}(\xi)$ does not significantly change on this time scale, we can replace $\hat{w}^{\mathrm{I}}_{\mathrm{atom}}(\xi)$ by $\hat{w}^{\mathrm{I}}_{\mathrm{atom}}(t)$ and get the master equation for the evolution of the reduced density matrix [69, 74]

$$\frac{d}{dt}\hat{w}^{\mathrm{I}}_{\mathrm{atom}}(t) = -\frac{1}{\hbar^2}\int_0^t \mathrm{Tr}_{\mathrm{bath}}\left\{\left[\hat{H}^{\mathrm{I}}_{\mathrm{int}}(t), \left[\hat{H}^{\mathrm{I}}_{\mathrm{int}}(\xi), \hat{w}^{\mathrm{I}}_{\mathrm{atom}}(t)\otimes\hat{w}_{\mathrm{bath}}\right]\right]\right\}\mathrm{d}\xi. \tag{6.17}$$

Because of the Markov approximation, the change of $\hat{w}^{\mathrm{I}}_{\mathrm{atom}}(t)$ does not depend anymore on its former evolution, but only on its current state as the fast bath dynamics smear out the history of $\hat{w}^{\mathrm{I}}_{\mathrm{atom}}(t)$.

6.1.3. Master Equation for the Bosonic Bath

Equation (6.17) is the master equation in the Born-Markov approximation in its general form. Now, we will specify the master equation to the bosonic bath from which we derive a set of differential equations in order to calculate the time evolution of the lithium atom in the bath. The derivation turns out to be lengthy and is thus only partly covered in the main part of this thesis. However, the omitted calculations are presented in appendix A.2.

After inserting the interaction Hamiltonian (eq. (6.11)) into the general master equation (6.17), we already get the master equation for the bosonic bath

$$\begin{aligned}\frac{d}{dt}\hat{w}^{\mathrm{I}}_{\mathrm{atom}}(t) = &-\frac{g^2_{\mathrm{NaLi}}\rho_0}{\hbar^2 V}\sum_{\vec{q},\vec{p}}\Big(\left(u_{\vec{q}}+v_{\vec{q}}\right)\left(u_{\vec{p}}+v_{\vec{p}}\right) \\ &\sum_{i,j=1}^{2}\int_0^t \mathrm{Tr}_{\mathrm{bath}}\left\{\left[\hat{s}^{\mathrm{I}}_{i,\vec{q}}(t)\hat{\Gamma}^{\mathrm{I}}_{i,\vec{q}}(t), \left[\hat{s}^{\mathrm{I}}_{j,\vec{p}}(\xi)\hat{\Gamma}^{\mathrm{I}}_{j,\vec{p}}(\xi), \hat{w}^{\mathrm{I}}_{\mathrm{atom}}(t)\otimes\hat{w}_{\mathrm{bath}}\right]\right]\right\}\mathrm{d}\xi\Big).\end{aligned} \tag{6.18}$$

From here on, we calculate the time evolution of the lithium atom in two steps. First, we perform the trace over the bath variables resulting in a simplified differential equation for the reduced

[1] This condition is not perfectly fulfilled in the experiment as we investigate more than one lithium atom and the number of sodium atoms is at most one order of magnitude larger than the number of lithium atoms.

[2] The correlation time is due to our bath temperature ($T \approx 500\,\mathrm{nK}$) on the order of $1\,\mu\mathrm{s}$ [70] which is more than three orders of magnitude faster than the dynamics induced by the bosonic bath (see chapter 7 and 8).

density operator which does not contain any bath operators. Secondly, we choose the energy eigenstates of the lithium atom as basis and represent the master equation as a set of coupled equations for the elements of the reduced density matrix.

Trace over the Bath Variables

After expanding the commutators in equation (6.18), we can factorize each summand of the master equation into a bath and an atom part. The first term we need to calculate is $\mathrm{Tr}_{\mathrm{bath}}\{\hat{\Gamma}^{\mathrm{I}}_{i,\vec{q}}(t)\hat{\Gamma}^{\mathrm{I}}_{j,\vec{p}}(\xi)\,\hat{w}_{\mathrm{bath}}\}$ which turns out to be only non zero for $i \neq j$ and $\vec{p} = \vec{q}$ (see appendix A.2). Thus, we either have

- $\mathrm{Tr}_{\mathrm{bath}}\{\hat{\Gamma}^{\mathrm{I}}_{i,\vec{q}}(t)\hat{\Gamma}^{\mathrm{I}}_{j,\vec{p}}(\xi)\hat{w}_{\mathrm{bath}}\} = \mathrm{Tr}_{\mathrm{bath}}\{\hat{b}^{I\dagger}_{\vec{q}}(t)\hat{b}^{I}_{\vec{q}}(\xi)\hat{w}_{\mathrm{bath}}\}$ which corresponds to the absorption of a Bogoliubov excitation with momentum $\vec{q}$ and energy $\epsilon_{\vec{q}}$ by the lithium atom and hence to heating of the atom. The absorption probability is proportional to the occupation probability of the corresponding Bogoliubov mode $N(\vec{q})$ which is governed by the Bose distribution $N(\vec{q}) = 1/(e^{\epsilon_{\vec{q}}/(k_{\mathrm{B}}T)} - 1)$ [27]. Hence, we get $\mathrm{Tr}_{\mathrm{bath}}\{\hat{b}^{I\dagger}_{\vec{q}}(t)\hat{b}^{I}_{\vec{q}}(\xi)\hat{w}_{\mathrm{bath}}\} \propto N(\vec{q})$.

or

- $\mathrm{Tr}_{\mathrm{bath}}\{\hat{\Gamma}^{\mathrm{I}}_{i,\vec{q}}(t)\hat{\Gamma}^{\mathrm{I}}_{j,\vec{p}}(\xi)\hat{w}_{\mathrm{bath}}\} = \mathrm{Tr}_{\mathrm{bath}}\{\hat{b}^{I}_{\vec{q}}(t)\hat{b}^{I\dagger}_{\vec{q}}(\xi)\hat{w}_{\mathrm{bath}}\}$ which is related to the opposite process, namely the creation of a Bogoliubov excitation with momentum $\vec{q}$ by the lithium atom. This process corresponds to the dissipation of energy to the bosonic bath, and one gets $\mathrm{Tr}_{\mathrm{bath}}\{\hat{b}^{I}_{\vec{q}}(t)\hat{b}^{I\dagger}_{\vec{q}}(\xi)\hat{w}_{\mathrm{bath}}\} \propto 1 + N(\vec{q})$ where $N(\vec{q})$ accounts for the bosonic stimulation of the creation process.

As the derivation of the interaction Hamiltonian neglects terms of second order in $\delta\hat{\Psi}(\vec{r})$ (see section 6.1.1), the master equation does not contain terms of fourth order in $\hat{\Gamma}$. Hence, there are no interaction processes which involve two Bogoliubov excitations as e. g. inelastic scattering of thermal excitations.

For our experiment, this assumption is justified in the central region of the bosonic gas where the density of the Bose-Einstein condensate is much larger than the density of the thermal component (see figure 2.5). However, the thermal component dominates in the outer regions of the sodium cloud. Though, we will see later on that the excitations governing the dynamics of the lithium atoms have larger momenta than the momenta which are occupied in a thermal gas. Thus, the finite momentum of the elementary excitations has no significant impact on the scattering process, and the momenta of the thermal component can in first approximation be considered as zero as for the Bose-Einstein condensate.

At this point, we omit a rigorous evaluation of the traces from equation (6.18) and just denote the result. The evaluation yields (eq. (A.10))

$$\begin{aligned}\frac{d}{dt}\hat{w}^{\mathrm{I}}_{\mathrm{atom}}(t) = -\frac{g^2_{\mathrm{NaLi}}\rho_0}{\hbar^2 V}\sum_{\vec{q}}\int_0^t \left(u_{\vec{q}} + v_{\vec{q}}\right)^2 \Big(\\ \hat{s}^{\mathrm{I}}_{1,\vec{q}}(t)\hat{s}^{\mathrm{I}}_{2,\vec{q}}(\xi)\hat{w}^{\mathrm{I}}_{\mathrm{atom}}(t)e^{i\epsilon_{\vec{q}}(\xi-t)/\hbar}\left(1+N(\vec{q})\right) + \hat{s}^{\mathrm{I}}_{2,\vec{q}}(t)\hat{s}^{\mathrm{I}}_{1,\vec{q}}(\xi)\hat{w}^{\mathrm{I}}_{\mathrm{atom}}(t)e^{i\epsilon_{\vec{q}}(t-\xi)/\hbar}N(\vec{q}) \\ - \hat{s}^{\mathrm{I}}_{2,\vec{q}}(t)\hat{w}^{\mathrm{I}}_{\mathrm{atom}}(t)\hat{s}^{\mathrm{I}}_{1,\vec{q}}(\xi)e^{i\epsilon_{\vec{q}}(t-\xi)/\hbar}\left(1+N(\vec{q})\right) - \hat{s}^{\mathrm{I}}_{1,\vec{q}}(t)\hat{w}^{\mathrm{I}}_{\mathrm{atom}}(t)\hat{s}^{\mathrm{I}}_{2,\vec{q}}(\xi)e^{i\epsilon_{\vec{q}}(\xi-t)/\hbar}N(\vec{q})\end{aligned} \tag{6.19}$$

$$
\begin{aligned}
&- \hat{s}^{\mathrm{I}}_{2,\vec{q}}(\xi)\hat{w}^{\mathrm{I}}_{\mathrm{atom}}(t)\hat{s}^{\mathrm{I}}_{1,\vec{q}}(t)e^{i\epsilon_{\vec{q}}(\xi-t)/\hbar}\,(1+N(\vec{q})) - \hat{s}^{\mathrm{I}}_{1,\vec{q}}(\xi)\hat{w}^{\mathrm{I}}_{\mathrm{atom}}(t)\hat{s}^{\mathrm{I}}_{2,\vec{q}}(t)e^{i\epsilon_{\vec{q}}(t-\xi)/\hbar}N(\vec{q}) \\
&+ \hat{w}^{\mathrm{I}}_{\mathrm{atom}}(t)\hat{s}^{\mathrm{I}}_{1,\vec{q}}(\xi)\hat{s}^{\mathrm{I}}_{2,\vec{q}}(t)e^{i\epsilon_{\vec{q}}(t-\xi)/\hbar}\,(1+N(\vec{q})) + \hat{w}^{\mathrm{I}}_{\mathrm{atom}}(t)\hat{s}^{\mathrm{I}}_{2,\vec{q}}(\xi)\hat{s}^{\mathrm{I}}_{1,\vec{q}}(t)e^{i\epsilon_{\vec{q}}(\xi-t)/\hbar}N(\vec{q})\Big)\,\mathrm{d}\xi.
\end{aligned}
$$

The terms in the left column denote the processes which include the creation of a Bogoliubov excitation, whereas the terms in the right column correspond to the absorption of thermal excitations.

Conversion into a Set of Coupled Differential Equations

As mentioned before, we intend to convert equation (6.19) into a set of differential equations which can be solved numerically. For this purpose, we consider the reduced density operator in the basis of the energy eigenstates of the lithium atom

$$
\hat{w}^{\mathrm{I}}_{\mathrm{atom}}(t) = \sum_{k,l} w_{k,l}(t)\,|k\rangle\,\langle l|\,. \tag{6.20}
$$

As the lithium atom is confined in a three-dimensional harmonic potential, k and l denote triples specifying the different harmonic oscillator modes (eq. (6.4)). It is convenient to choose the energy eigenstates as basis because they offer a straightforward evaluation of the time integral in equation (6.19). The integration restricts the energy difference of the coupled modes and leads to the conservation of energy, i. e. two modes are only coupled if their energy difference matches the energy $\epsilon_{\vec{q}}$ of the involved Bogoliubov excitation. As result, we get a set of differential equations for the $w_{k,l}(t)$ (eq.(A.27))

$$
\begin{aligned}
\frac{d}{dt}w_{k,l}(t) = &- \frac{\pi g^2_{\mathrm{NaLi}}\rho_0}{\hbar V}\sum_{j_1,j_2}\sum_{\vec{q}}\Big[\left(u_{\vec{q}}+v_{\vec{q}}\right)^2(1+N(\vec{q}))\Big(\\
&\quad S^{k,j_1}_{1,\vec{q}}S^{j_1,j_2}_{2,\vec{q}}w_{j_2,l}(t)e^{i(E_k-E_{j_2})t/\hbar}\delta(E_{j_2}-E_{j_1}-\epsilon_{\vec{q}}) \\
&- S^{k,j_1}_{2,\vec{q}}w_{j_1,j_2}(t)S^{j_2,l}_{1,\vec{q}}e^{i(E_k+E_{j_2}-E_{j_1}-E_l)t/\hbar}\delta(E_{j_2}-E_l-\epsilon_{\vec{q}}) \\
&- S^{k,j_1}_{2,\vec{q}}w_{j_1,j_2}(t)S^{j_2,l}_{1,\vec{q}}e^{i(E_k+E_{j_2}-E_{j_1}-E_l)t/\hbar}\delta(E_{j_1}-E_k-\epsilon_{\vec{q}}) \\
&+ w_{k,j_1}(t)S^{j_1,j_2}_{1,\vec{q}}S^{j_2,l}_{2,\vec{q}}e^{i(E_{j_1}-E_l)t/\hbar}\delta(E_{j_1}-E_{j_2}-\epsilon_{\vec{q}})\Big)\Big] \\
&- \frac{\pi g^2_{\mathrm{NaLi}}\rho_0}{\hbar V}\sum_{j_1,j_2}\sum_{\vec{q}}\Big[\left(u_{\vec{q}}+v_{\vec{q}}\right)^2 N(\vec{q})\Big(\\
&\quad S^{k,j_1}_{2,\vec{q}}S^{j_1,j_2}_{1,\vec{q}}w_{j_2,l}(t)e^{i(E_k-E_{j_2})t/\hbar}\delta(E_{j_1}-E_{j_2}-\epsilon_{\vec{q}}) \\
&- S^{k,j_1}_{1,\vec{q}}w_{j_1,j_2}(t)S^{j_2,l}_{2,\vec{q}}e^{i(E_k+E_{j_2}-E_{j_1}-E_l)t/\hbar}\delta(E_l-E_{j_2}-\epsilon_{\vec{q}}) \\
&- S^{k,j_1}_{1,\vec{q}}w_{j_1,j_2}(t)S^{j_2,l}_{2,\vec{q}}e^{i(E_k+E_{j_2}-E_{j_1}-E_l)t/\hbar}\delta(E_k-E_{j_1}-\epsilon_{\vec{q}}) \\
&+ w_{k,j_1}(t)S^{j_1,j_2}_{2,\vec{q}}S^{j_2,l}_{1,\vec{q}}e^{i(E_{j_1}-E_l)t/\hbar}\delta(E_{j_2}-E_{j_1}-\epsilon_{\vec{q}})\Big)\Big]
\end{aligned} \tag{6.21}
$$

with

$$
S^{j_1,j_2}_{i,\vec{q}} = \langle j_1|\,\hat{s}_{i,\vec{q}}\,|j_2\rangle\,. \tag{6.22}
$$

Equation (6.21) governs the time evolution of the lithium atom in the most general case. However, if the lithium atom is initially prepared in an energy eigenstate and not in a superposition of eigenstates, equation (6.21) can be further simplified. In this case, only one diagonal element of the density matrix $w_{k,k}$ is initially populated, whereas the off-diagonal elements characterizing the coherences are all zero. As coherences are not expected to build up due to the interaction with the bosonic bath, the off-diagonal elements are never occupied ($w_{k,l}(t) = 0$ for $k \neq l$), and the time evolution of the diagonal elements is governed by (eq. (A.29), [69])

$$\frac{d}{dt}w_{k,k}(t) = \sum_j \Big(R_{j\to k} w_{j,j}(t) - R_{k\to j} w_{k,k}(t) + H_{j\to k} w_{j,j}(t) - H_{k\to j} w_{k,k}(t) \Big) \quad (6.23)$$

with

$$R_{m\to n} = \frac{2\pi g_{\mathrm{NaLi}}^2 \rho_0}{\hbar V} \sum_{\vec{q}} \left(u_{\vec{q}} + v_{\vec{q}}\right)^2 \left(1 + N(\vec{q})\right) \left|S_{2,\vec{q}}^{n,m}\right|^2 \delta(E_m - E_n - \epsilon_{\vec{q}}) \quad (6.24)$$

and

$$H_{m\to n} = \frac{2\pi g_{\mathrm{NaLi}}^2 \rho_0}{\hbar V} \sum_{\vec{q}} \left(u_{\vec{q}} + v_{\vec{q}}\right)^2 N(\vec{q}) \left|S_{2,\vec{q}}^{n,m}\right|^2 \delta(E_n - E_m - \epsilon_{\vec{q}}). \quad (6.25)$$

Here, $R_{m\to n}$ denotes the transition or relaxation rate from state $|m\rangle$ to state $|n\rangle$ caused by the interaction with the bosonic bath which is identical to the transition rate obtained from Fermi's golden rule [75]. The heating rate $H_{m\to n}$ accounts for the finite temperature of the bath and allows transitions to energetically higher states. As both the relaxation and the heating rate are time-independent, the matrix elements $w_{k,k}(t)$ evolve exponentially. In the long term limit and for zero temperature, the lithium atom will relax to the ground state of the harmonic oscillator potential, whereas for finite temperature higher energy states are populated according to the Bose distribution.

6.2. Relaxation of Motionally Excited Lithium Atoms

This section investigates the characteristics of the relaxation of a motionally excited lithium atom as the understanding of the relaxation mechanics becomes important for interpreting the decay of coherences in the following section. For this purpose, the relaxation or equivalently the population decay is considered on the basis of the two system components. At first, we investigate the dependency of the relaxation rate on the external confinement of the lithium atom and secondly the dependency on the bath structure.

6.2.1. Decay Channels

To illustrate the impact of the trapping geometry on the population decay, we consider the relaxation process of a lithium atom which initially populates the first excited state $|m_{\mathrm{x}} = 0, m_{\mathrm{y}} = 0, m_{\mathrm{z}} = 1>$ along the z-direction (longitudinal direction). Because of the interaction with the

bosonic bath, the lithium atom can decay to any state $|n_x, n_y, 0>$ with lower energy than the initial state and can thereby change its excitation along the x- and y-direction (transversal directions). Hence, the decay to the ground state along the z-direction is characterized by the total relaxation rate $R = \sum_n R_{m\to n}$ which takes the relaxation processes into all possible modes n into account. Figure 6.1 a) depicts the total relaxation rate R depending on the confinement in the transversal directions for a parameter set which is similar to those realized in the experiment (the $R_{m\to n}$'s are evaluated in the appendix A.3).

Starting from weak transversal confinements, the total relaxation rate changes slowly for increasing confinement as long as the transversal trapping frequencies are weak compared to the one in the longitudinal direction ($\omega_{x,y}/\omega_z \lesssim 0.25$). This behavior originates from the small spacing of the energy levels in the transversal directions which provides an almost continuous phase space for the relaxation process.

As soon as the transversal and the longitudinal confinement are on the same order of magnitude ($0.25 \lesssim \omega_{x,y}/\omega_z < 1$), the relaxation rate changes faster which is mainly caused by the discrete changes in the number of energetically allowed decay channels. However, an additional reason is the dependency of the coupling strength on the transversal confinement. If the Bogoliubov excitation which is induced by the relaxation process propagates in z-direction, there is no coupling between different modes in the x- and y-direction

$$S_{2,\vec{q}}^{m,n} = \langle m| e^{-i\vec{q}\hat{\vec{r}}} |n\rangle = \langle m_x| \underbrace{e^{-iq_x\hat{x}}}_{=1} |n_x\rangle \langle m_y| \underbrace{e^{-iq_y\hat{y}}}_{=1} |n_y\rangle \langle m_z| e^{-iq_z\hat{z}} |n_z\rangle \tag{6.26}$$

and they remain unchanged during the relaxation. Hence, the coupling strength and the relax-

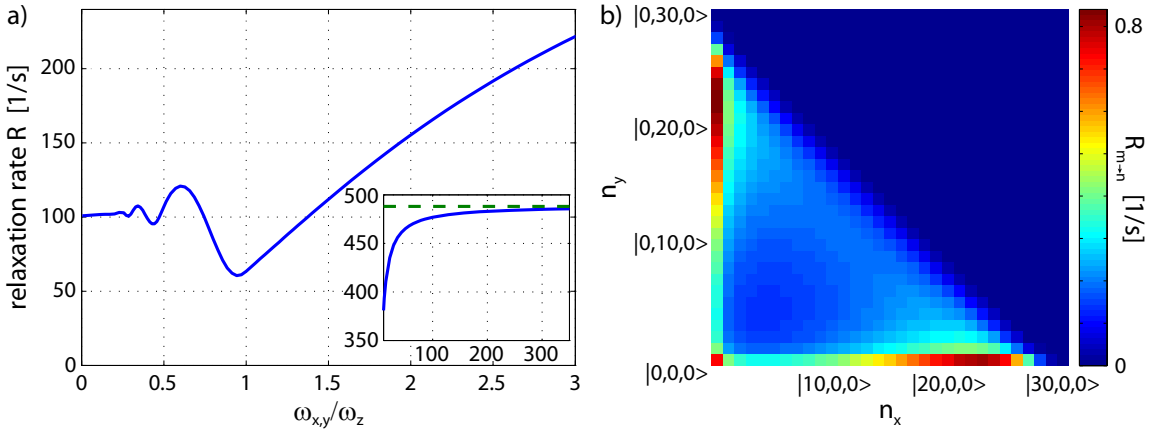

Figure 6.1.: a) Total relaxation rate from mode $|0,0,1\rangle$ into energetically lower modes depending on the confinement in x- and y-direction ($\omega_z = 2\pi\,70\,\text{kHz}$, $\rho_0 = 1\cdot 10^{13}\,\text{cm}^{-3}$, $T = 0\,\text{K}$). The blue line displays the calculations for an equal confinement in the transversal directions ($\omega_x = \omega_y$). The inset compares our calculations for strong transversal confinements to the one-dimensional (analytic) solution from [76] depicted as green dashed line. b) Relaxation rate resolved for the different transversal modes $|n_x, n_y, 0\rangle$ for $\omega_x = \omega_y = 2\pi\,2\,\text{kHz}$.

ation rate are unaffected by the confinement in x- and y-direction. Though, it turns out that these processes are in the minority and most relaxations induce a Bogoliubov excitation which does not propagate in z-direction. Thus, also the modes in x- and y-direction are coupled during the relaxation process. This fact is illustrated in figure 6.1 b) which displays the relaxation rates $R_{m\to n}$ for the different transversal modes. The red colored areas indicate that it is most likely to relax into modes which are either excited along the x- or the y-direction (but not anymore along the z-direction). As the relaxation rates for these decay channels depend on the confinement in x- and y-direction, the confinement affects the total relaxation rate not only by the number of possible decay channels, but also by its impact on the corresponding coupling strengths. This leads to the non-trivial oscillatory behavior of the total relaxation rate for similar confinements in x-, y- and z-direction.

As soon as the trapping frequencies in the transversal directions exceed the one in z-direction ($\omega_{\mathrm{x,y}}/\omega_{\mathrm{z}} > 1$), there is only the decay channel $|0,0,0\rangle$ left and the total relaxation rate evolves monotonically. However, the impact of the transversal confinement on the relaxation rate remains until the wavelength of the involved Bogoliubov excitation becomes large compared to the extent of the wavefunction in the transversal directions ($a_{\mathrm{ho}}^{\mathrm{x,y}} q \ll 1$). In this case, the lithium atom does not resolve the corresponding density modulation of the Bose gas in the transversal directions and their contribution to the matrix element $S_{2,\vec{q}}^{m,n}$ becomes unity ($e^{-iq_{\mathrm{x}}\hat{x}} \approx 1$, $e^{-iq_{\mathrm{y}}\hat{y}} \approx 1$) . As shown in the inset of figure 6.1 a), the total relaxation rate is only for $\omega_{\mathrm{z}} \ll \omega_{\mathrm{x,y}}$ completely independent from the transversal confinement and our results reproduce the one-dimensional calculations presented in [69, 76].

6.2.2. Bath Structure

The relaxation processes depend on several bath properties as e. g. its temperature and density. However, the probably most interesting feature is the bath's bosonic nature which is manifested in its dispersion relation (eq. (2.17)). To investigate the impact of this dispersion relation on the relaxation process, we study the relaxation rate from the first excited state to the ground state of a one-dimensional harmonic oscillator potential, i. e. $\omega_{\mathrm{z}} \ll \omega_{\mathrm{x,y}}$.[3] By tuning the trapping frequency ω_{z} for the lithium atom, we change the energy which is dissipated to the bosonic bath. This results in coupling to phonon-like Bogoliubov excitations for trapping frequencies below the chemical potential of the Bose gas ($\omega_{\mathrm{z}} < \mu_{\mathrm{Na}}/\hbar$) and in coupling to free-particle-like excitations for higher trapping frequencies ($\omega_{\mathrm{z}} > \mu_{\mathrm{Na}}/\hbar$).

Figure 6.2 depicts the relaxation rates for parameters which are experimentally realized in the center of our bosonic bath. The relaxation rate decreases monotonically with decreasing confinement (dissipated energy) and drops to zero for low energies. The graph depicts the result for zero as well as for finite temperature ($T = 550\,\mathrm{nK}$). In the latter case, the relaxation rates are for small trapping frequencies enhanced as the low energetic Bogoliubov modes are thermally populated which increases the relaxation rates due to bosonic stimulation.

Because of the phonon-like dispersion relation for low energetic excitations, the relaxation rate drops quickly for small dissipated energies [77]. However, in contrast to an atom in free space, the dissipation processes do not vanish if the atom's energy is below the chemical potential, and

[3] The bath is still considered three-dimensional.

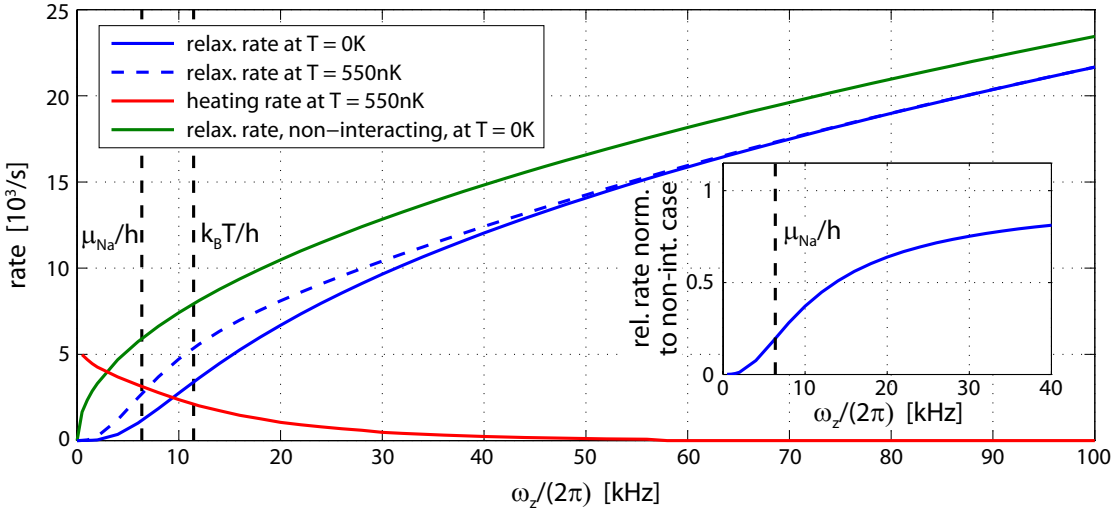

Figure 6.2.: Relaxation and heating rates for an atom populating the first excited state of a one-dimensional harmonic oscillator potential immersed in a three-dimensional bosonic bath ($\rho_0 = 4 \cdot 10^{14}\,\mathrm{cm}^{-3}$). The relaxation and heating rates are plotted versus the trapping frequency ω_z of the harmonic oscillator, which corresponds to the energy dissipated during the relaxation process. The vertical dashed lines indicate the temperature T and the chemical potential of the bosonic bath μ_{Na}. The inset displays the relaxation rate for the interacting Bose gas at zero temperature normalized to a non-interacting Bose gas which has a free-particle-like dispersion relation.

the relaxation rate stays finite. In order to point out the fast decrease of the relaxation rate due to the bath's bosonic nature, the inset of figure 6.2 displays the relaxation rate at zero temperature normalized to the relaxation rate of a non-interacting Bose gas which has for all excitation energies a free-particle-like dispersion relation. Clearly, the relaxation process for the interacting bath is for small dissipated energies much slower which stems from the linear behavior of the dispersion relation. For larger energies, which correspond to free-particle-like excitations, the relaxation rate for the interacting gas approaches the one for the non-interacting Bose gas.

Overall, figure 6.2 shows that neither the bath temperature nor its bosonic nature are important in order to describe the relaxation processes if the dissipated energy exceeds $40\,\mathrm{kHz}$. We will come back to this point during the discussion of the relaxation dynamics in chapter 7.

In the following section, we will investigate the loss of motional coherence due to interaction with the bosonic bath. In this context, the relaxation rate turns out to be helpful for interpreting the calculations at zero temperature, but do not suffice to explain the loss of coherence at finite temperature. In this case, we also need to include heating processes into our considerations. For this reason, figure 6.2 compares the total heating rate $H = \sum_n H_{m\to n}$ at $T = 550\,\mathrm{nK}$ to the relaxation rates. As expected, the heating processes become important if the energy gap between the harmonic oscillator levels is on the order of the bath temperature, and the heating rates exceed

for small energy gaps the relaxation rates.

6.3. Loss of Motional Coherence

The probably most prominent example for the loss of coherence due to interaction with a bath is the two-level atom coupling to the vacuum modes. In this case, the interaction causes the well-known phenomena of spontaneous emission [78] which corresponds according to our previous terminology to the relaxation from the excited to the ground state. Besides this population decay, the vacuum modes also induce the loss of coherence for an atom starting in a superposition of ground and excited state. For the two-level atom, it turns out that the coherence decays at half the spontaneous emission rate [74]. The intuitive explanation for this factor of two is the fact that only the atom fraction in the excited state decays, whereas the fraction in the ground state is unaffected by the vacuum modes. In the following, we try to adapt this interpretation approach and check if the loss of motional coherence due to the bosonic bath originates from relaxation processes.

For this purpose, we evaluate the evolution of a lithium atom within the bosonic bath according to equation (6.21). The loss of coherence can then be extracted from the decay of the off-diagonal density matrix elements. As the functional evolution of the density matrix is a priori unknown, we characterize the coherence loss by the decoherence time τ_{decoh} for which the off-diagonal matrix element decays to 1/e of its initial value.[4] Simultaneously, the relaxation time τ_{relax} is determined by the same approach using the diagonal elements of the density matrix in order to compare the two time scales imposed by the bosonic bath.

6.3.1. One-Dimensional Harmonic Oscillator Potential

At first, we investigate the dynamics of a lithium atom in one dimension and for zero temperature. Initially, the atom is prepared in an equal superposition of two harmonic oscillator modes

$$\frac{1}{\sqrt{2}}\left(|m\rangle + |n\rangle\right) \text{ with } m < n, \tag{6.27}$$

and we determine τ_{relax} and τ_{decoh} from the evolution of the density matrix elements $w_{n,n}(t)$ and $w_{n,m}(t)$, respectively. For this scenario, figure 6.3 a) shows the ratio $\tau_{\text{decoh}}/\tau_{\text{relax}}$ for superpositions between different modes and for the same bath parameters as for figure 6.2. If the ground state is selected as one of the superposition modes, the calculation yields $\tau_{\text{decoh}}/\tau_{\text{relax}} \approx 2$ as for the two-level atom. This observation is consistent with the interpretation of the coherence loss by means of relaxation processes. If both superposition modes are excited modes, the ratio drops below 2 and approaches 1 for modes having similar relaxation times (see figure 6.2). This result agrees at least qualitatively with our expectations as both modes relax in this case to energetically lower modes.

For a more quantitative check, we have to adapt the interpretation approach of the two-level atom and account for the fact that the bosonic bath couples both superposition modes to lower modes. The corresponding total relaxation rate for mode m and n is given by $\sum_k R_{m\to k}$ and

[4] Actually, we find for most calculation parameters an almost (but not perfect) exponential coherence decay.

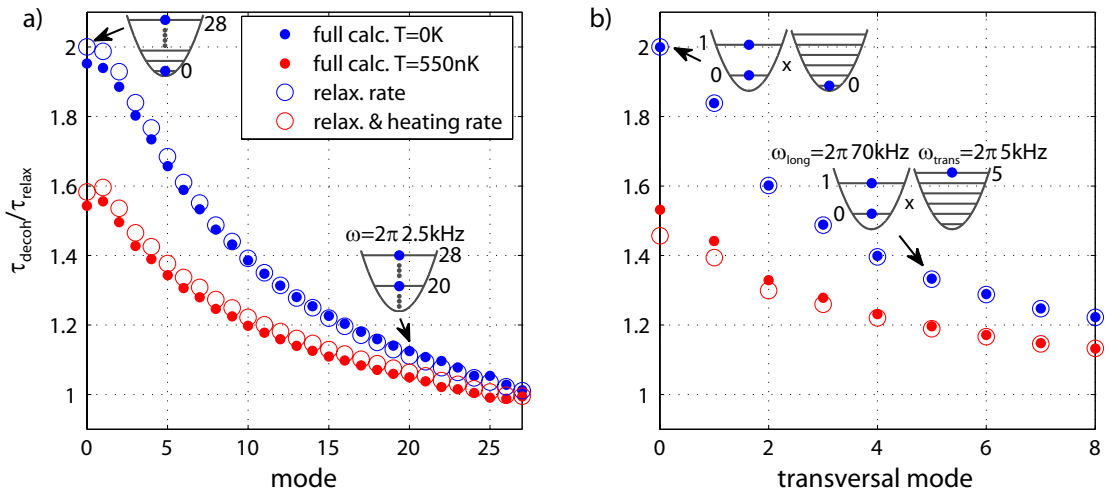

Figure 6.3.: Ratio of the decoherence time τ_{decoh} and the relaxation time τ_{relax} according to equation (6.21) and the corresponding approximation on the basis of the relaxation and heating rates. a) For different superpositions of two one-dimensional harmonic oscillator modes ($\omega = 2\pi\, 2.5\,\text{kHz}$). The lower superposition mode is alternated and the higher mode fixed to the 28^{th} mode as indicated by the insets. b) For different superpositions of two modes of a two-dimensional harmonic oscillator potential. Each superposition consists of a variable mode along one direction ($\omega_{\text{trans}} = 2\pi\, 5\,\text{kHz}$) and ground and first excited state along the other direction ($\omega_{\text{long}} = 2\pi\, 70\,\text{kHz}$).

$\sum_k R_{n\to k}$, respectively. As we expect that both modes contribute equally to the coherence loss, we approximate the characteristic time scale for the coherence decay τ_{decoh} at zero temperature by

$$\tau_{\text{decoh}}(T=0) = \frac{2}{\sum_k R_{m\to k} + \sum_k R_{n\to k}}. \tag{6.28}$$

Hence, the corresponding ratio of $\tau_{\text{decoh}}/\tau_{\text{relax}}$ reads as

$$\frac{\tau_{\text{decoh}}(T=0)}{\tau_{\text{relax}}(T=0)} = \frac{2\sum_k R_{n\to k}}{\sum_k R_{m\to k} + \sum_k R_{n\to k}}. \tag{6.29}$$

Figure 6.3 a) compares the approximated ratio $\tau_{\text{decoh}}/\tau_{\text{relax}}$ with the result from equation (6.21). Both calculations show good agreement which demonstrates that the loss of coherence stems mostly from relaxation processes.

Next, we include the bath temperature into our considerations. Figure 6.3 a) shows that in this case the ratio $\tau_{\text{decoh}}/\tau_{\text{relax}}$ decreases compared to the one for zero temperature and that the impact of the temperature is most severe if the lower superposition mode has a small energy. If we remain in the picture in which the coherence decay is related to relaxation processes, we now have to take the heating processes into account. For instance, the superposition between the ground and

excited state decays for zero temperature only because of relaxation processes of the excited state. Though, for finite temperature, also the ground state is affected by the bath and can be heated to higher modes. These heating processes cause a coherence loss and hence $\tau_{\text{decoh}}/\tau_{\text{relax}} < 2$. In general, the finite temperature becomes important for the coherence decay if the heating rate is for one of the two modes on the order of the relaxation rates. This condition also explains the convergence of the zero and finite temperature calculations if both superposition modes have high energies. In this case, the corresponding relaxation rates exceed the heating rates (fig. 6.2) and thus the relaxation processes dominate the dynamics of the lithium atom .

To check the validity of this interpretation, figure 6.3 a) depicts the approximation for the ratio $\tau_{\text{decoh}}/\tau_{\text{relax}}$ which is adapted to the heating processes

$$\frac{\tau_{\text{decoh}}(T>0)}{\tau_{\text{relax}}(T>0)} = \frac{2\sum_k R_{n\to k} + 2\sum_k H_{n\to k}}{\sum_k R_{m\to k} + \sum_k R_{n\to k} + \sum_k H_{m\to k} + \sum_k H_{n\to k}}. \tag{6.30}$$

Here, we also accounted for the decay of the diagonal density matrix elements due to heating effects and the corresponding impact on the relaxation time. The agreement between the approximation and the more complex calculation is almost as good as for the zero temperature case and shows that the coherence decay can be understood in terms of heating and relaxation processes.

6.3.2. Two-Dimensional Harmonic Oscillator Potential

So far, we considered the evolution of motional coherences for different superpositions in one dimension which allows the easiest access and interpretation of the coherence decay. However, experimentally we investigate a different system. Because of our preparation scheme, the lithium atom ideally starts its evolution in a superposition of ground and first excited state of the longitudinal lattice potential. Depending on the potential along the transversal lattice directions, the lithium atom occupies the lowest transversal mode (deep transversal lattice potentials) or one of the excited modes (e. g. no transversal lattice at all). To reflect this situation, we study the coherence decay in two dimensions and start the calculations with a superposition of ground and first excited state along one direction (longitudinal) and alternate the occupied mode along the other direction (transversal)

$$\frac{1}{\sqrt{2}}\Big(\underbrace{|0,l\rangle}_{:=|m\rangle} + \underbrace{|1,l\rangle}_{:=|n\rangle}\Big). \tag{6.31}$$

As previously, we analyze the evolution of the density matrix elements $w_{n,n}(t)$ and $w_{n,m}(t)$ in order to determine τ_{relax} and τ_{decoh}. Figure 6.3 b) depicts the calculated ratios $\tau_{\text{decoh}}/\tau_{\text{relax}}$ for various superpositions and compares the results to the approximations by means of equation (6.29) and (6.30).[5] The calculations do not reveal a qualitative difference between the coherence loss in one and two dimensions. As before, the evolution of $\tau_{\text{decoh}}/\tau_{\text{relax}}$ can be (at least qualitatively) explained in terms of relaxation and heating processes.

Moreover, the agreement is remarkably good at zero temperature. This is due to the fact that the time-dependent coupling terms in equation (6.21) oscillate for the two-dimensional calculations

[5] The calculations in two dimensions include less modes along each direction than in one dimension as the computational effort of equation (6.21) scales as (total number of modes)^4.

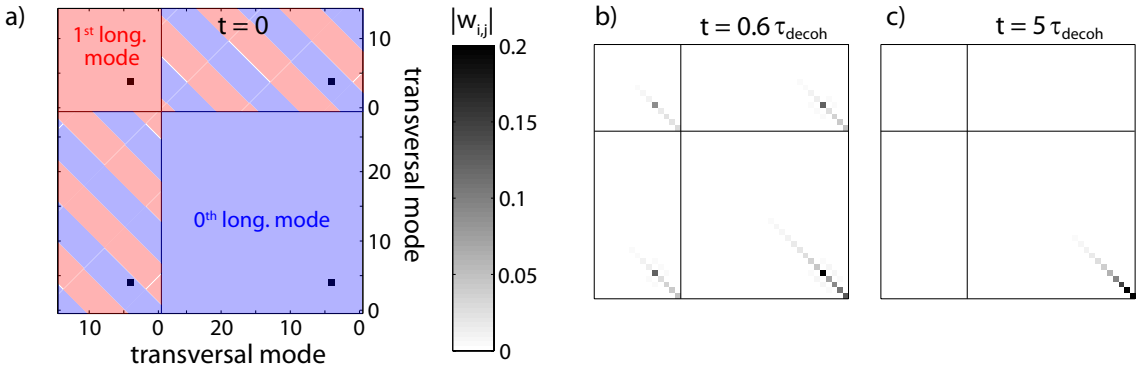

Figure 6.4.: a) Representation of $\frac{1}{\sqrt{2}}(|0,4\rangle + |1,4\rangle)$ as density matrix w. The blue shaded area corresponds to the transversal modes in the longitudinal ground state and the red shaded area to the modes in the first excited state. The density matrix is asymmetric as it contains all modes up to $140\,\mathrm{kHz}$ ($\omega_{\mathrm{trans}} = 2\pi\,5\,\mathrm{kHz}$, $\omega_{\mathrm{long}} = 2\pi\,70\,\mathrm{kHz}$). The red-blue shaded regions represent the matrix elements accounting for the coherence between the longitudinal ground and excited state. b) and c) Density matrix at later evolution times ($\rho_0 = 4 \cdot 10^{14}\,\mathrm{cm}^{-3}$, $T = 550\,\mathrm{nK}$). b) The initial coherence decays, but is for transversal relaxation and heating processes partly preserved. c) After long evolution times, no coherences are left. Because of the finite temperature, the lithium atom does not completely relax to the transversal ground state.

due to the larger energy splitting between the harmonic oscillator modes faster than the time scale of the relaxation and decoherence processes. Hence, their contribution to the dynamics of the lithium atom averages to zero and we get effectively a rotating wave approximation. The only remaining coupling terms are those which are responsible for the relaxation rates. Thus, we get a perfect agreement between the numerical calculation and the approximation on the basis of the relaxation rates. For finite temperature, the agreement is not as good because the heating processes counteract the relaxation processes and vice versa. This leads to a slightly non-exponential evolution of the density matrix elements, whereas the derivation of equation (6.30) assumes an exponential coherence and population decay.

Dynamics in the Longitudinal Direction

Up to now, our analysis of the dynamics in the two-dimensional harmonic oscillator potential based on the evolution of the single density matrix elements $w_{m,n}(t)$ and was consistent with our interpretation by means of the relaxation and heating processes. Experimentally we do not resolve the evolution along the transversal directions, but only detect the evolution along the longitudinal direction. Hence, we observe the dynamics of multiple $w_{m,n}(t)$'s at once.

Figure 6.4 a) illustrates this fact by coloring the elements of the density matrix w of the state $\frac{1}{\sqrt{2}}(|0,4\rangle + |1,4\rangle)$ with respect to the longitudinal modes. The evolution of this density matrix is displayed in figure 6.4 b) and c) and shows an interesting feature concerning the decay of motional coherences. According to figure 6.4 b), the initial off-diagonal element, which accounts for

the coherence between the ground and first excited state along the longitudinal direction, decays but the occupation of other off-diagonal elements increases. Thus, the relaxation and heating processes along the transversal directions do not necessarily imply a loss of coherence. This behavior stems from the fact that both superposition modes interact mutually with the bosonic bath, i. e. the matrix elements which couple the involved transversal modes agree for the longitudinal ground and excited state in sign and magnitude.

The preservation of the coherence in presence of interaction processes is not an exclusive characteristic of the bosonic bath, but has also been shown for ions exposed to a light field [79] and molecules immersed in a solvent [80, 81]. The common feature of all these systems is that the energy scale of the interaction processes is either larger (ion) or lower (molecule, bosonic bath) than the energy gap between the superposition modes. In case of the bosonic bath, most relaxation or heating processes along the transversal direction involve a Bogoliubov excitation whose wavelength is larger than the extent of the longitudinal wavefunctions. Thus, the excitation cannot resolve the difference between the longitudinal ground and excited state, and the corresponding matrix elements are almost identical.

In terms of a measurement process, the elementary excitation does not carry any information about the occupied longitudinal modes and their coherence is preserved. In contrast, excitations with shorter wavelengths correspond to an effective measurement of the longitudinal superposition which causes the loss of coherence.

In the following, we investigate the impact of the transversal on the longitudinal dynamics more systematically and determine the decoherence time τ_{decoh} with respect to the coherence between the longitudinal ground and excited state. For this purpose, we analyze the evolution of all off-diagonal density matrix elements

$$\sum_{l_0, l_1} w_{l_0, l_1}(t) \quad \text{with} \quad |l_i\rangle = |i, l\rangle \tag{6.32}$$

which leave the longitudinal mode unchanged (red-blue shaded area in figure 6.4 a)). In analogy, we get the relaxation time τ_{relax} from the population of the excited longitudinal mode (diagonal of the red shaded area in figure 6.4 a))

$$\sum_{l_1} w_{l_1, l_1}(t). \tag{6.33}$$

Figure 6.5 depicts the corresponding ratios of the decoherence and relaxation time $\tau_{\text{decoh}}/\tau_{\text{relax}}$ for the same scenarios as displayed in figure 6.3 b). As before, the ratio yields in case of zero temperature and for the occupation of the transversal ground state a factor of 2. But $\tau_{\text{decoh}}/\tau_{\text{relax}}$ drops for occupation of higher transversal modes much slower as previously. This behavior is consistent with our earlier interpretation which stated that the dynamics in transversal directions do not necessarily imply a coherence loss if low energetic Bogoliubov excitations are involved. Our explanation is further supported by the fact that the ratio decreases for higher transversal modes whose relaxation induces elementary excitations with higher energies. Because of the corresponding smaller wavelength, these excitations start resolving the wavefunction in longitudinal direction and cause a loss of coherence. Overall, the results reveal that the coherence decay is mostly governed by longitudinal dynamics as the ratio of $\tau_{\text{decoh}}/\tau_{\text{relax}}$ stays close to 2.

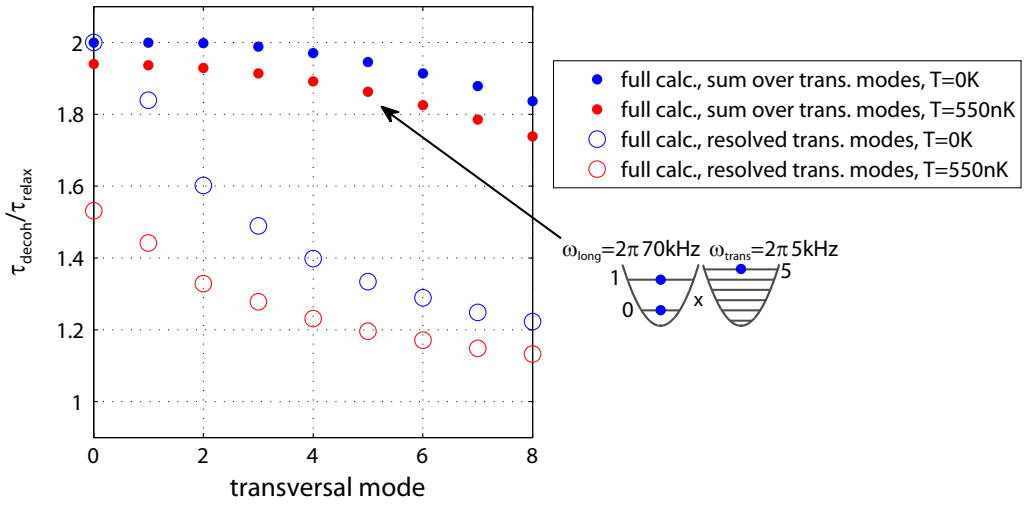

Figure 6.5.: Ratio of decoherence time τ_{decoh} and relaxation time τ_{relax} for a two-dimensional harmonic potential ($\omega_{\mathrm{trans}} = 2\pi\,5\,\mathrm{kHz}$, $\omega_{\mathrm{long}} = 2\pi\,70\,\mathrm{kHz}$, $\rho_0 = 4 \cdot 10^{14}\,\mathrm{cm}^{-3}$). The graph compares the results for the evolution of the single matrix elements (circles) with the analysis which considers the dynamics in longitudinal direction (dots). In the latter case, $\tau_{\mathrm{decoh}}/\tau_{\mathrm{relax}}$ is larger as the transversal dynamics do not necessarily imply a loss of coherence in the longitudinal direction.

Moreover, our considerations also hold for the finite temperature calculations which are also displayed in figure 6.5. The corresponding ratios of the decoherence and relaxation time $\tau_{\mathrm{decoh}}/\tau_{\mathrm{relax}}$ are slightly lower but follow qualitatively the zero temperature results. Compared to the calculations considering the single density matrix elements, the impact of the heating processes is much less severe. This is due to the fact that the involved elementary excitations have rather small energies ($k_{\mathrm{B}}T/h = 11\,\mathrm{kHz}$).

Concluding Remarks

In this chapter, we theoretically investigated the impact of a bosonic bath on the evolution of a single impurity confined in a harmonic potential. In this context, we studied the relaxation processes of a motionally excited lithium atom by means of Fermi's golden rule. Our considerations showed that the population decay depends on the transversal confinement as it affects both the available relaxation channels and the corresponding coupling strengths. Moreover, we explored the loss of motional coherence due to interaction between the impurity and the bosonic bath on the basis of the master equation. For the one-dimensional harmonic potential, our results agreed well with the approximations according to the relaxation and heating processes. Though, for the two-dimensional potential, the interpretation of our calculations was more involved. In this case, the coherence in the longitudinal direction is much less affected by the transversal dynamics. This feature originates from the separation of the involved energy scales and leads to an overestimation of the decoherence mechanisms by means of the heating and relaxation processes. Hence,

the relaxation and heating rates can only serve as a pessimistic estimate for the decoherence time.

In the following chapters, we apply our theoretical considerations in order to analyze our measurements of the population decay and the loss of motional coherence of lithium atoms immersed in a sodium background.

7. Relaxation Dynamics of Lithium

After the theoretical discussion in the last chapter, we investigate the impact of the sodium bath on the dynamics of the lithium atoms in the following experimentally. In analogy to our previous considerations, the investigation is divided into two parts. This chapter considers the relaxation process of motionally excited lithium atoms, whereas the subsequent chapter studies the loss of motional coherence due to the interaction between the lithium and sodium atoms.

First, we introduce the experimental procedure which is used in order to induce and investigate the relaxation between the first and second band of the longitudinal lattice potential. Subsequently, we analyze the relaxation dynamics or respectively the population decay by means of the band populations and band fractions. In this context, we develop a model which accounts for the inhomogeneities of the bosonic background and compare it to the observed relaxation dynamics. At the end of the chapter, we test our understanding of the population decay and the theory developed in the previous chapter, and explore the relaxation dynamics for different depths of the longitudinal lattice potential. The data which is presented throughout this chapter is obtained for experiments in the one-dimensional longitudinal lattice potential. However, the developed data analysis also applies to relaxation measurements in higher dimensional lattice potentials.

7.1. Experimental Procedure

In order to study the relaxation of motionally excited lithium atoms due to the interaction with the bosonic bath, we excite the lithium atoms to the second Bloch band of the longitudinal lattice potential and investigate the subsequent evolution of the band populations. The excitation of the lithium atoms is achieved by periodic modulation of the lattice position, more precisely by a π-pulse discussed in the context of the Rabi oscillations and the spin echo spectroscopy (chapter 5). If the sodium atoms are removed before the excitation pulse, we do not observe an increasing atom number in any of the Bloch bands and thus no dynamics between the different bands. This is due to the fermionic nature of the lithium atoms which suppresses the redistribution of energy between the lithium atoms at ultracold temperatures and hence the transition to energetically lower states.

Figure 7.1 depicts the typical evolution of the band populations in the sodium background and a one-dimensional lattice potential ($V_0 = 33\, E_{\mathrm{rec}}$). We observe a decay of the atom number in the second band, whereas the atom number in the first band rises. This is a clear signature of a relaxation process from the second to first the band. We also notice that the number of atoms in the third band is small compared to the total atom number and that the corresponding atom fraction decreases from $6\,\%$ ($1 \cdot 10^4$ atoms) to $3\,\%$ ($3 \cdot 10^3$ atoms) during the relaxation measurement. We attribute the finite population of the third band to imprecisions of our excitation scheme as the fraction of atoms in the third band amounts to $3\,\%$ prior to the excitation pulse. However, in the

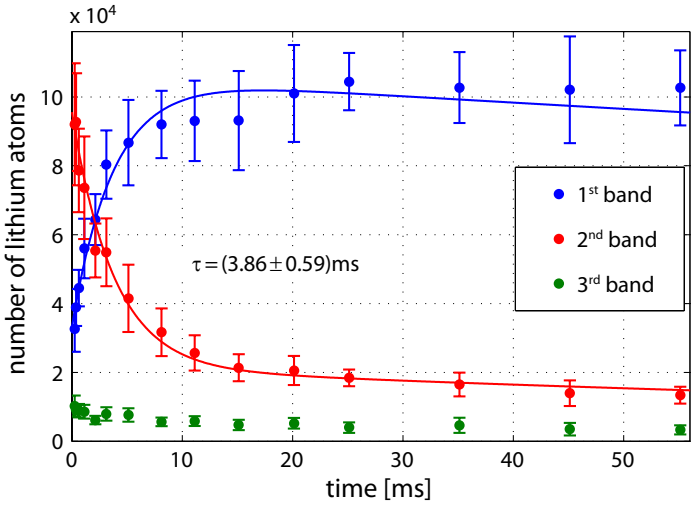

Figure 7.1.: Band populations of the lithium atoms evolving in a sodium bath ($\bar{N}_{\mathrm{Na}} = 6.9 \cdot 10^5$, $\bar{N}_{\mathrm{Li}} = 1.3 \cdot 10^5$). The increasing lithium atom number in the first and the decreasing atom number in the second band document the relaxation process. The solid lines are the solution of the rate equations (eq. (7.1), (7.2)) fitted to the data and yield a relaxation time of $\tau = (3.86 \pm 0.59)$ ms.

following analysis of the relaxation dynamics, we do not account for the atoms in the third band as the corresponding population is below the statistical uncertainties for the populations in the first and second band.

7.2. Analysis of the Relaxation Dynamics

In the previous chapter, we discussed the relaxation dynamics from the theoretical point of view and found a constant decay rate and hence an exponential decay of the band populations in the limit of vanishing temperature and constant bath density. Though, we need to modify this model in order to describe our experiments correctly. In this context, we have to account for the inhomogeneity of our system and the finite life time of the lithium atoms due to spontaneous emission. As the temperature of the sodium atoms ($T = 550\,\mathrm{nK} \mathrel{\hat{=}} 11\,\mathrm{kHz}$) is well below the energy gap between the first and second band ($\Delta E_{1\text{-}2}/h = 70\,\mathrm{kHz}$), we do not expect thermal excitations to the second band and neglect heating effects (see fig. 6.2).

7.2.1. Rate Equations for the Band Populations

In the following, we adjust our theoretical model stepwise to our experimental conditions. First, we take the finite life time of the lithium atoms in the optical lattice into account but neglect the experimental inhomogeneities. According to this simplification, the relaxation rate γ is for all excited lithium atoms identical and the band populations can be described by a set of rate

equations. The lithium atom number in the first Bloch band $N_1(t)$ rises at each point in time by the number of atoms relaxing from the second to the first band and decreases due to spontaneous emission processes

$$\frac{dN_1(t)}{dt} = \underbrace{\gamma N_2(t)}_{\text{relaxation}} \underbrace{-\gamma_1 N_1(t)}_{\substack{\text{spontaneous} \\ \text{emission}}} . \tag{7.1}$$

Here, $N_2(t)$ denotes the population in the second band and γ_1 the loss rate due to spontaneous emission. Accordingly, the atom number in the second Bloch band $N_2(t)$ changes by

$$\frac{dN_2(t)}{dt} = \underbrace{-\gamma N_2(t)}_{\text{relaxation}} \underbrace{-\gamma_2 N_2(t)}_{\substack{\text{spontaneous} \\ \text{emission}}} . \tag{7.2}$$

with γ_2 being the loss rate due to photon scattering for the second band. If we solve the coupled differential equations (7.1) and (7.2) with the boundary conditions $N_1(0) = N_{1,0}$ and $N_2(0) = N_{2,0}$, we get for the evolution of the band populations

$$N_1(t) = N_{1,0} e^{-t\gamma_1} + \frac{\gamma N_{2,0}}{\gamma + \gamma_2 - \gamma_1} e^{-t\gamma_1} \left(1 - e^{-t(\gamma+\gamma_2-\gamma_1)}\right) \tag{7.3}$$

and

$$N_2(t) = N_{2,0} e^{-t(\gamma+\gamma_2)}. \tag{7.4}$$

Figure 7.1 depicts the corresponding fit of these two equations to our experimental data. The fit is performed with $N_{1,0}$, $N_{2,0}$, γ and an additional offset for $N_2(t)$ as free parameters, whereas γ_1 and γ_2 are determined by independent life time measurements without the sodium background (section 4.5).

We expect that the life time of the lithium atoms in the lattice potential is identical with and without bosonic bath as the photon scattering does not depend on the type of the background. Moreover, the lithium atoms leave the sodium cloud within 200 µs due to the photon kick which is ten times faster than the time scale for the relaxation process. Hence, we can neglect the redistribution of the kinetic energy and the recapturing of lithium atoms by the sodium background. The additional offset parameter for the atom number in the second Bloch band is justified by the larger extent of the lithium atoms compared to the sodium cloud which prevents the relaxation of lithium atoms located outside of the sodium background.

The fit of equation (7.3) and (7.4) shows good agreement with the experimentally determined band populations and we get a relaxation rate of $\gamma = (259 \pm 36)\,\mathrm{s}^{-1}$, which corresponds to a decay time of $\tau = (3.86 \pm 0.59)$ ms. However, we also notice that the agreement becomes worse for long evolution times and that the shot to shot fluctuations of the band populations prevent a more accurate analysis of the relaxation dynamics.

7.2.2. Analysis of the Relative Band Populations

Identical Relaxation Processes

In the following, we investigate the relaxation on the basis of the relative instead of the absolute band populations. This approach allows a better analysis of our data as it is less sensitive to the

shot to shot variations of the lithium atom number. Moreover, the band fractions offer a more intuitive interpretation of our experimental results as the analogy to a spin system is more evident. Figure 7.2 depicts the decay of the atom fractions for the same data set as shown in figure 7.1. The error bars are in case of the band fractions much smaller than for the band populations which shows that the varying band populations are mostly due to fluctuations of the lithium atom number and not due to different bath preparations or other experimental imprecisions. Nevertheless, it is important to analyze the evolution of the band populations prior to the evolution of band fractions as the latter can also change due to loss processes as caused by spontaneous emission.

In order to determine the relaxation rate, we calculate the fraction of lithium atoms in the second band $f_{2\mathrm{nd}}(t)$ from equation (7.3) and (7.4)

$$f_{2\mathrm{nd}}(t) = \frac{N_2(t)}{N_1(t)+N_2(t)} = \frac{N_{2,0}e^{-t(\gamma+\gamma_{\mathrm{rel}})}}{N_{1,0}+\frac{\gamma N_{2,0}}{\gamma+\gamma_{\mathrm{rel}}}\left(1-e^{-t(\gamma+\gamma_{\mathrm{rel}})}\right)+N_{2,0}e^{-t(\gamma+\gamma_{\mathrm{rel}})}}. \tag{7.5}$$

Here, $\gamma_{\mathrm{rel}} = \gamma_2 - \gamma_1$ denotes the relative loss rate between the second and first band because of spontaneous emission. Figure 7.2 b) displays the corresponding fit which yields the almost identical relaxation time $\tau = (3.81 \pm 0.35)\,\mathrm{ms}$ as for the fit to the band populations. As in the latter case, the fit is performed for a fixed relative loss rate γ_{rel} and an additional offset parameter. Moreover, $N_{1,0}$ and $N_{2,0}$ cannot be fitted independently as we have to fulfill the boundary

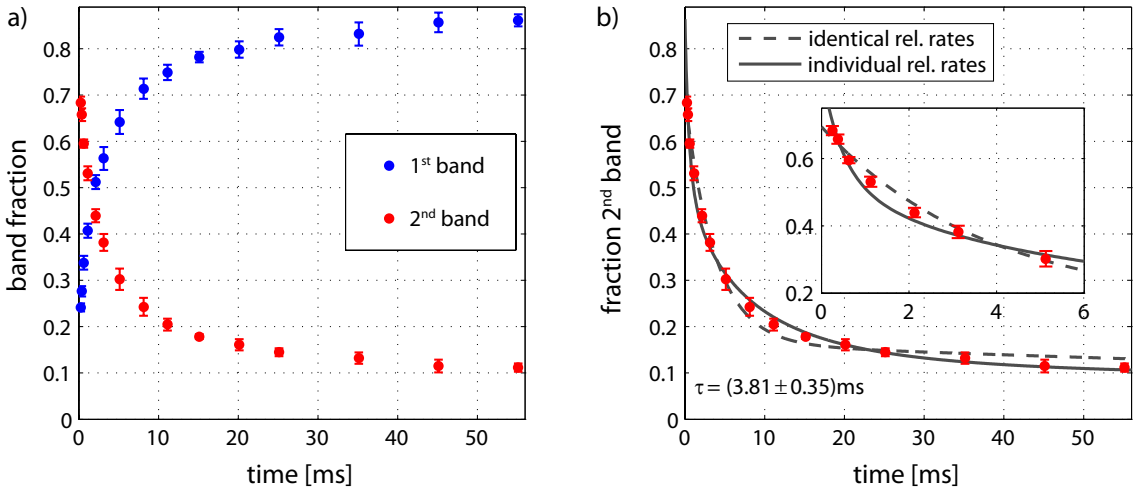

Figure 7.2.: a) Band fractions for the lithium atoms evolving in a sodium bath ($\bar{N}_{\mathrm{Na}} = 6.9 \cdot 10^5$, $\bar{N}_{\mathrm{Li}} = 1.3 \cdot 10^5$). b) Fits to the atom fraction in the second band assuming identical relaxation rates for all lithium atoms (dashed line, eq. (7.5)) and individual relaxation rates (solid line, eq. (7.10)). The latter model matches the data especially in the long term limit better and the corresponding $\chi^2_{\mathrm{red}} = 1.8$ is lower than for identical relaxation rates $\chi^2_{\mathrm{red}} = 2.9$. In case of identical relaxation processes, the fit yields a relaxation time of $\tau = (3.81 \pm 0.35)\,\mathrm{ms}$. The inset displays the relaxation dynamics for short evolution times.

condition $N_{1,0} + N_{2,0} = N_{\text{total}}$ with N_{total} being the total number of lithium atoms. Thus, we set $N_{1,0} = \eta N_{\text{total}}$ and $N_{2,0} = (1-\eta)N_{\text{total}}$, and we are left with η as fit parameter.

Beyond the agreement between the relaxation times determined by means of the band populations and band fractions, figure 7.2 b) also shows a second feature which is not as obvious from the band population data. Especially for long evolution times, the fit deviates from the experimental data and our simple model cannot account correctly for the decay in the long term limit. This deviation is due to the fact that our model involves only two time scales, namely the one given by the relative loss rate $1/\gamma_{\text{rel}}$ and the relaxation time $1/\gamma$. As the relaxation time is determined by the fast initial decay and the relative loss rate causes only a very slow decay, our model does not capture the decay for long evolution times correctly. This observation demonstrates that we need to include more than these two time scales in order to describe our data which means that not all lithium atoms relax with identical relaxation rates.

Individual Relaxation Processes

In the following, we discuss the most important reasons which cause non-identical relaxation rates for the lithium atoms and adapt our model to the most dominant effects. First of all, we regarded the lithium atoms during our previous considerations as single atoms and did not include their fermionic nature into our considerations. This approach is well justified in case of a deep three-dimensional lattice potential for which each single occupied lattice site can be considered independently. However, for the relaxation in a one-dimensional lattice potential, neglecting the fermionic properties of the lithium atoms seems to be a rather crude assumption as each lattice site is occupied by a few hundred fermions. Pauli blocking offers a plausible explanation for the slow-down of the relaxation dynamics because the lithium atoms gradually fill the first band which reduces the number of decay channels for the subsequent relaxation processes.

To determine if Pauli blocking is the relevant mechanism for the relaxation slow-down, we consider the central lattice for which the impact of the fermionic nature is most pronounced because of the large lithium atom number ($\approx 3 \cdot 10^3$ atoms). Pauli blocking has the strongest effect if all but one lithium atom relaxed to the first band and if these atoms occupy the decay channels with the highest relaxation rates. For this scenario, we obtain from equation (6.24) that the transition rate for the last atom is reduced by a factor of 4 compared to the relaxation rate without Pauli blocking.[1]

We observe that the relaxation processes in figure 7.2 slows down by more than a factor of 20 for long evolution times from which we conclude that the Pauli principle does not explain our observations. Moreover, our considerations set only a pessimistic upper bound for reduction of the relaxation rate as we discussed the central lattice site. Additionally, a more detailed investigation of the population decay shows that the lithium atoms do not permanently occupy the decay channels with the highest transition rates. Instead, the lithium atoms perform a cascading relaxation process which is illustrated in figure 7.3. During the first relaxation step, the lithium atoms dissipate on average an energy of $\bar{E}_{\text{dis}}/h \approx 40\,\text{kHz}$ and occupy subsequently excited transversal modes.[2]

[1] For this calculation, the last lithium atom occupies the 10^{th} excited mode in each transversal direction which corresponds to a transversal excitation energy of $15\,\text{kHz}$.

[2] The average of the dissipated energy is obtained by weighting the dissipated energy for all possible decay channels according to the corresponding relaxation rates (eq. (6.24), fig. 6.1 b)).

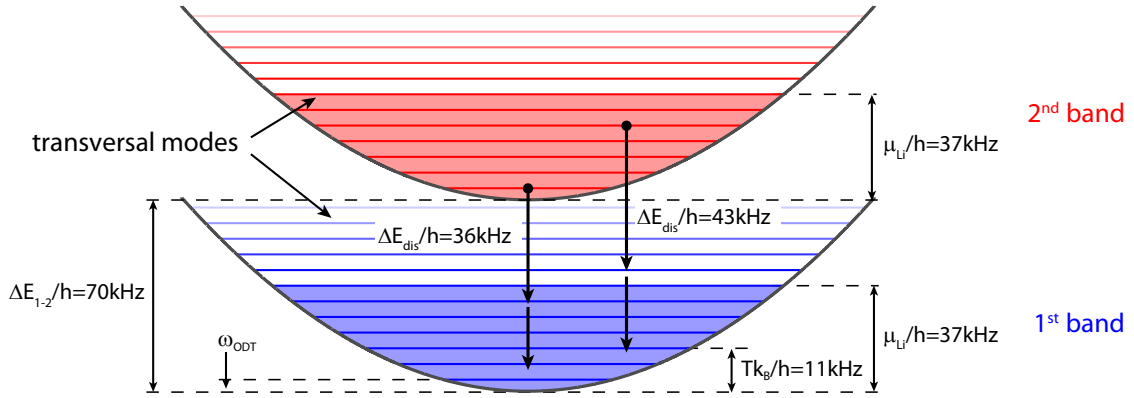

Figure 7.3.: Illustration of the energy scales during the relaxation process in two dimensions. The blue and red lines denote the transversal modes in the first and second band, respectively. The blue shading indicates the transversally occupied modes prior to the excitation pulse, whereas the red shading represents the occupation after the excitation. Depending on the initial mode, the lithium atoms dissipate during their first relaxation step different amounts of energy to the sodium bath and perform subsequently a second relaxation process.

As the energy of these modes is larger than the bath temperature ($(\Delta E_{1\text{-}2} - \bar{E}_{\mathrm{dis}})/h = 30\,\mathrm{kHz}$, $Tk_{\mathrm{B}}/h = 11\,\mathrm{kHz}$), the atoms perform a second relaxation step to less excited transversal modes. Since the second step occurs on the same time scale as the first one (figure 6.2), the atoms quickly leave the modes which have the highest rates for the transition from the second to the first band.

Thus, the impact of Pauli blocking on the relaxation dynamics is less severe than the estimated factor of 4, and the slow-down of the relaxation process is mainly caused by single particle effects. The most prominent reason for non-identical relaxation rates is the inhomogeneity of the bath density over the extent of the lithium cloud. For our experimental parameters, the lithium atoms probe a bath density which ranges from almost zero in the outer wings of the sodium cloud to the large densities in the center of the Bose-Einstein condensate. Thus, we observe an averaged relaxation process which depends on the location of the lithium atoms in the bosonic bath.

In contrast, the impact of the different initial conditions of the lithium atoms which populate different transversal modes is much less severe. The variation of the relaxation rates for the occupied transversal modes is well below 5 % (eq. (6.24)) and does not explain the slow decay of the band populations for long evolution times.

7.2.3. Relaxation Dynamics in the Inhomogeneous Bath

Subsequently, we include the density distributions of the lithium and sodium atoms into our considerations and test if the inhomogeneity of the bosonic bath explains the observed relaxation dynamics. For this purpose, we start from equation (7.5) and perform a further approximation in order to reduce the complexity of our calculations. As the relative loss rate γ_{rel}

($\gamma_{\text{rel}} = 1/\tau_{\text{rel}} \approx 5\,\text{s}^{-1}$) is for our experiments much lower than the relaxation rate γ ($\approx 250\,\text{s}^{-1}$), we can approximate $\frac{\gamma}{\gamma+\gamma_{\text{rel}}} \approx 1$ and get

$$f_{\text{2nd}}(t) = \frac{N_2(t)}{N_1(t) + N_2(t)} = \frac{N_{2,0} e^{-t(\gamma+\gamma_{\text{rel}})}}{N_{1,0} + N_{2,0}}. \tag{7.6}$$

To calculate the relaxation process in an inhomogeneous bath, we sum over the dynamics of the single lithium atoms [41]. For this purpose, we suppose that the relaxation rate is for each atom i time-independent, and we obtain for the atom fraction in the second band $f_{\text{2nd}}^{\text{inh}}(t)$ with individual relaxation rates

$$f_{\text{2nd}}^{\text{inh}}(t) = \frac{\sum_i e^{-t(\gamma_i+\gamma_{\text{rel}})}}{N_{1,0} + N_{2,0}}. \tag{7.7}$$

Here, the sum includes all lithium atoms which initially occupy the second band and the γ_i's denote the individual relaxation rates. As the energy which is dissipated during the relaxation process ($\bar{E}_{\text{dis}}/h \approx 40\,\text{kHz}$) is much larger than the chemical potential of the sodium atoms ($\mu_{\text{Na}}/h \approx 6\,\text{kHz}$), the relaxation rate is according to equation (6.24) proportional to the bath density $n_{\text{Na},i}$ at the position of the lithium atoms

$$\gamma_i = r n_{\text{Na},i} \tag{7.8}$$

with r being the relaxation constant. Because the lattice spacing is one order of magnitude smaller than the extent of the sodium cloud, we can approximate the sum in equation (7.7) by an integral. Moreover, we expect that the excitation to the second band is independent from the position of the lithium atoms as the detuning δ of the excitation pulse due to the inhomogeneity of the lattice potential is small compared to the Rabi frequency Ω ($\delta/\Omega < 0.25$). Hence, we can write the fraction in the second band in terms of the sodium $n_{\text{Na}}(\vec{r})$ and lithium density $n_{\text{Li}}(\vec{r})$

$$f_{\text{2nd}}^{\text{inh}}(t) = f_{\text{2nd}}^{\text{inh}}(0) \frac{\int n_{\text{Li}}(\vec{r}) e^{-t(r n_{\text{Na}}(\vec{r})+\gamma_{\text{rel}})}\,\mathrm{d}\vec{r}}{\int n_{\text{Li}}(\vec{r})\,\mathrm{d}\vec{r}}. \tag{7.9}$$

Though, for the one-dimensional lattice potential, equation (7.9) only holds for short evolution times as the lithium atoms probe for longer evolution times different bath densities in the transversal directions which means that the relaxation rates become time-dependent.

In the long term limit, the lithium atoms average over the bath density along the transversal directions since the relaxation time is a factor of two smaller than the time scale given by the transversal trapping frequencies. In this limit, we can modify equation (7.7) to

$$f_{\text{2nd}}^{\text{inh}}(t) = f_{\text{2nd}}^{\text{inh}}(0) \frac{\sum_j N_{\text{Li},j} e^{-t(r n_{\text{eff},j}^{\text{2d}}+\gamma_{\text{rel}})}}{\sum_j N_{\text{Li},j}}. \tag{7.10}$$

Here, the sum includes the lattice sites of the one-dimensional lattice and $N_{\text{Li},j}$ denotes the lithium atom number at site j. If the lattice axis points in x-direction, we get

$$N_{\text{Li},j} = \int_{x_j}^{x_{j+1}} \mathrm{d}x \int \mathrm{d}y \int \mathrm{d}z\, n_{\text{Li}}(\vec{r}) \;\text{ with }\; x_j = d_{\text{lat}}(j - 1/2). \tag{7.11}$$

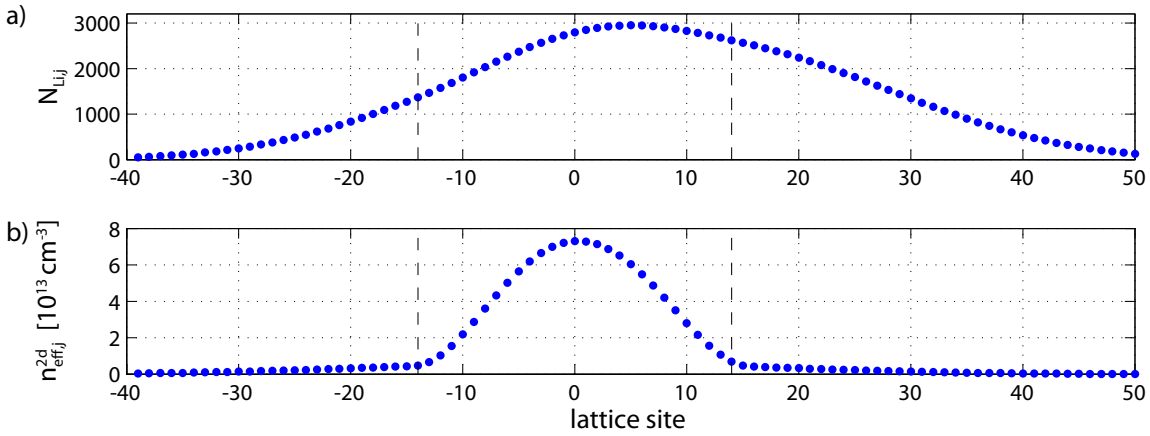

Figure 7.4.: a) Lithium atom number per lattice site in a one-dimensional lattice potential for $1.3 \cdot 10^5$ lithium, $6.9 \cdot 10^5$ sodium atoms and a condensate fraction of 66 %. The vertical dashed lines indicate the lithium atoms probing the Bose-Einstein condensate, which are about 55 % of all atoms. The asymmetry and the displacement arise from the different gravitational sag for sodium and lithium as well as the mean field potential created by the sodium atoms. b) Effective sodium density per lattice site.

Furthermore, $n^{2d}_{\text{eff},j}$ denotes the effective sodium density at site j which is probed by the lithium atoms

$$n^{2d}_{\text{eff},j} = \int_{x_j}^{x_{j+1}} \mathrm{d}x \int \mathrm{d}y \int \mathrm{d}z \, \frac{n_{\text{Li}}(\vec{r})}{N_{\text{Li},j}} n_{\text{Na}}(\vec{r}). \tag{7.12}$$

Figure 7.4 displays the calculated lithium atom number and the effective sodium density per lattice site (section 2.3.2) corresponding to the experimental conditions during the relaxation measurement shown in figure 7.1 and 7.2. These profiles exhibit the underlying mechanisms for the individual relaxation rates and for the different time scales of the relaxation process.

Shortly after the excitation to the second band, the lithium atoms which are centered in the Bose-Einstein condensate relax to the first band as they experience the largest sodium density. Hence, we observe a fast initial decay of the atom fraction in the second band. However, at some point, all of these atoms already relaxed to the first band, and the lithium atoms which are located in the wings of the Bose-Einstein condensate contribute most to the observed relaxation dynamics. Though, their band population changes slower due to the lower sodium density. Thus, we observe a relaxation process which gradually slows down. Moreover, the large difference between the relaxation rates in the beginning and the end of the dynamics stems from the large range of sodium densities probed by the lithium atoms.

In order to test our interpretation, we fit equation (7.10) with the calculated lithium atom number and the effective sodium density per lattice site to our experimental data. As for the identical relaxation rates, we are left with three fitting parameters, namely r, $f^{\text{inh}}_{\text{2nd}}(0)$ and an additional offset parameter. The result is displayed in figure 7.2 and matches the relaxation dynamics better than the fit for a homogeneous bath. Especially for long evolution times, the fit captures the

gradual slow-down of relaxation process more precisely which shows that the non-identical relaxation rates for the lithium atoms are caused by the inhomogeneities of the bosonic bath. But we also notice that the fit deviates from the experimental data for short evolution times as the assumptions leading to the effective density (eq. (7.12)) do not hold for short time scales.

7.3. Characterization of the Relaxation Dynamics

In the following, we employ our previous considerations in order to characterize the population decay and test our understanding of the relaxation process. For this purpose, we analyze the initial relaxation process instead of its whole evolution. The main reasoning for this approach is that we need to take the dynamics of the lithium in the transversal directions into account if we investigate the relaxation process for long time scales. For the derivation of equation (7.10), we argued that the dynamics in the transversal directions are about a factor of two faster than the relaxation process and we considered this fact by introducing the effective sodium density per lattice site. However, this concept is not properly valid for small evolution times as the lithium atoms do not have enough time to probe the whole sodium density distribution. This leads to systematic errors in our data evaluation. Though, if we restrict our investigations to the initial relaxation process, we can analyze the data on the basis of equation (7.9) as the lithium atoms experience for short evolution times only the local sodium density at their initial position.

Moreover, the impact of the relaxation dynamics on the sodium bath is for short evolution times smaller as less lithium atoms dissipate energy to the bath. We do not observe significant heating of the bosonic bath or loss of sodium atoms during the relaxation process, but we notice that the condensate fraction decreases after the relaxation dynamics, i. e. for times longer than $100\,\mathrm{ms}$, from 0.7 to 0.6. We attribute the delay between the dissipation of energy and the heating of the Bose gas to the slower thermalization processes of the sodium background. By restricting our investigations to the initial relaxation process, the effect on the bath is less pronounced and thus the back-action on the relaxation dynamics is smaller.

For short evolution times, we can expand equation (7.9) which yields

$$\begin{aligned} f_{\mathrm{2nd}}^{\mathrm{inh}}(t) &\approx \frac{f_{\mathrm{2nd}}^{\mathrm{inh}}(0)}{N_{\mathrm{Li}}} \int n_{\mathrm{Li}}(\vec{r})\,(1 - t(r n_{\mathrm{Na}}(\vec{r}) + \gamma_{\mathrm{rel}}))\,\mathrm{d}\vec{r} \\ &= f_{\mathrm{2nd}}^{\mathrm{inh}}(0)\Big(1 - t\gamma_{\mathrm{rel}} - tr \underbrace{\int \frac{n_{\mathrm{Li}}(\vec{r})}{N_{\mathrm{Li}}} n_{\mathrm{Na}}(\vec{r})\,\mathrm{d}\vec{r}}_{:=n_{\mathrm{eff}}}\Big). \end{aligned} \tag{7.13}$$

According to this equation, we expect that the initial relaxation of the population in the second band depends linearly on the density and hence the effective density n_{eff} of the bosonic bath. In case of a bosonic bath, this relation only holds if the excitations of the Bose gas which are induced during the relaxation process belong to the free-particle-like branch of the dispersion relation and not to the phonon-like part. This assumption is for our experimental parameters well justified as the energy dissipated during the relaxation process is much larger than the chemical potential of the bosonic bath. Thus, the induced Bogoliubov excitations belong to the free-particle regime of the dispersion relation. Figure 7.5 a) displays the atom fraction in the second band for a fixed

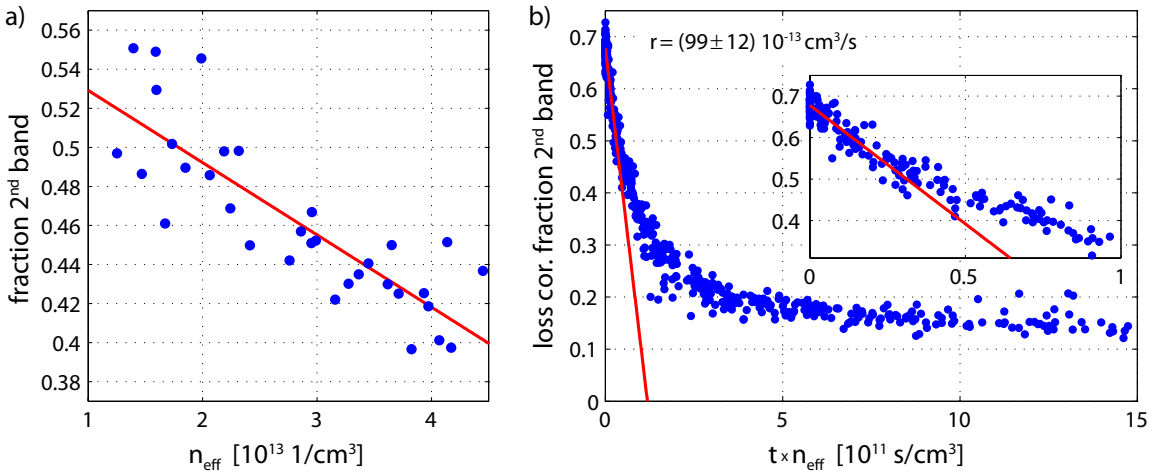

Figure 7.5.: a) Fraction of lithium atoms in the second band after 2 ms and for different effective sodium densities. The solid line depicts a linear fit to the data. b) The relaxation constant r is determined from a linear fit to the atom fraction in the second band, which is corrected for losses due to spontaneous emission, plotted versus the evolution time multiplied by the effective sodium density. The inset displays a zoom into the initial relaxation dynamics.

evolution time and for the same data set as before. The atom fraction is plotted versus the effective sodium density and shows the expected linear relationship which justifies the assumption experimentally.

Next, we study the relaxation dynamics for different lattice depths and change thereby the amount of dissipated energy. We extract for each lattice configuration the relaxation constant r and compare it to theory. In order to increase the accuracy of our evaluation, we rescale the data and analyze the dependency of the atom fraction in the second band on the time multiplied by the effective sodium density. For this purpose, we correct the atom fraction in the second band for spontaneous emission losses, which yields $f_{\mathrm{2nd}}^{\mathrm{inh}}(t)e^{t\gamma_{\mathrm{rel}}}$ or $f_{\mathrm{2nd}}^{\mathrm{inh}}(t)(1+t\gamma_{\mathrm{rel}})$ for the linear approximation, and we compute the effective sodium density for each data point. Figure 7.5 b) depicts the corresponding data for the one-dimensional lattice potential with $V_0 = 33\,E_{\mathrm{rec}}$ ($\Delta E_{1\text{-}2}/h = 70\,\mathrm{kHz}$). We get the relaxation constant from a linear fit to the initial decay which yields $r = (99 \pm 12) \cdot 10^{-13}\,\mathrm{cm}^3/\mathrm{s}$.

Figure 7.6 displays the relaxation constants for various lattice depths and compares them to theory (eq. (6.24)).[3] The graph documents that our calculations reproduce the observed relaxation rates for deep lattice potentials within the experimental accuracies and without any fit parameters. But we also notice a discrepancy for lower potentials. Moreover, we see that the theory depends for low lattice potentials on the bath density. This behavior indicates that our assumption considering the relaxation constant r as density-independent breaks down for small dissipated energies. But the deviation is not strong enough to account for the observed discrep-

[3] The relaxation constant is computed for the lowest transversal mode.

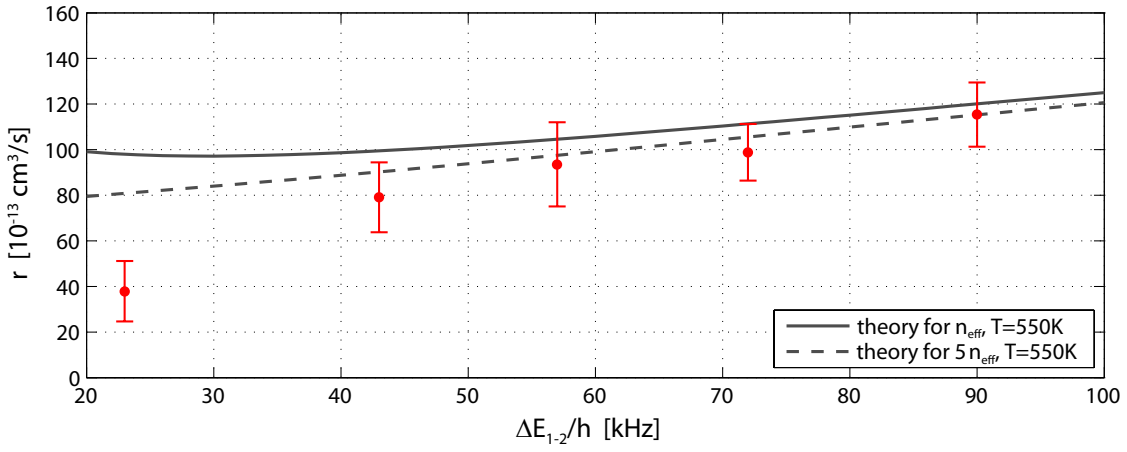

Figure 7.6.: Relaxation constant r for different one-dimensional lattice potentials characterized by the gap between first and second band $\Delta E_{1\text{-}2}$. The experimental values (red points) are for deep lattice potentials consistent with the theoretical calculations (gray lines, eq. (6.24)).

ancy for the data point at $\Delta E_{1\text{-}2}/h = 23\,\text{kHz}$. Hence, the deviation has to originate from other parameters which we discuss below.

- The impact of the species-selective lattice potential on the density of the sodium atoms cannot explain our observations as the reduction of the sodium density at each lattice site is for the deep lattices below $10\,\%$ [41]. This effect is barely on the order of our accuracy and is for low lattice depths, for which we observe the largest discrepancies between experiment and theory, even less severe.

- Also the uncertainties in the trapping frequencies and in the temperature determination cannot account for the observed discrepancies. Both parameters affect the precision of the density determination, but do not depend on the lattice depth.

- According to our previous discussion (section 7.2.2), the Fermi character of the lithium atoms has for lower lattice depths a larger impact on the relaxation dynamics. For the deep lattice potentials, we estimated that the relaxation rate could be reduced at most to $25\,\%$ of the single particle value due to Pauli blocking. Though, for low lattice depths, Pauli blocking becomes more important as the number of the possible decay channels decreases which provides an explanation for the deviation between the theoretical and experimental relaxation constant for the lowest investigated lattice depth.

Concluding Remarks

This chapter presented the relaxation of motionally excited lithium atoms due to interaction with the sodium atoms. In this context, we developed an understanding of the dynamics within the

bosonic bath and discussed the experimental parameters which are relevant for the data evaluation. We observed a non-exponential decay of the band populations for long evolution times which originates from the inhomogeneity of the bosonic bath. Moreover, we characterized the relaxation by means of the initial dynamics and demonstrated that the corresponding decay rates are, for deep lattice potentials, consistent with the theory presented in the previous chapter. In the subsequent chapter, we will make use of this knowledge in order to analyze the loss of motional coherence which is also induced by the interaction between the sodium and lithium atoms.

8. Interaction Induced Loss of Motional Coherence

In the following, we study the motional coherence of the lithium atoms during their evolution in the bosonic bath. For this purpose, we proceed in close analogy to the previous chapter and introduce at first the experimental procedure. In order to investigate the coherence loss, we apply the spin echo technique and analyze the impact of the sodium background on the dynamics of the lithium atoms by comparing the spin echo signal with and without bath. Subsequently, we adapt the relaxation model for the inhomogeneous bath to the loss of motional coherence, and determine the corresponding decay rate. The chapter concludes with the comparison of the characteristic time scales for the relaxation and decoherence processes. Both dynamics originate from the interaction between the bath and the immersed atoms as well as the large number of degrees of freedom of the bath [82], and we will investigate if the coherence loss and the relaxation dynamics are induced by the same underlying mechanics.

8.1. Experimental Procedure

To investigate the motional coherence of the lithium atoms in the bosonic bath, we prepare the lithium atoms in superpositions of states belonging to the first and second band, and probe the final states after different evolution times. For this purpose, we apply the spin echo technique which was introduced in section 5.3.

The corresponding measurement for a one-dimensional longitudinal lattice potential ($V_0 = 33\,E_{\mathrm{rec}}$) is shown in figure 8.1 a). The graph depicts the maxima and minima of the Ramsey fringes with and without bath for different evolution times. In contrast to the relaxation dynamics presented in the previous chapter, we cannot attribute the decay of the fringe amplitudes solely to the interaction between the sodium and lithium atoms as the Ramsey signal vanishes after long evolution times even without the sodium background. Hence, we compare the Ramsey signal with and without bosonic bath, and we observe a clear relative decay of the fringe amplitudes. For long evolution times, it is instructive to analyze the ratio between the amplitudes. The corresponding graph is shown in figure 8.1 b), and reveals that the ratio decreases monotonically. We assign the relative decay between the fringe amplitudes to the interaction between the lithium atoms and the bosonic bath and hence to the interaction induced loss of motional coherence.

In analogy to the relaxation, we consider the loss of motional coherence at first assuming identical dynamics for all lithium atoms. From our theoretical investigations, we expect that the coherence of the lithium atoms and hence the Ramsey fringe amplitude $a_{\mathrm{bath}}(t)$ decays in the bosonic bath exponentially

$$a_{\mathrm{bath}}(t) = a(t)e^{-t\gamma_{\mathrm{decoh}}}. \tag{8.1}$$

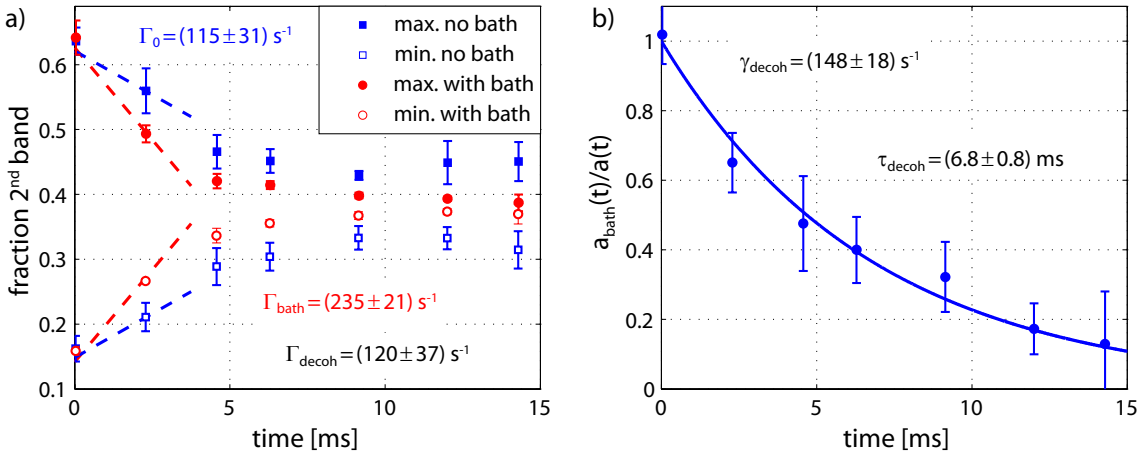

Figure 8.1.: a) Spin echo signal in the one-dimensional lattice ($V_0 = 33\,E_{\mathrm{rec}}$) for different evolution times. The presence of the bosonic bath reduces the Ramsey fringe amplitudes ($\bar{N}_{\mathrm{Na}} = 5.2 \cdot 10^5$, $\bar{N}_{\mathrm{Li}} = 2.1 \cdot 10^5$). The dashed lines indicate the initial decay of the fringe amplitudes and yield a decay rate of $\Gamma_0 = (115 \pm 31)\,\mathrm{s}^{-1}$ without and of $\Gamma_{\mathrm{bath}} = (235 \pm 21)\,\mathrm{s}^{-1}$ with bath which corresponds to an effective coherence loss rate of $\Gamma_{\mathrm{decoh}} = (120 \pm 37)\,\mathrm{s}^{-1}$. b) Ratio between the fringe amplitudes with and without bath $a_{\mathrm{bath}}(t)/a(t)$. The solid line displays an exponential fit which yields for the decoherence time $\tau_{\mathrm{decoh}} = (6.8 \pm 0.8)\,\mathrm{ms}$ and for the coherence decay rate $\gamma_{\mathrm{decoh}} = 1/\tau_{\mathrm{decoh}} = (148 \pm 18)\,\mathrm{s}^{-1}$.

Here, $a(t)$ denotes the fringe amplitude in absence of the bath and γ_{decoh} the decay rate of the motional coherence. Figure 8.1 b) depicts an exponential fit to the ratio of the amplitudes $a_{\mathrm{bath}}(t)/a(t)$ which yields a coherence decay rate of $\gamma_{\mathrm{decoh}} = (148 \pm 18)\,\mathrm{s}^{-1}$.[1]

Moreover, we note that we do not expect a significant impact of the bath on the efficiency of the spin echo technique as the lithium atoms in the first and second Bloch band probe for a deep lattice, i. e. low tunneling rates, the same bath density. Experimentally, we verified this assumption by performing Rabi oscillations and spectroscopy measurements with and without bosonic bath, but we do not observe different Rabi or resonance frequencies within our experimental precision. Thus, we can clearly attribute the relative decay of the spin echo signals to the interaction between the sodium and lithium atoms.

In contrast to the relaxation experiments, we do not have to include the different life times in the first and second band into our analysis as we automatically take care of this effect by comparing the evolution with and without bosonic bath. Furthermore, we do not observe a discrepancy between the coherence decay and the exponential fit. Though, this is due to the fact that the error bars of the amplitude ratio are larger than for the band fraction in the context of the relaxation

[1] Alternatively, we could also analyze the ratio of the visibilities. This approach yields the same coherence decay as we do not observe a different fringe offset for the measurements with and without bath.

dynamics. Additionally, we are not able to study the loss of motional coherence for evolution times beyond 20 ms, for which the deviation from an exponential decay was for the relaxation most evident, as the spin echo signal vanishes even without sodium background. However, we are aware that the inhomogeneities of the bosonic bath impact the relaxation dynamics of the lithium atoms. Hence, we adapt our analysis in the following to the inhomogeneities of our experiment in order to avoid systematic errors in the data evaluation.

8.2. Loss Rate of the Motional Coherence

We can analyze the loss of motional coherence in close analogy to the population decay in the inhomogeneous bath. The motional coherence of a certain lithium atom can be preserved, but the atom does not need to contribute to or it can even decrease the observed fringe amplitude due to dephasing mechanisms. We know from our investigation of the spin echo technique that high trapping frequencies are essential for long lasting spin echo signals (section 5.3.1). We explain this effect by reduced tunneling rates between neighboring lattice sites because of different offset potentials. In contrast to the related Wannier-Stark effect, the offset potential is for our dipole trap potential not identical for different lattice sites. Hence, we have to take into account that the contribution of the lithium atoms to the spin echo signal depends on their position in the trapping potential.

For this reason, we split the evolution of the fringe amplitude $a(t)$ in absence of the bath into the contributions $a_i(t)$ of the single lithium atoms

$$a(t) = \sum_i a_i(t) \text{ with } a_i(t) \in [-1/N_{\mathrm{Li}}, 1/N_{\mathrm{Li}}]. \tag{8.2}$$

Hence, the amplitude in presence of the bosonic bath $a_{\mathrm{bath}}(t)$ can be written as

$$a_{\mathrm{bath}}(t) = \sum_i a_i(t) e^{-t\gamma_{\mathrm{decoh},i}}, \tag{8.3}$$

where the $\gamma_{\mathrm{decoh},i}$'s are the coherence loss rates of the different lithium atoms. Experimentally we do not resolve the dynamics of the single atoms $a_i(t)$ as we detect the evolution of all atoms at once. However, for evolution times which are short compared to the time scales given by the tunneling rates and trapping frequencies, we expect that the lithium atoms evolve similarly, i. e.

$$a_i(t) \approx a_j(t) \tag{8.4}$$

for sufficiently small t. Thus, we investigate the loss of coherence for short evolution times, for which $a_i'(0) \approx a_j'(0)$, and expand equation (8.3) up to first order

$$\begin{aligned} a_{\mathrm{bath}}(t) &= \sum_i a_i(0) + t \sum_i \left(a_i'(0) - a_i(0)\gamma_{\mathrm{decoh},i} \right) + \mathcal{O}(t^2) \\ &\approx a(0) + ta'(0) - t\frac{a(0)}{N_{\mathrm{Li}}} \sum_i \gamma_{\mathrm{decoh},i}. \end{aligned} \tag{8.5}$$

In analogy to the relaxation dynamics, the lithium atoms probe during the early evolution only the sodium density at their initial position, and we get

$$\begin{aligned} a_{\text{bath}}(t) &\approx a(0)\Big(1 + t\underbrace{\frac{a'(0)}{a(0)}}_{:=-\Gamma_0} - t\underbrace{\int \frac{n_{\text{Li}}(\vec{r})}{N_{\text{Li}}}\gamma_{\text{decoh}}(\vec{r})\,\mathrm{d}\vec{r}}_{:=\Gamma_{\text{decoh}}}\Big) \\ &= a(0)\left(1 - t\Gamma_0 - t\Gamma_{\text{decoh}}\right). \end{aligned} \tag{8.6}$$

Here, Γ_0 denotes the decay rate of the spin echo signal in absence of the sodium background and Γ_{decoh} the effective coherence loss rate which is induced by the interaction between the sodium and lithium atoms.

In contrast to the population decay, we can in principle not assume that the coherence loss rate $\gamma_{\text{decoh}}(\vec{r})$ scales linearly with the bath density. This is due to the fact that the motional coherence can also be lost by relaxation and heating processes in the transversal directions which do not change the band population. These processes include low-energetic, phonon-like excitations of the Bose gas for which the coupling between the lithium and sodium atoms depends on the bath density. We have already noticed this effect in the context of the relaxation constant r which becomes for low-energetic excitations density dependent (see figure 7.6).

Hence, we do not characterize the loss of motional coherence by a density-independent decay constant, but introduce the effective coherence loss rate Γ_{decoh}. To obtain Γ_{decoh}, we analyze the envelope of the Ramsey fringes for small evolution times, and determine the decay rate with and without bath, $\Gamma_{\text{bath}} = \Gamma_0 + \Gamma_{\text{decoh}}$ and Γ_0, respectively . For this purpose, we fit the linear decay

$$\pm\, a_0\,(1 - \Gamma t) + b_0 \tag{8.7}$$

simultaneously to the fringe maxima (+) and minima (-). Here, a_0 refers to the initial fringe amplitude and b_0 to the fringe offset. As we do not observe a drift of the offset for the investigated time scales, we determine b_0 prior to the fitting procedure from the Ramsey fringes after long evolution times. Figure 8.1 a) depicts the initial decay of the fringe amplitudes.[2] We obtain a decay rate of $\Gamma_0 = (115 \pm 31)\,\mathrm{s}^{-1}$ in absence of sodium atoms and $\Gamma_{\text{bath}} = (235 \pm 21)\,\mathrm{s}^{-1}$ with bosonic bath. Hence, the interaction between the sodium and the lithium atoms leads to the loss of motional coherence at a rate of $\Gamma_{\text{decoh}} = (120 \pm 37)\,\mathrm{s}^{-1}$.

This result agrees with the decay rate $\gamma_{\text{decoh}} = (148 \pm 18)\,\mathrm{s}^{-1}$ which we determined by means of an exponential fit to the ratio of the amplitudes $a_{\text{bath}}(t)/a(t)$, and suggests that it is irrelevant if we analyze the coherence loss on the basis of the initial decay or the ratio of the amplitudes. Though, in the following, we compare the time scales of the coherence loss and the population decay to investigate the decoherence mechanisms. As we noticed for the relaxation dynamics a (small) discrepancy between our observations and an exponential decay, we stick to the evaluation of the coherence loss by means of the initial decay in order to analyze both dynamics on the same footing.

[2] We are aware of the fact that our fit does not provide a test for the linearity of the initial decay as it takes only two different evolution times into account. Though, the two parameters a_0 and Γ are not under-determined because we fit 4 independent data points at once (2 for the maxima and the minima).

8.3. Loss Mechanisms for the Motional Coherence

In this section, we investigate the mechanisms which cause the loss of motional coherence in the bosonic bath more closely and develop a microscopic picture of the decoherence processes. In this context, we adapt the considerations from our theoretical discussion in chapter 6 to our experimental conditions and interpret the coherence loss in terms of relaxation and heating processes. For this purpose, we compare the characteristic time scales of the population decay and of the coherence loss, and consider the dynamics in the one- and three-dimensional lattice potential. The latter offers a more intuitive interpretation of our observations as the dynamics in the transversal directions can be neglected. Though, spontaneous emission processes reduce the life time in the three-dimensional potential significantly and restrict thereby our experimental accuracy.

8.3.1. One-Dimensional Lattice Potential

In the following discussion, we distinguish between decoherence processes which originate from the population decay and processes which do not imply a population change as e. g. relaxation and heating processes in the transversal directions. As the lithium atoms are prepared in an equal superposition of states belonging to the first and second band, the population decay contributes only with half the relaxation rate to the loss of coherence, and we can write the effective coherence loss rate as

$$\Gamma_{\text{decoh}} = \frac{\Gamma_{\text{relax}}}{2} + \Gamma^*_{\text{decoh}}. \tag{8.8}$$

Here, Γ^*_{decoh} denotes the pure coherence loss rate which originates from population conserving processes, and $\Gamma_{\text{relax}} = rn_{\text{eff}}$ (eq. (7.13)) is the effective relaxation rate in analogy to the effective coherence loss rate Γ_{decoh}.

As previously, we characterize the dynamics of the lithium atoms by means of the ratio between the relaxation and decoherence time $\tau_{\text{decoh}}/\tau_{\text{relax}} = \Gamma_{\text{relax}}/\Gamma_{\text{decoh}}$. According to equation (8.8), the relaxation processes dominate the loss of coherence if $\tau_{\text{decoh}}/\tau_{\text{relax}} > 1$ and the dynamics are governed by pure decoherence processes if $\tau_{\text{decoh}}/\tau_{\text{relax}} < 1$.

To determine the characteristics of the coherence loss in the bosonic bath, we investigate the relaxation and the decoherence dynamics for the same experimental conditions. For this purpose, we post-select our data with respect to the number of sodium atoms as we extract Γ_{decoh} and Γ_{relax} from two independent measurements. Figure 8.2 a) displays the measurement of the effective coherence loss rate $\Gamma_{\text{decoh}} = (120 \pm 37)\,\text{s}^{-1}$, which we analyzed in the previous section, and figure 8.2 b) the corresponding relaxation dynamics for identical post-selection conditions which yield $\Gamma_{\text{relax}} = (168 \pm 26)\,\text{s}^{-1}$. Hence, we get for the pure coherence loss rate $\Gamma^*_{\text{decoh}} = (36 \pm 39)\,\text{s}^{-1}$ or respectively for the ratio between the relaxation and decoherence time $\tau_{\text{decoh}}/\tau_{\text{relax}} = 1.4 \pm 0.5$. Hence, the relaxation processes are the most dominant mechanism for the loss of motional coherence.

This behavior is qualitatively different from the observations in many spin systems. E. g. in nuclear magnetic resonance experiments[3] [84] or experiments investigating the dynamics of an ion immersed in a Bose-Einstein condensate [9], the ratio $\tau_{\text{decoh}}/\tau_{\text{relax}}$ is below 1 as population

[3] In NMR experiments, τ_{relax} is usually referred to as the longitudinal coherence time T_1 and τ_{decoh} as the transverse coherence time T_2 [83].

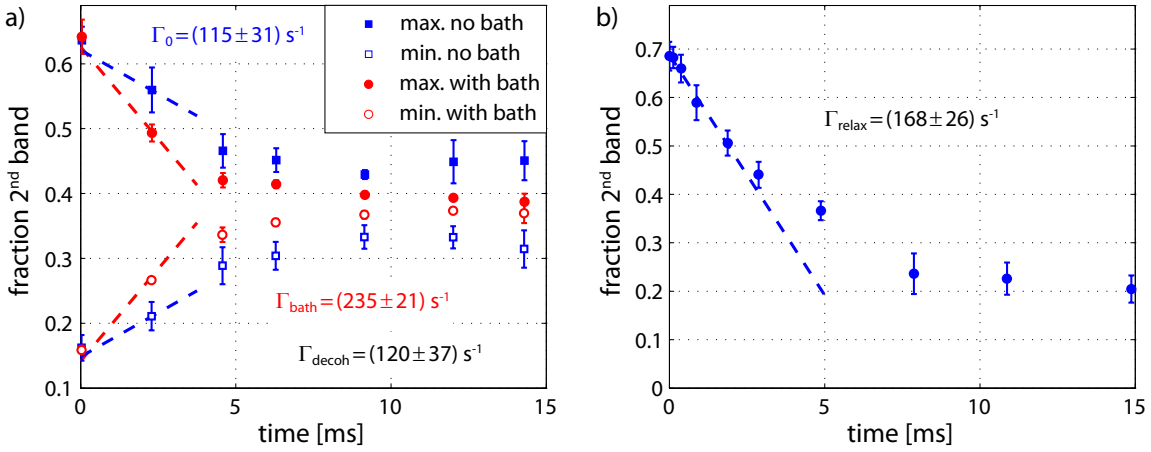

Figure 8.2.: Dynamics in a one-dimensional longitudinal lattice potential ($V_0 = 33\, E_{rec}$). a) Loss of motional coherence in a bosonic bath with $N_{Na} = (5.2 \pm 0.4) \cdot 10^5$ sodium atoms and a condensate fraction of $\eta = 0.59 \pm 0.06$ ($N_{Li} = (2.1 \pm 0.5) \cdot 10^5$). The dashed lines indicate the initial decay of the spin echo signals. b) Relaxation in a background of $N_{Na} = (5.3 \pm 0.4) \cdot 10^5$ sodium atoms and a condensate fraction of $\eta = 0.58 \pm 0.09$ ($N_{Li} = (1.8 \pm 0.4) \cdot 10^5$). The initial, linear decay is depicted as dashed line.

conserving spin-spin interactions dominate the loss of coherence. In contrast, the decoherence time is in case of spontaneous emission twice the relaxation time as both time scales are governed by the same mechanism [74].

Population Conserving Loss of Coherence

Our previous analysis showed that the population decay or respectively the relaxation processes are the dominant mechanism for the loss of motional coherence. But we also noticed that population conserving processes induce an additional coherence loss as $\tau_{decoh}/\tau_{relax} < 2$. According to the theoretical considerations in section 6.3, we attribute these processes to heating and relaxation processes in the transversal directions. Though, we cannot rigorously calculate $\tau_{decoh}/\tau_{relax}$ by means of equation (6.21) as the computational effort is for the one-dimensional lattice potential tremendous. For this reason, we estimate $\tau_{decoh}/\tau_{relax}$ on the basis of the relaxation and heating rates, and test if the result is consistent with our interpretation.

In the following, we adapt our previous discussion from section 6.3 to the more complex experimental situation which is illustrated in figure 8.3. We consider the dynamics of a single atom prepared in an equal superposition of the state $|m_1>$ belonging to the first band and the state $|m_2>$ belonging to the second band. Moreover, both states have the same transversal modes. In analogy to the derivation of equation (6.30), the effective relaxation rate is given by the sum over

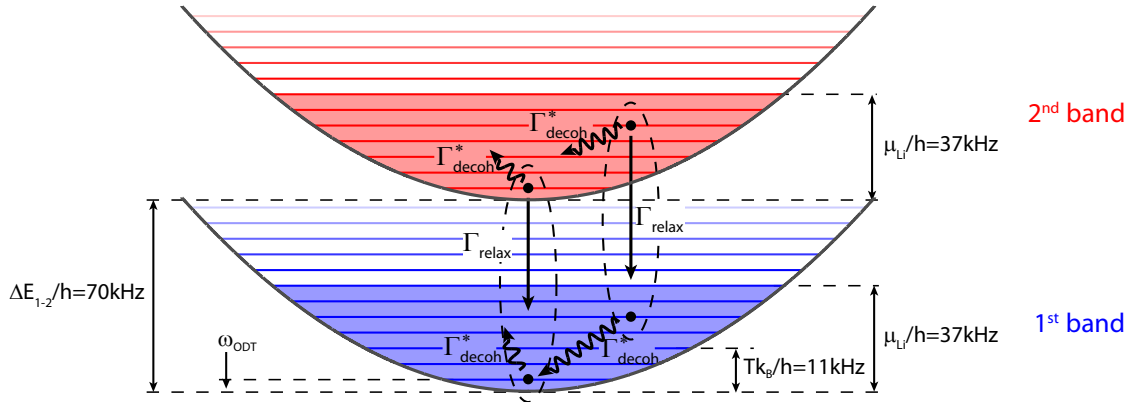

Figure 8.3.: Coherence loss and energy scales in two dimensions. The blue and red lines represent the transversal modes in the first and second band, and the shading indicates the occupied modes. The vertical arrows denote relaxation processes in the longitudinal direction, whereas the wiggled arrows mark transversal heating and relaxation processes. The superposition of two modes from the first and second band is indicated by the dashed ellipses.

the relaxation rates from state $|m_2>$ into the transversal modes $|n>$ of the first band (eq. (6.24))

$$\Gamma_{\text{relax}} = \sum_{n \in 1.\text{ band}} R_{m_2 \to n}. \tag{8.9}$$

Correspondingly, the pure coherence loss rate originates from the heating and relaxation processes which preserve the band population (eq. (6.24) and eq. (6.25))

$$\Gamma^*_{\text{decoh}} = \frac{1}{2} \sum_{n \in 1.\text{ band}} \left(R_{m_1 \to n} + H_{m_1 \to n} \right) + \frac{1}{2} \sum_{n \in 2.\text{ band}} \left(R_{m_2 \to n} + H_{m_2 \to n} \right). \tag{8.10}$$

Here, the factor $1/2$ takes care of the fact that the atom is prepared in a superposition of states belonging to the first and second band.

In order to calculate the ratio $\tau_{\text{decoh}}/\tau_{\text{relax}}$ by means of Γ_{relax}, Γ^*_{decoh} and equation (8.8)

$$\frac{\tau_{\text{decoh}}}{\tau_{\text{relax}}} = \frac{\Gamma_{\text{relax}}}{\Gamma_{\text{decoh}}} = \frac{2}{1 + 2\frac{\Gamma^*_{\text{decoh}}}{\Gamma_{\text{relax}}}}, \tag{8.11}$$

we have to take into account that the lithium atoms occupy different transversal modes and that the bath density varies over the extent of the lithium cloud. For this reason, we make several approximations.

- To reduce the complexity of the calculation, we approximate the occupation of the different transversal modes assuming zero temperature and according to the population of the different lattice sites (see figure 7.4). We calculate $\tau_{\text{decoh}}/\tau_{\text{relax}}$ for each occupied transversal

mode and compute the corresponding average. To test the sensitivity of the computed average on the occupied transversal modes, we manually divide the population of the lattice sites by 2. The result differs by 2 % from our former computation which indicates that our calculation is insensitive to the exact occupation of the transversal modes, and is hence not severely limited by the zero temperature approximation.

- We do not account for the inhomogeneity of the bosonic bath, but consider its peak density ($\rho_0 = 4 \cdot 10^{14}\,\mathrm{cm}^{-3}$, $T = 550\,\mathrm{nK}$). This approach corresponds to an underestimation of the low-energetic processes, which involve phonon-like excitations of the Bose gas, relative to the high-energetic processes (see inset of figure 6.2). Hence, we overestimate Γ_{relax} compared to $\Gamma^*_{\mathrm{decoh}}$ and get thereby an upper bound for $\tau_{\mathrm{decoh}}/\tau_{\mathrm{relax}}$.

According to these approximations, we obtain for the ratio between the decoherence and the relaxation time $\tau_{\mathrm{decoh}}/\tau_{\mathrm{relax}} = 0.5$ which is below our experimental observations and is not consistent within the statistical errors.

Our discussion in section 6.3 already showed that the calculation of the decoherence rate on the basis of the transversal heating and relaxation rates can only serve as a pessimistic estimate for $\tau_{\mathrm{decoh}}/\tau_{\mathrm{relax}}$. This follows from the fact that the low-energetic excitations of the Bose gas cannot resolve the wavefunctions in the longitudinal direction which preserves the motional coherence. In this context, we noticed that the impact of the temperature on the motional coherence is rather small as the ratio of $\tau_{\mathrm{decoh}}/\tau_{\mathrm{relax}}$ decreases from the zero temperature to the finite temperature calculations by less than 10 % (see figure 6.5). This observation suggests that the transversal heating and relaxation processes which involve a Bogoliubov excitation with an energy below $k_{\mathrm{B}}T$ have a negligible impact on the motional coherence in the longitudinal direction. Hence, we introduce this energy scale as a lower cut-off into our estimation for $\tau_{\mathrm{decoh}}/\tau_{\mathrm{relax}}$, and account only for transversal processes with higher energies.

In this case, we get $\tau_{\mathrm{decoh}}/\tau_{\mathrm{relax}} = 1.0$ which is consistent with our observations. Because of our approximations, the agreement does not identify the transversal relaxation and heating processes as only source for the population conserving loss of coherence. But the analysis shows that not each transversal process induces a coherence loss in longitudinal direction as the estimation without cut-off yields an upper bound for $\tau_{\mathrm{decoh}}/\tau_{\mathrm{relax}}$ which is well below our observations. According to our discussion in section 6.3, we attribute this behavior to the preservation of coherence by low-energetic transversal processes which imply a mutual interaction of the superposition modes.

Systematic Errors and Pauli Blocking

Our interpretation of the decoherence processes which conserve the population relies on the large discrepancy between the experimentally observed value $\tau_{\mathrm{decoh}}/\tau_{\mathrm{relax}} = 1.4 \pm 0.5$ and the theoretical estimate without energy cut-off $\tau_{\mathrm{decoh}}/\tau_{\mathrm{relax}} = 0.5$. We do not expect that our experimental precision or systematic errors can account for the discrepancy between theory and experiment. This is due to the fact that

- the determination of $\tau_{\mathrm{decoh}}/\tau_{\mathrm{relax}}$ is experimentally a robust approach as we compare two time scales relatively. Hence, we are not sensitive to the systematic errors in the determination of the atom numbers, bath temperature or trapping frequencies as these errors affect the relaxation and coherence loss measurement similarly.

- the determination of the relaxation and heating rates is insensitive to the different analysis approaches that means the rates determined by an exponential fit agree within the error bars with those obtained from a linear fit to the initial dynamics. Moreover, the effective relaxation rate (figure 8.2 b)) changes only by 12 % to $\Gamma_{\text{relax}} = (188 \pm 62)\,\text{s}^{-1}$ if we reduce the range of the linear fit by a factor of 2. This value is consistent with the former result, and indicates that the impact of the exact fit range on our analysis is negligible.

Our theoretical estimate is more uncertain than our experimental observations. We accounted for this fact by calculating an upper bound for $\tau_{\text{decoh}}/\tau_{\text{relax}}$. However, we considered the transversal relaxation and heating processes on the basis of single particles. This approach led in case of the relaxation dynamics to good agreement between the calculations and the experiment. For the motional coherence measurements, this procedure is not as plausible as for the relaxation measurements because of the different energy scales (see figure 8.3). More specifically, the transversal heating and relaxation processes involve the coupling to final states which are already populated by lithium atoms. This argument indicates that we overestimate the pure coherence loss rate $\Gamma^{*}_{\text{decoh}}$ as Pauli blocking partly suppresses the transversal processes.

To quantify the impact of this effect on the ratio $\tau_{\text{decoh}}/\tau_{\text{relax}}$, we insert Pauli blocking empirically into the calculation of $\Gamma^{*}_{\text{decoh}}$ [85]. For this purpose, we assume that all lithium atoms are in superpositions of states belonging to the first and second band. As each atom can be considered as a particle-hole-pair in the first and second band superimposed with a particle-hole-pair in the second and first band, the occupation probability of mode $|n>$ is governed by the Fermi-Dirac distribution $f(E_n)$ (eq. (2.20)) divided by 2. Here, E_n denotes the energy of $|n>$ according to the occupied transversal modes. Hence, the coupling to state $|n>$ is due to Pauli blocking suppressed by the factor $1 - f(E_n)/2$, and we get for the pure coherence loss rate (eq. (8.10))

$$\begin{aligned}\Gamma^{*}_{\text{decoh}} = &\frac{1}{2}\sum_{n\in\text{1. band}}\left(1-\frac{f(E_n)}{2}\right)\left(R_{m_1\to n}+H_{m_1\to n}\right)\\ &+\frac{1}{2}\sum_{n\in\text{2. band}}\left(1-\frac{f(E_n)}{2}\right)\left(R_{m_2\to n}+H_{m_2\to n}\right).\end{aligned} \tag{8.12}$$

The impact of Pauli blocking on the dynamics of the lithium atoms varies between the lattice sites due to their different occupations, and is most severe for the sites in the lattice center which are populated by the most lithium atoms. Thus, we consider the ratio between the decoherence and relaxation time with respect to the central site ($3 \cdot 10^3$ lithium atoms) as it provides an upper estimate for the effect of Pauli blocking and our calculations become less demanding. If we apply our previous approximations and estimate the corresponding mean ratio of $\tau_{\text{decoh}}/\tau_{\text{relax}}$ by means of equation (8.12) without energy cut-off, $\tau_{\text{decoh}}/\tau_{\text{relax}}$ increases for the central site from 0.5 without to 0.7 with Pauli blocking. This value is only slightly larger than our previous estimate and shows that we cannot resolve the discrepancy between our observations and the theoretical estimate without energy cut-off by means of Pauli blocking.

8.3.2. Three-Dimensional Lattice Potential

So far, we attributed the population conserving loss of coherence solely to the transversal heating and relaxation processes. To test our assignment, we investigate the evolution of the lithium

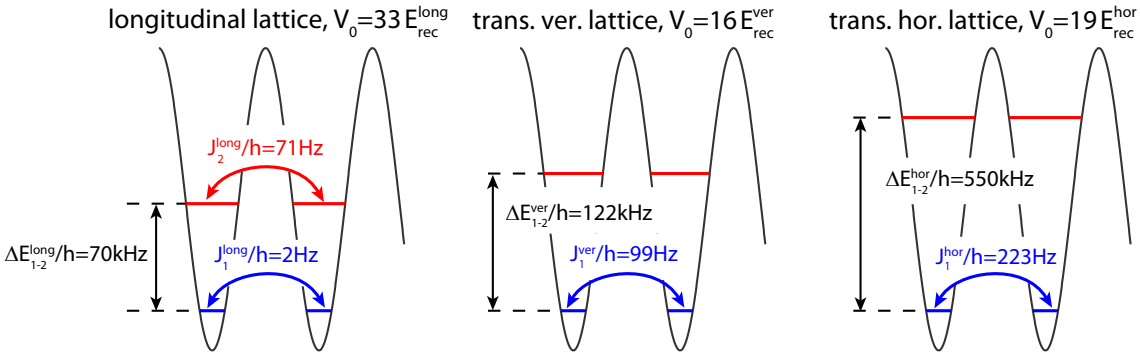

Figure 8.4.: Band gaps and tunneling rates of the three-dimensional lattice potential

atoms in a deep three-dimensional lattice potential as illustrated in figure 8.4. The lattice geometry is chosen such that the band gaps in the transversal directions exceed the gap in longitudinal direction. Moreover, the tunneling rates in the transversal directions are slow compared to the investigated evolution times, and the temperature of the Bose gas is more than a factor of five smaller than the band gap in the longitudinal direction ($\Delta E_{1\text{-}2}^{\text{long}}/h = 70\,\text{kHz}$, $k_\text{B}T/h = 11\,\text{kHz}$). Hence, we can neglect transversal relaxation and heating processes, and we expect that the relaxation processes along the longitudinal direction dominate the evolution of the lithium atoms.

Additionally, only lattice sites which are initially populated by exactly one lithium atom contribute to the observed dynamics. This follows from the fact that the first excited mode of each lattice site corresponds to an excitation along the longitudinal lattice direction. As the sodium background prepares the lithium atoms during the lattice loading in the energetically lowest modes, higher occupation numbers automatically imply an occupation of the first and second band of the longitudinal lattice. Hence, Pauli blocking prohibits for multiply occupied sites dynamics between the first and second band, and we do not have to account for many body effects between the lithium atoms.

Overall, we can interpret the three-dimensional lattice as a set of two-level systems whose dynamics are governed by the relaxation processes from the excited to the ground states. In this case, our theory (eq. (6.21)) predicts that the ratio between the decoherence and relaxation time is given by $\tau_\text{decoh}/\tau_\text{relax} = \Gamma_\text{relax}/\Gamma_\text{decoh} = 2$ as for the two-level atom which couples to the vacuum modes.

Figure 8.5 a) depicts a measurement for the loss of motional coherence in the three-dimensional lattice potential. As for the one-dimensional case, we observe a decay of the Ramsey fringe amplitudes due to the bosonic background. The decay rates of the spin echo signal with and without sodium background yield an effective coherence loss rate of $\Gamma_\text{decoh} = (102 \pm 90)\,\text{s}^{-1}$.

The statistical uncertainties for the coherence loss are about three times as larger as for the one-dimensional lattice which is mainly caused by two factors. The first contribution stems from the shorter lithium life time due to spontaneous emission which leads to lower atom numbers and hence to higher inaccuracies in the determination of the band populations. The second factor

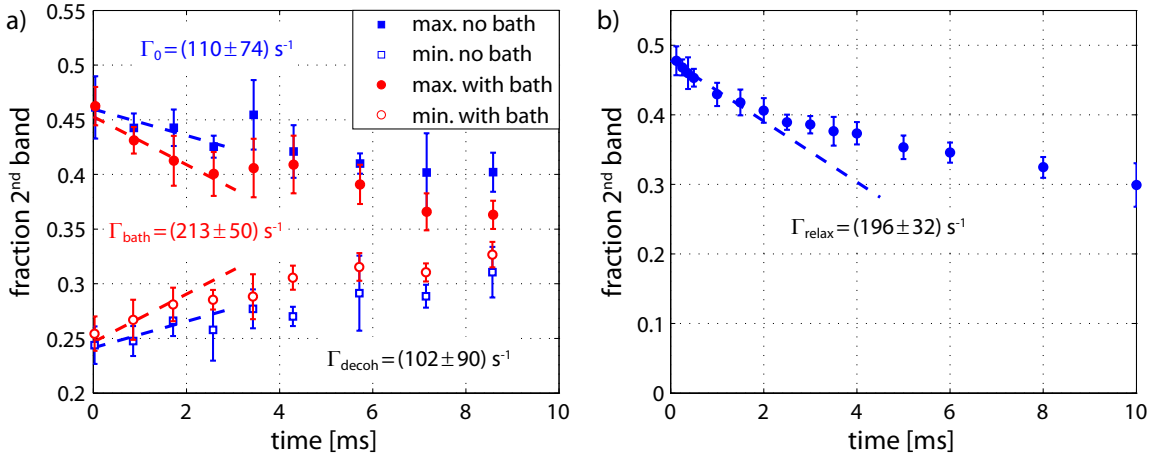

Figure 8.5.: Dynamics in a three-dimensional lattice potential a) Coherence loss in the sodium background ($N_{\mathrm{Na}} = (3.0 \pm 0.4) \cdot 10^5$, $N_{\mathrm{Li}} = (8.3 \pm 2.1) \cdot 10^4$). The dashed lines denote the initial decay of the spin echo signals. b) Relaxation with the same number of sodium atoms ($N_{\mathrm{Na}} = (3.0 \pm 0.5) \cdot 10^5$, $N_{\mathrm{Li}} = (9.8 \pm 1.9) \cdot 10^4$). The initial decay is depicted as dashed line.

originates from lattice sites which are occupied by more than one lithium atom. After the lattice loading, we observe an atom fraction of about 0.26 in the second band which cannot be transferred to the first band because of Pauli blocking. Because of the increase of 0.16 compared to the experiments in the one-dimensional lattice, we expect that the initial fringe amplitude decreases by 0.32 as the lithium atoms in doubly occupied lattice sites do not contribute to the spin echo signal. This value is consistent with the observed fringe amplitudes and corresponds to a lower visibility which leads to larger uncertainties in the determination of the coherence loss rate.

We compare the effective coherence loss rate to the corresponding effective relaxation rate whose measurement is displayed in figure 8.5 b). In analogy to the one-dimensional lattice potential, the presented data is post-selected with respect to the atom numbers. The initial decay of the atom fraction in the second band yields an effective relaxation rate of $\Gamma_{\mathrm{relax}} = (196 \pm 32)\,\mathrm{s}^{-1}$.

Hence, we get for the ratio of decoherence and relaxation time $\tau_{\mathrm{decoh}}/\tau_{\mathrm{relax}} = \Gamma_{\mathrm{relax}}/\Gamma_{\mathrm{decoh}} = 1.9 \pm 1.7$. This results is consistent with our calculations but does not provide a stringent test as the time scale for the loss of motional coherence is within the uncertainties as fast as the relaxation dynamics. Moreover, we cannot make a more precise statement about the mechanisms for the coherence loss than in the case of the one-dimensional lattice potential. Nevertheless, the result reveals that the relaxation processes also dominate the loss of motional coherence in the three-dimensional lattice since the coherence loss does not occur on a faster time scale than the population decay ($\Gamma_{\mathrm{decoh}} \lesssim \Gamma_{\mathrm{relax}}$) .

Concluding Remarks

In this chapter, we studied the loss of motional coherence due to the sodium background in the one- and three-dimensional lattice, and determined the characteristic time scale from the initial coherence decay. To investigate the underlying mechanisms, we compared the dynamics of the coherence loss with the population decay which showed that the relaxation processes are the dominant loss mechanism. For the one-dimensional lattice, our analysis revealed that the population decay is not the only relevant processes. For this reason, we estimated the ratio between the decoherence and relaxation time by means of Fermi's golden rule, and tested if transversal relaxation and heating processes explain our observations. In this context, we found that the motional coherence decays slower than estimated which we attributed to the conservation of coherence by low-energetic transversal processes.

9. Conclusion and Outlook

In the course of this thesis, we investigated the dynamics of fermionic impurities immersed in a Bose gas and set the foundations for future polaron experiments. For this purpose, we designed and implemented a species-selective lattice potential for the lithium atoms. The control of the lattice position enables us to address the atoms' motional degrees of freedom and periodic displacement of the lattice potential induces Rabi oscillations between the first and second Bloch band.

We utilized this coherent coupling in order to prepare the lithium atoms in a superposition of states belonging to the two lowest Bloch bands and probed their subsequent evolution by a Ramsey technique. This approach allowed us to determine the band gap $\Delta E_{1\text{-}2}$ in the deep lattice regime within $0.2\,\%$ which sets the detection limit for future polaron experiments on the basis of the effective mass m_{eff} to $0.4\,\%$ ($\Delta E_{1\text{-}2} \propto 1/\sqrt{m_{\text{eff}}}$, eq. (3.13)).[1] The Ramsey signal decays on the order of $0.5\,\text{ms}$ because of the lattice potential inhomogeneity originating from the envelope of the lattice beams.

To circumvent this limitation, a spin echo sequence compensates the impact of the potential inhomogeneity and extends the probe time for the motional coherence to more than $10\,\text{ms}$. We attributed the remaining decay to dynamics in the directions transverse to the lattice axis and to tunneling processes between neighboring lattice sites, and tested the latter explanation by modifying the tunneling rates by means of the dipole trap confinement. The observed spin echo signals last longer for stronger confinements which is consistent with our expectations and agrees qualitatively with the one-dimensional simulations of the spin echo experiments.

In order to analyze the impact of the Bose gas on the motional coherence of the lithium atoms, we introduced a master equation within the Born-Markov approximation. Because of the large computational effort, our calculations were restricted to dynamics of single impurities in a harmonic trapping potential and to smaller model systems. These computations demonstrated that the loss of motional coherence in the bosonic bath originates from heating and relaxation processes which indicates that these mechanisms dominate the dynamics of the lithium atoms in our experiments. But our analysis also showed that these processes preserve the motional coherence if they imply a mutual interaction of the superposition modes with the bosonic background.

We tested our calculations on the basis of relaxation measurements in deep one-dimensional lattice potentials and found good agreement between the predicted and measured relaxation rates. In this context, we observed a non-exponential decay of the lithium population in the second

[1] Previous analysis showed that theory predicts a mass increase of $0.7\,\%$ for the lithium atoms which probe the center of our Bose-Einstein condensate [41]. However, the sodium background is inhomogeneous and it turns out that the averaged mass increase amounts to $0.1\text{-}0.2\,\%$ if we calculate the average in analogy to the effective density (eq. (7.13)).

Bloch band which we attributed to the inhomogeneity of the sodium bath. Indeed, our measurements are reproduced more accurately by a model which accounts for the sodium density at each lattice site and averages over the corresponding relaxation dynamics.

For the investigation of the motional coherence, we treated the inhomogeneous bath density by characterizing the coherence loss of the lithium atoms based on their initial dynamics. Our measurements showed that the interaction between the bosonic bath and the lithium atoms induces a loss of motional coherence, and we determined the corresponding coherence loss rate Γ_{decoh}. In case of the one-dimensional lattice potential, the relaxation rate Γ_{relax} exceeds the observed coherence loss rate Γ_{decoh} by a factor 1.4 ± 0.5 which demonstrates that relaxation processes are the dominant mechanism for the coherence loss. We compared this observation to the corresponding estimate by means of relaxation and heating rates which yields $\Gamma_{\text{relax}}/\Gamma_{\text{decoh}} = 0.5$, and attributed the discrepancy to relaxation and heating processes transversal to the lattice direction. These processes do not inevitably induce a coherence loss as they affect the superposition modes mutually if the absorbed or emitted energy is small compared to the band gap.

Moreover, we performed identical measurements in a deep three-dimensional lattice potential for which transversal dynamics and heating effects can be neglect to first order. These experiments confirm the relaxation processes as the leading mechanism for the coherence loss ($\Gamma_{\text{decoh}} \lesssim \Gamma_{\text{relax}}$) and yield $\Gamma_{\text{relax}}/\Gamma_{\text{decoh}} = 1.9 \pm 1.7$ for the ratio between the relaxation and heating rate which agrees with the theoretical prediction of 2.

Outlook

According to our previous discussion, the dissipative processes in the Bose gas restrict the coherent evolution of the lithium atoms to a few milliseconds. Hence, the precision of our Ramsey technique is not limited by the coherence loss but by the faster dephasing mechanisms. However, due to the quick signal decay, the Ramsey technique does not provide the appropriate tool in order to study the quasi-particle formation in the Bose gas as the predicted effective mass induces for our experimental conditions a trap frequency shift on the order of $0.1\,\%$ [41] which is barely on the order of our experimental accuracy.

For this reason, we intend to apply a modified spin echo sequence which removes the sodium atoms simultaneous with the π-pulse by resonant light. If the interaction between the Bose gas and the lithium atoms induces the formation of a quasi-particle, the lithium atoms evolve before and after the π-pulse differently ($\Delta E_{\text{1-2}} \propto 1/\sqrt{m_{\text{eff}}}$), and we observe a phase shifted Ramsey fringe for symmetric evolution times. This approach is ultimately limited by the loss of motional coherence which restricts the maximal probe time to about $10\,\text{ms}$. Based on this observation, we can estimate the detection sensitivity for the frequency shift by means of the expected precision of the phase determination ($\Delta\phi \approx 0.05\,2\pi$) and the typical band gap ($\Delta E_{\text{1-2}}/h = 70\,\text{kHz}$) to $0.01\,\%$. This precision surpasses the accuracy of the Ramsey technique by one order of magnitude and allows testing for quasi-particle formation.

So far, we referred to quasi-particles in general as the polaron terminology is usually employed for impurities with small momenta which does not apply to our current experiments as the velocity of the lithium atoms exceeds the critical velocity of the Bose gas due to the strong lattice confinement. We can extend our detection scheme to weaker confinements by implementing a

lattice geometry with larger spacing and test for the formation of quasi-particles in the polaronic regime [17, 18].

Recently, we have developed a novel band mapping technique which builds on the different Landau-Zener tunneling rates for the different Bloch bands and separates the band populations by a potential gradient along the lattice axis. This procedure reduces the number of lithium atoms which is necessary for an accurate determination of the band fractions by one order of magnitude, and creates new opportunities for our experiment. The larger ratio between the bath and the impurity atoms enables the implementation of a new cooling scheme which relies on multiple excitation and relaxation cycles [86]. In weak lattice potentials with strongly bended Bloch bands, the excitation from the first to the second band can be restricted to lithium atoms with large quasimomenta and energies [60]. The subsequent relaxation processes is not quasimomentum selective and transfers the lithium atoms in average to states with smaller quasimomenta and energies than before the excitation. This cooling mechanism is finally limited by the width of the first Bloch band and thus provides a promising route to lower temperatures which are e. g. required for quantum magnetism [87].

Moreover, the smaller number of impurity atoms reduces their impact on the Bose gas and offers the possibility to use them as local probe for the Bose-Einstein condensate. Because of the spatial control over the lattice potential, the lithium atoms can be dragged through the Bose gas at a well defined speed which allows testing for finite viscosity in the superfluid regime [88] or investigating the drag force in the normal fluid regime for which semi-classical and perturbative calculations predict a different velocity dependence [89, 90].

The previously outlined experiments study a Bose-Fermi mixture with a bosonic majority. However, we can as well address the sodium atoms by a species-selective lattice and reverse the role of the two components. Such a system would then provide the opportunity to investigate the impact of a few impurities on the dynamics of the Fermi gas and to study e. g. Anderson's orthogonality catastrophe in an ultracold quantum gas [91, 92].

A. Auxiliary Calculations for Chapter 6

This chapter presents the auxiliary calculations to chapter 6.

A.1. General Master Equation

For the derivation of the general master equation (6.17), we performed the trace over the bath variables, and omitted the term of first order in the interaction Hamiltonian

$$\mathrm{Tr}_{\mathrm{bath}}\left\{\left[\hat{H}^{\mathrm{I}}_{\mathrm{int}}(t),\hat{w}^{\mathrm{I}}_{\mathrm{atom}}(0)\otimes\hat{w}_{\mathrm{bath}}\right]\right\} \tag{A.1}$$

which we justify in the following. As the interaction Hamiltonian between the lithium atom and the bosonic bath is given by (eq. (6.10))

$$\hat{H}_{\mathrm{int}}=g_{\mathrm{NaLi}}\sqrt{\frac{\rho_0}{V}}\sum_{\vec{q}}\left(u_{\vec{q}}+v_{\vec{q}}\right)\left(e^{i\vec{q}\hat{\vec{r}}}\hat{b}_{\vec{q}}+e^{-i\vec{q}\hat{\vec{r}}}\hat{b}^{\dagger}_{\vec{q}}\right), \tag{A.2}$$

we need to evaluate $\mathrm{Tr}_{\mathrm{bath}}\{\hat{b}^{\mathrm{I}}_{\vec{q}}(t)\hat{w}_{\mathrm{bath}}\}$ and $\mathrm{Tr}_{\mathrm{bath}}\{\hat{b}^{I\dagger}_{\vec{q}}(t)\hat{w}_{\mathrm{bath}}\}$. It is convenient to carry out these traces on the basis of the multi-mode Fock states

$$\left|n_{\mathrm{q}_0},n_{\mathrm{q}_1},...,n_{\mathrm{q}_k},...\right\rangle=\left|\{n_{\mathrm{q}}\}\right\rangle \tag{A.3}$$

which are the eigenstates to the Hamiltonian of the bosonic bath (eq.(6.1))

$$\hat{H}_{\mathrm{bath}}=E_0+\sum_{\vec{q}\neq 0}\epsilon_{\vec{q}}\hat{b}^{\dagger}_{\vec{q}}.\hat{b}_{\vec{q}}. \tag{A.4}$$

In the following, we exemplarily consider $\mathrm{Tr}_{\mathrm{bath}}\{\hat{b}^{\mathrm{I}}_{\vec{q}}(t)\hat{w}_{\mathrm{bath}}\}$ as $\mathrm{Tr}_{\mathrm{bath}}\{\hat{b}^{\mathrm{I}\dagger}_{\vec{q}}(t)\hat{w}_{\mathrm{bath}}\}$ can be obtained analogously

$$\begin{aligned}\mathrm{Tr}_{\mathrm{bath}}\left\{\hat{b}^{\mathrm{I}}_{\vec{q}}(t)\hat{w}_{\mathrm{bath}}\right\}&=e^{-i\epsilon_{\vec{q}}t/\hbar}\mathrm{Tr}_{\mathrm{bath}}\left\{\hat{b}_{\vec{q}}\hat{w}_{\mathrm{bath}}\right\}\\&=e^{-i\epsilon_{\vec{q}}t/\hbar}\sum_{\{n_{\mathrm{p}}\}}\left\langle n_{\mathrm{p}_0},n_{\mathrm{p}_1},...n_{\mathrm{q}},...\right|\hat{b}_{\vec{q}}w_{\mathrm{bath},\{n_{\mathrm{p}}\}}\left|n_{\mathrm{p}_0},n_{\mathrm{p}_1},...n_{\mathrm{q}},...\right\rangle\\&=e^{-i\epsilon_{\vec{q}}t/\hbar}\sum_{\{n_{\mathrm{p}}\}}\underbrace{\left\langle n_{\mathrm{p}_0},n_{\mathrm{p}_1},...n_{\mathrm{q}},...\right|\sqrt{n_{\mathrm{q}}}w_{\mathrm{bath},\{n_{\mathrm{p}}\}}\left|n_{\mathrm{p}_0},n_{\mathrm{p}_1},...n_{\mathrm{q}}-1,...\right\rangle}_{=0}=0.\end{aligned} \tag{A.5}$$

Here, we used the fact that the Fock states are eigenstates of $\hat{w}_{\mathrm{bath}}$ (indicated by the eigenvalue $w_{\mathrm{bath},\{n_{\mathrm{p}}\}}$) as they are energy eigenstates of the bath Hamiltonian, and that $\hat{b}^{\mathrm{I}}_{\vec{q}}(t)=e^{-i\epsilon_{\vec{q}}t/\hbar}\hat{b}_{\vec{q}}$.[1] The calculation of $\mathrm{Tr}_{\mathrm{bath}}\{\hat{b}^{\mathrm{I}\dagger}_{\vec{q}}(t)\hat{w}_{\mathrm{bath}}\}$ works analogously and yields also zero. Hence, we get

$$\mathrm{Tr}_{\mathrm{bath}}\left\{\left[\hat{H}^{\mathrm{I}}_{\mathrm{int}}(t),\hat{w}^{\mathrm{I}}_{\mathrm{atom}}(0)\otimes\hat{w}_{\mathrm{bath}}\right]\right\}=0. \tag{A.6}$$

[1] $i\hbar\frac{d}{dt}\hat{b}^{\mathrm{I}}_{\vec{q}}(t)=[\hat{b}^{\mathrm{I}}_{\vec{q}}(t),\hat{H}_{\mathrm{bath}}]=e^{i\hat{H}_{\mathrm{bath}}t/\hbar}\,[\hat{b}_{\vec{q}},\hat{H}_{\mathrm{bath}}]\,e^{-i\hat{H}_{\mathrm{bath}}t/\hbar}=\epsilon_{\vec{q}}\hat{b}^{\mathrm{I}}_{\vec{q}}(t)\;\Rightarrow\;\hat{b}^{\mathrm{I}}_{\vec{q}}(t)=e^{-i\epsilon_{\vec{q}}t/\hbar}\hat{b}_{\vec{q}}$

A.2. Master Equation for the Bosonic Bath

In order to obtain the master equation for the lithium atom immersed in a bosonic bath from the general master equation (6.17)

$$\frac{d}{dt}\hat{w}^{\mathrm{I}}_{\mathrm{atom}}(t) = -\frac{1}{\hbar^2}\int_0^t \mathrm{Tr}_{\mathrm{bath}}\left\{\left[\hat{H}^{\mathrm{I}}_{\mathrm{int}}(t),\left[\hat{H}^{\mathrm{I}}_{\mathrm{int}}(\xi),\hat{w}^{\mathrm{I}}_{\mathrm{atom}}(t)\otimes\hat{w}_{\mathrm{bath}}\right]\right]\right\}\mathrm{d}\xi, \tag{A.7}$$

we need to insert the corresponding interaction Hamiltonian (eq. (6.11))

$$\hat{H}_{\mathrm{int}} = g_{\mathrm{NaLi}}\sqrt{\frac{\rho_0}{V}}\sum_{\vec{q}}\left(u_{\vec{q}}+v_{\vec{q}}\right)\sum_{i=1}^{2}\hat{s}_{i,\vec{q}}\hat{\Gamma}_{i,\vec{q}} \tag{A.8}$$

with

$$\hat{s}_{1,\vec{q}} = e^{i\vec{q}\hat{\vec{r}}},\ \hat{s}_{2,\vec{q}} = e^{-i\vec{q}\hat{\vec{r}}},\ \hat{\Gamma}_{1,\vec{q}} = \hat{b}_{\vec{q}}\ \text{ and }\ \hat{\Gamma}_{2,\vec{q}} = \hat{b}^{\dagger}_{\vec{q}}.$$

And we get the master equation for the bosonic bath in Lindblad form

$$\begin{aligned}\frac{d}{dt}\hat{w}^{\mathrm{I}}_{\mathrm{atom}}(t) = &-\frac{g^2_{\mathrm{NaLi}}\rho_0}{\hbar^2 V}\sum_{\vec{q},\vec{p}}\Big(\left(u_{\vec{q}}+v_{\vec{q}}\right)\left(u_{\vec{p}}+v_{\vec{p}}\right)\\ &\sum_{i,j=1}^{2}\int_0^t \mathrm{Tr}_{\mathrm{bath}}\left\{\left[\hat{s}^{\mathrm{I}}_{i,\vec{q}}(t)\hat{\Gamma}^{\mathrm{I}}_{i,\vec{q}}(t),\left[\hat{s}^{\mathrm{I}}_{j,\vec{p}}(\xi)\hat{\Gamma}^{\mathrm{I}}_{j,\vec{p}}(\xi),\hat{w}^{\mathrm{I}}_{\mathrm{atom}}(t)\otimes\hat{w}_{\mathrm{bath}}\right]\right]\right\}\mathrm{d}\xi\Big).\end{aligned} \tag{A.9}$$

A.2.1. Trace over the Bath Variables

Next, we have to perform the trace $\mathrm{Tr}_{\mathrm{bath}}\{[\hat{H}^{\mathrm{I}}_{\mathrm{int}}(t),[\hat{H}^{\mathrm{I}}_{\mathrm{int}}(\xi),\hat{w}^{\mathrm{I}}_{\mathrm{atom}}(t)\otimes\hat{w}_{\mathrm{bath}}]]\}$ over the bath variables. For this purpose, it is sufficient to consider the trace

$$\begin{aligned}&\mathrm{Tr}_{\mathrm{bath}}\left\{\left[\hat{s}^{\mathrm{I}}_{i,\vec{q}}(t)\hat{\Gamma}^{\mathrm{I}}_{i,\vec{q}}(t),\left[\hat{s}^{\mathrm{I}}_{j,\vec{p}}(\xi)\hat{\Gamma}^{\mathrm{I}}_{j,\vec{p}}(\xi),\hat{w}^{\mathrm{I}}_{\mathrm{atom}}(t)\otimes\hat{w}_{\mathrm{bath}}\right]\right]\right\}\\ &\quad= \hat{s}^{\mathrm{I}}_{i,\vec{q}}(t)\hat{s}^{\mathrm{I}}_{j,\vec{p}}(\xi)\hat{w}^{\mathrm{I}}_{\mathrm{atom}}(t)\underbrace{Tr_{\mathrm{bath}}\left\{\hat{\Gamma}^{\mathrm{I}}_{i,\vec{q}}(t)\hat{\Gamma}^{\mathrm{I}}_{j,\vec{p}}(\xi)\hat{w}_{\mathrm{bath}}\right\}}_{\mathrm{I}}\\ &\quad- \hat{s}^{\mathrm{I}}_{i,\vec{q}}(t)\hat{w}^{\mathrm{I}}_{\mathrm{atom}}(t)\hat{s}^{\mathrm{I}}_{j,\vec{p}}(\xi)\underbrace{Tr_{\mathrm{bath}}\left\{\hat{\Gamma}^{\mathrm{I}}_{i,\vec{q}}(t)\hat{w}_{\mathrm{bath}}\hat{\Gamma}^{\mathrm{I}}_{j,\vec{p}}(\xi)\right\}}_{\mathrm{II}}\\ &\quad- \hat{s}^{\mathrm{I}}_{j,\vec{p}}(\xi)\hat{w}^{\mathrm{I}}_{\mathrm{atom}}(t)\hat{s}^{\mathrm{I}}_{i,\vec{q}}(t)\underbrace{Tr_{\mathrm{bath}}\left\{\hat{\Gamma}^{\mathrm{I}}_{j,\vec{p}}(\xi)\hat{w}_{\mathrm{bath}}\hat{\Gamma}^{\mathrm{I}}_{i,\vec{q}}(t)\right\}}_{\mathrm{III}}\\ &\quad+ \hat{w}^{\mathrm{I}}_{\mathrm{atom}}(t)\hat{s}^{\mathrm{I}}_{j,\vec{p}}(\xi)\hat{s}^{\mathrm{I}}_{i,\vec{q}}(t)\underbrace{Tr_{\mathrm{bath}}\left\{\hat{w}_{\mathrm{bath}}\hat{\Gamma}^{\mathrm{I}}_{j,\vec{p}}(\xi)\hat{\Gamma}^{\mathrm{I}}_{i,\vec{q}}(t)\right\}}_{\mathrm{IV}}.\end{aligned}$$

In the following, we evaluate I, I, II, III and IV independently. For the calculation, we take into account that

- the trace is cyclic.

- $\hat{\Gamma}_{1,\vec{q}} = \hat{b}_{\vec{q}}$ and $\hat{\Gamma}_{2,\vec{q}} = \hat{b}^\dagger_{\vec{q}}$ are bosonic field operators which obey the bosonic commutation relation $\left[\hat{b}_{\vec{q}}, \hat{b}^\dagger_{\vec{p}}\right] = \delta_{\vec{q},\vec{p}}$.
- $\hat{\Gamma}^{\mathrm{I}}_{1,\vec{q}}(t) = \hat{b}^{\mathrm{I}}_{\vec{q}}(t) = e^{-i\epsilon_{\vec{q}}t/\hbar}\hat{b}_{\vec{q}}$ and $\hat{\Gamma}^{\mathrm{I}}_{2,\vec{q}}(t) = e^{i\epsilon_{\vec{q}}t/\hbar}\hat{b}^\dagger_{\vec{q}}$.
- $\mathrm{Tr}_{\mathrm{bath}}\left\{\hat{\Gamma}_{i,\vec{q}}\hat{\Gamma}_{j,\vec{p}}\hat{w}_{\mathrm{bath}}\right\}$ is only nonzero for $i \neq j$ and $\vec{p} = \vec{q}$. [2]
- $\mathrm{Tr}_{\mathrm{bath}}\left\{\hat{b}^\dagger_{\vec{q}}\hat{b}_{\vec{p}}\hat{w}_{\mathrm{bath}}\right\} = \delta_{\vec{q},\vec{p}}N(\vec{q})$ with $N(\vec{q}) = 1/(e^{\epsilon_{\vec{q}}/(k_{\mathrm{B}}T)} - 1)$ being the occupation probability of the Bogoliubov excitation with momentum $\vec{q}$ according to the Bose distribution [27].
- $\mathrm{Tr}_{\mathrm{bath}}\left\{\hat{b}_{\vec{q}}\hat{b}^\dagger_{\vec{p}}\hat{w}_{\mathrm{bath}}\right\} = \mathrm{Tr}_{\mathrm{bath}}\left\{\left(\left[\hat{b}_{\vec{q}}, \hat{b}^\dagger_{\vec{p}}\right] + \hat{b}^\dagger_{\vec{p}}\hat{b}_{\vec{q}}\right)\hat{w}_{\mathrm{bath}}\right\} = \delta_{\vec{q},\vec{p}}\,(1 + N(\vec{q}))$

Hence, we get for the first trace (I)

$$\begin{aligned}\mathrm{Tr}_{\mathrm{bath}}\left\{\hat{\Gamma}^{\mathrm{I}}_{i,\vec{q}}(t)\hat{\Gamma}^{\mathrm{I}}_{j,\vec{p}}(\xi)\hat{w}_{\mathrm{bath}}\right\} &= \delta_{\vec{q},\vec{p}}\delta_{i,1}\delta_{j,2}e^{i\epsilon_{\vec{q}}(\xi-t)/\hbar}\mathrm{Tr}_{\mathrm{bath}}\left\{\hat{b}_{\vec{q}}\hat{b}^\dagger_{\vec{q}}\hat{w}_{\mathrm{bath}}\right\}\\ &+ \delta_{\vec{q},\vec{p}}\delta_{i,2}\delta_{j,1}e^{i\epsilon_{\vec{q}}(t-\xi)/\hbar}\mathrm{Tr}_{\mathrm{bath}}\left\{\hat{b}^\dagger_{\vec{q}}\hat{b}_{\vec{q}}\hat{w}_{\mathrm{bath}}\right\}\\ &= \delta_{\vec{q},\vec{p}}\delta_{i,1}\delta_{j,2}e^{i\epsilon_{\vec{q}}(\xi-t)/\hbar}\,(1 + N(\vec{q}))\\ &+ \delta_{\vec{q},\vec{p}}\delta_{i,2}\delta_{j,1}e^{i\epsilon_{\vec{q}}(t-\xi)/\hbar}N(\vec{q})\end{aligned}$$

and similarly for the second trace (II)

$$\begin{aligned}\mathrm{Tr}_{\mathrm{bath}}\left\{\hat{\Gamma}^{\mathrm{I}}_{i,\vec{q}}(t)\hat{w}_{\mathrm{bath}}\hat{\Gamma}^{\mathrm{I}}_{j,\vec{p}}(\xi)\right\} &= \mathrm{Tr}_{\mathrm{bath}}\left\{\hat{\Gamma}^{\mathrm{I}}_{j,\vec{p}}(\xi)\hat{\Gamma}^{\mathrm{I}}_{i,\vec{q}}(t)\hat{w}_{\mathrm{bath}}\right\}\\ &= \delta_{\vec{q},\vec{p}}\delta_{j,1}\delta_{i,2}e^{i\epsilon_{\vec{q}}(t-\xi)/\hbar}\,(1 + N(\vec{q}))\\ &+ \delta_{\vec{q},\vec{p}}\delta_{j,2}\delta_{i,1}e^{i\epsilon_{\vec{q}}(\xi-t)/\hbar}N(\vec{q}).\end{aligned}$$

As the trace is cyclic, the third trace (III) is identical to the first one (I) and the fourth trace (IV) identical to the second one (II). We can now plug all traces into the master equation (A.9) and we end up with

$$\begin{aligned}\frac{d}{dt}\hat{w}^{\mathrm{I}}_{\mathrm{atom}}(t) = -\frac{g^2_{\mathrm{NaLi}}\rho_0}{\hbar^2 V}\sum_{\vec{q}}\int_0^t \left(u_{\vec{q}} + v_{\vec{q}}\right)^2 \Big(\qquad (A.10)\\ \underbrace{\hat{s}^{\mathrm{I}}_{1,\vec{q}}(t)\hat{s}^{\mathrm{I}}_{2,\vec{q}}(\xi)\hat{w}^{\mathrm{I}}_{\mathrm{atom}}(t)e^{i\epsilon_{\vec{q}}(\xi-t)/\hbar}\,(1 + N(\vec{q}))}_{\mathrm{Ia}} + \underbrace{\hat{s}^{\mathrm{I}}_{2,\vec{q}}(t)\hat{s}^{\mathrm{I}}_{1,\vec{q}}(\xi)\hat{w}^{\mathrm{I}}_{\mathrm{atom}}(t)e^{i\epsilon_{\vec{q}}(t-\xi)/\hbar}N(\vec{q})}_{\mathrm{Ib}}\\ - \underbrace{\hat{s}^{\mathrm{I}}_{2,\vec{q}}(t)\hat{w}^{\mathrm{I}}_{\mathrm{atom}}(t)\hat{s}^{\mathrm{I}}_{1,\vec{q}}(\xi)e^{i\epsilon_{\vec{q}}(t-\xi)/\hbar}\,(1 + N(\vec{q}))}_{\mathrm{IIa}} - \underbrace{\hat{s}^{\mathrm{I}}_{1,\vec{q}}(t)\hat{w}^{\mathrm{I}}_{\mathrm{atom}}(t)\hat{s}^{\mathrm{I}}_{2,\vec{q}}(\xi)e^{i\epsilon_{\vec{q}}(\xi-t)/\hbar}N(\vec{q})}_{\mathrm{IIb}}\\ - \underbrace{\hat{s}^{\mathrm{I}}_{2,\vec{q}}(\xi)\hat{w}^{\mathrm{I}}_{\mathrm{atom}}(t)\hat{s}^{\mathrm{I}}_{1,\vec{q}}(t)e^{i\epsilon_{\vec{q}}(\xi-t)/\hbar}\,(1 + N(\vec{q}))}_{\mathrm{IIIa}} - \underbrace{\hat{s}^{\mathrm{I}}_{1,\vec{q}}(\xi)\hat{w}^{\mathrm{I}}_{\mathrm{atom}}(t)\hat{s}^{\mathrm{I}}_{2,\vec{q}}(t)e^{i\epsilon_{\vec{q}}(t-\xi)/\hbar}N(\vec{q})}_{\mathrm{IIIb}}\end{aligned}$$

[2] This is due to the fact that the Fock states $|\{n_{\mathrm{q}}\}\rangle$ are eigenstates of $\hat{w}_{\mathrm{bath}}$ and thus $\langle\{n_{\mathrm{q}}\}|\,\hat{\Gamma}_{i,\vec{q}}\hat{\Gamma}_{j,\vec{p}}\hat{w}_{\mathrm{bath}}\,|\{n_{\mathrm{q}}\}\rangle \propto \langle\{n_{\mathrm{q}}\}|\,\hat{\Gamma}_{i,\vec{q}}\hat{\Gamma}_{j,\vec{p}}\,|\{n_{\mathrm{q}}\}\rangle$ which is only nonzero if $|\{n_{\mathrm{q}}\}\rangle$ is an eigenstate of $\hat{\Gamma}_{i,\vec{q}}\hat{\Gamma}_{j,\vec{p}}$.

$$+ \underbrace{\hat{w}^{\mathrm{I}}_{\mathrm{atom}}(t)\hat{s}^{\mathrm{I}}_{1,\vec{q}}(\xi)\hat{s}^{\mathrm{I}}_{2,\vec{q}}(t)e^{i\epsilon_{\vec{q}}(t-\xi)/\hbar}\left(1+N(\vec{q})\right)}_{\mathrm{IVa}} + \underbrace{\hat{w}^{\mathrm{I}}_{\mathrm{atom}}(t)\hat{s}^{\mathrm{I}}_{2,\vec{q}}(\xi)\hat{s}^{\mathrm{I}}_{1,\vec{q}}(t)e^{i\epsilon_{\vec{q}}(\xi-t)/\hbar}N(\vec{q})}_{\mathrm{IVb}}\Big)\,\mathrm{d}\xi.$$

A.2.2. Conversion into a Set of Coupled Differential Equations

In order to calculate the time evolution of the lithium atom confined in a harmonic potential, we consider the reduced density operator in the corresponding basis

$$\hat{w}^{\mathrm{I}}_{\mathrm{atom}}(t) = \sum_{k,l} w_{k,l}(t)\,|k\rangle\,\langle l|\,, \tag{A.11}$$

where k and l denote triples specifying the mode of the three-dimensional harmonic oscillator (eq. (6.4)). We plug this ansatz into equation (A.10) which will lead to a set of coupled differential equations for the $w_{k,l}(t)$. In the following, we concentrate on the term Ia from equation (A.10) as all other terms can be computed analogously. Its contribution to the time derivative $\frac{d}{dt}w_{k,l}(t)$ is given by

$$\frac{d}{dt}w^{\mathrm{Ia}}_{k,l}(t) = -\frac{g^2_{\mathrm{NaLi}}\rho_0}{\hbar^2 V}\sum_{\vec{q}}\int_0^t\Big(\left(u_{\vec{q}}+v_{\vec{q}}\right)^2 e^{i\epsilon_{\vec{q}}(\xi-t)/\hbar}\left(1+N(\vec{q})\right) \tag{A.12}$$
$$\langle k|\,\hat{s}^{\mathrm{I}}_{1,\vec{q}}(t)\hat{s}^{\mathrm{I}}_{2,\vec{q}}(\xi)\hat{w}^{\mathrm{I}}_{\mathrm{atom}}(t)\,|l\rangle\Big)\,\mathrm{d}\xi.$$

At first, we consider the operator-part of the above equation and denote the eigenenergy of state $|j\rangle$ with E_j (eq. (6.5))

$$\begin{aligned}
&\langle k|\,\hat{s}^{\mathrm{I}}_{1,\vec{q}}(t)\hat{s}^{\mathrm{I}}_{2,\vec{q}}(\xi)\hat{w}^{\mathrm{I}}_{\mathrm{atom}}(t)\,|l\rangle = \sum_{j_1,j_2}\langle k|\,\hat{s}^{\mathrm{I}}_{1,\vec{q}}(t)\,|j_1\rangle\,\langle j_1|\,\hat{s}^{\mathrm{I}}_{2,\vec{q}}(\xi)\,|j_2\rangle\,\langle j_2|\,\hat{w}^{\mathrm{I}}_{\mathrm{atom}}(t)\,|l\rangle \qquad (A.13)\\
&= \sum_{j_1,j_2}\langle k|\,e^{i\hat{H}_{\mathrm{atom}}t/\hbar}\hat{s}_{1,\vec{q}}e^{-i\hat{H}_{\mathrm{atom}}t/\hbar}\,|j_1\rangle\,\langle j_1|\,e^{i\hat{H}_{\mathrm{atom}}\xi/\hbar}\hat{s}_{2,\vec{q}}e^{-i\hat{H}_{\mathrm{atom}}\xi/\hbar}\,|j_2\rangle\,\langle j_2|\,\hat{w}^{\mathrm{I}}_{\mathrm{atom}}(t)\,|l\rangle\\
&= \sum_{j_1,j_2}\langle k|\,e^{i(E_k-E_{j_1})t/\hbar}\hat{s}_{1,\vec{q}}\,|j_1\rangle\,\langle j_1|\,e^{i(E_{j_1}-E_{j_2})\xi/\hbar}\hat{s}_{2,\vec{q}}\,|j_2\rangle\,\langle j_2|\sum_{m,n}w_{m,n}(t)\,|m\rangle\,\langle n|\,|l\rangle\\
&= \sum_{j_1,j_2}\langle k|\,\hat{s}_{1,\vec{q}}\,|j_1\rangle\,\langle j_1|\,\hat{s}_{2,\vec{q}}\,|j_2\rangle\,w_{j_2,l}(t)e^{i(E_k-E_{j_1})t/\hbar}e^{i(E_{j_1}-E_{j_2})\xi/\hbar}.
\end{aligned}$$

With

$$S^{j_1,j_2}_{i,\vec{q}} = \langle j_1|\,\hat{s}_{i,\vec{q}}\,|j_2\rangle \tag{A.14}$$

we get

$$\frac{d}{dt}w^{\mathrm{Ia}}_{k,l}(t) = -\frac{g^2_{\mathrm{NaLi}}\rho_0}{\hbar^2 V}\sum_{j_1,j_2}\sum_{\vec{q}}\left(u_{\vec{q}}+v_{\vec{q}}\right)^2\left(1+N(\vec{q})\right)S^{k,j_1}_{1,\vec{q}}S^{j_1,j_2}_{2,\vec{q}}w_{j_2,l}(t)e^{i(E_k-E_{j_1}-\epsilon_{\vec{q}})t/\hbar} \tag{A.15}$$
$$\int_0^t e^{i(\epsilon_{\vec{q}}+E_{j_1}-E_{j_2})\xi/\hbar}\,\mathrm{d}\xi.$$

Next, the time integration is evaluated. For this purpose, we can extend the integration range from $[0,t]$ to $[0,\infty]$ as the correlation time is much shorter than the integration range (see section 6.1.2)

$$\int_0^\infty e^{i(\epsilon_{\vec{q}}+E_{j_1}-E_{j_2})\xi/\hbar}\,\mathrm{d}\xi = \lim_{\Delta\to 0}\int_0^\infty e^{i(\epsilon_{\vec{q}}+E_{j_1}-E_{j_2}+i\Delta)\xi/\hbar}\,\mathrm{d}\xi \tag{A.16}$$

$$= \lim_{\Delta\to 0}\frac{-\hbar}{i(\epsilon_{\vec{q}}+E_{j_1}-E_{j_2})-\Delta} \tag{A.17}$$

$$= \hbar\underbrace{\lim_{\Delta\to 0}\frac{\Delta}{(E_{j_2}-E_{j_1}-\epsilon_{\vec{q}})^2+\Delta^2}}_{=\pi\delta(E_{j_2}-E_{j_1}-\epsilon_{\vec{q}})} - \hbar\lim_{\Delta\to 0}\frac{i(E_{j_2}-E_{j_1}-\epsilon_{\vec{q}})}{(E_{j_2}-E_{j_1}-\epsilon_{\vec{q}})^2+\Delta^2}. \tag{A.18}$$

Here, we used the definition of the delta distribution by means of the Lorentz distribution [93]. In the following, we drop the imaginary part which corresponds to an energy shift of the harmonic oscillator levels as it is usually small compared to the eigenenergies and obtain

$$\frac{d}{dt}w^{\mathrm{Ia}}_{k,l}(t) = -\frac{\pi g^2_{\mathrm{NaLi}}\rho_0}{\hbar V}\sum_{j_1,j_2}\sum_{\vec{q}}\Big(\left(u_{\vec{q}}+v_{\vec{q}}\right)^2\left(1+N(\vec{q})\right)S^{k,j_1}_{1,\vec{q}}S^{j_1,j_2}_{2,\vec{q}}w_{j_2,l}(t) \\ e^{i(E_k-E_{j_2})t/\hbar}\delta(E_{j_2}-E_{j_1}-\epsilon_{\vec{q}})\Big). \tag{A.19}$$

Similarly, one gets for the other contributions to the time derivative $\frac{d}{dt}w_{k,l}(t)$

$$\frac{d}{dt}w^{\mathrm{Ib}}_{k,l}(t) = -\frac{\pi g^2_{\mathrm{NaLi}}\rho_0}{\hbar V}\sum_{j_1,j_2}\sum_{\vec{q}}\Big(\left(u_{\vec{q}}+v_{\vec{q}}\right)^2 N(\vec{q})S^{k,j_1}_{2,\vec{q}}S^{j_1,j_2}_{1,\vec{q}}w_{j_2,l}(t) \\ e^{i(E_k-E_{j_2})t/\hbar}\delta(E_{j_1}-E_{j_2}-\epsilon_{\vec{q}})\Big), \tag{A.20}$$

$$\frac{d}{dt}w^{\mathrm{IIa}}_{k,l}(t) = \frac{\pi g^2_{\mathrm{NaLi}}\rho_0}{\hbar V}\sum_{j_1,j_2}\sum_{\vec{q}}\Big(\left(u_{\vec{q}}+v_{\vec{q}}\right)^2\left(1+N(\vec{q})\right)S^{k,j_1}_{2,\vec{q}}w_{j_1,j_2}(t)S^{j_2,l}_{1,\vec{q}} \\ e^{i(E_k+E_{j_2}-E_{j_1}-E_l)t/\hbar}\delta(E_{j_2}-E_l-\epsilon_{\vec{q}})\Big), \tag{A.21}$$

$$\frac{d}{dt}w^{\mathrm{IIb}}_{k,l}(t) = \frac{\pi g^2_{\mathrm{NaLi}}\rho_0}{\hbar V}\sum_{j_1,j_2}\sum_{\vec{q}}\Big(\left(u_{\vec{q}}+v_{\vec{q}}\right)^2 N(\vec{q})S^{k,j_1}_{1,\vec{q}}w_{j_1,j_2}(t)S^{j_2,l}_{2,\vec{q}} \\ e^{i(E_k+E_{j_2}-E_{j_1}-E_l)t/\hbar}\delta(E_l-E_{j_2}-\epsilon_{\vec{q}})\Big), \tag{A.22}$$

$$\frac{d}{dt}w^{\mathrm{IIIa}}_{k,l}(t) = \frac{\pi g^2_{\mathrm{NaLi}}\rho_0}{\hbar V}\sum_{j_1,j_2}\sum_{\vec{q}}\Big(\left(u_{\vec{q}}+v_{\vec{q}}\right)^2\left(1+N(\vec{q})\right)S^{k,j_1}_{2,\vec{q}}w_{j_1,j_2}(t)S^{j_2,l}_{1,\vec{q}} \\ e^{i(E_k+E_{j_2}-E_{j_1}-E_l)t/\hbar}\delta(E_{j_1}-E_k-\epsilon_{\vec{q}})\Big), \tag{A.23}$$

$$\frac{d}{dt}w^{\mathrm{IIIb}}_{k,l}(t) = \frac{\pi g^2_{\mathrm{NaLi}}\rho_0}{\hbar V}\sum_{j_1,j_2}\sum_{\vec{q}}\Big(\left(u_{\vec{q}}+v_{\vec{q}}\right)^2 N(\vec{q})S^{k,j_1}_{1,\vec{q}}w_{j_1,j_2}(t)S^{j_2,l}_{2,\vec{q}} \\ e^{i(E_k+E_{j_2}-E_{j_1}-E_l)t/\hbar}\delta(E_k-E_{j_1}-\epsilon_{\vec{q}})\Big), \tag{A.24}$$

$$\frac{d}{dt}w^{\mathrm{IVa}}_{k,l}(t) = -\frac{\pi g^2_{\mathrm{NaLi}}\rho_0}{\hbar V}\sum_{j_1,j_2}\sum_{\vec{q}}\Big(\left(u_{\vec{q}}+v_{\vec{q}}\right)^2 \left(1+N(\vec{q})\right) w_{k,j_1}(t)S^{j_1,j_2}_{1,\vec{q}}S^{j_2,l}_{2,\vec{q}} \\ e^{i(E_{j_1}-E_l)t/\hbar}\delta(E_{j_1}-E_{j_2}-\epsilon_{\vec{q}})\Big), \tag{A.25}$$

and

$$\frac{d}{dt}w^{\mathrm{IVb}}_{k,l}(t) = -\frac{\pi g^2_{\mathrm{NaLi}}\rho_0}{\hbar V}\sum_{j_1,j_2}\sum_{\vec{q}}\Big(\left(u_{\vec{q}}+v_{\vec{q}}\right)^2 N(\vec{q})w_{k,j_1}(t)S^{j_1,j_2}_{2,\vec{q}}S^{j_2,l}_{1,\vec{q}} \\ e^{i(E_{j_1}-E_l)t/\hbar}\delta(E_{j_2}-E_{j_1}-\epsilon_{\vec{q}})\Big). \tag{A.26}$$

Thus, the set of differential equations for the $w_{k,l}(t)$'s is finally given by

$$\begin{aligned}\frac{d}{dt}w_{k,l}(t) =& -\frac{\pi g^2_{\mathrm{NaLi}}\rho_0}{\hbar V}\sum_{j_1,j_2}\sum_{\vec{q}}\Big[\left(u_{\vec{q}}+v_{\vec{q}}\right)^2\left(1+N(\vec{q})\right)\Big(\\ & S^{k,j_1}_{1,\vec{q}}S^{j_1,j_2}_{2,\vec{q}}w_{j_2,l}(t)e^{i(E_k-E_{j_2})t/\hbar}\delta(E_{j_2}-E_{j_1}-\epsilon_{\vec{q}}) \\ & - S^{k,j_1}_{2,\vec{q}}w_{j_1,j_2}(t)S^{j_2,l}_{1,\vec{q}}e^{i(E_k+E_{j_2}-E_{j_1}-E_l)t/\hbar}\delta(E_{j_2}-E_l-\epsilon_{\vec{q}}) \\ & - S^{k,j_1}_{2,\vec{q}}w_{j_1,j_2}(t)S^{j_2,l}_{1,\vec{q}}e^{i(E_k+E_{j_2}-E_{j_1}-E_l)t/\hbar}\delta(E_{j_1}-E_k-\epsilon_{\vec{q}}) \\ & + w_{k,j_1}(t)S^{j_1,j_2}_{1,\vec{q}}S^{j_2,l}_{2,\vec{q}}e^{i(E_{j_1}-E_l)t/\hbar}\delta(E_{j_1}-E_{j_2}-\epsilon_{\vec{q}})\Big)\Big] \\ & - \frac{\pi g^2_{\mathrm{NaLi}}\rho_0}{\hbar V}\sum_{j_1,j_2}\sum_{\vec{q}}\Big[\left(u_{\vec{q}}+v_{\vec{q}}\right)^2 N(\vec{q})\Big(\\ & S^{k,j_1}_{2,\vec{q}}S^{j_1,j_2}_{1,\vec{q}}w_{j_2,l}(t)e^{i(E_k-E_{j_2})t/\hbar}\delta(E_{j_1}-E_{j_2}-\epsilon_{\vec{q}}) \\ & - S^{k,j_1}_{1,\vec{q}}w_{j_1,j_2}(t)S^{j_2,l}_{2,\vec{q}}e^{i(E_k+E_{j_2}-E_{j_1}-E_l)t/\hbar}\delta(E_l-E_{j_2}-\epsilon_{\vec{q}}) \\ & - S^{k,j_1}_{1,\vec{q}}w_{j_1,j_2}(t)S^{j_2,l}_{2,\vec{q}}e^{i(E_k+E_{j_2}-E_{j_1}-E_l)t/\hbar}\delta(E_k-E_{j_1}-\epsilon_{\vec{q}}) \\ & + w_{k,j_1}(t)S^{j_1,j_2}_{2,\vec{q}}S^{j_2,l}_{1,\vec{q}}e^{i(E_{j_1}-E_l)t/\hbar}\delta(E_{j_2}-E_{j_1}-\epsilon_{\vec{q}})\Big)\Big].\end{aligned} \tag{A.27}$$

This equation covers the time evolution of the lithium atom in the most general case. However, for a lithium atom which initially occupies an energy eigenstate the differential equation becomes more simple. In this case, the off-diagonal elements of the density matrix are always zero ($w_{k,l}(t) = 0$ for $k \neq l$) as the bath does not induce coherences, and one gets [69]

$$\begin{aligned}\frac{d}{dt}w_{k,k}(t) =& -\frac{2\pi g^2_{\mathrm{NaLi}}\rho_0}{\hbar V}\sum_{j}\sum_{\vec{q}}\left(u_{\vec{q}}+v_{\vec{q}}\right)^2\Big[\\ & \left(1+N(\vec{q})\right)\Big(\left|S^{j,k}_{2,\vec{q}}\right|^2 w_{k,k}(t)\delta(E_k-E_j-\epsilon_{\vec{q}}) - \left|S^{k,j}_{2,\vec{q}}\right|^2 w_{j,j}(t)\delta(E_j-E_k-\epsilon_{\vec{q}})\Big) \\ & + N(\vec{q})\Big(\left|S^{j,k}_{2,\vec{q}}\right|^2 w_{k,k}(t)\delta(E_j-E_k-\epsilon_{\vec{q}}) - \left|S^{k,j}_{2,\vec{q}}\right|^2 w_{j,j}(t)\delta(E_k-E_j-\epsilon_{\vec{q}})\Big)\Big].\end{aligned} \tag{A.28}$$

It is instructive to rewrite equation (A.28) as rate equation

$$\frac{d}{dt}w_{k,k}(t) = \sum_j \Big(R_{j\to k} w_{j,j}(t) - R_{k\to j} w_{k,k}(t) + H_{j\to k} w_{j,j}(t) - H_{k\to j} w_{k,k}(t) \Big). \quad \text{(A.29)}$$

Where

$$R_{m\to n} = \frac{2\pi g_{\mathrm{NaLi}}^2 \rho_0}{\hbar V} \sum_{\vec{q}} \left(u_{\vec{q}} + v_{\vec{q}}\right)^2 (1 + N(\vec{q})) \left|S_{2,\vec{q}}^{n,m}\right|^2 \delta(E_m - E_n - \epsilon_{\vec{q}}) \quad \text{(A.30)}$$

corresponds to the relaxation rate from state $|m\rangle$ to state $|n\rangle$ according to Fermi's golden rule [75] and

$$H_{m\to n} = \frac{2\pi g_{\mathrm{NaLi}}^2 \rho_0}{\hbar V} \sum_{\vec{q}} \left(u_{\vec{q}} + v_{\vec{q}}\right)^2 N(\vec{q}) \left|S_{2,\vec{q}}^{n,m}\right|^2 \delta(E_n - E_m - \epsilon_{\vec{q}}) \quad \text{(A.31)}$$

to the heating rate from state $|m\rangle$ to state $|n\rangle$ because of the bath's finite temperature.

A.3. Numerical Evaluation

This section shortly introduces the numerics used for calculating the relaxation rates in section 6.2 and the time evolution of the density matrix in section 6.3.

A.3.1. Matrix Elements

In order to calculate the matrix element

$$S_{2,\vec{q}}^{m,n} = \langle m| e^{-i\vec{q}\hat{\vec{r}}} |n\rangle, \quad \text{(A.32)}$$

the element is split into three matrix elements one for each spatial direction

$$S_{2,\vec{q}}^{m,n} = \langle m_{\mathrm{x}}| e^{-iq_{\mathrm{x}}\hat{x}} |n_{\mathrm{x}}\rangle \langle m_{\mathrm{y}}| e^{-iq_{\mathrm{y}}\hat{y}} |n_{\mathrm{y}}\rangle \langle m_{\mathrm{z}}| e^{-iq_{\mathrm{z}}\hat{z}} |n_{\mathrm{z}}\rangle. \quad \text{(A.33)}$$

According to [69], each of these elements is for a harmonic potential and for $m_j \leq n_j$ given by

$$\begin{aligned} \langle m_j| e^{-iq_j\hat{x_j}} |n_j\rangle &= \int_{-\infty}^{\infty} \psi_{m_j}^*(x_j) e^{-iq_j x_j} \psi_{n_j}(x_j)\, \mathrm{d}x_j \quad \text{(A.34)} \\ &= \sqrt{\frac{m_j!}{n_j!}} e^{-a_{\mathrm{ho}}^2 q_j^2/4} \left(\frac{-ia_{\mathrm{ho}} q_j}{\sqrt{2}}\right)^{n_j - m_j} \mathrm{L}_{m_j}^{n_j - m_j}\left(\frac{a_{\mathrm{ho}}^2 q_j^2}{2}\right), \end{aligned}$$

where a_{ho} is the harmonic oscillator length along the j-th direction and $\mathrm{L}_{m_j}^{n_j-m_j}$ the associated Laguerre polynomial. To obtain the matrix element $\langle m_j| e^{-iq_j\hat{x_j}} |n_j\rangle$ for $n_j \leq m_j$, we make use of the fact that the eigenfunctions of the harmonic oscillator $\psi_n(x)$ are real. Hence, one gets $\langle m_j| e^{-iq_j\hat{x_j}} |n_j\rangle = \langle n_j| e^{-iq_j\hat{x_j}} |m_j\rangle$ which can be calculated by the above formula.
Moreover, the calculation of

$$S_{1,\vec{q}}^{m,n} = \langle m| e^{i\vec{q}\hat{\vec{r}}} |n\rangle \quad \text{(A.35)}$$

also reduces to the calculation of $S_{2,\vec{q}}^{m,n}$ as $S_{1,\vec{q}}^{m,n} = \left(S_{2,\vec{q}}^{n,m}\right)^*$.

A.3.2. Sum over the Excitation Modes

As the excitation modes of a homogeneous Bose gas are continuous, the sum over the excitation modes in equation (A.27) and (A.28) can be replaced by an integral

$$\sum_{\vec{q}} \to \frac{V}{(2\pi)^3} \int \mathrm{d}^3 p. \tag{A.36}$$

If we e. g. insert this approach into the first summand of equation (A.27) and consider that the dispersion relation of the Bogoliubov excitations is monotonically increasing, the three-dimensional integral turns into a two-dimensional integral

$$\begin{aligned} &\frac{\pi g_{\mathrm{NaLi}}^2 \rho_0}{\hbar V} \sum_{\vec{q}} \left(u_{\vec{q}} + v_{\vec{q}}\right)^2 \left(1 + N(\vec{q})\right) S_{1,\vec{q}}^{k,j_1} S_{2,\vec{q}}^{j_1,j_2} e^{i(E_k - E_{j_2})t/\hbar} \delta(E_{j_2} - E_{j_1} - \epsilon_{\vec{q}}) \qquad (A.37) \\ &= \frac{g_{\mathrm{NaLi}}^2 \rho_0}{2^3 \pi^2 \hbar} \int \mathrm{d}^3 p \left(u_{\vec{q}} + v_{\vec{q}}\right)^2 \left(1 + N(\vec{q})\right) S_{1,\vec{q}}^{k,j_1} S_{2,\vec{q}}^{j_1,j_2} e^{i(E_k - E_{j_2})t/\hbar} \delta(E_{j_2} - E_{j_1} - \epsilon_{\vec{q}}) \\ &= \frac{g_{\mathrm{NaLi}}^2 \rho_0}{2^3 \pi^2 \hbar} \left(u_{q_0} + v_{q_0}\right)^2 \left(1 + N(q_0)\right) \left| \frac{d}{dq} \epsilon_q \right|_{q=q_0}^{-1} q_0^2 \int \sin(\theta) \, S_{1,\vec{q}_0}^{k,j_1} S_{2,\vec{q}_0}^{j_1,j_2} \, \mathrm{d}\theta \mathrm{d}\phi \; e^{i(E_k - E_{j_2})t/\hbar} \end{aligned}$$

with $E_{j_2} - E_{j_1} = \epsilon_{\vec{q}_0}$. In general, this integral is not analytically solvable and has to be computed numerically.

B. List of Constants

The following table lists the constants and their abbreviations used in this thesis and the presented calculations.

natural constants [94]	symbol	value
Planck constant	$\hbar$	$1.05457 \cdot 10^{-34}$ Js
	h	$\hbar \cdot 2\pi$
Boltzmann constant	k_{B}	$1.38065 \cdot 10^{-23}$ J/K
speed of light	c	299,792,458 m/s
standard acceleration of gravity	g_{grav}	$9.80665\,\mathrm{m/s^2}$
Bohr radius	a_0	$5.29177 \cdot 10^{-11}$ m
sodium constants [95]		
mass	m_{Na}	$3.81754 \cdot 10^{-26}$ kg
D_2- transition frequency	$\omega_{\mathrm{Na,D_2}}$	$2\pi \cdot 508.84872$ THz
natural line width D_2-line	$\Gamma_{\mathrm{Na,D_2}}$	$2\pi \cdot 9.7946$ MHz
lithium constants [96]		
mass	m_{Li}	$9.98834 \cdot 10^{-27}$ kg
D_1- transition frequency	$\omega_{\mathrm{Li,D_1}}$	$2\pi \cdot 446.78963$ THz
natural line width D_1-line	$\Gamma_{\mathrm{Li,D_1}}$	$2\pi \cdot 5.8724$ MHz
D_2- transition frequency	$\omega_{\mathrm{Li,D_2}}$	$2\pi \cdot 446.79968$ THz
natural line width D_2-line	$\Gamma_{\mathrm{Li,D_2}}$	$2\pi \cdot 5.8724$ MHz
scattering lengths for the lowest hyperfine states		
sodium-sodium [97]	$a_{\mathrm{Na,Na}}$	$54.54\,a_0$
sodium-lithium [41]	$a_{\mathrm{Na,Li}}$	$-75\,a_0$

Bibliography

[1] N. Bohr. “The Quantum Postulate and the Recent Development of Atomic Theory”. In: *Nature* 121 (1928), pp. 580–590.

[2] David Bohm. “A Suggested Interpretation of the Quantum Theory in Terms of "Hidden" Variables. I”. In: *Phys. Rev.* 85 (1952), pp. 166–179.

[3] Hugh Everett. “Relative State Formulation of Quantum Mechanics”. In: *Rev. Mod. Phys.* 29 (1957), pp. 454–462.

[4] E. Schrödinger. “Die gegenwärtige Situation in der Quantenmechanik”. In: *Naturwissenschaften* 23 (1935), pp. 807–812.

[5] W. H. Zurek. “Decoherence and the transition from quantum to classical”. In: *Physics Today* 44 (1991), pp. 36–44.

[6] F. B. J. Buchkremer et al. “Wave Packet Echoes in the Motion of Trapped Atoms”. In: *Phys. Rev. Lett.* 85 (2000), pp. 3121–3124.

[7] C. J. Myatt et al. “Decoherence of quantum superpositions through coupling to engineered reservoirs”. In: *Nature* 403 (2000), pp. 269–273.

[8] R. Hanson et al. “Coherent Dynamics of a Single Spin Interacting with an Adjustable Spin Bath”. In: *Science* 320 (2008), pp. 352–355.

[9] L. Ratschbacher et al. “Dynamics and decoherence of a single spin-qubit in a tunable environment”. In: *ArXiv:1301.5452* (2013).

[10] Richard Feynman. “Simulating physics with computers”. In: *International Journal of Theoretical Physics* 21 (1982), p. 467.

[11] J. Bardeen, L. N. Cooper, and J. R. Schrieffer. “Theory of Superconductivity”. In: *Physical Review* 108 (1957), pp. 1175–1204.

[12] M.W. Zwierlein et al. “Vortices and superfluidity in a strongly interacting Fermi gas”. In: *Nature* 435 (2005), pp. 1047–1051.

[13] M. W. Zwierlein et al. “Direct observation of the superfluid phase transition in ultracold Fermi gases”. In: *Nature* 442 (2006), pp. 54–58.

[14] S. Inouye et al. “Observation of Feshbach resonances in a Bose-Einstein condensate”. In: *Nature* 392 (1998), pp. 151–154.

[15] Cheng Chin et al. “Feshbach resonances in ultracold gases”. In: *Rev. Mod. Phys.* 82 (2010), pp. 1225–1286.

[16] A. S. Alexandrov and A. B. Krebs. “REVIEWS OF TOPICAL PROBLEMS: Polarons in high-temperature superconductors”. In: *Soviet Physics Uspekhi* 35 (1992), pp. 345–383.

[17] F. M. Cucchietti and E. Timmermans. "Strong-Coupling Polarons in Dilute Gas Bose-Einstein Condensates". In: *Phys. Rev. Lett.* 96 (2006), p. 210401.

[18] J. Tempere et al. "Feynman path-integral treatment of the BEC-impurity polaron". In: *Phys. Rev. B* 80 (2009), p. 184504.

[19] M. H. Anderson et al. "Observation of Bose-Einstein Condensation in a Dilute Atomic Vapor". In: *Science* 269 (1995), pp. 198–201.

[20] K. B. Davis et al. "Bose-Einstein Condensation in a Gas of Sodium Atoms". In: *Phys. Rev. Lett.* 75 (1995), pp. 3969–3973.

[21] Sebastian Will et al. "Coherent Interaction of a Single Fermion with a Small Bosonic Field". In: *Phys. Rev. Lett.* 106 (2011), p. 115305.

[22] J. Catani et al. "Quantum dynamics of impurities in a one-dimensional Bose gas". In: *Phys. Rev. A* 85 (2012), p. 023623.

[23] W. Ketterle, D. S. Durfee, and D. M. Stamper-Kurn. "Making, probing and understanding Bose-Einstein condensates". In: *Bose-Einstein condensation in atomic gases*. 1999, pp. 67–176.

[24] Lev Pitaevskii and Sandro Stringari. *Bose-Einstein Condensation*. Oxford Science Publications, 2002.

[25] E. P. Gross. "Structure of a quantized vortex in Boson systems". In: *Il Nuovo Cimento* 20 (1961), p. 454.

[26] L. P. Pitaevskii. "Vortex lines in an imperfect Bose gas". In: *Sov. Phys. JETP* 13 (1961), p. 451.

[27] H. Smith and C. J. Pethick. *Bose-Einstein condensate in dilute gases*. Cambridge Universtiy Press, 2002.

[28] Vanderlei Bagnato, David E. Pritchard, and Daniel Kleppner. "Bose-Einstein condensation in an external potential". In: *Phys. Rev. A* 35 (1987), pp. 4354–4358.

[29] N. N. Bogoliubov. "On the Theory of Superfluidity". In: *Journal of Physics* 11 (1947), pp. 23–32.

[30] Neil W. Ashcroft and N. David Mermini. *Solid State Physics*. Holt-Saunders International Editions, 1976.

[31] Wolfgang Ketterle and Martin W. Zwierlein. *Making, probing and understanding ultracold Fermi gases*. 2008.

[32] Harold J. Metcalf and Peter van der Straten. *Laser Cooling and Trapping*. Springer-Verlag, 2002.

[33] Z. Hadzibabic et al. "Fiftyfold Improvement in the Number of Quantum Degenerate Fermionic Atoms". In: *Phys. Rev. Lett.* 91 (2003), p. 160401.

[34] K. M. R. van der Stam et al. "Spin-polarizing cold sodium atoms in a strong magnetic field". In: *Phys. Rev. A* 73 (2006), p. 063412.

[35] C. J. Myatt et al. "Production of Two Overlapping Bose-Einstein Condensates by Sympathetic Cooling". In: *Phys. Rev. Lett.* 78 (1997), pp. 586–589.

[36] Marc Repp. *Aufbau einer Vakuumapparatur für Experimente mit ultrakalten fermionischen und bosonischen Quantengasen*. diploma thesis, 2007.

[37] Stefan Weis. *Setup of a Laser System for Ultracold Sodium - Towards a Degenerate Gas of Ultracold Fermions*. diploma thesis, 2007.

[38] Jan Krieger. *Zeeman-Slower und Experimentsteuerung für das NaLi-Experiment*. diploma thesis, 2008.

[39] Valentin Volchkov. *Cold Lithium Atoms For Future Polaron Experiments*. diploma thesis, 2009.

[40] Jens Appmeier. *Immersed Quantum Systems: A Sodium Bose-Einstein Condensate for Polaron Studies*. PhD thesis, university of Heidelberg, 2010.

[41] Tobias Schuster. *Feshbach Resonances and Periodic Potentials in Ultracold Bose-Fermi Mixtures*. PhD thesis, university of Heidelberg, 2012.

[42] R. Grimm, M. Weidemüller, and Y. B. Ovchinnikov. "Optical dipole traps for neutral atoms". In: *Advances in Atomic, Molecular and Optical Physics* 42 (2000), p. 95.

[43] Georg M. Bruun and Charles W. Clark. "Ideal gases in time-dependent traps". In: *Phys. Rev. A* 61 (2000), p. 061601.

[44] T. Schuster et al. "Feshbach spectroscopy and scattering properties of ultracold Li + Na mixtures". In: *Phys. Rev. A* 85 (2012), p. 042721.

[45] L. J. LeBlanc and J. H. Thywissen. "Species-specific optical lattices". In: *Phys. Rev. A* 75 (2007), p. 053612.

[46] J. Catani et al. "Entropy Exchange in a Mixture of Ultracold Atoms". In: *Phys. Rev. Lett.* 103 (2009), p. 140401.

[47] D. Jaksch et al. "Cold Bosonic Atoms in Optical Lattices". In: *Phys. Rev. Lett.* 81 (1998), pp. 3108–3111.

[48] Dieter Jaksch. *Bose-Einstein condensation and Applications*. PhD thesis, university of Innsbruck, 1999.

[49] Subir Sachdev, K. Sengupta, and S. M. Girvin. "Mott insulators in strong electric fields". In: *Phys. Rev. B* 66 (2002), p. 075128.

[50] Henning Moritz et al. "Confinement Induced Molecules in a 1D Fermi Gas". In: *Phys. Rev. Lett.* 94 (2005), p. 210401.

[51] Bernd Fröhlich et al. "Radio-Frequency Spectroscopy of a Strongly Interacting Two-Dimensional Fermi Gas". In: *Phys. Rev. Lett.* 106 (2011), p. 105301.

[52] Elisabeth Brühl. *A Species Selective Optical Dipole Trap for the NaLi Experiment*. bachelor thesis, university of Heidelberg, 2011.

[53] L. Viverit et al. "Efficient and Robust Initialization of a Qubit Register with Fermionic Atoms". In: *Phys. Rev. Lett.* 93 (2004), p. 110401.

[54] Michael Köhl et al. "Fermionic Atoms in a Three Dimensional Optical Lattice: Observing Fermi Surfaces, Dynamics, and Interactions". In: *Phys. Rev. Lett.* 94 (2005), p. 080403.

[55] Markus Greiner et al. "Exploring Phase Coherence in a 2D Lattice of Bose-Einstein Condensates". In: *Phys. Rev. Lett.* 87 (2001), p. 160405.

[56] G. Raithel, W. D. Phillips, and S. L. Rolston. "Collapse and Revivals of Wave Packets in Optical Lattices". In: *Phys. Rev. Lett.* 81 (1998), pp. 3615–3618.

[57] J. J. Sakurai. *Modern Quantum Mechanics*. Prentice Hall, 1994.

[58] Govind P. Agrawal. *Nonlinear Fiber Optics*. 1995.

[59] J. Hecker Denschlag et al. "A Bose-Einstein condensate in an optical lattice". In: *Journal of Physics B: Atomic, Molecular and Optical Physics* 35 (2002), p. 3095.

[60] J. Heinze et al. "Multiband Spectroscopy of Ultracold Fermions: Observation of Reduced Tunneling in Attractive Bose-Fermi Mixtures". In: *Phys. Rev. Lett.* 107 (2011), p. 135303.

[61] Norman F. Ramsey. "A Molecular Beam Resonance Method with Separated Oscillating Fields". In: *Phys. Rev.* 78 (1950), pp. 695–699.

[62] Norman F. Ramsey. "Experiments with Separated Oscillatory Fields and Hydrogen Masers". In: *Science* 248 (1990), pp. 1612–1619.

[63] G. Santarelli et al. "Quantum Projection Noise in an Atomic Fountain: A High Stability Cesium Frequency Standard". In: *Phys. Rev. Lett.* 82 (1999), pp. 4619–4622.

[64] E. L. Hahn. "Spin Echoes". In: *Phys. Rev.* 80 (1950), pp. 580–594.

[65] H. Y. Carr and E. M. Purcell. "Effects of Diffusion on Free Precession in Nuclear Magnetic Resonance Experiments". In: *Phys. Rev.* 94 (1954), pp. 630–638.

[66] A. Görlitz et al. "Sodium Bose-Einstein Condensates in the $F = 2$ State in a Large-Volume Optical Trap". In: *Phys. Rev. Lett.* 90 (2003), p. 090401.

[67] G. Lindblad. "On the generators of quantum dynamical semigroups". In: *Communications in Mathematical Physics* 48 (1976), pp. 119–130.

[68] V. Gorini, A. Kossakowski, and E. C. G. Sudarshan. "Completely positive dynamical semigroups of N-level systems". In: *Journal of Mathematical Physics* 17 (1976), pp. 821–825.

[69] A. J. Daley, P. O. Fedichev, and P. Zoller. "Single-atom cooling by superfluid immersion: A nondestructive method for qubits". In: *Phys. Rev. A* 69 (2004), p. 022306.

[70] G. W. Gardiner and P. Zoller. *Quantum Noise*. Springer, 2000.

[71] P. Haikka et al. "Quantifying, characterizing, and controlling information flow in ultracold atomic gases". In: *Phys. Rev. A* 84 (2011), p. 031602.

[72] M. A. Cirone et al. "Collective decoherence of cold atoms coupled to a Bose-Einstein condensate". In: *New Journal of Physics* 11.10 (2009), p. 103055.

[73] M. Bruderer and D. Jaksch. "Probing BEC phase fluctuations with atomic quantum dots". In: *New Journal of Physics* 8 (2006), p. 87.

[74] D. F. Walls and Gerad J. Milburni. *Quantum Optics*. Springer, 2008.

[75] P. A. M. Dirac. "The Quantum Theory of the Emission and Absorption of Radiation". In: *Royal Society of London Proceedings Series A* 114 (1927), pp. 243–265.

[76] A. Griessner et al. “Dissipative dynamics of atomic Hubbard models coupled to a phonon bath: dark state cooling of atoms within a Bloch band of an optical lattice”. In: *New Journal of Physics* 9 (2007), p. 44.

[77] D. C. McKay and B. DeMarco. “Slow Thermalization Between a Lattice and Free Bose Gas”. In: *ArXiv:1211.4772* (2012).

[78] A. Kreuter et al. “Spontaneous Emission Lifetime of a Single Trapped Ca^+ Ion in a High Finesse Cavity”. In: *Phys. Rev. Lett.* 92 (2004), p. 203002.

[79] R. Ozeri et al. “Hyperfine Coherence in the Presence of Spontaneous Photon Scattering”. In: *Phys. Rev. Lett.* 95 (2005), p. 030403.

[80] M. Khalil, N. Demirdöven, and A. Tokmakoff. “Vibrational coherence transfer characterized with Fourier-transform 2D IR spectroscopy”. In: *J. Phys. Chem.* 121 (2004), pp. 362–373.

[81] M. J. Nee et al. “Multilevel vibrational coherence transfer and wavepacket dynamics probed with multidimensional IR spectroscopy”. In: *J. Phys. Chem.* 129 (2008), p. 084503.

[82] Roland Omnès. “Consistent interpretations of quantum mechanics”. In: *Rev. Mod. Phys.* 64 (1992), pp. 339–382.

[83] Malcolm H. Levitt. *Spin dynamics*. Wiley, 2002.

[84] R. Kreis, T. Ernst, and B.D. Ross. “Absolute Quantitation of Water and Metabolites in the Human Brain. II. Metabolite Concentrations”. In: *Journal of Magnetic Resonance, Series B* 102 (1993), pp. 9–19.

[85] Florian Marquardt et al. “Decoherence in weak localization. I. Pauli principle in influence functional”. In: *Phys. Rev. B* 76 (2007), p. 195331.

[86] A. Griessner et al. “Dark-State Cooling of Atoms by Superfluid Immersion”. In: *Phys. Rev. Lett.* 97 (2006), p. 220403.

[87] Immanuel Bloch, Jean Dalibard, and Wilhelm Zwerger. “Many-body physics with ultracold gases”. In: *Rev. Mod. Phys.* 80 (2008), pp. 885–964.

[88] Andrew G. Sykes, Matthew J. Davis, and David C. Roberts. “Drag Force on an Impurity below the Superfluid Critical Velocity in a Quasi-One-Dimensional Bose-Einstein Condensate”. In: *Phys. Rev. Lett.* 103 (2009), p. 085302.

[89] D. Dasenbrook and A. Komnik. “Semiclassical polaron dynamics of impurities in ultracold gases”. In: *ArXiv:1210.1466* (2012).

[90] D. Kovrizhin. “"Cherenkov radiation" of a sound in a Bose condensed gas”. In: *Physics Letters A* 282 (2001), pp. 421–427.

[91] P. W. Anderson. “Infrared Catastrophe in Fermi Gases with Local Scattering Potentials”. In: *Phys. Rev. Lett.* 18 (1967), pp. 1049–1051.

[92] Michael Knap et al. “Time-Dependent Impurity in Ultracold Fermions: Orthogonality Catastrophe and Beyond”. In: *Phys. Rev. X* 2 (2012), p. 041020.

[93] I. N. Bronstein et al. *Taschenbuch der Mathematik*. Harri Deutsch, 2001.

[94] NIST reference. URL: `http://physics.nist.gov/cuu/Constants/`.

[95] D.A. Steck. *Sodium D line data*. 2003.

[96] Michael E. Gehm. *Properties of ^{6}Li*. 2003.

[97] S. Knoop et al. "Feshbach spectroscopy and analysis of the interaction potentials of ultracold sodium". In: *Phys. Rev. A* 83 (2011), p. 042704.

Danksagung

Schlussendlich möchte ich mich bei allen bedanken, die mich während meiner Doktorarbeit unterstützt und die zum Gelingen dieser Arbeit beigetragen haben:

- Zuallererst bedanke ich mich besonders bei meinem Betreuer Prof. Dr. Markus K. Oberthaler für die Aufnahme in seine Arbeitsgruppe und seinen Optimismus, der mich auch in schwierigen Phasen immer wieder aufs Neue motiviert hat. Ohne seine unkomplizierte Art und seinen fairen Umgang wäre die gute Atmosphäre in der Gruppe undenkbar. Vor allem sein großes Vertrauen und die damit verbundenen Freiheiten haben die Laborarbeit zu einer spannenden und interessanten Zeit gemacht.
- Weiterhin danke ich Prof. Dr. Selim Jochim für die Begutachtung dieser Arbeit und für die gemütlichen Grill- und Feuerzangenbowle-Abende mit ihm und seiner Gruppe.
- Dem gesamten NaLi-Team möchte ich für die entspannte Atmosphäre und die gute Zeit, die wir im Labor und bei diversen Pizza-, Grill- und Fußballabenden hatten, danken:
  - Tobias Schuster für sein vorausschauendes Arbeiten beim Wiederaufbau des Experimentes und seinen unermüdlichen Einsatz, ohne den diese Ergebnisse nicht möglich gewesen wären. Unsere intensiven Diskussionen waren für mein Verständnis der Physik und des Experimentes stets hilfreich und unsere gemeinsame Zeit im Labor wird mir in guter Erinnerung bleiben. Ich hätte mir keinen besseren Kollegen wünschen können.
  - Tobias Rentrop für seinen Elan mit dem er die Arbeit im Labor übernommen hat und mit dem er das Experiment vorantreibt. Sein ausgeprägter Humor und seine Unterstützung im und außerhalb des Labors haben mir über so manche Durststrecke hinweggeholfen.
  - Arno Trautmann für seine technischen Spielereien und sein Engagement, die das Experiment immer wieder am Laufen halten. Seine Latex-Kenntnisse haben mir das Erstellen dieses Dokumentes deutlich erleichtert.
  - Steven Knoop, der den Wiederaufbau in den ersten anderthalb Jahren als Postdoc begleitet und geprägt hat. An seine Begeisterung für die Physik, seine Geduld beim Erklären derselben und seinen freundlichen Charakter denke ich immer wieder gerne zurück.
  - Jens Appmeier, der mit seiner Expertise und seiner Ruhe großen Anteil am Aufbau des Experimentes hat. Ich danke ihm besonders für seine geduldigen Erläuterungen all der kleinen und großen technischen Details, die mir beim Experimentieren sehr geholfen haben.

  - Andrea Bergschneider, Elisabeth Brühl und Mathias Neidig danke ich für ihre sorgfältige Arbeit am Lithium- und Gitterlasersystem.

- Vielen Dank an die Mitglieder des ACE-, AEgIS-, ATTA- und BEC-Experimentes für die gute Gruppenatmosphäre und ihre Hilfsbereitschaft. Auf eure Unterstützung war egal, ob bei Matlab-Problemen oder bei fehlenden Vakuumkomponenten immer Verlass. Ich werde unsere Grillabende im KIP-Innenhof und die Radtouren auf den Königsstuhl oder den Weißen Stein vermissen.

- Prof. Dr. Andreas Komnik und seiner Arbeitsgruppe danke ich für die aufschlussreichen Diskussionen und Erklärungen über das Polaron und dessen theoretischer Beschreibung.

- Zudem möchte ich mich bei Dr. Jörg Evers und Kilian Heeg für die Diskussionen über die Herleitung und Lösung der Mastergleichung bedanken.

- Mein Dank gilt auch den beiden Team-Assistants Dagmar Hufnagel und Christiane Jäger, die sich um die organisatorischen und bürokratischen Angelegenheiten kümmern und uns den Rücken für unsere Experimente freihalten.

- Herzlichen Dank an die mechanische Werkstatt, insbesondere an Herrn Lamade und Herrn Weißer, die uns bei der Entwicklung der Magnetfalle tatkräftig unterstützt haben. Außerdem danke ich Herrn Herdt für seinen Einsatz für die Natrium-und Lithiumöfen sowie Herrn Spiegel für seine guten Ratschläge bei mechanischen Problemen aller Art.

- Der Elektronikabteilung, vor allem Jürgen Schölles und Alexander Leonhardt, bin ich für ihre geduldigen Erklärungen diverser Schaltungen und für die Reparaturen unser Netzteile dankbar.

- Dankeschön an die Heidelberg Graduate School of Fundamental Physics (HGSFP) als Ansprechpartner für alle Promotionsfragen und für ihr Graduiertenprogramm, insbesondere die Graduiertentage.

- Der Landesgraduiertenförderung Baden-Württemberg danke ich für ihre finanzielle Unterstützung durch die ich mich voll auf meine Dissertation konzentrieren konnte.

- Ein ganz spezieller Dank gilt meinen Freunden, meinen Geschwistern und meinen Eltern, die mich immer unterstützt haben und ohne die diese Arbeit nicht möglich gewesen wäre.

- Zuletzt möchte ich mich besonders bei meiner Freundin Anne für die nötige Ablenkung von der Laborarbeit und ihr Verständnis bedanken. Ihr Rückhalt in der nicht immer einfachen Zeit bedeutet mir mehr als ich in Worte fassen kann.